MICROSTRUCTURE OF SUPER–DUPLEX STAINLESS STEELS

By
Shahriar Sharafi
St. Edmund College

Department of Materials Science and Metallurgy
Pembroke Street
Cambridge
CB2 3QZ

A dissertation submitted for the
degree of Doctor of Philosophy
at the University of Cambridge

September 1993

آنانکه محیط فضل و آداب شدند در جمع علوم شمع اصحاب شدند

زین شب تاریک نبردند بروز گفتند فسانه‌ای و در خواب شدند

The experts of Science and Culture are like candles
Which light the way through the darkness for humanity
But they never find daylight
They just tell a tale and leave.

OMAR KHAYYAM
The great Persian Scientist, Philosopher and Poet
Late 11th/early 12th Century

Dedicated to My Parents
Mrs Effat and Mr Hassan Sharafi
and My Sisters Shohreh and Shahrzad

PREFACE

This dissertation is submitted for the degree of Doctor of Philosophy at the University of Cambridge. The investigation described herein was carried out under the supervision of Dr. H.K.D.H. Bhadeshia in the Department of Materials Science and Metallurgy, Cambridge, between April 1990 and September 1993.

Except where acknowledgement and reference to previous work is made, this work is, to the best of my knowledge, original and has been carried out without collaboration. Neither this, nor any substantially similar dissertation has been, or is being submitted for any degree, diploma or other qualification at any other university. This dissertation contains less than 60,000 words.

Shahriar Sharafi

September 1993

ACKNOWLEDGEMENTS

I wish to thank Professor C. Humphreys for the provision of laboratory facilities in the Department of Materials Science and Metallurgy at the University of Cambridge. I am indebted to Dr H.K.D.H. Bhadeshia for his encouragement and enthusiasm during the course of this work.

Thanks are also extended to the technical staff of the department, particularly Mr T. Pettit, Mr J. Leader, the electron microscopy department - Mr D. Nicol for valuable advice on electron microscopy and carbon replica preparation, the photographic department - Mrs C. Best and Mr B. Barber for their generous help, and Mr G. Morgan and his staff in the workshop for making some of my specimens.

I must also thank my friends and colleagues in the department, especially members of the Phase Transformations group, with whom it has been very enjoyable to work.

Finally, I would like to thank both my father, Mr Hasan Sharafi and the Ministry of Culture and Higher Education of Iran for their financial support and ESAB AB of Sweden for providing the materials.

ABSTRACT

Corrosion resistant stainless steels with a mixed microstructure of δ–ferrite and austenite in approximately equal proportion are called "duplex stainless steels". The corrosion resistance can be improved by boosting the chromium concentration, and maintaining the phase balance by a compensating increment in the nickel concentration. These enhanced alloys are called the "super–duplex stainless steels" and are the subject of this dissertation.

The stabilities of a variety of common phases (liquid, ferrite, austenite and sigma) have been assessed for a series of alloys using available phase diagram calculation software and associated thermodynamic data. The alloys chosen covered both duplex and super–duplex systems, of the type typical in the wrought and welded conditions. The results are to some extent verified experimentally using long term heat–treatments, quantitative microscopy, differential scanning calorimetry and microanalytical techniques.

The calculations of the equilibrium state are then used as an aid to the interpretation of microstructural studies. One of the most interesting results is that unlike the duplex stainless steels, it is impossible for super–duplex stainless steels to solidify into a fully ferritic microstructure. Thermodynamic calculations indicate that the suppression of the austenite phase in super–duplex alloys would lead to the persistence of liquid to incredibly low temperatures, a phenomenon which is unlikely and has not been observed experimentally. Indeed, it is found experimentally that the chemical composition of some of the austenite present in super–duplex welds is consistent with its formation directly from the liquid state. The austenite does, however, precipitate by the solid state transformation of δ–ferrite is not only of a different composition but also a different morphology.

Attempts at inducing the super–duplex alloys to solidify into a ferritic state using laser welds which traverse dissimilar metal junctions failed, confirming the mixed mode of solidification. These experiments lend further weight to the argument that super duplex stainless steels are highly unlikely to solidify in the fully ferritic condition.

The morphology and kinetics of sigma phase formation has also been studied. The results are on the whole found to be consistent with expectations from thermodynamic calculations. Local changes in chemistry as a consequence of sigma phase formation often induces the further transformation of ferrite to austenite, in some cases leading to the complete absence of ferrite in the final microstructure. Other precipitate phases have also been studied, in particular, the precipitation of chromium nitride has been observed when the nitrogen concentration is exceptionally high in super–duplex alloys.

An attempt is also made to develop some simple equations for estimating the ferritisation temperature and austenite fraction as a function of alloy chemistry, using the output from thermodynamic calculations as the database.

CONTENTS

NOMENCLATURE AND ABBREVIATIONS

a	Lattice parameter
AF	Austenitic–Ferritic
at.%	concentration in atomic percent
γ	austenite
δ	delta–ferrite
σ	sigma–phase
AOD	Argon–Oxygen Decarburisation
b.c.c.	body–centered cubic
C_p	specific heat at constant pressure
Cr_{eq}	chromium equivalent
DSC	Differential Scanning Calorimetry
EDX	Energy–Dispersive X–ray analysis
FA	Ferritic–Austenitic
f.c.c.	face–centered cubic
HAZ	Heat Affected Zone
h.c.p.	hexagonal close packed
I	arc current
i	current density
M_s	martensite start temperature
MMA	Manual Metal Arc–welding
MTDATA	Metallurgical and Thermodynamic Data service
Ni_{eq}	nickel equivalent
NPL	National Physic Laboratory
P.R.E.	Pitting Resistance Equivalent
q	heat input
SCC	Stress Corrosion Cracking
SEM	scanning electron microscopy
T_δ	ferritisation temperature
$T_{\sigma s}$	sigma start temperature
TEM	Transmission Electron Microscopy
TPL	Task Programming Language
TTT	Time–Temperature–Transformation

V	arc voltage
V_γ	Volume fraction of austenite
VOD	vacuum–oxygen decarburisation
VHN	Vickers hardness number
v	welding speed (mm/sec)
wt.%	concentration in weight percent

Chapter 1

GENERAL INTRODUCTION TO STAINLESS STEELS

1.1 Introduction

Stainless steels are extremely useful as engineering materials because of their wide range of properties and general resistance to environmental conditions. For example, their proof stress values range from 200 MPa to 2000 MPa, they have high ductility and toughness over a wide range of temperatures, exhibit excellent corrosion and high temperature oxidation resistance. They can be used not only for structural and containment applications but also as creep resistant materials in power plant engineering. The temperature range over which they are used extends from the boiling point of nitrogen to temperatures well above the melting point of aluminium. They are readily formed and welded, exhibit no ductile-brittle transition during fracture in the austenitic condition, and can be produced with a wide range of magnetic and thermal properties. Their main disadvantage is, of course, their cost although in the context of other advanced materials, the cost is negligible. The most important property of stainless steels is undoubtedly their corrosion resistance, without which they would find little use because their mechanical properties and formability can be equalled or exceeded by much cheaper but non-stainless steel (Pickering, 1984).

One of the first industrial development of a stainless steel was done by H. Brealey some seventy five years ago (Truman, 1980) after establishing the corrosion resistance of chromium containing steels. The 13 wt.% Cr, 0.25 wt.% C martensitic stainless steel thus commercially launched as a cutlery material is still almost identical with the current steel that is used for stainless knives. Actually, some of the earliest work carried out almost 100 years earlier noted that chromium improved the corrosion resistance of steel. These observations did not receive the attention they deserved, largely because the detrimental effect of carbon was not then appreciated and also because an extensive programme of research by Hadfield in 1892 had shown that chromium decreased the corrosion resistance of steel in sulphuric acid. Between 1904 and 1914, several workers

(for example Guillet, 1904; Geisen, 1909) studied the metallurgy and properties of Cr and Cr-Ni steels, some of which had austenitic, ferritic and martensitic structures. The martensitic steels, first exploited commercially, were not suitable for sheet manufacture, but the development of the austenitic steels just prior to the first World War formed the basis for the now ubiquitous '18 Cr - 8 Ni' alloys which are ideal for the production of flat rolled products and for subsequent fabrication.

Since the early 1920's the development of the various types of stainless steel has proceeded with ever increasing rapidity. It was quickly recognised that more than 10 wt.% Cr imparted good corrosion resistance and that somewhat higher Cr contents conferred high temperature oxidation resistance as well. Thus the stainless steels came to be used as heat resisting materials, and when suitably alloyed, as creep resisting steels. The use of the stainless steels for these special applications was perhaps the first indication that, whilst corrosion resistance was paramount, it had to be combined with other properties and optimum combinations of properties are obviously highly desirable. Such properties are:

(i) Corrosion/oxidation resistance in the operating environment.

(ii) Good fabricability, both during hot and cold processing.

(iii) Weldability without impairment of either corrosion resistance or mechanical properties.

(iv) Requisite physical and mechanical properties.

1.2 Types of Stainless Steels

Stainless steels have been conventionally classified into several categories. Some of these categories are:

1.2.1 Transformable or Martensitic Steels

They usually contain 12-17 wt.% Cr and 0.1-1.5 wt.% C. The higher carbon varieties mainly being cutlery and tool materials. The lower carbon varieties still

have high hardenability, which renders them air hardenable so that tempering is necessary to produce useful combinations of strength, toughness and ductility. The common type of steel, 11-13 wt.% Cr (Briggs and Parker, 1965) is alloyed with Mo, W, V and Nb to increase its tempering resistance, which often necessitates the addition of up to 3 wt.% Ni to eliminate ferrite from the structure, which would otherwise decrease the potential strength.

Table 1.1. Chemical Composition (in wt.%) of Martensitic Steels (Schweitzer, 1983).

AISI type	Nominal composition (%)					
	C	Mn max.	Si max.	Cr	Ni	Other[a]
403	0.15 max.	1.00	0.50	11.50-13.00		
410	0.15 max.	1.00	1.00	11.50-13.50		
414	0.15 max.	1.00	1.00	11.50-13.50	1.25-2.50	
416	0.15 max.	1.25	1.00	12.00-14.00		0.15 S min.
416(Se)	0.15 max.	1.25	1.00	12.00-14.00		0.15 S min.
420	0.15 min.	1.00	1.00	12.00-14.00		
431	0.20 max.	1.00	1.00	15.00-17.00	1.25-2.50	
440A	0.60-0.75	1.00	1.00	16.00-18.00		0.75 Mo max.
440B	0.75-0.95	1.00	1.00	16.00-18.00		0.75 Mo max.
440C	0.95-1.20	1.00	1.00	16.00-18.00		0.75 Mo max.
501	0.10 min.	1.00	1.00	4.00-6.00		0.40-0.65 Mo
502	1.10 max.	1.00	1.00	4.00-6.00		0.40-0.65 Mo

[a]Other elements in addition to those shown are as follows: Phosphorus is 0.06% max. in types 416 and 416(Se); sulfur is 0.03% max. in types 403, 410, 414, 420, 431, 440A, 440B, 440C, 501, and 502.

The 14-17 wt.% Cr steels may also be alloyed with up to 7 wt.% Ni or 5 wt.% Mn, with other alloying elements such as Mo, Al, Ti, Co and Cu. In these steels, control can be exerted such that the steel be austenite in the solution treated condition and can be formed readily, but can then be transformed to martensite which is subsequently tempered (Briggs and Parker, 1965).

In these 'Controlled Transformation' steels the additional alloying elements are used to improve tempering resistance, but more especially to introduce precipitation hardening, and the same elements can be used to promote precipitation hardening in the base 12 wt.% Cr steels. In the precipitation hardened

condition proof stress values up to 1400 MPa can be achieved. The uses of controlled transformation stainless steels lie in the aerospace and aircraft industries for such applications as missile casting, and in military hardware and high strength:weight ratio applications. Table 1.1 gives the chemical composition of the various martensitic alloys, and Table 1.2 gives the mechanical properties.

Table 1.2. Mechanical Properties of Martensitic Stainless Steels (Schweitzer, 1983).

Stainless steel type	Form and condition	Yield strength (0.2% offset), MPa	Tensile strength, MPa	Elongation in 2 in. , %
403	Annealed	517	276	30
410	Annealed	276	517	30
410	Heat treated	793	1034	15
414	Annealed	552	689	22
414	Heat treated	1034	1379	17
416	Annealed	517	276	30
416(Se)	Annealed	517	276	30
420	Annealed	414	676	28
420	Heat treated	1379	1723	8
431	Annealed	586	827	25
431	Heat treated	1634	1351	20
440A	Annealed	724	414	20
440B	Annealed	738	428	18
440C	Annealed	758	448	13
501	Annealed	483	207	28
502	Annealed	483	207	30

1.2.2 Ferritic Stainless Steels

These steels usually contain 15-30 wt.% Cr with alloying additions of Mo, Ti or Nb and are fully ferritic up to the melting point. They have relatively low work hardening rates compared with the austenitic stainless steels, but higher yield stresses due to their body- centred cubic (b.c.c.) crystal structure. They exhibit a ductile-brittle fracture transition which often leads to a lack of toughness, but they have the advantage over the austenitic steels of showing virtual

immunity to chloride induced stress corrosion cracking. Whilst having good corrosion resistance, which can be increased by higher Cr contents and Mo additions, they are generally less corrosion resistant than the austenitic steels and also somewhat less formable. They substitute however for the more expensive austenitic materials in the less severe corrosion environments and where formability requirements are less stringent. Over recent years the interstitial contents C and N have been greatly decreased to improve corrosion, toughness, ductility and weldability. These are super-ferritic steels with C and N contents often less than 0.02 wt.% each, but they can suffer from more exaggerated grain growth which may offset the beneficial effect of low interstitial content on toughness.

Table 1.3. Chemical Composition (in wt.%) of Ferritic Steel (Schweitzer, 1983).

AISI type	Nominal Composition (%)				
	C max.	Mn max.	Si min.	Cr	Other[a]
405	0.08	1.00	1.00	11.50-14.50	0.10-0.30 Al
403	0.12	1.00	1.00	14.00-18.00	
430F	0.12	1.25	1.00	14.00-18.00	0.15 S min.
430 (Se)	0.12	1.25	1.00	14.00-18.00	0.15 Se min.
444	0.025	1.00	1.00 (max)	17.5-19.5	1.75-2.50 Mo
446	0.20	1.50	1.00	23.00-17.00	0.25 max. N

[a]Other elements in addition to those shown are as follows: Phosphorus is 0.06% max. in types 430F and 430 (Se); sulfur is 0.030% max. in types 405, 430, 444, and 446; 0.15% min. in type 430F; nickel 1.00% max. in type 444; titanium + niobium 0.80% max. in type 444.

Typical applications of fully ferritic steels are in domestic, catering, architectural and decorative uses. They are used widely in the chemical, food, transportation and automobile industries, whilst the super ferritic steels are being used increasingly in seawater cooled condensers, desalination plant and more recently in heat exchangers (Redmond and Miska, 1982). Table 1.3 lists the chemical composition of the members of this group, and Table 1.4 gives the mechanical properties.

Table 1.4. Mechanical Properties of Ferritic Stainless Steels (Schweitzer, 1983).

Stainless steel type	Form and condition	Yield strength (0.2% offset), MPa	Tensile strength, MPa	Elongation in 2 in. , %
405	Annealed	483	276	30
430	Annealed	517	310	30
430F	Annealed	276	483	350
430F	Cold rolled	655	758	10
430(Se)	Annealed	552	379	25
446	Annealed	344	552	30

1.2.3 Austenitic Stainless Steels

These types of stainless steels are the most widely used, comprising 70-80 wt.% of stainless production (Leach, 1982). They usually contain 16-25 wt.% Cr, 7-20 wt.% Ni and current developments have decreased the carbon content to well below 0.03 wt.%. They are frequently alloyed with Mo, Ti and Nb to promote creep resistance and, with other than lowest carbon contents, stabilisation against intergranular corrosion. The higher Cr steels, which may exceed 35 wt.% Cr, usually require to be balanced constitutionally by high Ni contents up to 35 wt.% when they approach the iron-base superalloys.

The austenitic steels have lower proof stresses but higher work hardening rates than the ferritic stainless steels, and are more easily welded and cold formed. Their toughness is high, exhibiting no ductile-brittle fracture transition and their exceptional corrosion resistance is mainly marred by their susceptibility to chloride induced stress corrosion cracking. Whilst being essentially austenitic at all temperatures, the austenitic steels may contain (delta) ferrite, a small amount of which is detrimental to hot workability (Bywater and Gladman, 1976). Anyway some delta ferrite is essential for good weldability.

Table 1.5. Chemical Composition in wt.% of Austenitic Stainless Steels after Schweitzer (1983).

AISI type	Nominal composition, %					
	C max.	Mn max.	Si max.	Cr	Ni	Others[a]
201	0.15	7.5[b]	1.00	16.00-8.00	3.50-5.50	0.25 max. N
202	0.15	10.00[c]	1.00	17.00-19.00	4.00-6.00	0.25 max. N
205	0.25	15.50[d]	0.50	16.50-18.00	1.00-1.75	0.32/0.4 max. N
301	0.15	2.00	1.00	16.00-18.00	6.00-8.00	
302	0.15	2.00	1.00	17.00-19.00	8.00-10.00	
302B	0.15	2.00	3.00[e]	17.00-19.00	8.00-10.00	
303	0.15	2.00	1.00	17.00-19.00	8.00-10.00	0.15 min. S
303(Se)	0.15	2.00	1.00	17.00-19.00	8.00-10.00	0.15 min. Se
304	0.08	2.00	1.00	18.00-20.00	8.00-12.00	
304L	0.03	2.00	1.00	18.00-20.00	8.00-12.00	
304N	0.08	2.00	1.00	18.00-20.00	8.00-10.50	0.1/0.16 N
305	0.12	2.00	1.00	17.00-19.00	10.00-13.00	
308	0.08	2.00	1.00	19.00-21.00	10.00-12.00	
309	0.20	2.00	1.00	22.00-24.00	12.00-15.00	
309S	0.08	2.00	1.00	22.00-24.00	12.00-15.00	
310	0.25	2.00	1.50	24.00-26.00	19.00-22.00	
310S	0.08	2.00	1.50	24.00-26.00	19.00-22.00	
314	0.25	2.00	3.00[f]	23.00-26.00	19.00-22.00	
316	0.08	2.00	1.00	16.00-18.00	10.00-14.00	2.00-3.00 Mo
316F	0.08	2.00	1.00	16.00-18.00	10.00-14.00	1.75-2.50 Mo
316L	0.03	2.00	1.00	16.00-18.00	10.00-14.00	2.00/3.00 Mo
316N	0.08	2.00	1.00	16.00-18.00	10.00-14.00	2.00-3.00 Mo
317	0.08	2.00	1.00	18.00-20.00	11.00-15.00	3.00-4.00 Mo
317L	0.03	2.00	1.00	18.00-20.00	11.00-15.00	3.00-4.00 Mo
321	0.08	2.00	1.00	17.00-19.00	9.00-12.00	5XC min Cb-Ta
330	0.08	2.00	1.5[g]	17.00-20.00	34.00-37.00	0.10TA 0.20 Cb
347	0.08	2.00	1.00	17.00-19.00	9.00-13.00	10XC min. Cb-Ta
348	0.08	2.00	1.00	17.00-19.00	9.00-13.00	10C min. Cb-Ta

[a]Other elements in addition to those shown are as follows: Phosporus is 0.03% max. in type 205; 0.06% max. in types 201 and 202; 0.045% max. in types 301, 302, 302B, 304, 304L, 304N, 305, 308, 309, 309S, 310, 310S, 314, 316, 316N, 316L, 317, 317L, 321, 330, 347, and 348; 0.20% max. in types 303, 303(Se), and 316D. Sulfur is 0.030% max, in types 201, 202, 205, 301, 302, 302B, 304, 304L, 304N, 305, 308, 309, 309S, 310, 310X, 314, 316, 316L, 316N, 317, 317L, 321, 330, 347, and 348; 0.15% min, in type 303; 0.10 min. in type 316D.

[b]Mn range 4.40 to 7.50.

[c]Mn range 7.50 to 10.00.

[d]Mn range 14.00 to 15.50.

[e]Si range 2.00 to 3.00.

[f]Si range 1.50 to 3.00.

Table 1.6. Mechanical Properties of Austenitic Stainless Steels after Schweitzer (1983).

Stainless steel type	Form and condition	Yield strength (0.2% offset), MPa	Tensile strength, MPa	Elongation in 2 in. , %
201	Annealed	379	793	55
202	Annealed	344	689	60
205	Annealed	476	827	58
301	Annealed	207	689	72
301	Cold rolled	up to 1138	up to 1379	15
302	Annealed	207	620	60
302	Cold rolled	up to 1138	up to 1310	8
302B	Annealed	276	655	50
303	Annealed	241	620	50
303(Se)	Annealed	241	620	50
304	Annealed	207	586	62
304	Cold rolled	up to 1103	up to 1275	8
304L	Annealed	207	552	60
304L	Cold drawn	655	862	25
304N	Annealed	331	620	50
305	Annealed	586	255	55
308	Annealed	586	241	55
309	Annealed	207	565	50
309	Cold rolled	up to 827	up to 965	4
309S	Annealed	620	276	45
310	Annealed	689	344	50
310S	Annealed	655	276	45
314	Annealed	689	344	45
316	Annealed	207	620	50
316	Cold rolled	up to 827	up to 1034	8
316F	Annealed	262	586	60
316L	Annealed	207	552	60
316L	Cold drawn	414	620	45
316N	Annealed	331	552	48
317	Annealed	552	276	50
317L	Annealed	262	593	55
321	Annealed	207	586	50
321	Cold rolled	up to 827	up to 1034	5
330	Annealed	262	552	40
347	Annealed	207	586	50
347	Cold rolled	up to 827	up to 1034	5
348	Annealed	634	241	50

A little used type of austenitic stainless steel nowadays is the lower nickel content type in which a reduced concentration is compensated by up to 10 wt.% Mn and 0.25 wt.% N. These steels have higher strengths than the conventional austenitic steels by virtue mainly of the solid solution strengthening by N. The applications of austenitic stainless steels are widespread in the chemical processing, food, constructional, power plant and other industries in which their corrosion resistance, cryogenic properties, creep and oxidation resistance are of predominant importance. Table 1.5 gives the chemical compositions of the various austenitic stainless steels, and Table 1.6 provides the mechanical properties.

1.2.4 Duplex Stainless Steels

Duplex stainless steels are a relatively new class in the stainless steels family, although they have been known for almost 45 years (Truman, 1979). They comprise virtually equal amounts of austenite and ferrite. Many austenitic stainless steels contain up to 20 vol.% ferrite, but the modern duplex stainless steels contain 50 vol.% ferrite and were originally conceived as a super plastic alloy, although this potential has not been fully utilised. The presence of ferrite considerably increases the strength, and also greatly improves the stress corrosion resistance although decreasing the toughness at low temperature. Also the presence of the ferrite causes a marked refinement of the grain size both the austenite and the ferrite, and this can improve the resistance to intergranular corrosion (Truman, 1980). Anyway, the tendency in these steels is to very low carbon contents which makes intergranular corrosion much less of problem.

Table 1.7. Composition in wt.% of Some Duplex Stainless Steels (Sedriks, 1979).

Designation	Typical Composition[a], (%)							
	Cr	Ni	C	Mn	Si	P	S	Other
AISI Type 329	28.0	6.0	0.10	2.00	1.0	0.04	0.03	Mo 1.5
326[b]	26.0	6.5	0.05	1.00	0.6	0.01	0.01	Ti 0.25
SANDVIK 3RE60	18.5	4.5	0.02	1.50	1.6	0.01	0.01	Mo 2.5

[a] Balance iron.
[b] Earlier version known as developmental alloy IN-744; commercially available since 1970 under proprietary designations of UNILOY 326, AL 326 and H-326.
Sources: Various.

The appropriate structure can be produced by a wide range of compositions, usually relatively lean in Ni and varying in Cr from 18-30 wt.%, with additions of Mo and in some cases stabilisation by Nb or Ti. The addition of N is a recent development. Whilst there is partitioning of alloying elements between the ferrite and austenite, it is stated that this is not excessive (Redmond and Miska, 1982) and has no serious effect on corrosion resistance. The partitioning does lead to increase Cr in the ferrite, which leads to various forms of embrittlement by alpha prime or sigma phase.

Table 1.8. Typical Mechanical Properties of Some Duplex Stainless Steels after Sedriks (1979).

Designation	Tensile Strength, MPa[a]	Yield Strength (0.2% Offset) MPa	Elongation, %	Hardness, Rockwell B
AISI Type 329	724	551	25	98
326	689	517	35	95
SANDVIK 3RE60	717	482	48	92

[a]Mill annealed condition.
[b]1 MPa = 145.03 ksi.
Sources: Various.

The applications of modern duplex stainless steels is in plate form and as tubes in the paper industry, as heat exchangers and for various uses in chemical engineering. A major use however is as a casting alloy or forgings in pumps, valves and general marine engineering.

The compositions of some of the currently available duplex stainless steels are shown in Table 1.7 and their mechanical properties are listed in Table 1.8. Only type 329 is an AISI grade.

1.3 Stainless Steelmaking Processes

Up to 20 years ago, stainless steels were mainly made in the electric arc furnace, using more or less conventional oxidation and refining methods. The problem with the process was to obtain a high enough oxygen potential to oxidise the carbon to very low levels, less than 0.03 wt%, without oxidising too much

Cr. The thermodynamics of the Fe-Cr-C-O system show that as C is oxidised from the melt, by oxygen lancing in the electric arc furnace, Cr is also oxidised out, Figure 1.1. However as the bath temperature is increased, the amount of Cr which can be retained at a given C content increases rapidly (Hilty and Kaveney, 1977). The high temperatures necessary to retain 18 wt.% Cr in the bath and thus facilitate the economic use of large amounts of stainless steel scrap in the base furnace charge, about 2000°C for carbon contents below 0.03 wt.%, lead to major problems associated with wear of the furnace refractory linings. Consequently lower temperatures had to be used, with the penalty that low Cr contents only could be retained, which necessitated additions of ferro-chromium to achieve the requisite Cr content of some 17-19 wt.%. If a very low carbon content was deemed necessary in the final alloy, very low carbon ferro-chromium was required as the addition with further cost penalty. Thus the simple electric arc process is unsatisfactory for the manufacture of extra low carbon stainless steel from predominantly scrap stainless steel charges, and the minimum economic carbon content was no less than 0.06 wt.%.

The thermodynamics of carbon oxidation from Fe-Cr melt shows that a given retained Cr content in the melt is inversely proportional to the partial pressure of carbon monoxide in the system, Figure 1.2. This fact led to the development of several processes which used low partial pressures of CO to enable low C and high Cr contents to be obtained in the steel bath without recourse to very high temperatures (Leach, Rodgers and Sheehan, 1978). Predominant among these processes is the Argon-Oxygen Decarburisation (AOD) but there are others using Vacuum-Oxygen Decarburisation (VOD) and steam as the diluent gas -Cruesot-Loire-Uddeholm process (CLU). In the AOD process the electric arc furnace is essentially used as a melting unit, the charge comprising stainless scrap and ferro - chromium to achieve more or less the correct Cr (and Ni) content but with up to 2 wt.% C. The melt is then transferred into a converter and blown with argon/oxygen gas mixtures through tuyeres. The ratio of the two gases varies with the carbon content of the melt, finally achieving a partial pressure of CO of about 0.1 atmospheres which achieves a C content below 0.02 wt.%. The AOD process produces cleaner steels than the electric

arc process due to the lower oxygen content which can be as low as 0.005/0.010 wt.% after the final reducing blow with pure argon.

In the conventional AOD process, expensive argon can be replaced by nitrogen in the earlier stages of the blow, but if very low nitrogen contents are required, argon must be used for the final stages of the process. Because of the high Cr content, the solubility of nitrogen in the steel is increased (Figure 1.3) and Mn has a similar effect.

The VOD process is related to the AOD process by using a reduced partial pressure of CO. The ladle containing the liquid steel is top blown with oxygen in a vacuum tank, and argon is bubbled through the melt. The oxygen blow enhances nitrogen removal to 0.001/0.004 wt.%, and at the end of the blow the carbon content can be 0.01 wt.% or less. Continued argon bubbling then allows continuing reaction of C and O dissolved in the steel (as can also be achieved in the AOD process) so the ultra low carbon contents are reported to be achieved (Climax Molybdenum Co. 1977). It is the advent of these pneumatic processes which has allowed very low carbon contents to be an economic reality for stainless steels, and for the ultra low interstitial contents to be available for the super-ferritic steels.

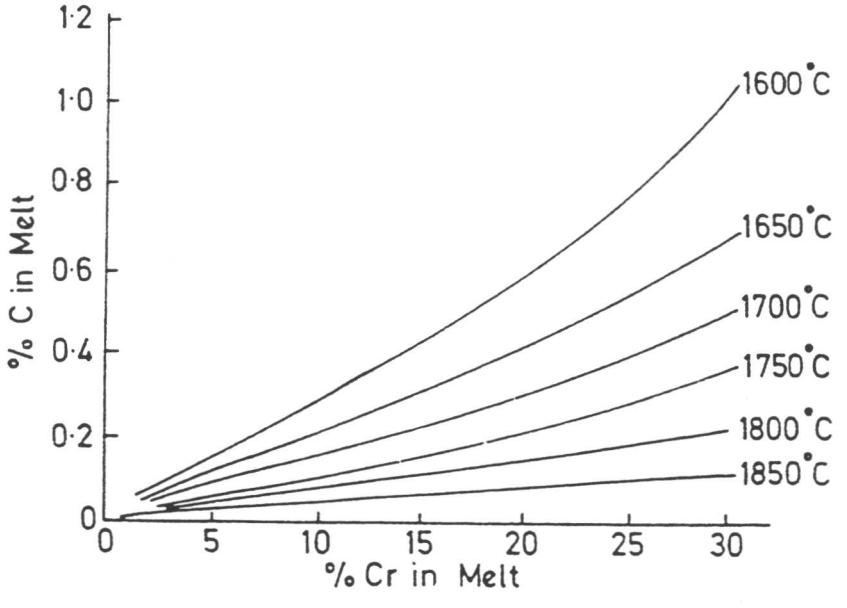

Figure 1.1. Effect of temperature on equilibrium between C and Cr in iron melts. The compositions are in wt.%. (Pickering, 1984).

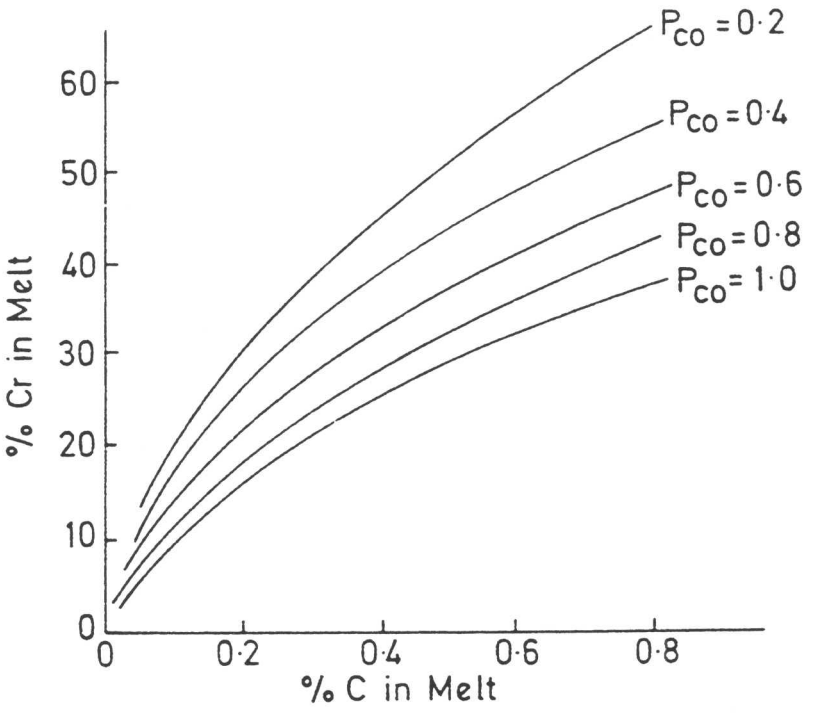

Figure 1.2. Effect of P_{CO} on Cr - C equilibrium in iron melts at 1700°C. The compositions are in wt.% (Pickering, 1984).

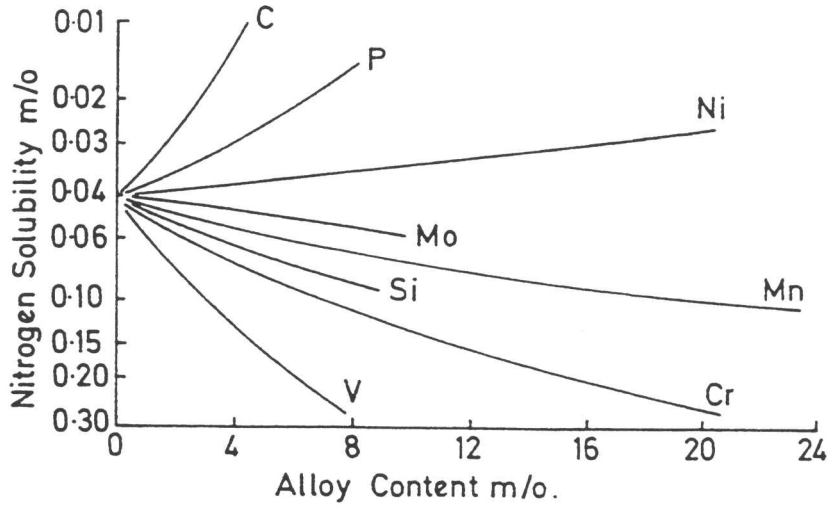

Figure 1.3. Effect of alloys on N solubility in iron at 1600°C (1 Atmosphere N), compositions are in mole% (Pickering, 1984).

1.4 Summary

Although many kinds of stainless steels especially martensitic and austenitic have been available for more than 75 years, the demand for better corrosion and mechanical properties has led to the development of duplex stainless steels. These have been designed to combine the favourable properties of ferrite (δ) and austenite (γ) and for an enhanced resistance to stress corrosion cracking compared with austenitic stainless steels. Super-duplex stainless steels with even higher Cr, Mo and N contents compared with conventional duplex stainless steels have more recently been available commercially. These are designed to be particularly resistance to pitting corrosion resistance and are the main topic of this study.

Chapter 2

EXPERIMENTAL TECHNIQUES

2.1 Introduction

In this chapter, the materials, heat treatment, high temperature differential scanning calorimetry (DSC) and the other experimental procedures are explained. As the work has concentrated on the relationship between the microstructure and properties of super duplex stainless steel weld metals, the microstructure as well as the behaviour under isothermal and continuous heating and cooling has been examined. A series of heat treatment experiments was carried out, firstly to determine the ferritisation temperature and secondly to measure a portion of the time-temperature-transformation (TTT) diagram of super duplex stainless steels in the temperature range 600-1000 °C, where they are susceptible to sigma phase formation.

2.2 Materials

All the materials used in this work have been provided by ESAB AB of Sweden. Their chemical compositions are presented in Table 2.1. The first materials available were wrought alloys designated IC373, IC378 and IC381, in the form of small slabs. These are commercial duplex stainless steels. Later, weldments of super duplex stainless steels designated A199 to A219 were received. These multi-run weld pads are deposited on mild steel plates, 8 mm thick, with approximately 8 runs being deposited on top of each other. To study the laser welding of dissimilar stainless steels, an austenitic stainless steel 904L was also provided by ESAB AB.

2.3 Welding

The weld pads A119, A200 and A201 were deposited on mild steel plates using the manual metal arc (MMA) welding technique. This welding process has been used for all of the welds in this investigation. The welding conditions are presented in Table 2.2. Heat inputs are in the range of 0.6-1.4 kJ/mm. The interpass temperatures were kept below 150°C.

2.3.1 Laser welding

To study the solidification behaviour of stainless steels and to elucidate the role of austenite or ferrite nucleation, a series of laser welds traversing stainless steels of different chemical compositions were investigated. The welds were made on thin sheet couples of stainless steels of two different compositions butted together, the weld starting on a sheet of one composition and running into the other across the junction (Figure 2.1). Laser beam welding was carried out using a pulsed Nd:YAG laser (Lumonics Model JK701) capable of delivering an average power of 400 W. A 152 mm lens was used to focus the beam sharply onto the specimen surface. A pulse length of 1 ms and a pulse rate of 200 s^{-1} were used. In order to get a full penetration all the specimens were rolled down to 1 mm thickness and the welding speed was 1.2 mm s^{-1} unless otherwise stated. The laser power level was set to 200-210 W. These conditions leads to a energy input rate of about 0.17 kJ/mm. In all cases, the length of travel of the laser was about 30 mm and the laser was focused precisely onto the surface of the samples.

Table 2.1. Chemical compositions (wt.%) of the alloys used in this investigation.

Material	C	Si	Mn	P	S	Cr	Ni	Mo	V	Nb	Ti	Al	Cu	N	O
IC373	0.02	0.50	0.67	0.02	0.01	25.9	5.1	3.68	0.05	0.03	<0.01	-	1.83	0.14	0.003
IC378	0.03	0.39	1.38	0.03	0.01	21.8	5.5	3.03	0.07	<0.01	<0.01	-	0.18	0.14	0.006
IC381	0.02	0.48	1.92	0.03	0.01	22.1	5.8	3.17	0.13	<0.01	<0.01	-	0.07	0.14	0.007
A199	0.02	0.54	0.68	0.02	0.01	25.7	9.3	4.62	0.09	0.02	0.02	0.001	0.02	0.26	0.09
A200	0.02	0.53	0.62	0.02	0.001	25.1	10.2	3.30	0.09	0.02	0.02	0.001	0.08	0.27	0.09
A201	0.02	0.54	0.64	0.02	0.01	26.1	9.1	4.15	0.09	0.02	0.02	0.001	0.02	0.26	0.09
A213	0.03	0.68	0.68	0.02	0.002	25.4	9.5	4.10	0.09	0.02	0.01	0.002	0.09	0.24	0.08
A214	0.03	0.62	0.62	0.02	0.002	25.4	9.5	4.15	0.09	0.02	0.01	0.002	0.09	0.25	0.07
A215	0.03	0.64	0.65	0.02	0.002	25.5	9.5	4.08	0.08	0.02	0.01	0.002	1.0	0.24	0.07
A216	0.03	0.64	0.68	0.02	0.002	25.5	9.5	4.10	0.08	0.02	0.02	0.002	1.0	0.25	0.08
A219	0.03	0.60	0.70	0.02	0.007	25.6	9.4	4.08	-	-	-	-	-	0.27	-
904L	0.017	0.30	1.53	0.01	0.01	20.0	24.7	-	-	-	-	-	1.5	0.05	0.003

Table 2.2. Welding conditions for the weld alloys studied.

Material	ϕ (mm)	length (mm)	width (mm)	height (mm)	Inter-pass temp,°C		V	Amps	speed mm/s	Heat input kJ/mm
A213	3.25	90	40	25	<100	DC+	22.8	114	4.16	0.62
A214	3.25	90	40	25	<100	DC+	25.7	114	2.04	1.44
A215	3.25	90	40	25	<100	DC+	25.2	115	2.50	1.16
A216	3.25	90	40	25	<150	DC+	28.0	114	2.94	1.08
A219	3.25	140	50	40	<150	DC+	22.3	100	2.5	1.0

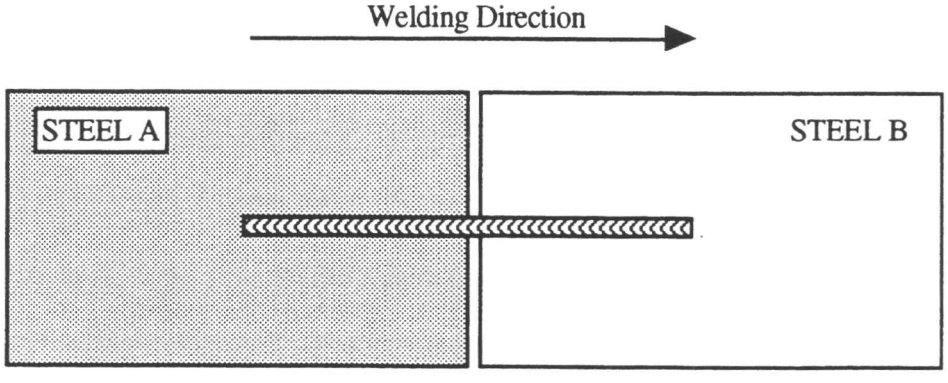

Figure 2.1. Schematic illustration of butt weld across dissimilar metal junction.

2.4 Optical Microscopy

The specimens for metallography were prepared in the following manner. Small sections of metal were hot mounted in acrylic moulding powder, thin large sections of weld metals were cold mounted and even larger specimens were prepared without mounting. Then all the specimens were ground on silicon carbide paper down to 1200 grit size. Finally, they were polished with 6, 1 and $\frac{1}{4}$ micron diamond paste coated on cloth. The specimens were then thoroughly cleaned with soap and running water and washed with alcohol before drying.

Two different etchants were used. Beraha's colour etchant 10 ml HCl, 100 ml H_2O and 0.5 to 1 gram $K_2S_2O_5$ was used for optical microscopy. This darkens

the ferrite phase. This etchant should always be used in a freshly prepared condition and discarded immediately after use. The second etchant was 12.5 g $CuCl_2$, 50 ml ethanol and 30 ml HCl; this etchant was used for preparing samples for SEM EDX microanalysis as Beraha 's reagent interferes with microanalysis (gives a false sulphur signal).

2.5 Hardness Measurements

The surfaces of the specimens were polished before measuring their hardness. A Vickers hardness testing machine with a diamond indentor was used. The indentation loads applied were either 10 or 20 kg with an $\frac{2}{3}$" objective. All indentations were located at a suitable distance from the specimen edge in order to avoid any spurious effects. At least fifteen readings were recorded for each specimen and an average value calculated.

2.6 Heat Treatment

To study whether it is possible to obtain a wholly ferritic microstructure in duplex stainless steels by solution heat treatment at or above ferritisation temperatures, specimens were quenched into iced water after different holding times at 1300 °C. The results are discussed in the chapters that follow. In another series of experiments, specimens of super duplex stainless steels were heated in the range 600-1000 °C for different ageing times to investigate the precipitation behaviour, the effects on microstructure and hardness, and to attempt to determine the C-curve for sigma phase precipitation.

A resistance heated tube furnace was used for all heat treatment experiments and the temperature was maintained to within ±5 °C, monitored using a Pt-Pt/13Rh wt.% thermocouple. To prevent oxidation, all the specimens were sealed in silica tubes under partial pressure of argon (about 100 mm Hg). The quartz tubes were then placed on ceramic boats inside furnaces to prevent any contamination by contact with the base of the furnace.

2.7 Seescan Image Analysis

Optical specimens were used for mean linear intercept and image analysis methods. In the Seescan method the metallographic image is transferred by the

means of a video camera from either a photograph or directly from the specimen to a TV screen. To allow it to be converted to a computer format for processing, the image is first digitised. It is changed from continuously varying signals to an array of points, where each point is assigned a grey level. The task programming language (TPL) used permits 128 grey levels, where 0 represents black and 127 represents white. The array is assigned coordinates; the origin is in top left hand corner of Figure 2.2 (this is because of the way in which TV rate signals are scanned), and the TPL assigns an X axis of 0 to 255 and a Y axis of 0 to 255.

The volume fraction is measured by means of a frame measurement made on regions delineated by a circular or rectangular frame. The processed image is thresholded; a process by which the number of pixels within a range of grey shades in the frame is calculated. The total area of all the regions within the frame that have been selected using a grey scale threshold are also determined to enable fractions to be calculated. The measurement as such is influenced strongly by the thresholding process, i.e. the quality of the image transferred to the screen.

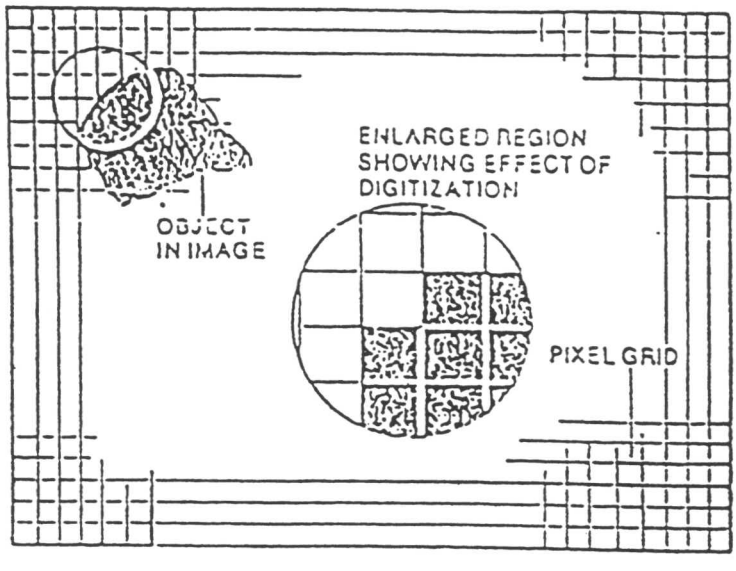

Figure 2.2. Image digitisation in the Seescan.

2.8 Scanning Electron Microscopy (SEM)

Scanning electron microscopy was used to study the precipitates in the ferrite grain and at grain boundaries at a higher magnification than is achievable in optical microscopy. Imaging was carried out in a Camscan S2 microscope operated at 30 kV using secondary electrons and 45° tilt with a working distance of about 30 mm.

2.9 Transmission Electron Microscopy (TEM)

Transmission electron microscopy was carried out on thin foil and carbon replica specimens using a Philips EM 400T electron microscope operated at 120 kV.

2.9.1 Thin foil preparation

Thin 3 mm discs are required as the starting point for thin foil preparation. These were cut directly from the heat-treated 3 mm rods using a SiC slitting wheel with a coolant to avoid heating during slitting. In the case of specimens with diameter larger than 3 mm thin slices were cut in 0.30 mm thickness and then 3 mm discs were mechanically punch out of thin slices. The discs were then mechanically ground by hand to 50 μm and then twin-jet electropolished to electron transparency at 50 V, with the solution being cooled to -5 °C using liquid nitrogen. The polishing solution was a mixture of 7 vol.% perchloric acid and 23 vol.% glycerol in methanol. Some difficulties were encountered when electropolishing welded metals, because the inclusions tended to fall out.

2.9.2 Extraction replica preparation

The extraction replica technique is very useful for the identification of carbide, nitride and precipitate phases in a metallic system. The main advantage of replicas over thin foils is that they eliminate any effect due to the steel matrix and thus enable the chemical composition of the particle to be measured more accurately.

Single-stage carbon extraction replicas were prepared using the method described by Smith and Nutting (1956) from surface prepared as for optical

microscopy. A carbon coating of 200-300 Å (colour blue-brown) was deposited in a vacuum of 10^{-5} torr on the etched specimens. The carbon film was scored using a sharp blade to enable removal of several small sections covering the whole area of the sample. The thin film was then removed by electrolytic etching in a solution containing 5% hydrochloric acid in methanol at +1.5 V. The film was then washed in industrial methylated spirits and floated off in distilled water and collected on 400 square mesh copper grids for TEM examination.

2.10 Energy Dispersive X-ray analysis (EDX)

For the detailed experimental results of alloying elements partitioning between δ-ferrite and austenite microanalyses were carried out using thin foils while for determining the chemical composition of fine precipitates (such as nitrides) carbon extraction replicas were used. A LINK series 860 energy dispersive X-ray spectrometer attached to a Phillips 400T 120 kV TEM was used for all the analyses. X-ray spectra were recorded at a specimen tilt of 35^o, and live time of at least 200 seconds were used to ensure statistically significant results, depending on the count rate from individual particles. The dead time was not allowed to exceed 25%. The data were analysed using the LINK RTS2-FLS software. The incident spot size was about 1000 Å and at least 20 different area of austenite and ferrite phases were analysed in the case of thin foils (in the case of particles on carbon replica also at least 20 isolated particles on each specimen were analysed).

Molybdenum has a much larger atomic mass compared with iron, chromium or nickel. Since the microanalytic measurements are carried out assuming that all elements absorb the X-ray to a similar degree, the molybdenum data are likely to be flawed, the extent of the error depending on the thickness of the particle along the electron beam direction (a parameter which is very difficult to determine for each individual particle).

2.11 High Temperature Differential Scanning Calorimetry (DSC)

Differential scanning calorimetry was used to measure the ferritisation temperature (T_δ) and solidus and liquidus temperatures of super duplex stainless steels.

To interpret the results obtained from a DSC experiment it is necessary to define specific heat. Specific heat at constant pressure (C_p) is the energy required to heat 1 gram of a substance by one Kelvin so the unit is: $Jg^{-1}K^{-1}$. The specific heat is generally a function of the temperature. The C_p-temperature function is equivalent to the first derivative of the enthalpy with respect to the temperature, and vice versa the change in enthalpy is equivalent to the integral of the specific heat with respect to the temperature.

The specific heat is a characteristic feature of all substances and covers a wide range of values, typically in the range of 0.1 to 5 $Jg^{-1}K^{-1}$. The C_p-curves for some substances are presented in Figure 2.3. It is important that the test parameters remain the same during a series of measurements. These parameters include: furnace atmosphere, gas operation, start temperature and heating rate. The test parameters of a series of measurements are determined during the baseline measurement. It is important to obtain a straight baseline. To obtain a straight baseline the weights of the crucibles should be matched as closely as possible. An even straighter baseline can be obtained by exchanging the sample and reference crucibles.

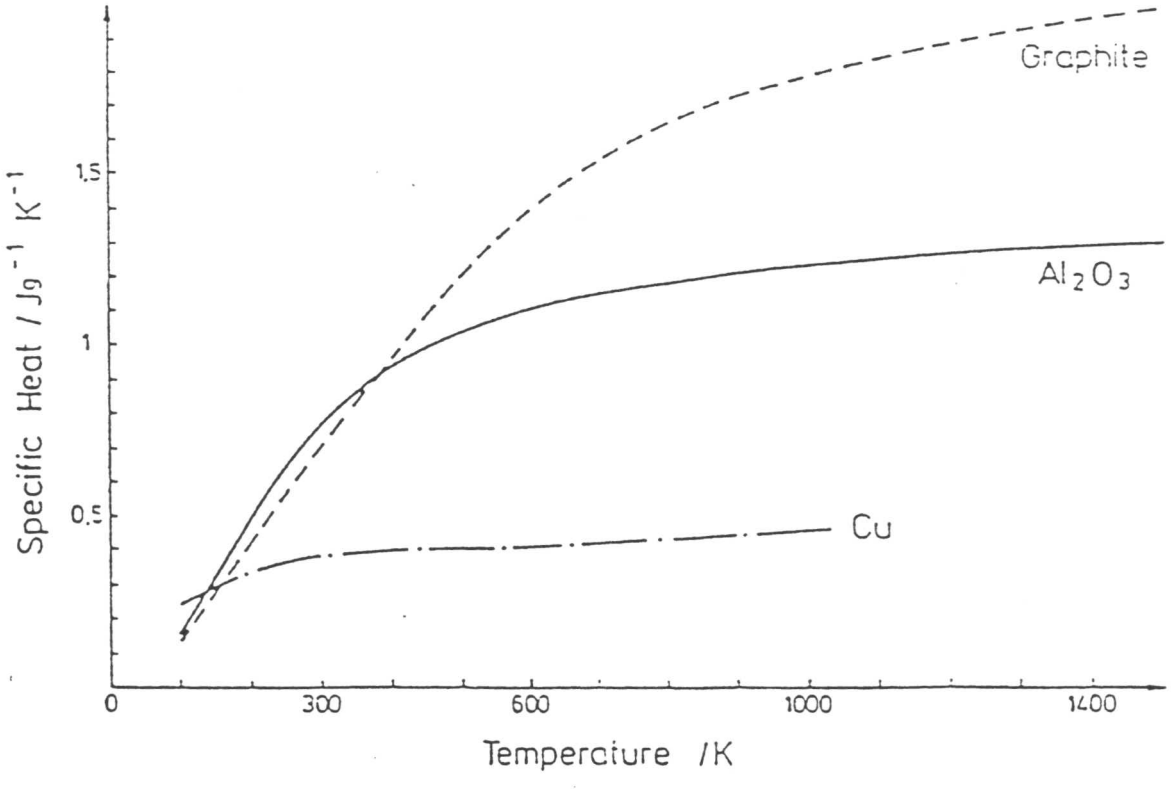

Figure 2.3. Specific heat curves for some substances (Netzsch company, 1989).

A measurement consists of at least three segments: the first segment is heating to a defined start temperature (e.g. 40°C), in the second segment temperature is held constant at the starting temperature for about 10 minutes to get the isothermal phase, and segment three is the start of the actual measurement.

2.12 Thermomechanical Simulator Heat Treatments

A thermomechanical simulator ('Thermecmastor' manufactured by Fuji Electronic Industrial Co. Ltd.) was used to study phase transformation under continuous heating and cooling as well as to investigate the application of stress on the transformation of δ-ferrite to austenite and formation of sigma phase. The Thermecmaster incorporates a sophisticated dilatometer, although is usually used for investigations of the effects of stress on transformation because the strain can be monitored in two orthogonal directions. It has a high frequency induction heating system and is computer controlled enabling the heat treatment cycle to be programmed and monitored with ease. Heating can be done under a vacuum or with a gas atmosphere (Ar, N_2). Rapid heating and cooling at specified rates are also possible, with gases He or N_2 being used for quenching. Temperature is measured using a Pt/Pt-13 wt.% Rh thermocouple resistance welded to the specimen. The dilatation of the specimen in radial direction during experiment is measured using a laser beam. Specimens for tests (under compression or with no applied load) are cylinders of 8 mm diameter and 12 mm long.

Chapter 3

DUPLEX STRUCTURE IN STAINLESS STEELS AND THE EFFECT OF CHEMICAL COMPOSITION ON THE AUSTENITE/FERRITE BALANCE

3.1 Introduction

Austenitic-ferritic (duplex-) stainless steels with low carbon content were developed primarily for reasons of elevated corrosion resistance (Perteneder *et al.*, 1986). The additional advantage of high strength renders these steels highly suitable for applications involving intensive mechanical stresses and for corrosive environments containing of chemically aggressive media. At present, they are employed in oilfield engineering for the production and transportation of crude oil, oil-water mixtures and crude gas as well as for special applications in chemical, waste water and marine plant engineering.

Duplex stainless steels are being increasingly used because of their good mechanical and corrosion properties in comparison with fully austenitic and ferritic grades. The traditional highly-alloyed austenitic construction materials such as steel grades to DIN X 5 Cr Ni 18 9 (1.4301); AISI 304 or X 2 Cr Ni Mo 18 10 (1.4404); AISI 316 L (see Table 1.5 for their chemical compositions) are not suited for these applications as they exhibit only limited resistance to stress corrosion cracking (SCC) in the presence of chloride ions (Perteneder *et al.*, 1986). So far, the ferritic extra low interstitial (ELI)-steels, which are resistant to stress corrosion cracking, have not been put to industrial-scale application on account of their poor weldability. The use of duplex stainless steels constitutes a convenient compromise of corrosion properties as well as processing aspects and costs.

Table 3.1 shows the chemical compositions of various austenitic-ferritic steels presently offered on the market. Generally, one can say that the chromium contents of these duplex steels range between 19 and 26 wt.%, while the nickel contents usually amount to 4-7 wt.%. These steels also contain 1.5-3 wt.%

molybdenum (Perteneder *et al.*, 1986). The microstructures of these steels consist of roughly 50 vol.% austenite and 50 vol.% ferrite. To get the optimum mechanical and corrosion properties the balance between the amount of austenite and ferrite is important. Figure 3.1 shows the microstructure of duplex stainless steel alloy IC378. The material has been produced by hot rolling and available in plate with 4 mm thickness. The grains are of that shape because the sample has been rolled. TEM electron diffraction patterns (Figures 3.21 and 3.23) confirm that the dark phase is δ-ferrite and the bright one is austenite. The measured volume fraction of austenite in this steel (in as received condition) is about 0.57 (see section 3.6). Anyway as we will see later the volume fraction of austenite and δ-ferrite depends not only on chemical composition of the steel but also on the thermal history of the steel. The effect of alloying elements on microstructure and phase transformation behaviour are discussed in this chapter while the effect of thermal history and heat treatment will be the main topic of chapters six and seven.

Table 3.1. Chemical composition (in wt%) of common duplex stainless steel grades (Perteneder *et al.*, 1986).

Steel grade Designation (acc. DIN 17006)	Chemical composition (%)						
	C_{max}	Cr	Mo	Ni	Cu	N	Others
X 2 CrNiMoSi 18 5 3	0,02	18,5	2,7	5	1,5	0,07	Si = 1,7
X 6 CrNiMoTi 20 6 2	0,06	20	2	6	—	—	Ti = 0,4
X 2 CrNiMoCu 21 7 3 2	0,025	21	2,5	6,5	1,8	—	—
X 2 CrNiMoN 22 5 3	0,02	22	3	5,5	—	0,15	—
X 3 CrNiMo 25 6 2	0,025	25	1,5	5,5	—	≤ 0,1	—
X 2 CrNiMoN 25 6 2	0,025	25	1,7	6	—	0,17	—
X 2 CrNiMoCu 24 7 3	0,03	24	2,8	7	0,4	—	—
X 2 CrNiMoCu 25 5 3	0,03	25	3	6	0,4	≥ 0,1	W = 0,3
X 3 CrNiMoCu 24 5 2 1	0,03	24	1,5	5	1	0,1	—
X 6 CrNiMoCu 25 5 2 2	0,06	25	2	5	2	≥ 0,01	—
X 3 CrNiMoN 25 4 2	0,03	25,5	2,3	3,7	—	0,37	Mn = 5,8

3.2 The Fe-Cr-Ni System

3.2.1 Iron

Pure iron exists in two allotropic forms at temperatures below its melting

point (1536 °C) and at ambient pressure (Rivlin *et al.*, 1980) Table 3.2. The phase equilibria of binary or higher systems of iron depend roughly on whether the added elements are more soluble in b.c.c. or f.c.c. iron. Solid solutions in the f.c.c. and b.c.c. phases are designated γ and α respectively (Sully *et al.*, 1967).

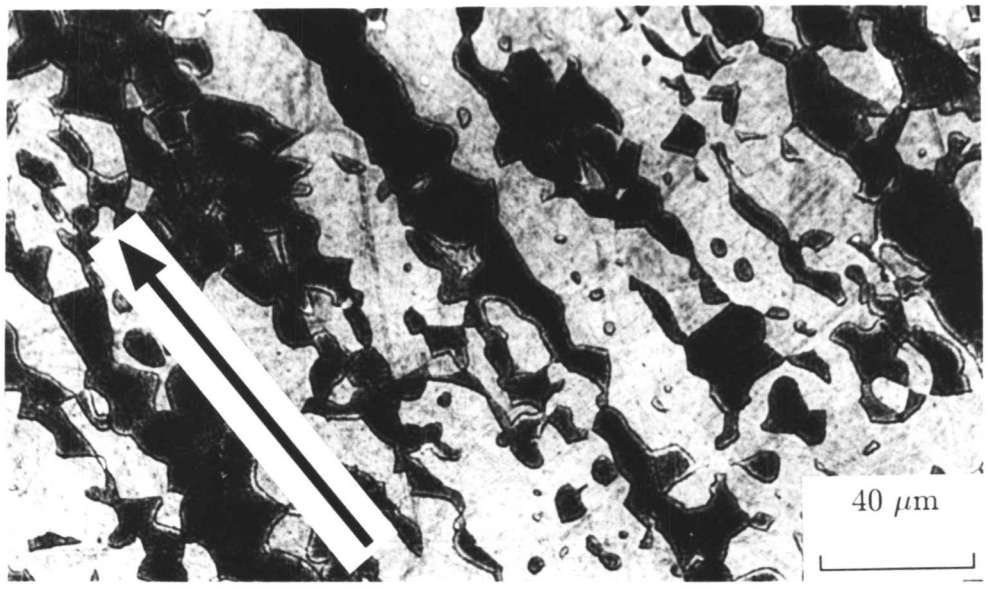

Figure 3.1. The microstructure of longitudinal section of duplex stainless steel rolled metal IC378 (see Table 2.1 for chemical composition). The grains show a rolling microstructure (arrow shows the rolling direction) SEM EDX microanalysis and TEM electron diffraction (see section 3.6) confirm that the bright phase with the measured volume fraction of about 0.57 is austenite and the dark one is ferrite.

Table 3.2. Allotropes of Iron at Ambient Pressure (Rivlin *et al.*, 1980).

Temperature Range (°C)	Symbol	Crystal Structure
1536-1392	δ	body centred cubic (b.c.c.)
1392-911	γ	face centred cubic (f.c.c.)
911 and below	α	body centred cubic (b.c.c.)

Thermodynamic equilibrium calculations using the MTDATA computer package show naturally that chromium will partition into ferrite. (MTDATA is a computer package which has been developed by National Physical Laboratory (NPL) in which the equilibria in multicomponent, multiphase systems can be calculated using critically assessed data for simpler systems. The module MULTIPHASE, within MTDATA, can calculate the phases present and the amount of species within each phase, for a given temperature and pressure or volume, using an optimisation routine to minimise the Gibbs Free Energy of the system for specified component amounts. There are two levels of calculation; stage 1 is used to determine which phases are present and the distribution of the species amount within each phase to a given accuracy, and then stage 2 can be used to increase the accuracy if required.

The interactions between system components in solid solution phases can be relatively large, resulting in some degree of ordering between the phase. It is well-known crystallographically (Hillert *et al.*, 1988) that certain elements distribute themselves within sublattices (e.g. in austenite the carbon atoms will often occupy an interstitial sublattice), and so higher order interactions can be estimated using the sublattice model. Hence the Gibbs free energy of a multicomponent system can be calculated from a knowledge of unary, binary, and possibly ternary, interactions. The complete theory of MULTIPHASE is presented by Hodson (1989) in the documentation for the NPL Metallurgical and Thermodynamic Databank.)

Figure 3.4 shows the result of these calculations for alloy IC378 . The calculated solidus temperature of this alloy is 1382 °C and sigma phase will start to precipitate below 865 °C . The chromium partitioning is shown over the temperature range of 1350-900 °C where microstructure is only a mixture of austenite and ferrite and free of any precipitation according to the calculations. As the temperature decreases from 1350 °C the equilibrium concentration of chromium in ferrite will increase. This will lead to very enriched ferrite grains at temperatures below 1000 °C where the equilibrium volume fraction of ferrite has been decreased sharply (Figure 3.5). These ferrite grains with high chromium concentration should enhance the formation of sigma phase.

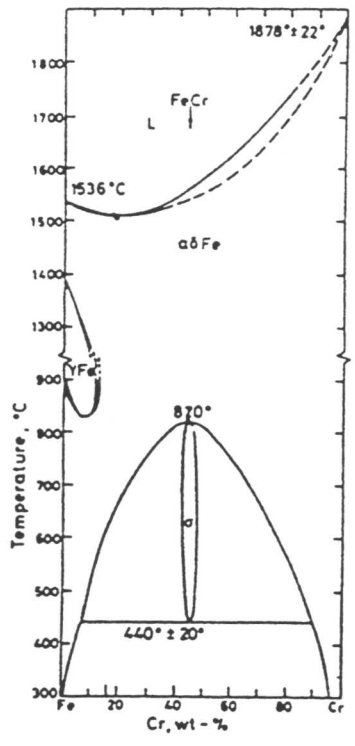

Figure 3.3. Fe-Cr Binary Phase Diagram (Hansen *et al.*, 1958).

3.2.3 Nickel

Nickel has a f.c.c. crystal structure below its melting point of 1453 °C. It is a strong austenite stabiliser and has often been used to represent the effect of other alloying elements which tend to stabilise austenite, in the form of 'nickel equivalent' . Duplex stainless steels usually contain 4 to 9 wt.% Ni. As can be seen from the Fe-Ni binary phase diagram (Figure 3.6) nickel dissolves preferentially in γ-Fe and its solubility in α-Fe and δ-Fe is restricted (Rivlin and Raynor, 1980).

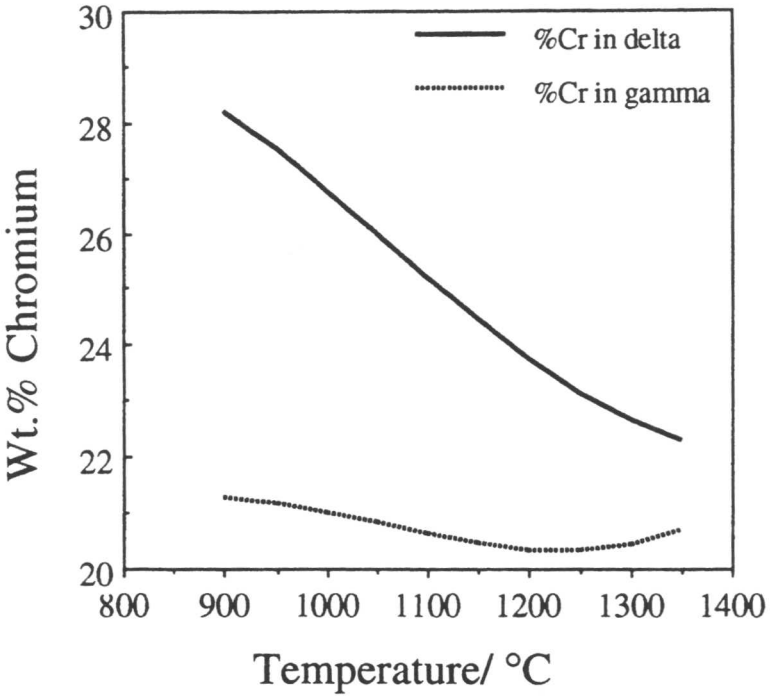

Figure 3.4. Calculated equilibrium partitioning of chromium between δ-ferrite and austenite in duplex stainless steel rolled metal IC378. The chromium content of the alloy is 21.8 wt.%.

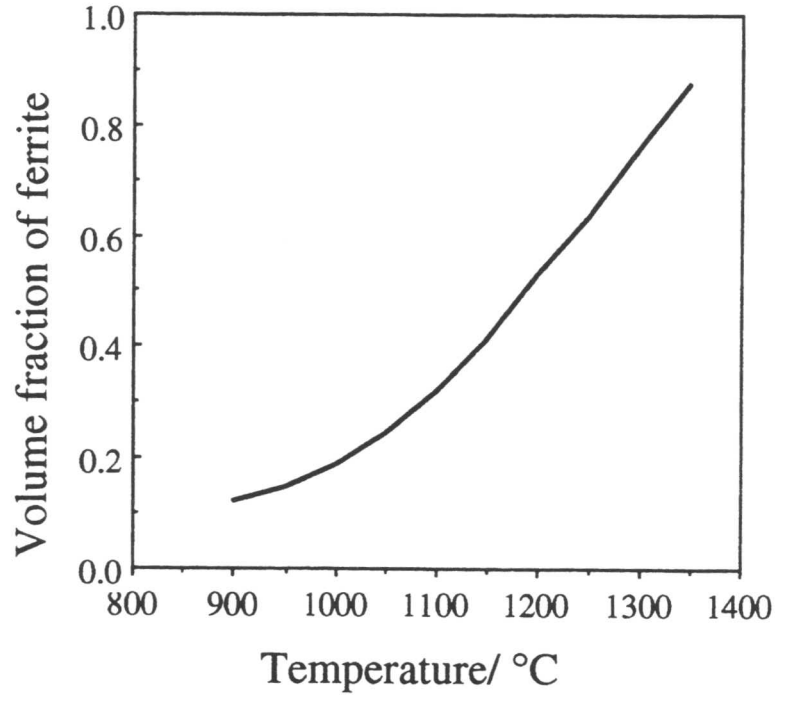

Figure 3.5. Calculated equilibrium volume fraction of ferrite in duplex stainless steel rolled metal IC378. The calculation has been done in the temperature range where only austenite and ferrite are thermodynamically stable.

Nagano *et al.* (1981) have reported that a nickel level of around 7 wt.% in duplex stainless steels is effective in reducing crevice corrosion of sensitised alloys. The effect of nickel in reducing the pitting corrosion of duplex stainless steels has been demonstrated by Sakai *et al.* (1982) who has shown that the nickel content should be maintained between 4 and 8 wt.% for 25 wt.% Cr alloys and 4-7 wt.% for 22 wt.% Cr alloys in order to obtain the optimum pitting resistance. If the nickel concentration is significantly in excess of that required for optimum pitting resistance then the austenite content increases markedly above 50%. The resulting residual, more highly alloyed ferrite (as a result of alloying element partitioning) will more readily transform to the brittle sigma phase at temperatures in the range 650-950°C (Roscoe *et al.*, 1986). This will adversely affect the hot working characteristics of wrought steels, impact toughness, ductility and weldability of cast duplex stainless steels (Guha *et al.*, 1982). Conversely if the nickel content is reduced below the optimum level for pitting resistance, leading to high ferrite contents, low toughness will result. This is because the delta ferrite formed immediately on solidification tends to have low ductility associated with larger grain size (Guha *et al.*, 1982).

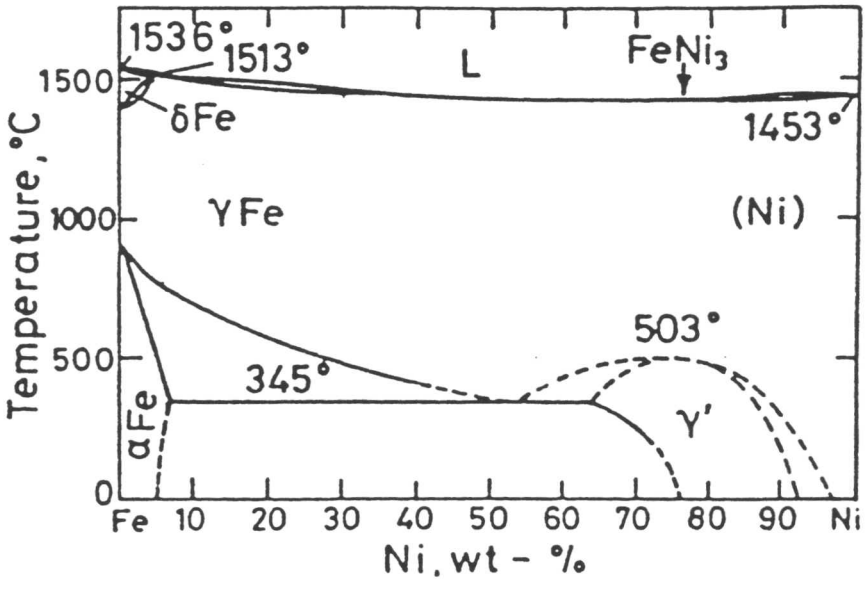

Figure 3.6. Fe-Ni Binary Phase Diagram (Rivlin and Raynor, 1980)

As a strong austenite stabiliser, nickel partitions into austenite and the Ni content of ferrite is much lower than in austenite. Figure 3.7 shows the calculated equilibrium partitioning of Ni between the two phases in alloy IC378 over the temperature range where the calculations indicate a microstructure of only ferrite and austenite. The amount of nickel in ferrite decreases with temperature from the amount of 5.6 wt.% at 1350 °C to only 2.8 wt.% at 900 °C. Correspondingly, its concentration in austenite appears to be much less sensitive to temperature change and it decreases from 7.1 wt.% at 1350 °C to about 6.3 wt.% at 900°C. This discrepancy in the changes in nickel concentration in the ferrite and austenite is accounted for by changes in the relative volume fraction of the two phases.

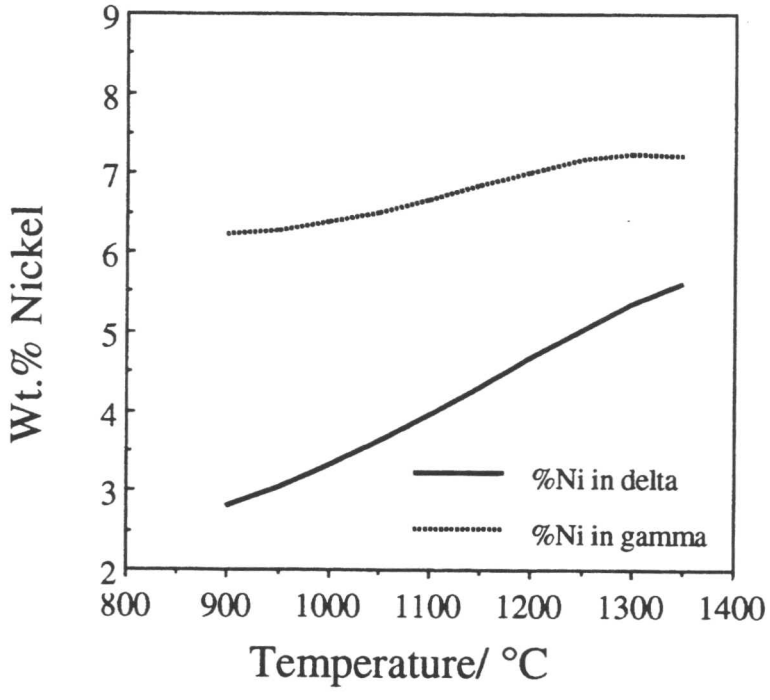

Figure 3.7. The calculated equilibrium Ni content of austenite and ferrite in duplex stainless steel alloy IC378.

Bain and Griffiths in 1927 identified four phases in the Fe-Cr-Ni system; γ-f.c.c. based on γ-Fe and Ni, α-b.c.c. based on α-Fe, $\alpha\prime$-b.c.c. based on Cr and the σ phase. Since then many researchers have worked on the equilibria in Fe-Cr-Ni system and have reported their results in the form of isothermal

sections of the ternary Fe-Cr-Ni systems. Rivlin *et al.* (1980) have recently studied the liquidus and solidus projection of the system; Marshall (1984) and Mundt *et al.* (1983) have investigated isothermal sections of the Fe-Cr-Ni ternary phase diagram. All of these data show that the common duplex stainless steels which usually contain 18 to 30 wt.% of chromium and 4 to 9 wt.% of nickel can solidify completely as austenite or ferrite or the mixture of the two phases. Either phase can solidify first depending on the Ni and Cr contents. Below the solidus temperature, the solid phases that can exist are ferrite, austenite, sigma phase or a mixture of two or three of them. Figure 3.8 shows a vertical section of the Fe-Cr-Ni phase diagram at 63.5 wt.% Fe (Easterling, 1983). The broken vertical lines show that the typical compositions of the duplex weld metals (over alloyed with Ni to ensure enough austenite, see next chapter) will solidify under equilibrium conditions to mixture of ferrite and austenite.

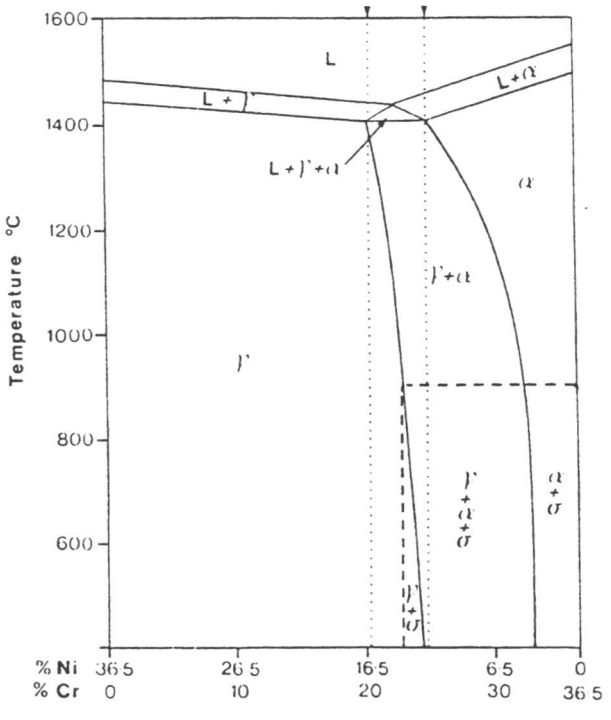

Figure 3.8. Vertical section of the ternary Fe-Cr-Ni phase diagram at 63.5 wt.%Fe. Both the Ni and Cr amount are in wt.%. (after Easterling, 1983).

3.3 The Alloying Elements in Duplex Stainless Steels

3.3.1 Carbon

Duplex stainless steels usually contain less than 0.08 wt.% carbon. It is a

γ stabiliser and increases the maximum solubility of Cr in austenite, a feature important for corrosion resistance (Gordon, 1977). The precipitation of carbon as $Cr_{23}C_6$ at the austenite grain boundaries in austenitic stainless steels can make them particularly prone to intergranular corrosion by depleting chromium from solid solution (Abron *et al.*, 1930). In duplex stainless steels, carbon has been found to be beneficial when precipitated as $M_{23}C_6$, since this renders the formation of more detrimental intermetallic phases less likely by tying up molybdenum (Farrar, 1987). Anyway, to ensure good hot workability it is advisable to restrict carbon content to a maximum of 0.030 wt%. The low carbon concentration inevitably suppresses carbide precipitation and further reduces the susceptibility of duplex stainless steel to localised corrosion in the as-welded condition (Roscoe *et al.*, 1986).

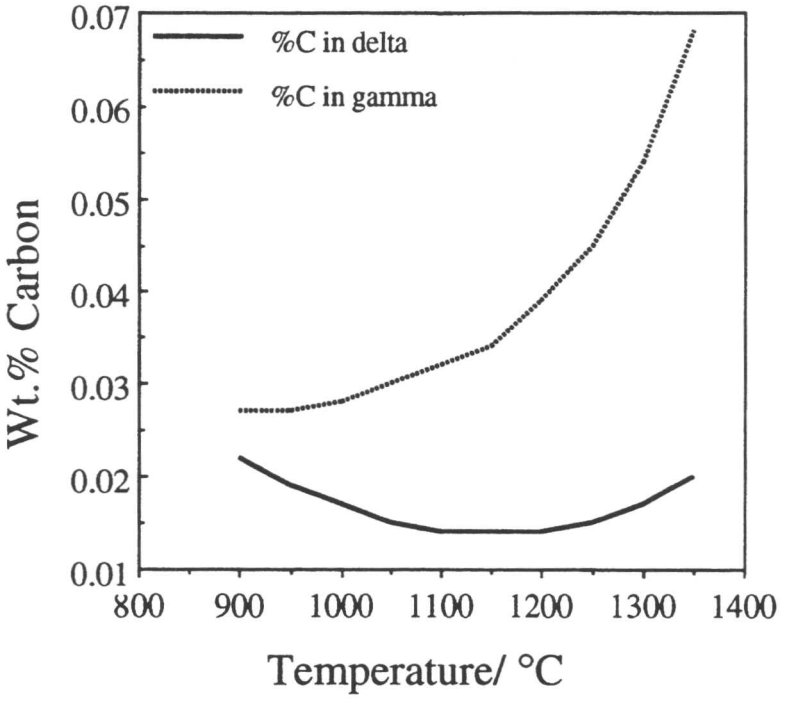

Figure 3.9. The calculated equilibrium partitioning of carbon between ferrite and austenite in duplex stainless steel alloy IC378.

Figure 3.9 shows the calculated equilibrium partitioning of carbon between ferrite and austenite in alloy IC378. At 1350 °C the carbon content of austenite is about five times as much as of ferrite. This shows that although the density of austenite is higher than ferrite the solubility of interstitial carbon atoms is greater in austenite. This is because of the fact that the empty spaces in

the f.c.c. structure are fewer but larger for interstitial carbon atoms. As the temperature decreases the carbon content of ferrite approaches that for austenite and the remaining ferrite with high carbon content becomes unstable and ready to transform to austenite.

3.3.2 Molybdenum

Duplex stainless steels usually contain 1 to 3.9 wt.% Mo. Molybdenum is a ferrite stabiliser, and promotes the formation of σ phase (Pickering, 1984) and its most important effect is to improve the corrosion resistance of duplex stainless steels. Figure 3.10 shows the calculated equilibrium partitioning of Mo between ferrite and austenite in alloy IC378. Molybdenum has a tendency to combine with iron to form intermetallic phases. The most important of them is the Laves phase Fe_2Mo which can be precipitated at a relatively low average Mo concentration of around 5 wt.% in the Fe-Mo binary alloys (Folkhard, 1988). Bechtoldt and Vancher (1957) investigated the intermetallic compound formation in the quaternary Fe-Cr-Ni-Mo system. They found that Laves and Chi phases could be induced to form at temperature as high as 1093 °C at an iron content of 70 wt.%, Figure 3.11.

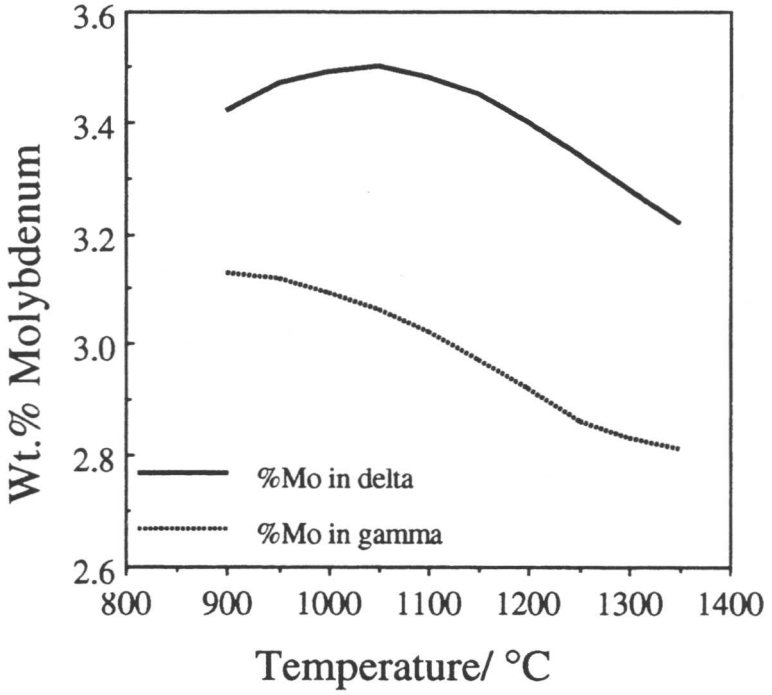

Figure 3.10. The calculated equilibrium partitioning of Mo between ferrite and austenite in duplex stainless steel alloy IC378.

Clarck *et al.* (1986) have proposed the following equation for calculating the pitting resistance equivalent (PRE) and claimed that steels with PRE values higher than 40 have better corrosion properties.

$$\text{PRE} = \%\text{Cr} + 3.3\%\text{Mo} + 15\%\text{N} \qquad \text{(Clarck, Gentil and Guha; 1986)}$$

with all concentrations in wt.%. It has been established that more than 3 wt.% molybdenum is essential for the prevention of crevice corrosion in high temperature sea water (Nagano *et al.*, 1981). The maximum level of Mo which can be added to duplex stainless steels is restricted to around 4 wt.% since larger additions widen the sigma phase field and can extend it to temperatures in excess of 1000°C (Roscoe *et al.*, 1986).

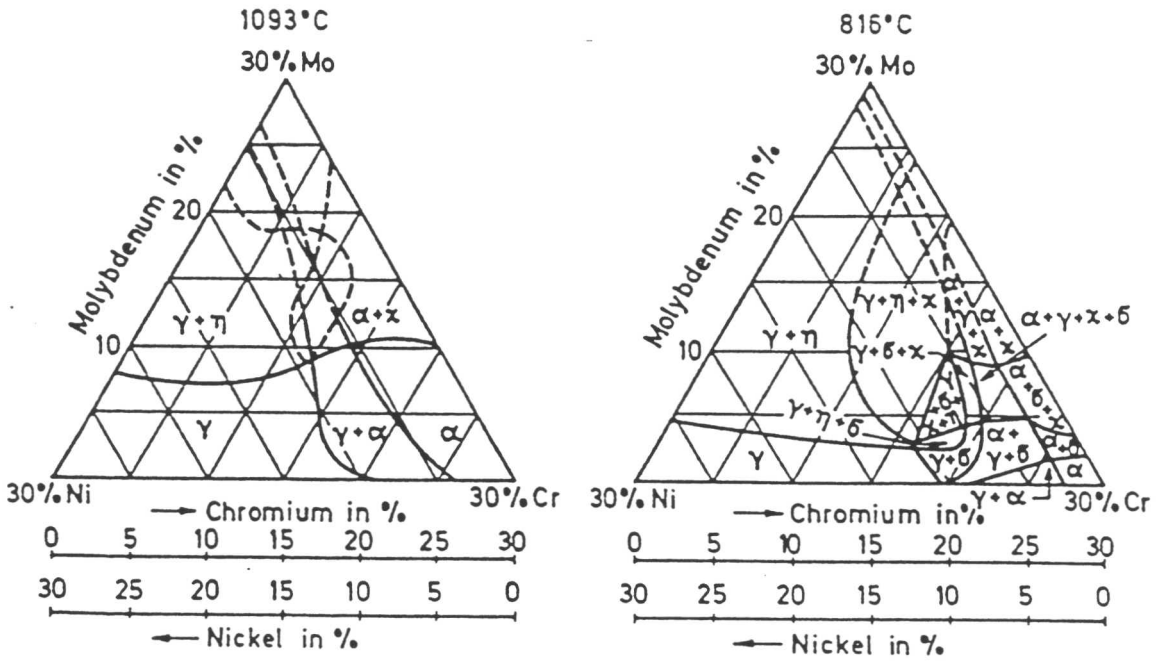

Figure 3.11. Isothermal profiles in the Fe-Cr-Ni-Mo system with constant iron content of 70 wt.% at 1093 °C and 816 °C, after Bechtoldt and Vancher (1957). All the concentrations are in wt.%. σ = sigma phase, χ = chi phase, η = eta phase (Laves phase Fe_2Mo).

3.3.3 Nitrogen

Duplex stainless steels can have up to 0.3 wt.% nitrogen which is an austenite stabiliser. Nitrogen is more soluble than carbon in the Fe-Cr-Ni system. The addition of 3 to 5 wt.% Mn increases nitrogen solubility in duplex stainless steel

castings to 0.35 wt.% with acceptable internal soundness. Chance (1982) has shown that high levels of nitrogen will necessitate high levels of manganese. It is often used as a cheap nickel substitute in austenitic and duplex stainless steels (Leslie, 1981). As far as the corrosion properties are concerned, one of the most significant improvements in the localised corrosion performance of duplex stainless steels is obtained by increasing nitrogen levels in the region of 0.2-0.3 wt.% (Chance *et al.*, 1982). PRE equation (see section 3.3.2) also emphasise the beneficial effect of nitrogen on pitting resistance. Truman *et al.* (1977) have shown that the beneficial effects of nitrogen appear to be enhanced in the presence of molybdenum. Nitrogen levels of 0.2-0.3 wt.% also indirectly improve the ductility and toughness of duplex stainless steels, since nitrogen is an austenite forming element. Furthermore the nitrogen in solid solution increases the strength of the alloy (Roscoe *et al.*, 1986).

Figure 3.12 shows the effect of nitrogen in stabilising the austenite in the duplex stainless steel alloy IC378. As an austenite stabiliser, nitrogen will partition into austenite. Figure 3.13 shows the calculated equilibrium concentrations of nitrogen in ferrite and austenite in alloy IC378.

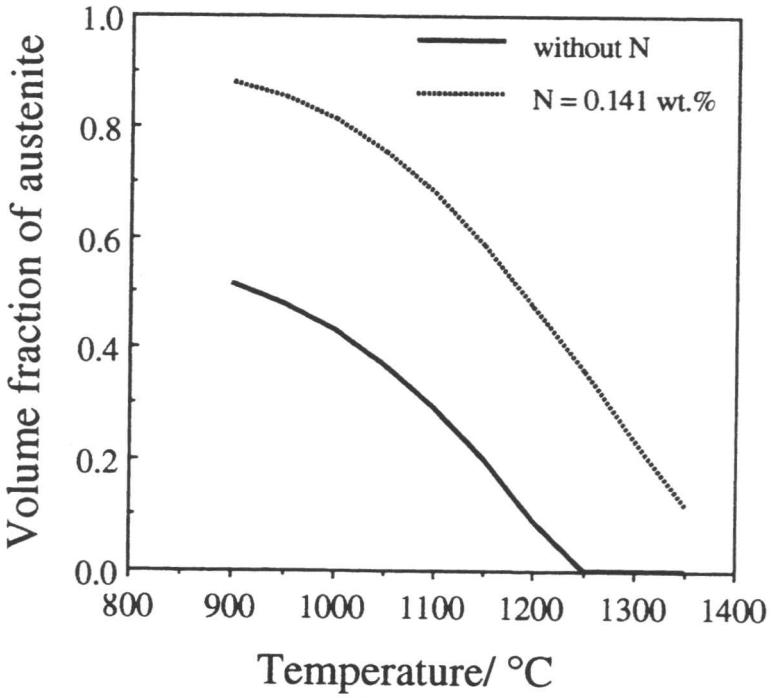

Figure 3.12. The calculated equilibrium volume fraction of austenite in duplex stainless steel alloy IC378 showing the effect of nitrogen on volume fraction of austenite.

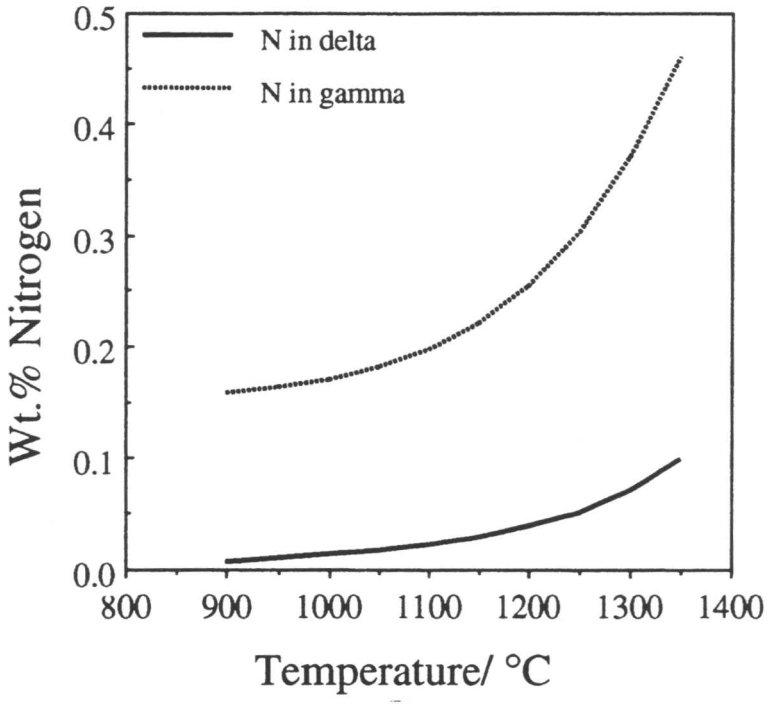

Figure 3.13. The calculated equilibrium concentration of nitrogen in austenite and ferrite in alloy IC378.

3.3.4 Manganese

Manganese is considered to be an austenite stabiliser. It is important in duplex stainless steels weld metals as an oxygen and sulphur scavenger (Easterling, 1983). Another important effect of Mn, as is mentioned in previous section, is its influence on nitrogen solubility in duplex stainless steels. High levels of nitrogen have necessitated high levels of manganese (e.g. 4 wt.%) to increase the solid solubility of the nitrogen (Chance *et al.*, 1982). As an austenite stabiliser the Mn content of austenite is higher than of ferrite. Figure 3.14 shows the calculated equilibrium concentration of Mn in ferrite and austenite in alloy IC378.

Whereas manganese is generally considered detrimental to the pitting resistance of stainless steels due to the formation of manganese sulphides, the combined addition of molybdenum plus nitrogen tends to override this effect. However, it is well established that manganese sulphide inclusions are favourable sites for pit initiation in stainless steels (Sedriks, 1983). Thus, maintaining manganese to extremely low levels (e.g. 0.5 wt.%) results in the preferential formation of chromium sulphides which render pit initiation more difficult.

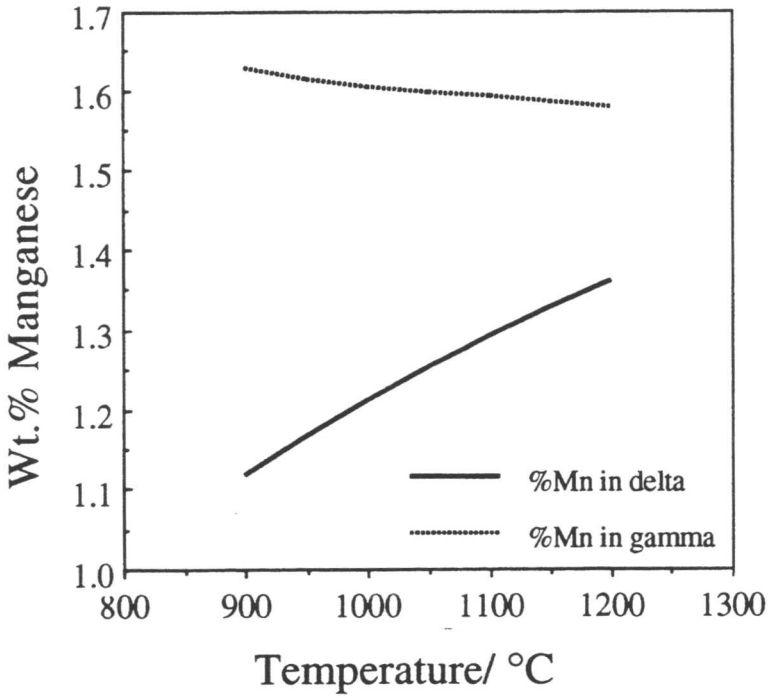

Figure 3.14. The calculated equilibrium partitioning of Mn between ferrite and austenite in alloy duplex stainless steel alloy IC378.

3.3.5 Copper

Up to 3.5 wt.% copper has been added to stainless steels to improve corrosion resistance and to increase tensile strength by means of precipitation hardening, which takes place as a result of the decreasing solubility of copper in ferrite as the temperature falls (Kubaschewski, 1982). Guha and Clark (1982) state that the addition of copper required to achieve the optimum corrosion resistance in 70 vol.% H_2SO_4 at 60 °C decreases from 1.5 wt.% in a 25 wt.%Cr duplex stainless steels to 1 wt.% in a 28 wt.% Cr duplex stainless steels.

The maximum level of copper utilised in wrought duplex stainless steels is limited to approximately 2 wt.% since higher contents reduce hot ductility. Furthermore, additions of copper have been reported to promote precipitation hardening in duplex stainless steels (Guha *et al.*, 1982).

3.3.6 Silicon

Silicon is a ferrite stabiliser and the addition of 3-5 wt.% Si to duplex stainless steel castings considerably improves the pitting resistance in acidified ferric

chloride solution, and at the same time impairs the resistance to intergranular corrosion in boiling nitric acid solution (Sump *et al.*, 1983). Wilde (1977) has patented compositions of high silicon (3.5-5.5 wt.%) duplex stainless steels that are reported to be immune from stress corrosion cracking using the boiling magnesium chloride solution tests. However silicon contents in excess of approximately 1.0 wt.% disproportionately enhance sigma phase formation and can lead to poorer corrosion resistance in duplex stainless steels retained in the as welded condition (Roscoe *et al.*, 1986). In the Fe-Cr binary system and Fe-Cr-Ni ternary system, silicon expands the sigma phase range to lower chromium and higher temperatures (Kubaschewski, 1982; Folkhard, 1988; Schuller, 1965).

As a ferrite stabiliser Si will partition into ferrite. Figure 3.15 shows the calculated equilibrium silicon concentrations of austenite and ferrite in duplex stainless steel alloy IC378. As the temperature decreases the difference between Si content of austenite and ferrite will increase.

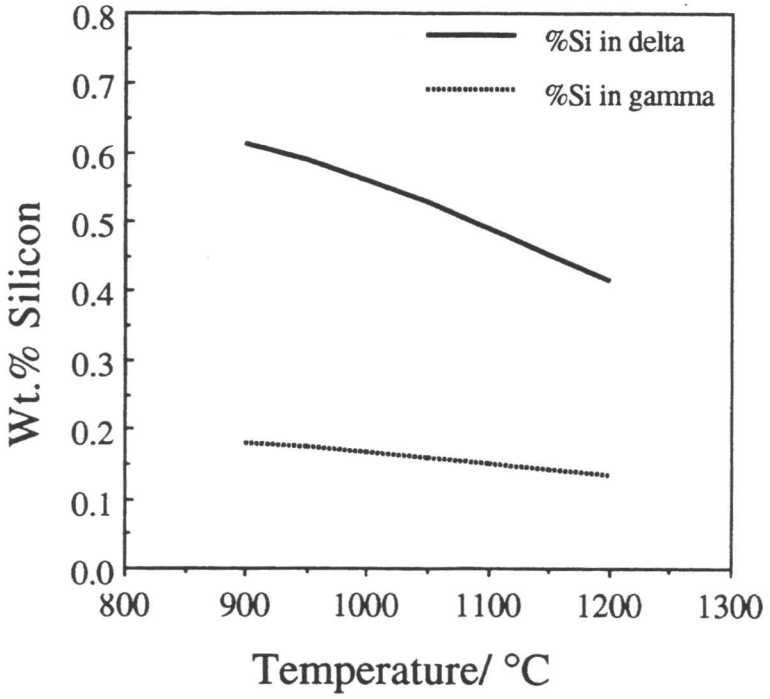

Figure 3.15. The calculated equilibrium partitioning of Si between austenite and ferrite in duplex stainless steel alloy IC378. The concentration of Si in the alloy is 0.39 wt.%.

3.3.7 Titanium and Niobium

Ti and Nb are ferrite stabilisers and have been used in austenitic stainless steels, with other than the lowest carbon contents, mainly to stabilise them against intergranular corrosion (Pickering, 1985). The addition of these elements to duplex stainless steels also suppresses the formation of $Cr_{23}C_6$ as TiC and NbC precipitation is very rapid, and all the free carbon will be consumed. Precipitation of TiC and NbC will leave the Cr in solution and hence safe guard the corrosion resistance. Anyway it should be kept in mind that by rapid removal of carbon from solution the amount of the Cr left in solution will be increased and this can increase the rate of sigma formation in duplex stainless steels (Southwick, 1978).

3.3.8 Tungsten

Tungsten is a ferrite stabiliser and at a level of approximately 0.6 wt.% has been added to duplex stainless steels to improve corrosion resistance (Roscoe *et al.*, 1984). Nagano *et al.* (1981) state the tungsten increases the immunity potentials to crevice corrosion of duplex stainless steels in high temperature chloride solutions to levels above which crevice corrosion starts. It can be said that tungsten will act in a similar manner to molybdenum with respect to enhanced sigma phase formation. Consequently there is a limit on the level of the alloying that is practicable otherwise the sigma kinetics are enhanced, potentially reducing the ductility and toughness of the alloy (Roscoe *et al.*, 1986).

3.3.9 Sulphur and phosphorus

The damaging role of sulphur and phosphorus in solidification and liquation cracking is general knowledge. Fortunately, modern melting techniques have made it possible to obtain extremely low sulphur and phosphorus steels (Roscoe *et al.*, 1986). However, user demand for very low sulphur steels received something of a blow, when it was discovered that such steels with less than 0.01 wt.% S were unreasonably susceptible to hydrogen cracking (Dawson *et al.*, 1982). However, new work on the effect of sulphur on the hydrogen cracking (Ha, Pyun and Lim; 1991) shows that the sulphur segregated at grain

boundaries acts as deep trap sites for hydrogen and so contradicts with Dawson's idea.

3.4 Chromium and Nickel Equivalents

The effect of alloying elements in stainless steels has often been expressed in terms of 'Ni equivalent' if they tend to stabilise austenite and as 'Cr equivalent' if they stabilise ferrite. The different empirical formulae reported in the literature are listed below with the concentrations expressed in wt.% (Haddad, 1989):

$$Cr_{eq} = Cr + Mo + 1.5Si + 0.5Nb$$

(Schaeffler, 1949)

$$Ni_{eq} = Ni + 30C + 0.5Mn$$

$$Cr_{eq} = Cr + Mo + 1.5Si + 0.5Nb$$

(Seferian, 1959)

$$Ni_{eq} = Ni + 30C + 30N + 0.5Mn$$

$$Cr_{eq} = Cr + 2Si + 1.5Mo + 5V + 5.5Al + 0.75Nb + 1.5Ti + 0.75W$$

(Pickering, 1984)

$$Ni_{eq} = Ni + Co + 0.5Mn + 0.3Cu + 30C + 25N$$

$$Cr_{eq} = Cr + 3Si + Mo + 10Ti + 4Nb$$

(Pickering, 1984)

$$Ni_{eq} = Ni + 0.5Mn + 21C + 11.5N$$

$$Cr_{eq} = Cr + 3Si + 7Ti + 12Al$$

(Skuin *et al.*, 1978)

$$Ni_{eq} = Ni + 30C + 26N + 0.7Mn$$

$$Cr_{eq} = Cr + Mo + 3Si$$

(Honeycombe *et al.*, 1985)

$$Ni_{eq} = Ni + 15C + 10N + 0.7Mn$$

$$Cr_{eq} = Cr + 1.37Mo + 1.5Si + 2Nb + 3Ti$$

(Suutala *et al.*, 1979)

$$Ni_{eq} = Ni + 0.31Mn + 22C + 14.2N + Cu$$

$$Cr_{eq} = Cr + 1.5Mo + 2Mn + 0.25Si$$

(Noble *et al.*, 1986)

$$Ni_{eq} = Ni + 12C + 12N$$

$$Cr_{eq} = Cr + Mo + 1.5Si + 0.5Nb$$

(Machara, 1983)

$$Ni_{eq} = Ni + 30(C + N) + 0.5Mn$$

$$Cr_{eq} = Cr + 1.37Mo + 1.5Si$$

(Hammar and Svensson; 1979)

$$Ni_{eq} = Ni + 0.31Mn + 22C + 14.2N$$

Anyway this method does not accurately represent the effect of the alloying elements because the elements can sometimes be both ferrite or austenite stabilisers at the same time when considering different transformations, e.g. the effect of Cr in restricting the austenite phase field to a γ loop, and at the same time, depressing the M_s temperature. It is also noticeable that the above mentioned empirical formulae vary significantly and were in each case designed to solve specific problems and hence cannot be accepted as general solutions.

3.5 The effect of Cr_{eq}/Ni_{eq} ratio on equilibrium volume fraction of γ

Thermodynamic calculations have shown that the equilibrium volume fraction of austenite will decrease as the Cr_{eq}/Ni_{eq} ratio of steel increase. Table 3.3 shows the Cr_{eq}/Ni_{eq} of hot rolled duplex stainless steels IC373, IC378 and IC381 calculated using the Hammar and Svensson (1979) equation. Figure 3.16 shows that the equilibrium volume fraction of austenite of IC373 with Cr_{eq}/Ni_{eq}=4.09 is much lower than of IC381 with Cr_{eq}/Ni_{eq}=3.04. The calculations were done

for the temperature range where only austenite and ferrite are thermodynamically stable.

Table 3.3. Calculated solidus and liquidus temperatures of duplex stainless steels IC373, IC378 and IC381. Cr_{eq} and Ni_{eq} have been calculated using Hammar and Svensson (1979) equation. The measured hardness and volume fraction of austenite of these alloys are also shown.

Steel Grade	Cr_{eq}/Ni_{eq}	Liquidus Temp. °C	Solidus Temp. °C	Hardness	Austenite Volume fraction
IC373	4.09	1484	1382	313	0.30
IC378	3.12	1474	1384	281	0.57
IC381	3.04	1470	1382	273	0.63

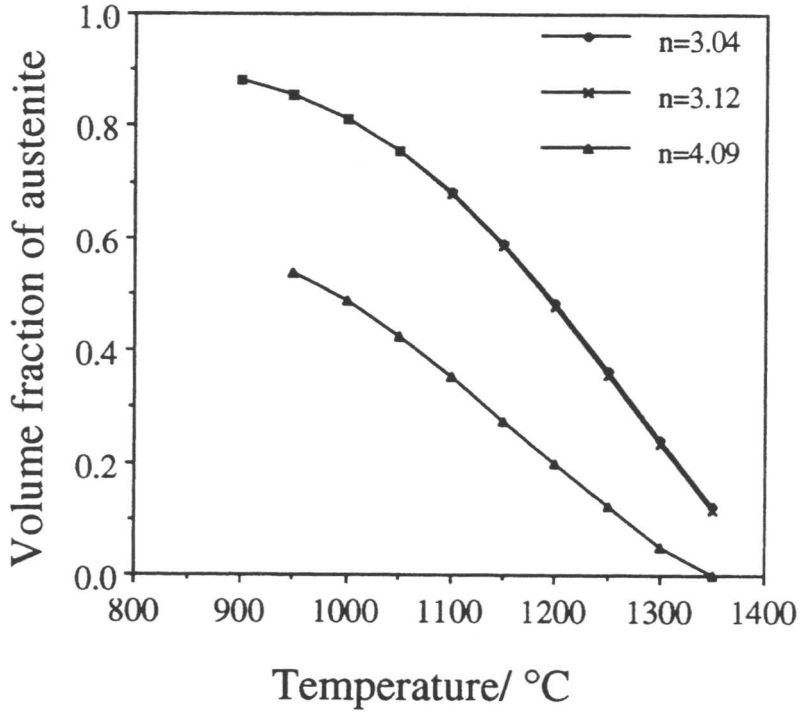

Figure 3.16. Calculated equilibrium volume fraction of austenite in duplex stainless steel alloys IC373, IC378 and IC381 with Cr_{eq}/Ni_{eq} of 4.09, 3.12 and 3.04 respectively. 'n' represents the Cr_{eq}/Ni_{eq} ratio.

3.6 Microstructure of hot rolled duplex stainless steel

All the three duplex stainless steel alloys IC373, IC378 and IC381 have been produced by hot rolling and have the same thermal history. Under the optical microscope the phase which is darker was found usually to be ferrite (Figure 3.1) while in SEM micrographs the darker phase is austenite unless the image is inverted. Figure 3.17 shows the SEM micrographs of microstructure of alloys IC373, IC378 and IC381. These micrographs show that the microstructure consists of austenite and δ-ferrite grains aligned in the rolling direction while inside the ferrite grains fine precipitation of austenite occurred (Figure 3.18). The examination of their microstructures by optical and electron microscopy show that the one with the highest amount of Cr_{eq}/Ni_{eq} has the maximum volume fraction of austenite together with the maximum hardness among the three grades. The volume fraction of austenite measured using image analysing and linear point counting techniques. The chromium content of alloy IC373 is 25.9 wt.% which is much higher than chromium contents of alloys IC378 and IC381. As chromium is a strong ferrite stabiliser the volume fraction of austenite is much lower in alloy IC373 compared with IC378 and IC381.

Energy dispersive X-ray (EDX) microanalysis using a scanning electron microscope shows the partitioning of Cr, Mo and Si in ferrite and Ni and Mn in austenite as it was predicted by thermodynamic calculations. The chemical composition of each phase was analysed twenty times and the error bars (Table 3.4-3.6) show the standard deviation. Table 3.4 shows the results of these data for δ-ferrite and Table 3.5 shows the same thing for austenite . Figure 3.19 shows the results of these analysis for the above said steels. The transmission electron microscopy observations of these steels show that austenite (Figure 3.20) has a f.c.c. structure and ferrite has a b.c.c. crystal structure. Figure 3.21 shows the diffraction pattern of δ-ferrite and Figure 3.23 is the diffraction pattern of austenite . The direction of the incident beam in the real space for the electron diffraction pattern of Figure 3.21 is $[0\bar{1}1]$ and for the Figure 3.22 is $[\bar{1}\bar{1}0]$.

The TEM EDX microanalysis also show the partitioning of Cr and Mo to ferrite and Ni and Mn to austenite. Table 3.6 show the typical microanalysis of the austenite and δ-ferrite in alloy IC378. Figure 3.24 shows the relationship

between the Cr_{eq}/Ni_{eq} ratio of the steel and the volume fraction of austenite and the hardness for duplex stainless steel grades IC373, IC378 and IC381. As it was predicted by the calculations the volume fraction of austenite will decrease as the Cr_{eq}/Ni_{eq} ratio of the steel increases. At the same time the hardness of the steel will increase as the result of higher volume fraction of ferrite.

Table 3.4. SEM EDX microanalysis data of ferrite in duplex rolled metals IC373, IC378 and IC381 (all concentrations are in wt.%).

Alloy	Fe	Cr	Ni	Mo	Mn	Si
IC373	60.5±1.7	30.0±1.5	4.0±0.6	4.2±0.4	0.6±0.1	0.6±0.1
IC378	66.9±1.9	25.2±0.7	3.9±0.5	3.6±0.3	1.2±0.3	0.5±0.1
IC381	64.4±1.9	27.1±1.6	3.6±0.5	3.9±0.4	1.5±0.2	0.6±0.1

Table 3.5. SEM EDX microanalysis data of austenite in duplex rolled metals IC373, IC378 and IC381 (all concentrations are in wt.%).

Alloy	Fe	Cr	Ni	Mo	Mn	Si
IC373	66.5±1.5	24.0±1.3	6.9±0.8	2.4±0.3	0.9±0.2	0.4±0.1
IC378	68.6±1.7	20.1±1.2	6.8±0.7	2.5±0.3	1.8±0.4	0.3±0.1
IC381	67.9±1.9	20.3±1.2	7.5±0.6	2.1±0.2	2.3±0.3	0.3±0.1

Table 3.6. TEM EDX microanalysis data of the phases shown in Figures 3.20 and 3.22. The one which is richer in Cr and Mo is δ-ferrite while the other one which is richer in Ni and Mn is austenite. All the concentrations are in wt.%.

Phase	Fe	Cr	Ni	Mo	Mn	Si
δ-ferrite	61.4±1.3	25.1±1.1	4.3±0.8	3.8±0.6	0.6±0.1	0.6±0.1
austenite	64.7±1.9	21.2±1.1	7.4±0.9	2.7±0.5	1.8±0.5	0.3±0.1

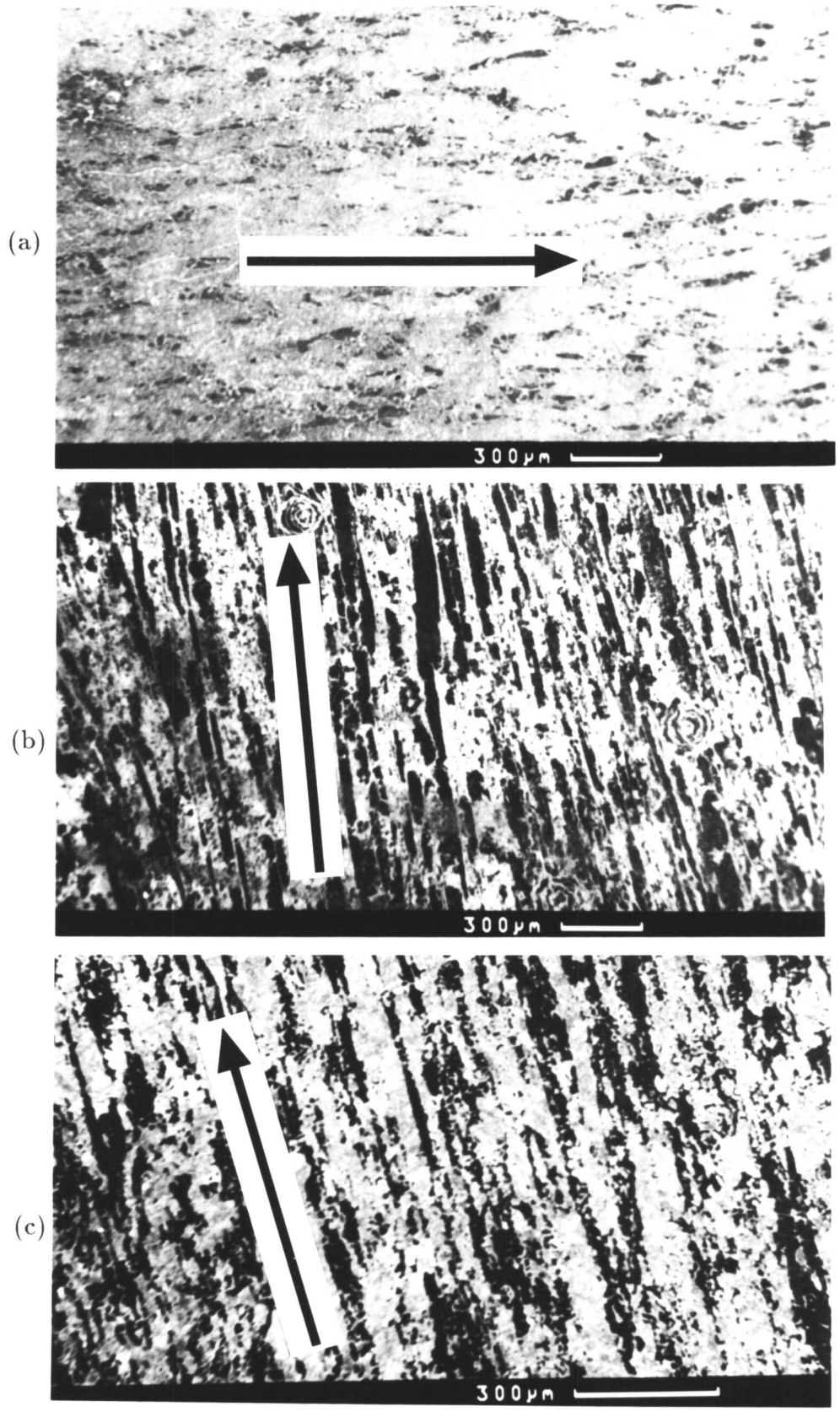

Figure 3.17. SEM micrographs showing the microstructures of duplex stainless steel alloys a) IC373 $V_\gamma = 0.30$ b) IC378 $V_\gamma = 0.57$ c) IC381 $V_\gamma = 0.63$. The darker phase is austenite and the grains are aligned in the rolling direction which is indicated by an arrow.

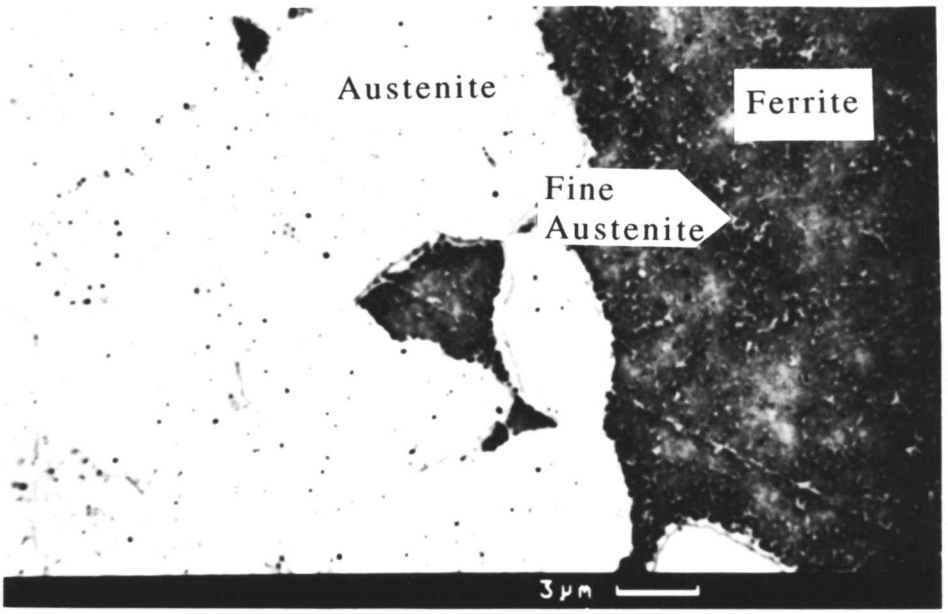

(a)

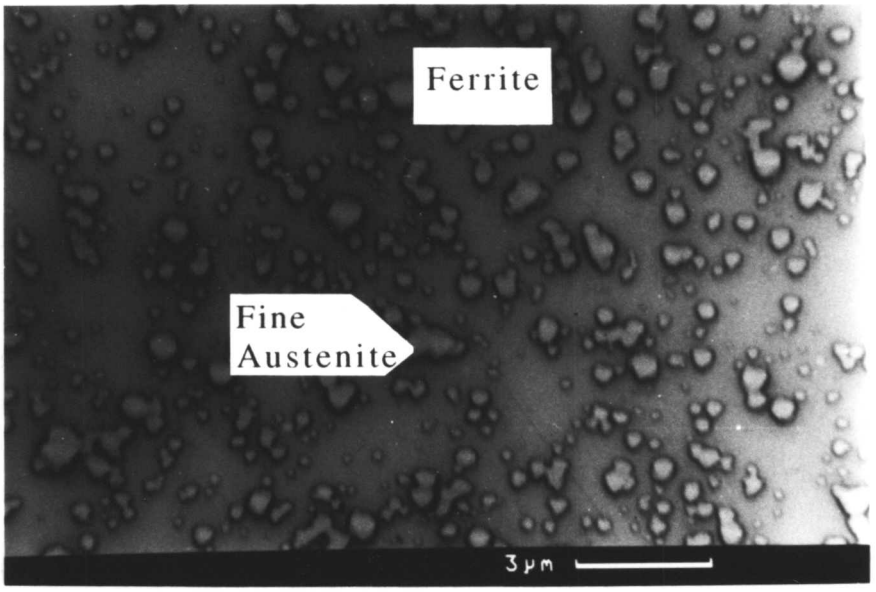

(b)

Figure 3.18. SEM micrographs showing the precipitation of fine austenite inside the δ-ferrite grain in alloys a) IC378, b) IC373.

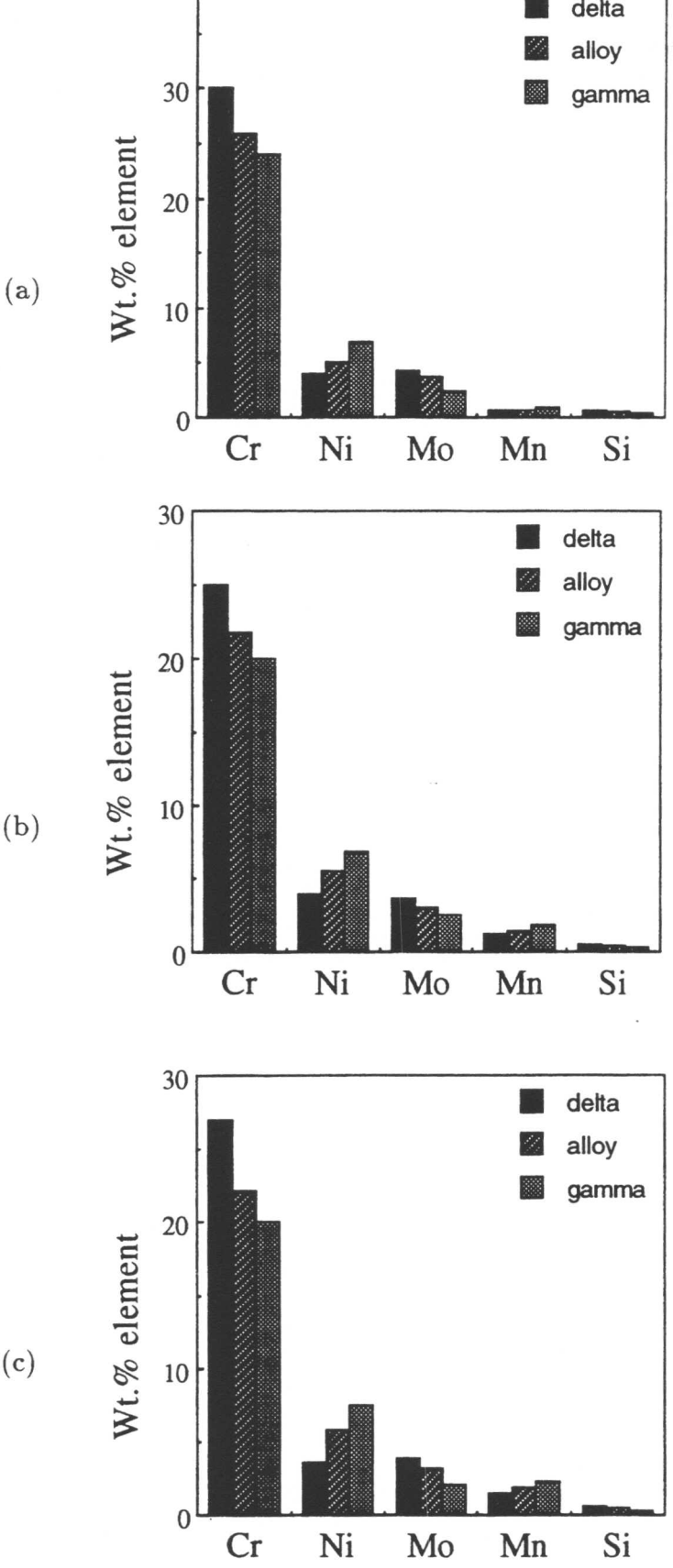

Figure 3.19. SEM EDX microanalysis data showing the chemical composition of ferrite and austenite in duplex stainless steel alloys a) IC373, b) IC378 and c) IC381.

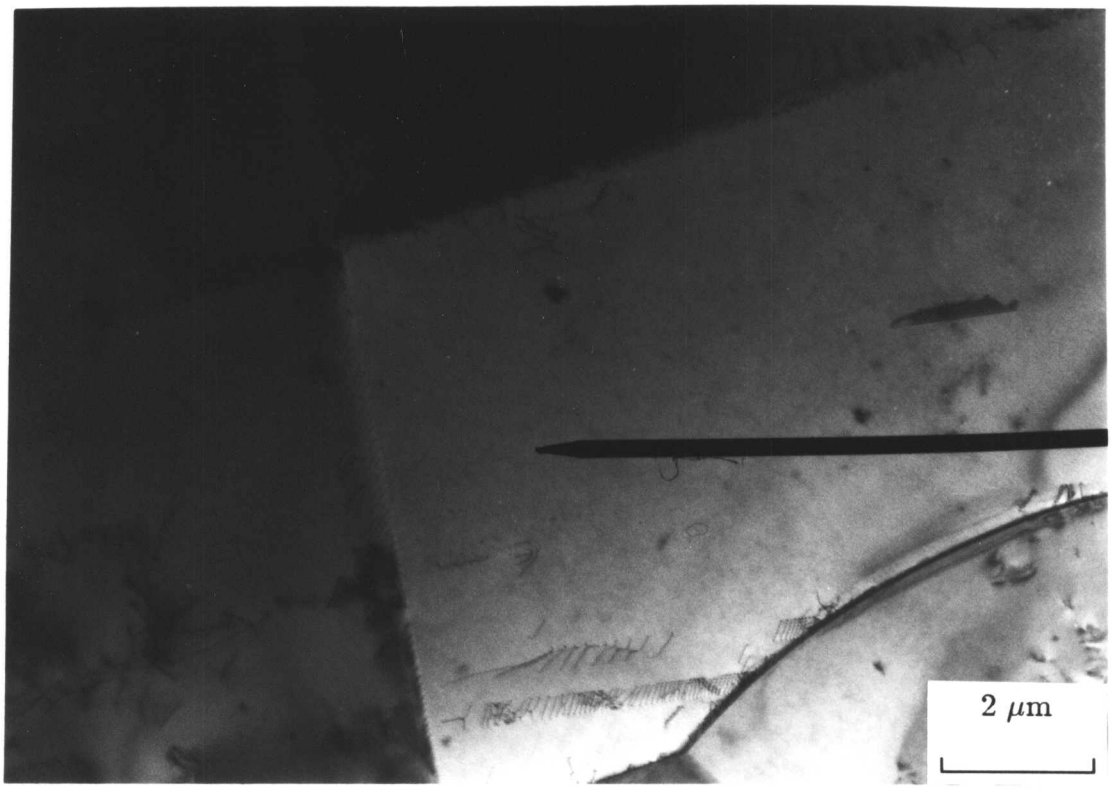

Figure 3.20. TEM micrograph showing the microstructure of rolled duplex stainless steel alloy IC378. The electron diffraction pattern of the pointed phase (Figure 3.21) confirms that its crystal structure is b.c.c. and the TEM EDX microanalysis of this phase (Table 3.6) shows the partition of ferrite stabilisers in this phase confirming it is ferrite.

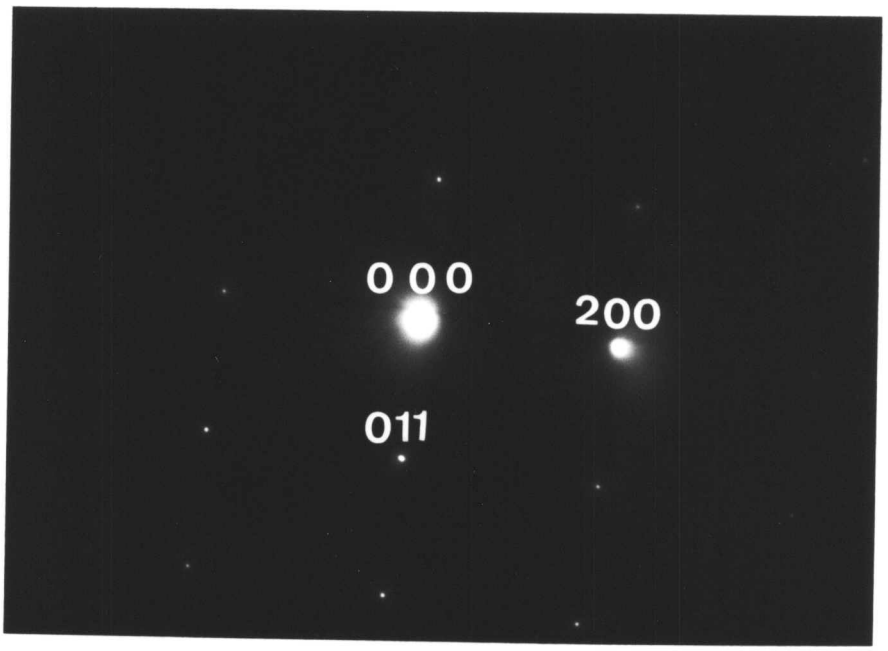

Figure 3.21. The electron diffraction pattern of the phase indicated by pointer in Figure 3.20 confirming that it has a b.c.c. crystal structure. The incident beam direction in the real space is $[0\bar{1}1]$.

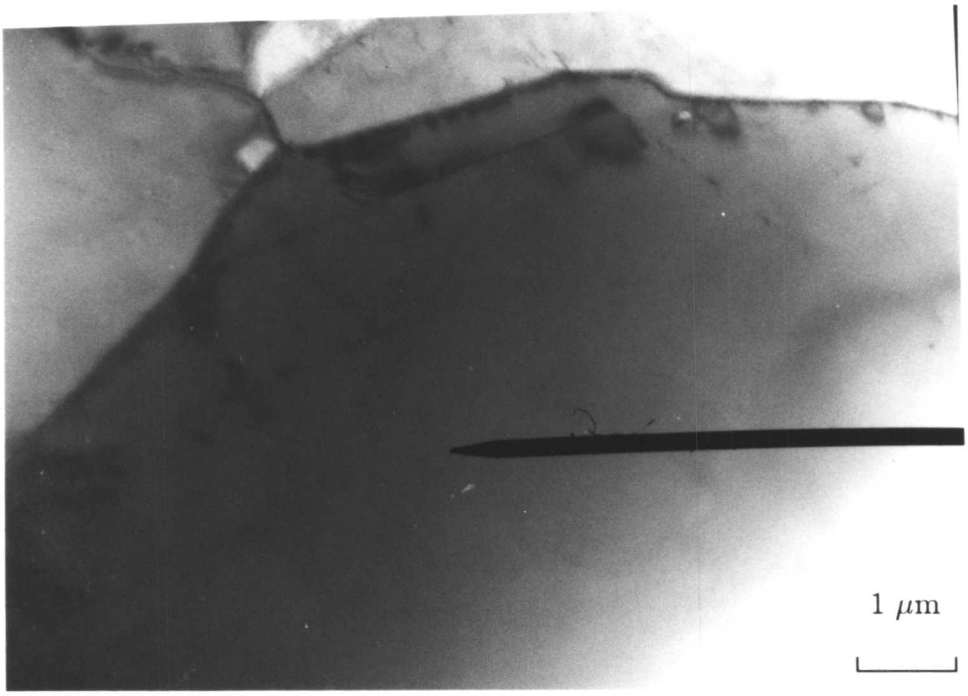

Figure 3.22. TEM micrograph showing the microstructure of rolled duplex stainless steel alloy IC378. The pointer in the figure identifies a grain where its diffraction pattern (Figure 3.23) shows that its crystal structure is f.c.c. and its TEM EDX microanalysis is present in Table 3.4 showing the partition of austenite stabilisers to this phase confirming it is austenite.

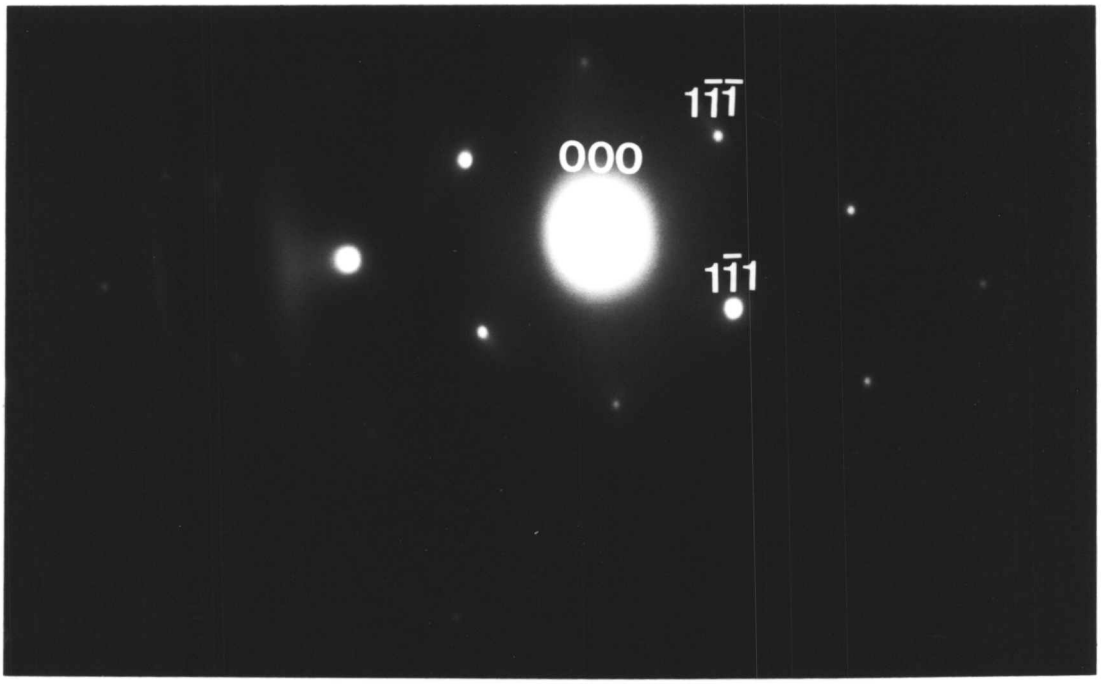

Figure 3.23. The electron diffraction pattern of the pointed phase in Figure 3.22 showing that it has a f.c.c. crystal structure. The incident beam direction in the real space is $[\overline{1}\overline{1}0]$.

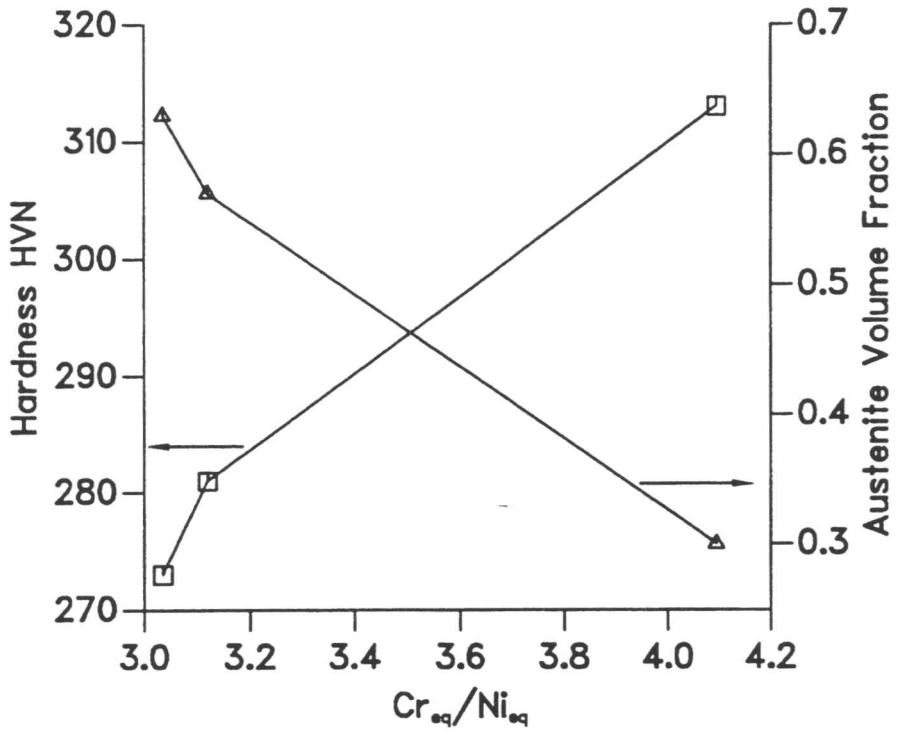

Figure 3.24. Measured vickers hardness and austenite volume fraction against the chemical composition for duplex stainless steel alloys IC373, IC378 and IC381 showing as Cr_{eq}/Ni_{eq} increases the hardness of steel will increase while the austenite volume fraction will decrease.

3.7 Conclusions

1. The microstructure of hot rolled duplex stainless steels (alloys IC373, IC378 and IC381) consists of austenite (f.c.c.) and δ-ferrite (b.c.c.).

2. The balance between ferrite and austenite can be controlled by the chemical composition of the steel.

3. While Cr and Mo are strong ferrite stabilisers and will partition into ferrite, Ni is a strong austenite stabiliser and will partition into the austenite. Thermodynamic calculations showed that N is a very strong austenite stabiliser.

4. An increase in the volume fraction of ferrite will lead to an increase in the hardness of the steel.

5. As Cr_{eq}/Ni_{eq} ratio of the steel increases, the volume fraction of ferrite will increase, causing an increase in the hardness of the steel.

Chapter 4

MICROSTRUCTURE OF SUPER DUPLEX STAINLESS STEEL WELD METALS

4.1 Introduction

Ferritic-austenitic or duplex stainless steels have been available commercially for approximately 50 years. However, the very first duplex steels had an unfavourable ferrite-austenite balance which resulted in rather poor mechanical properties in the heat affected zone (HAZ) created by welding. The HAZ in some circumstances is found to be prone to intergranular corrosion due to a high carbon level. Notwithstanding these difficulties, duplex stainless steels can in principle have applications for general engineering purposes which exploit the combination of high mechanical strength, good corrosion resistance, good weldability and good formability. At the moment, the main field of application for modern duplex stainless steels has been piping for oil and gas exploration and to some extent heat exchanger tubing, which, from the design and fabrication point of view, are rather simple applications (Olsson and Nordin, 1986).

As the failure reports on conventional duplex stainless steels accumulated during the early 1970's, research was carried out to modify the chemical composition for better service performance. The majority of the service failures have been reported to be due either to stress corrosion cracking or localised corrosion mainly in the heat affected zones of welded parts. Usually the environments in which failures have occurred contained chloride ions (Olsson and Nordin, 1986).

One of the techniques that has been suggested to resolve these problems is to increase the amount of some of the alloying elements in duplex stainless steels. These highly alloyed duplex stainless steels are called 'super duplex stainless steels' and are the main topic of this study.

4.2 Chemical Composition of Super Duplex Stainless Steels

It is generally accepted that the pitting resistance of a stainless steel depends on the chromium and molybdenum contents and that it is further enhanced by

the presence of nitrogen. The empirical equation that has been proposed for the pitting resistance equivalent (P.R.E.) for duplex steels (Clark, Gentil and Guha; 1986) is as follows:

$$\text{P.R.E.} = \text{Cr} + 3.3 \times \text{Mo} + 15 \times \text{N} \tag{4.1}$$

where all the concentrations are expressed in wt%. It is clearly desirable, if possible, to increase chromium, molybdenum and nitrogen contents. The equation is, however, over simplified and does not entirely correlate with results in practice because it omits the effects of nickel and copper. These elements can have significant effects on the microstructure and corrosion resistance, whilst a change in the balance of all the main elements can affect both the casting and hot working characteristics.

Table 4.1 shows the chemical composition of super duplex stainless steel Zeron 100. A comparison of the typical composition of coventional duplex of Cr-Ni-Mo-N, 21.5 / 5 / 2.0 / 0.14 (Table 3.1) with super duplex Cr-Ni-Mo-N, 25.5 / 7 / 4.10 / 0.25 (Table 4.1) reveals the following points:

i) The Cr concentration has been increased to improve corrosion resistance and to get a higher tensile strength.

ii) The Ni concentration has been increased to maintain the austenite/ferrite balance which is disrupted by the increased concentration of Cr.

iii) Mo has been increased to improve pitting resistance.

iv) N has been increased to improve localised corrosion resistance and also because it is an austenite stabiliser.

Table 4.1. Chemical compositions (wt.%) of some super duplex stainless steels.

Steel Grade	C	Si	Mn	P	S	Cr	Ni	Mo	Cu	W	N
Zeron100	<0.03	<1.0	<1.0	<0.02	<0.01	26	7.0	4.0	<1.0	<1.0	0.3
SAF2507	0.02	0.3	0.4	<0.02	<0.01	25	7.0	4.0	-	-	0.28

Even larger increases in the nitrogen content of these steels have proved difficult in practice, because of the onset of gas porosity in heavy cast sections.

Appreciable increases in molybdenum could be achieved only at the expense of hot ductility and impact toughness at room temperature, whilst increases in chromium had a similar effect and did not greatly improve the pitting resistance. However, a tighter control on all the elements to optimise composition and corrosion resistance, together with a slight increase in the nickel content in order to maintain a 50:50 austenite-ferrite ratio, enabled a P.R.E. value of about 38 to be achieved. Moreover, alloy development based on steel with an austenite-ferrite ratio of 60:40 has enabled further increases in chromium and nitrogen content to be achieved, to give a P.R.E. index of about 40 (Clark, Gentil and Guha; 1986).

4.3 Chemical Composition of Super Duplex Stainless Steel Weld Metals

During normal arc welding, the cooling rates are not sufficiently slow to give an equilibrium austenite content. A reduced austenite content can lead to a very sharp drop in the weld metal ductility. To avoid the decrease in toughness of the weld metal, the filler metal has to be overalloyed with nickel (up to 9 wt.%). This ensures enough austenite content in the weld metal. Table 4.2 shows the chemical compositions of the weld metals used in this investigation.

Table 4.2. Chemical compositions (wt.%) of the weld metals used in this investigation.

Material	C	Si	Mn	P	S	Cr	Ni	Mo	V	Nb	Ti	Al	Cu	N	O
A199	0.02	0.54	0.68	0.02	0.01	25.7	9.3	4.62	0.09	0.02	0.02	0.001	0.02	0.26	0.09
A200	0.02	0.53	0.62	0.02	0.001	25.1	10.2	3.30	0.09	0.02	0.02	0.001	0.08	0.27	0.09
A201	0.02	0.54	0.64	0.02	0.01	26.1	9.1	4.15	0.09	0.02	0.02	0.001	0.02	0.26	0.09
A213	0.03	0.68	0.68	0.02	0.002	25.4	9.5	4.10	0.09	0.02	0.01	0.002	0.09	0.24	0.08
A214	0.03	0.62	0.62	0.02	0.002	25.4	9.5	4.15	0.09	0.02	0.01	0.002	0.09	0.25	0.07
A215	0.03	0.64	0.65	0.02	0.002	25.5	9.5	4.08	0.08	0.02	0.01	0.002	1.0	0.24	0.07
A216	0.03	0.64	0.68	0.02	0.002	25.5	9.5	4.10	0.08	0.02	0.02	0.002	1.0	0.25	0.08
A219	0.03	0.60	0.70	0.02	0.007	25.6	9.4	4.08	-	-	-	-	-	0.27	-

4.4 Welding Conditions

The welding conditions include parameters such as the choice of welding process, welding voltage and current, preheat or the maximum interpass tem-

perature in the multi-pass weldments, etc. All of these can have an effect on the weld microstructure via their influence on the cooling rate. In the welding of duplex and super duplex stainless steels the choice of heat input has a determining role on the mechanical characteristics of welds due to its influence on the ferrite level in the weld and in the heat affected zone (HAZ) when the welds remain in the 'as welded' condition. Faucheur and Gilber (1986) have studied the welding of duplex stainless steel and have suggested that the nominal heat input should not be less than 1.5 kJ/mm to ensure sufficient austenite. On the other hand, they found that excessive heat input during welding can cause the precipitation of sigma phase in the HAZ which has a detrimental effect on the corrosion resistance in some media. Because of these problems they have also suggested that the heat input should not exceed 3 kJ/mm and that the maximum interpass temperature should be kept below 150 °C. Laing *et al.* (1986) have investigated the effect of heat input on the ferrite-austenite balance in duplex stainless steel pipe welds. They have shown that as the heat input of the root and hot pass was increased from 0.5 kJ/mm to 1.2 kJ/mm, the ferrite content in the root HAZ was significantly decreased.

Table 2.2 shows the welding conditions for the welds used in this investigation. All of them have been produced by using the manual metal arc (MMA) process. All the weld pads were deposited on a mild steel (approximately 8 mm thick). In each case approximately 10 runs have been deposited top of each other. Heat inputs are in the range of 0.6-1.4 kJ/mm. As pointed out earlier, a low heat input is expected to lead to rapid cooling and insufficient time for ferrite to transform to austenite. The resulting high volume fraction of ferrite should cause a sharp decrease in the weld metal toughness. Excessive heat inputs will lead to a slow cooling rate. There may then be δ-ferrite grain coarsening and also an increased possibility of sigma phase formation, especially in the reheated weld metal. Both of these will again decrease the weld metal ductility.

4.5 Thermodynamic Calculations

Thermodynamic calculations have been done for duplex rolled metals IC373 and IC378 (see Table 2.1 for their chemical compositions); super duplex rolled metal Zeron100 (Table 4.1) and super duplex weld metals A200, A201 and A219

(Table 4.2). The equilibrium volume fraction of austenite (Figure 4.1) was found to be much higher in super duplex stainless steel weld metals compared with super duplex alloys. This is due to overalloying of the weld metal with nickel to avoid the decrease in toughness. The equilibrium volume fraction of austenite was found to be dependent only on chemical composition as expressed by the Cr_{eq}/Ni_{eq} ratio. However, it must be kept in the mind that as the cooling rate is not slow enough in welding process the volume fraction of austenite is in practice much lower than indicated by the equilibrium state. The chemical compositions of conventional duplex stainless steel alloys IC378 and IC373 are presented in Table 2.1.

Table 4.3. Cr_{eq}/Ni_{eq} ratios of different steels studied using thermodynamic calculations. The ratios have been calculated using Hammar and Svensson (1979) equation (see section 3.4).

Material	IC373	IC378	ZERON100	A201	A219	A200
Cr_{eq}/Ni_{eq}	4.09	3.12	2.64	2.40	2.24	2.04

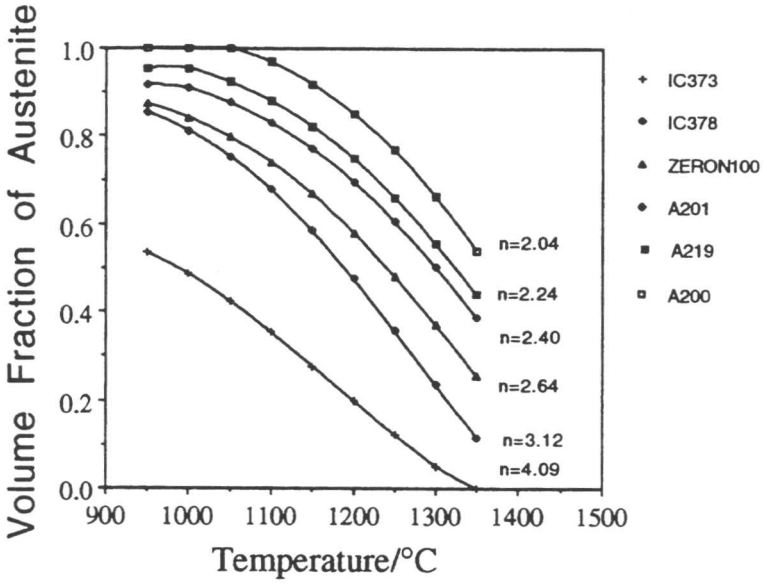

Figure 4.1. Calculated equilibrium volume fraction of austenite in different duplex and super duplex stainless steels (n in the figure correspond to Cr_{eq}/Ni_{eq} ratio). It can be seen that as the Cr_{eq}/Ni_{eq} of the steel (Tables 4.3) decreases the volume fraction of austenite increases.

4.5.1 Partitioning of Alloying Elements

Figures 4.2 to 4.6 show the calculated equilibrium partitioning of alloying elements during solidification (i.e. a three phase equilibrium among liquid, ferrite and austenite) in super duplex weld metal alloy A219. The solidification mode for this alloy (see chapter five) is a mixture of completely ferritic and ferritic-austenitic modes. For all the alloying elements (with the exception of nickel) the equilibrium concentration in the liquid increases during the solidification process. The last drops of liquid to solidify are enriched in solute elements. However, in the case of nickel (Figure 4.3), its equilibrium concentration in the liquid decreases as austenite begins to form. This is probably due to the fact that the solubility of nickel in austenite which has a f.c.c. crystal structure is higher than its solubility in liquid at the solidification temperature. For equilibrium between γ and δ the austenite formers nickel, carbon and nitrogen as expected partition into austenite while chromium and molybdenum which are ferrite stabilisers will partition into ferrite.

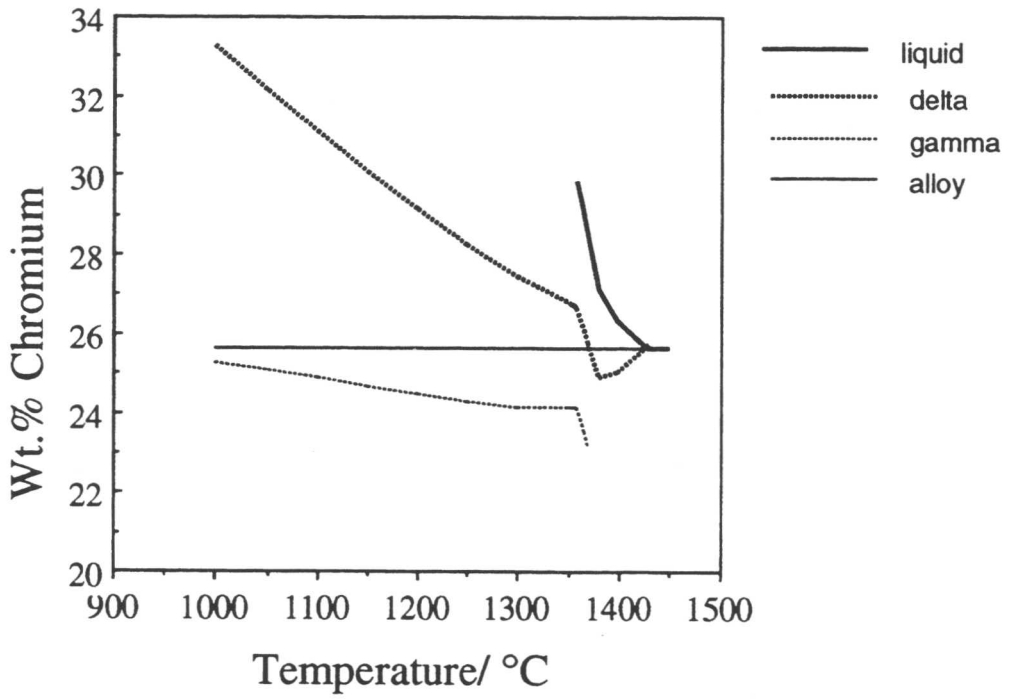

Figure 4.2. Calculated equilibrium partitioning of chromium in super duplex weld metal A219.

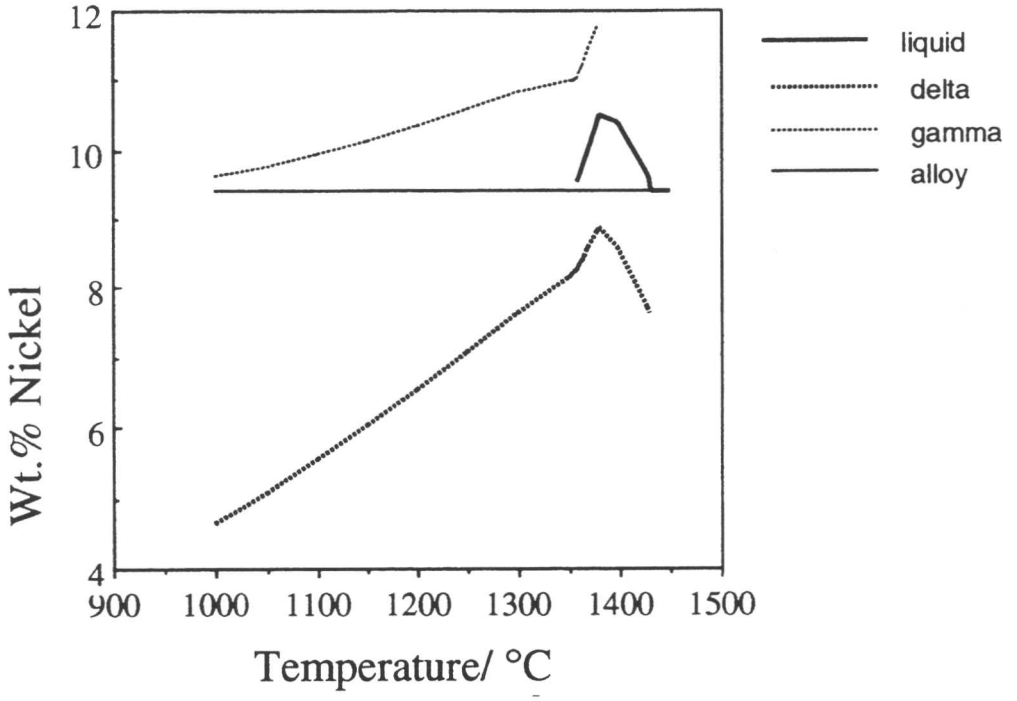

Figure 4.3. Calculated equilibrium partitioning of nickel in super duplex weld metal A219.

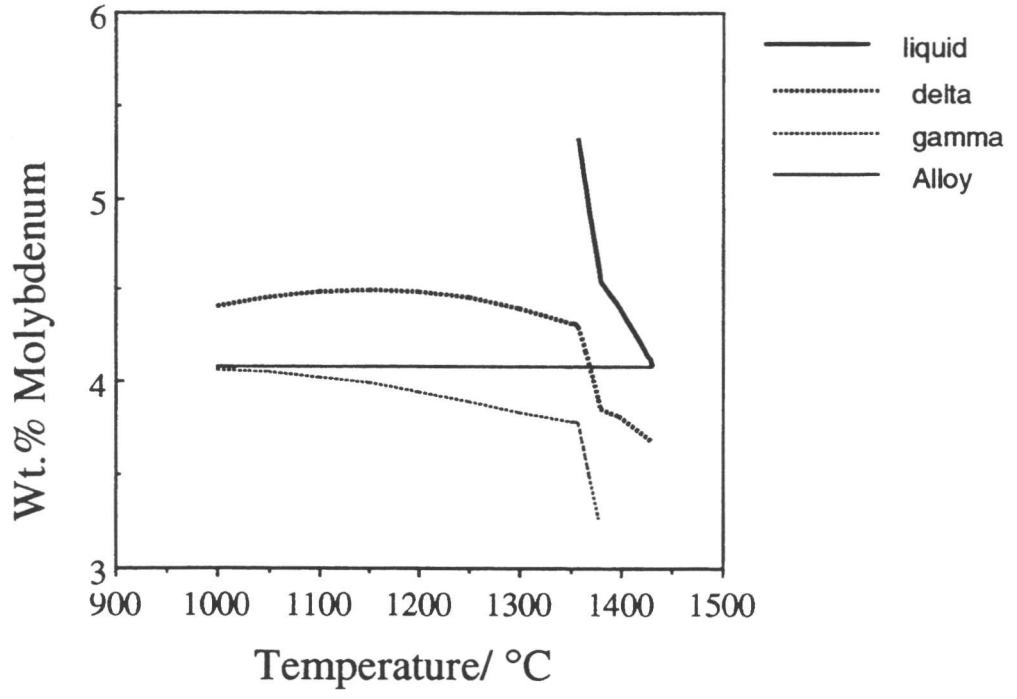

Figure 4.4. Calculated equilibrium partitioning of molybdenum in super duplex weld metal A219.

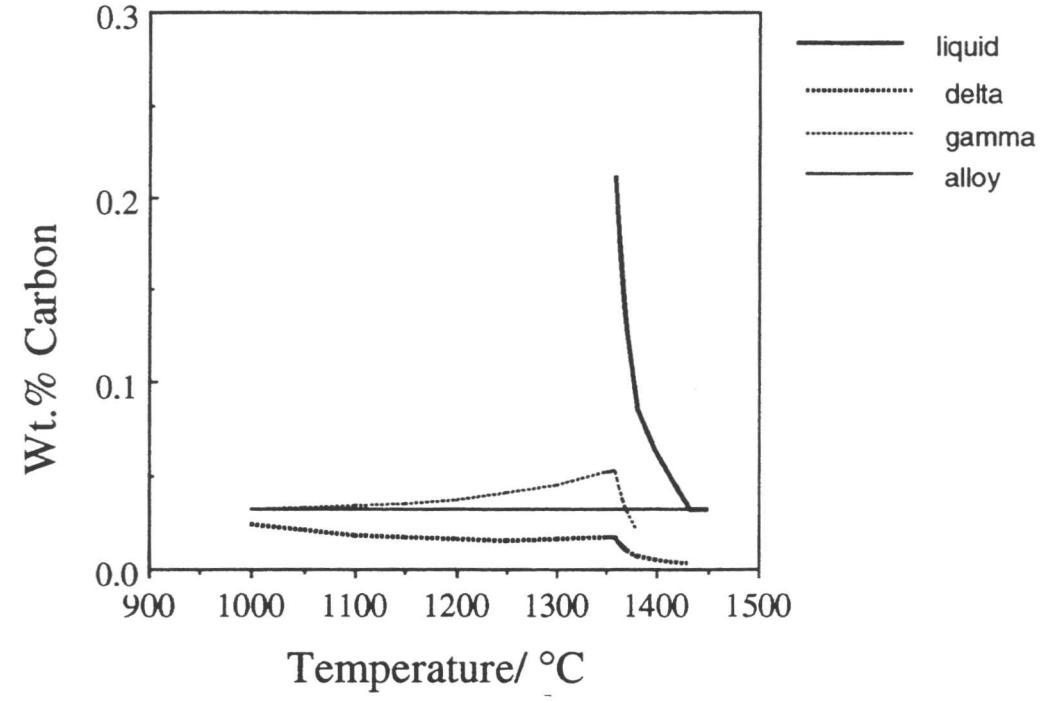

Figure 4.5. Calculated equilibrium partitioning of carbon in super duplex weld metal A219.

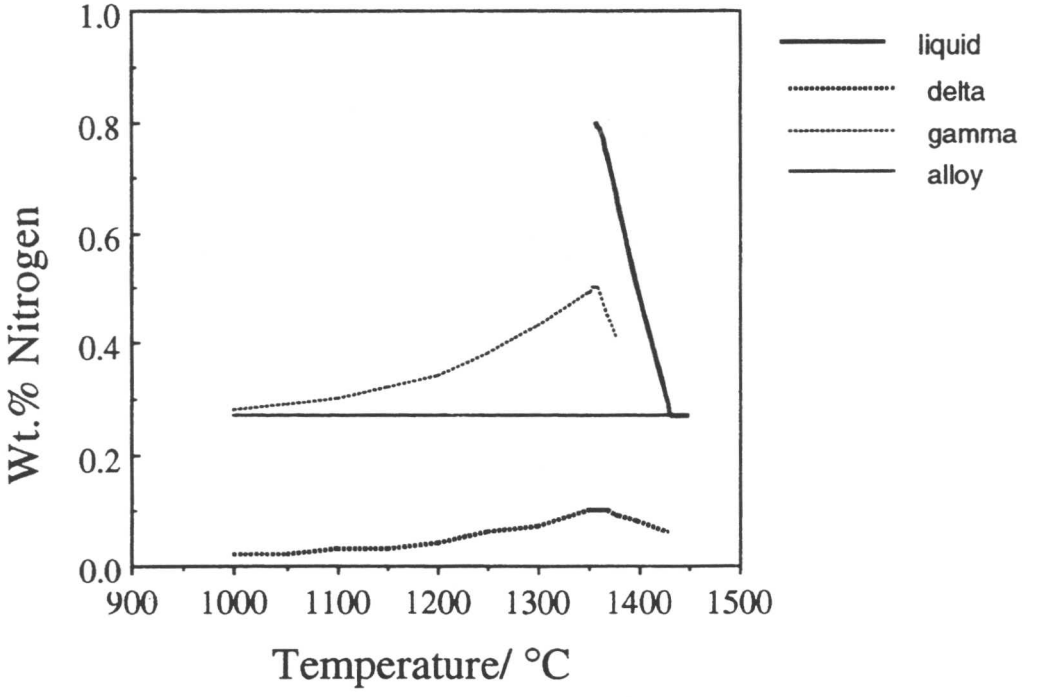

Figure 4.6. Calculated equilibrium partitioning of nitrogen in super duplex weld metal A219.

4.6 Microstructure of Super Duplex Stainless Steel Weld Metal

The weld metal microstructures of these alloys can be divided into two groups according to their solidification modes. Super duplex weld metals with Cr_{eq}/Ni_{eq} ratio less than 2.40 will solidify as a mixture of two modes (see chapter five) with primary ferrite forming first followed by a mixed ferritic-austenitic mode of solidification (Karlsson *et al.*, 1991). Figure 4.7 shows the schematic illustation of fully ferritic and ferritic-austenitic solidification. Figure 4.8 shows the microstructure of the as-deposited super duplex stainless steel weld metal A219. The right hand side solidified as primary ferrite and subsequently decomposed to ferrite plus austenite while the left hand side solidified as a mixture of ferrite and austenite. The region with primary ferrite will produce a so-called 'normal' duplex microstructure in the weld metal (Figure 4.9). This normal duplex microstructure consists of primary ferrite grains with austenite mainly precipitated in a Widmanstätten manner. Both the inter-granular and intra-granular Widmanstätten plates can be seen in Figure 4.9 indicating that during the transformation of δ-ferrite to austenite, nucleation occurred both on the grain boundaries and inside the δ-ferrite grains. The TEM micrograph of this primary Widmanstätten plates is shown in Figure 4.10. The selected area diffraction pattern (SADP) of these plates (Figure 4.11) indicates that the crystal structure is f.c.c. while that of the matrix (Figure 4.12) is b.c.c. The TEM EDX microanalysis show (Figure 4.13) that there is little difference in chemical composition between these Widmanstätten plates and the matrix compared with the difference between austenite and ferrite grains in the rolled structure (Figure 3.19). This is probably due to high cooling rate in welding which does not allow the Widmanstätten austenite to achieve the equilibrium composition.

Several studies (Solomon and Devine, 1979; Southwick and Honeycombe, 1980) have been conducted on the decomposition of ferrite to austenite in duplex stainless steels and the mechanisms of austenite formation would appear to vary according to the temperature of formation. The formation of high temperature austenite occurs by a nucleation and growth process and follows C-curve kinetics. The precipitation of austenite occurs preferentially on dislocations. The analysis of the growth kinetics is extremely complex since nucleation and

growth are occurring simultaneously. When the equilibrium volume fraction of austenite has been attained for each treatment temperature, competitive coarsening occurs. This is aided by the formation of sub-boundaries within the ferrite which act as short circuit diffusion paths (Solomon and Devine, 1979). Throughout the growth and coarsening stages the austenite and ferrite are related by a Kurdjumov-Sachs type orientation relationship (Karlsson *et al.*, 1991).

The austenite morphologies produced by decomposition of ferrite include the Widmanstätten side plates, the grain boundary Widmanstätten sawteeth, the Widmanstätten side plates emanating from allotriomorphs, and Widmanstätten side plates having an acicular appearance (Figure 4.9).

The region that solidifies to a mixture of ferrite plus austenite (Figure 4.14) gives a different microstructure. Unlike the Widmanstätten plates in the normal duplex region which is due to a solid state transformation from ferrite, the solidified austenite has a blocky morphology. Ferrite in this region has a vermicular shape.

The SADP from the blocky austenite shows that it has f.c.c. crystal structure. Unlike the Widmanstätten austenite that has orientation relationship with adjacent ferrite grain, this type of austenite has found to have no reproducible orientation relationship with the adjacent ferrite grain (Karlsson *et al.*, 1991). Table 4.5 and Figure 4.15 show the TEM EDX microanalysis data for this blocky austenite compared against the chemical composition of the Widmanstätten austenite. As predicted by thermodynamic calculations (Figures 4.2 and 4.3) the chromium content of these solidified austenite is lower than that of Widmanstätten austenite (which is a product of solid solution transformation from δ-ferrite). However, this result is far from conclusive since the experimental Cr concentrations are really identical within the limits of experimental errors. On the other hand the nickel content of the blocky austenite is higher than the nickel content of Widmanstätten austenite. Their higher nickel content as was pointed out in section 4.5.1 is due to the fact that the solubility of nickel in austenite is higher than in liquid at solidification temperature.

Table 4.4. TEM EDX microanalysis data of Widmanstätten plates (austenite) and matrix (ferrite) of Figure 4.8. All the concentrations are in wt.%.

Phase	Cr	Ni	Mo	Mn	Si
austenite	24.4±2.1	10.4±0.8	2.9±0.4	0.8±0.1	0.6±0.1
δ-ferrite	28.4±2.4	6.3±0.7	5.0±0.7	0.4±0.1	0.7±0.1

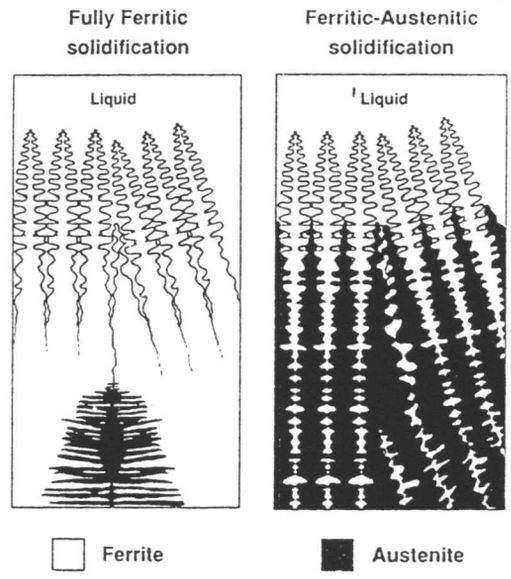

Figure 4.7. Schematic illustration of fully ferritic and ferritic-austenitic solidification (Karlsson *et al.*, 1991).

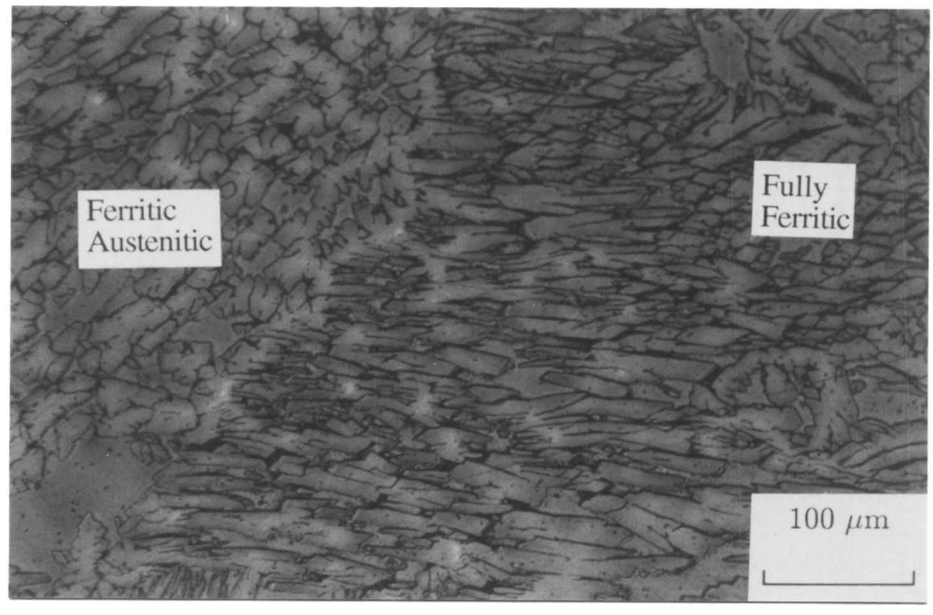

Figure 4.8. Light micrograph showing the as-deposited microstructure in super duplex stainless steel weld metal A219.

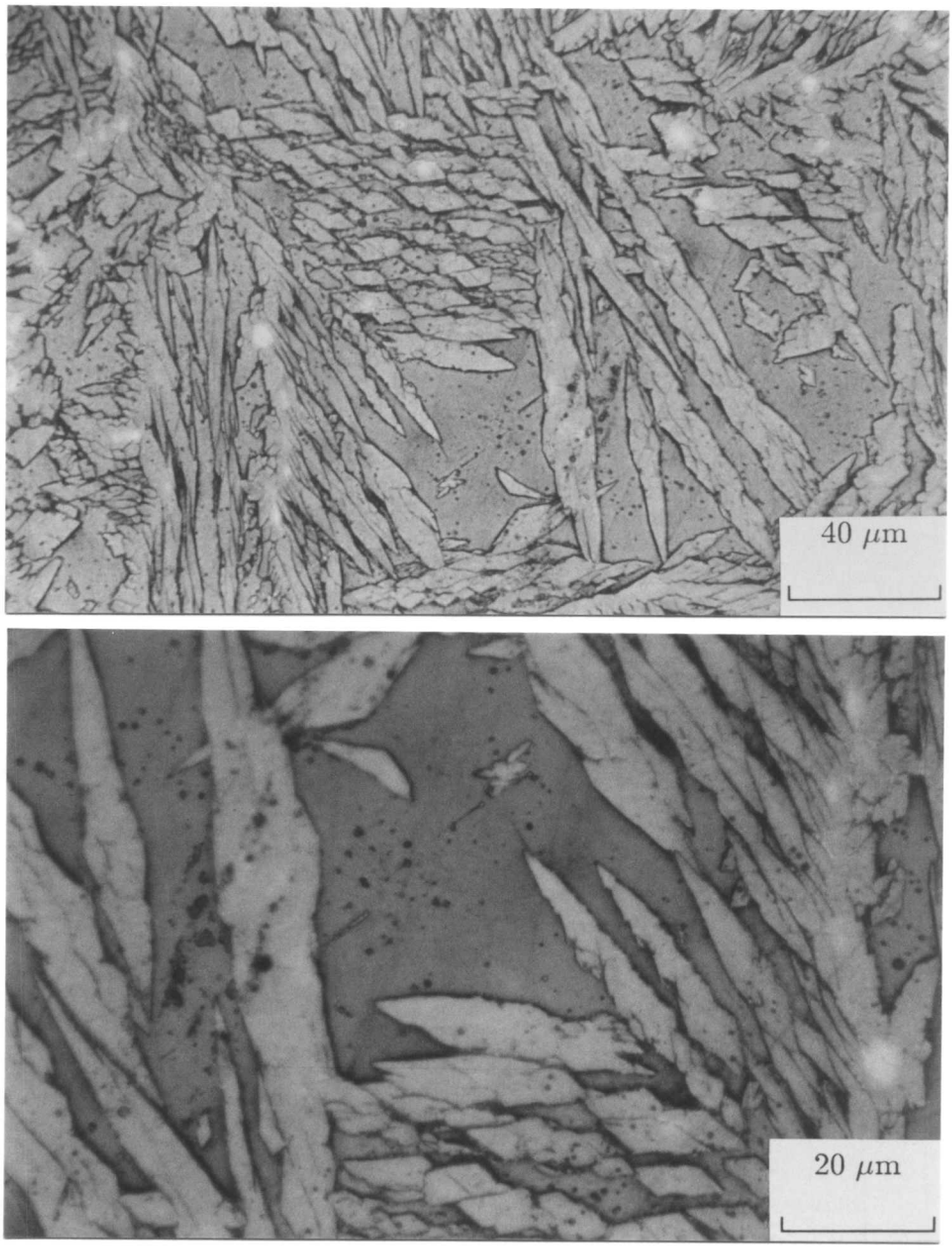

Figure 4.9. Light micrographs show the as-deposited microstructure in super duplex stainless steel weld metal A219. The picture is from normal duplex region and the yellow colour Widmanstätten plates are austenite and blue matrix is ferrite.

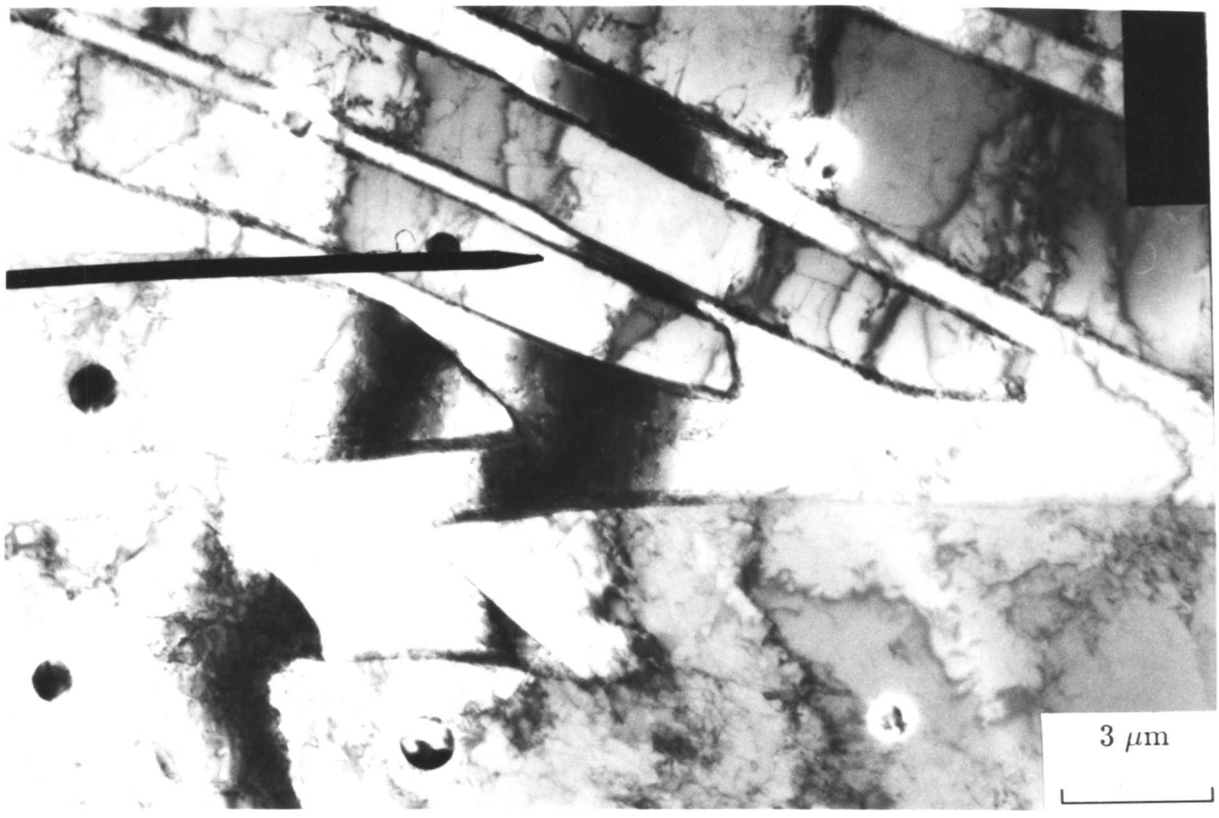

Figure 4.10. Bright field TEM micrograph shows the as-deposited microstructure in the normal duplex region of super duplex stainless steel weld metal alloy A219. The pointer indicates a Widmanstätten austenite plate.

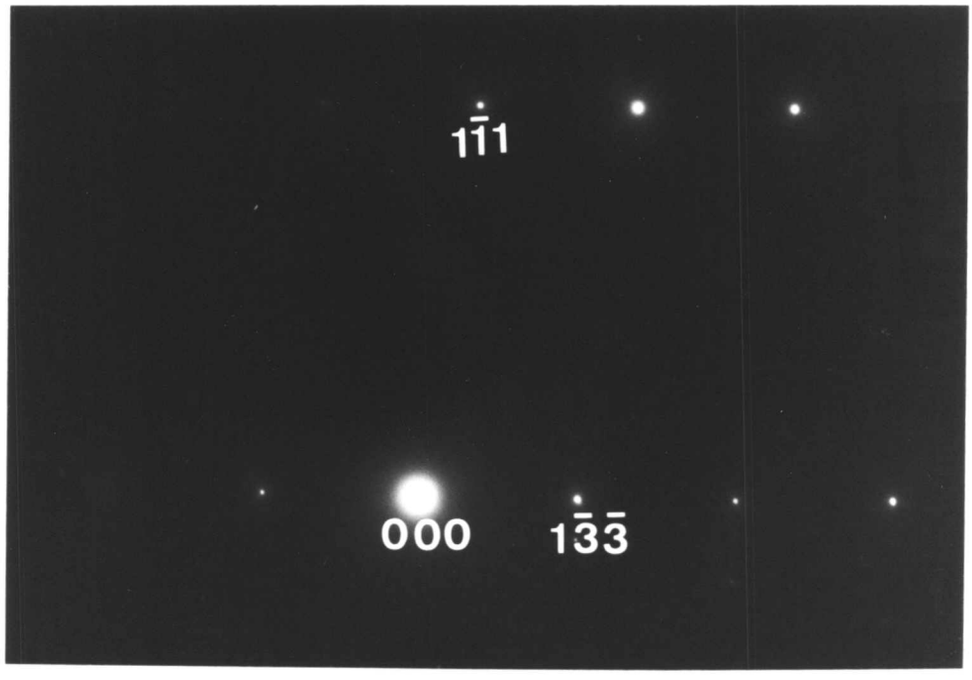

Figure 4.11. Electron diffraction pattern from the Widmanstätten plate marked by the pointer in figure 4.8 showing that the plate has a f.c.c. crystal structure. The zone direction of the diffraction pattern is $[\overline{3}2\overline{1}]$.

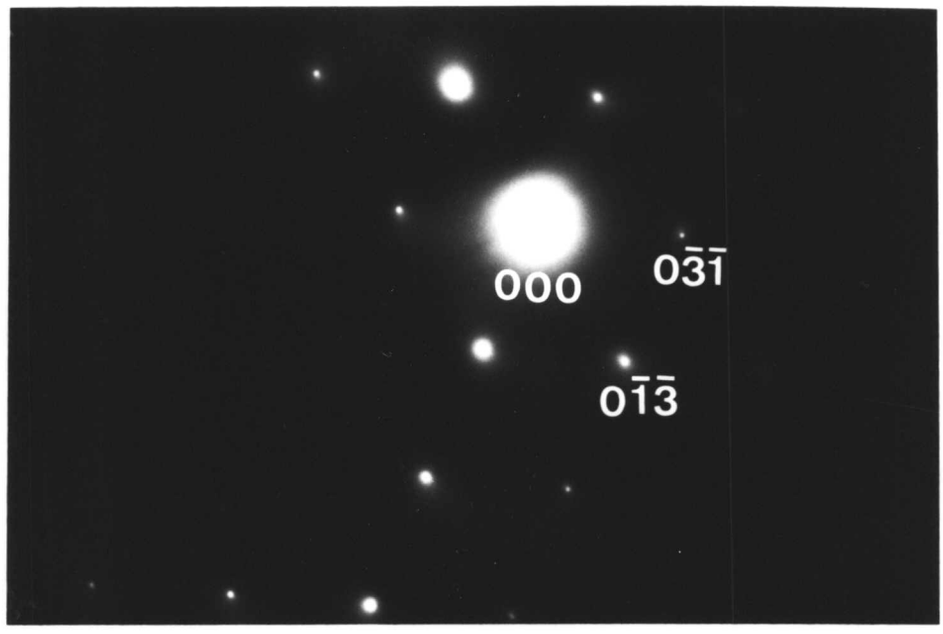

Figure 4.12. Electron diffraction pattern of the matrix adjacent to the Widmanstätten plate illustrated in figure 4.8 showing that the matrix has a b.c.c. crystal structure. The zone direction of the diffraction pattern is [100].

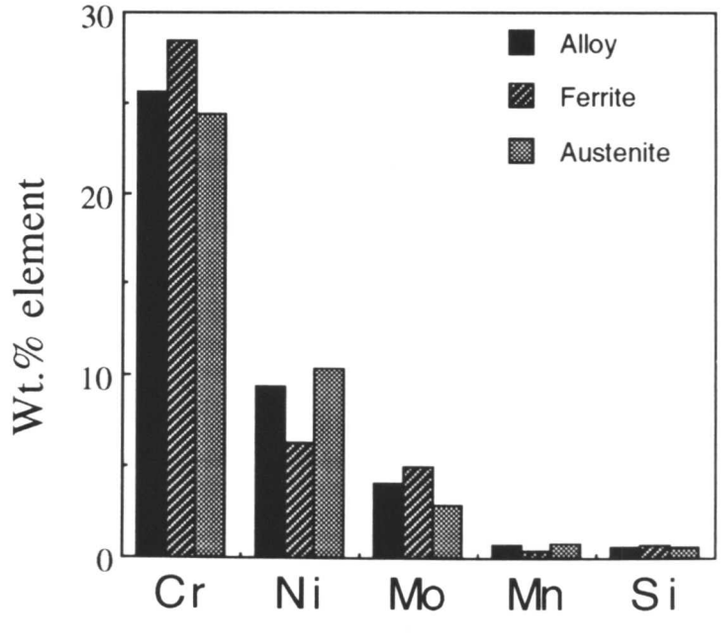

Figure 4.13. TEM EDX data showing the chemical compositions of the matrix (ferrite) and the Widmanstätten plate (austenite) of Figure 4.10.

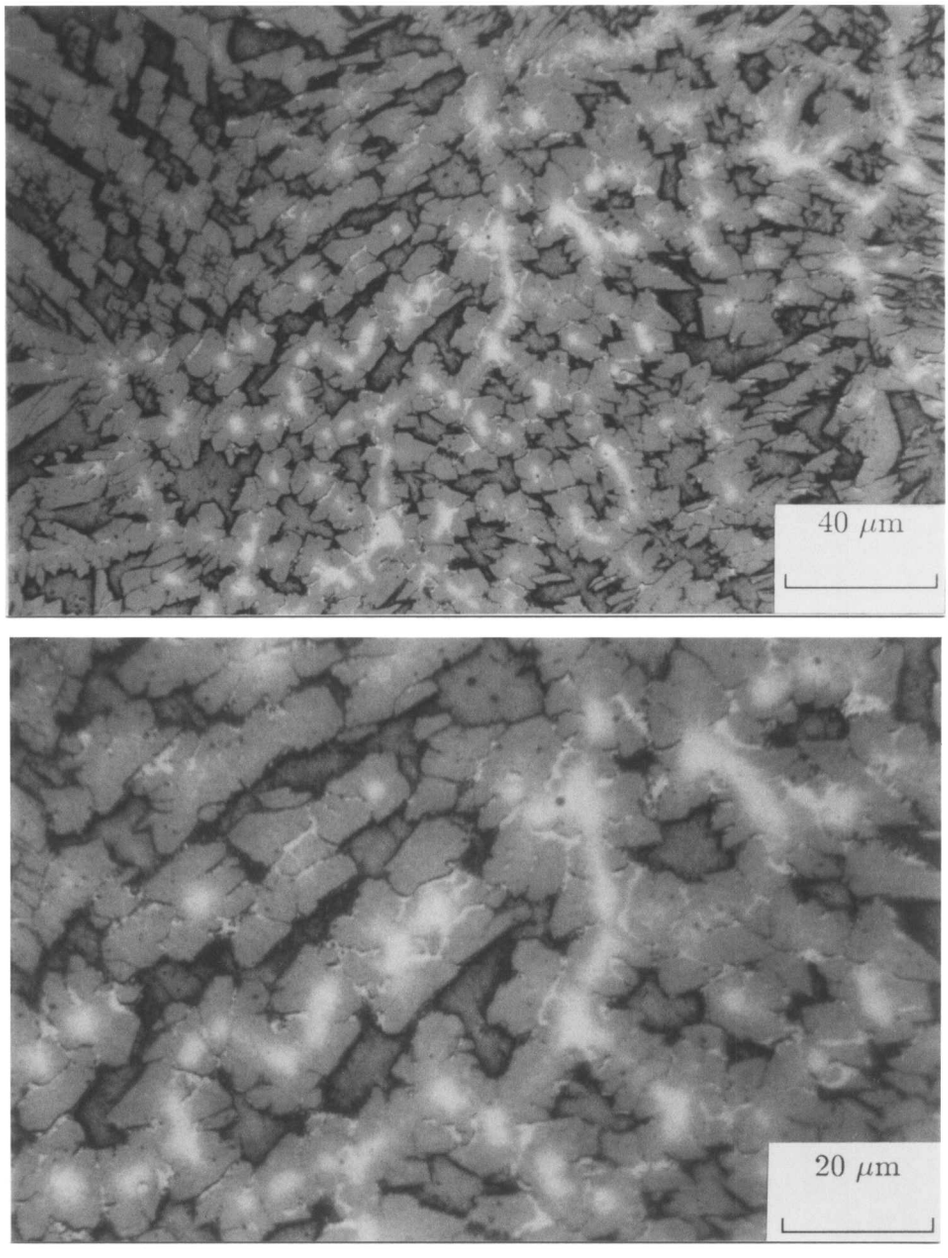

Figure 4.14. Light micrographs showing the as-deposited microstructure in super duplex stainless steel weld metal A219. The picture is from a region which has solidified to a mixture of γ and δ. The yellow colour phase is austenite and the blue one is ferrite.

Table 4.5. TEM EDX microanalysis data of Widmanstätten austenite and blocky austenite in super duplex weld metal A219. All the concentrations are in wt.%.

Phase	Cr	Ni	Mo	Mn	Si
Widmanstätten austenite	24.4±1.9	10.4±1.3	2.9±0.3	0.8±0.1	0.6±0.1
blocky austenite	24.0±1.1	12.0±0.8	3.7±0.5	1.0±0.2	0.5±0.1

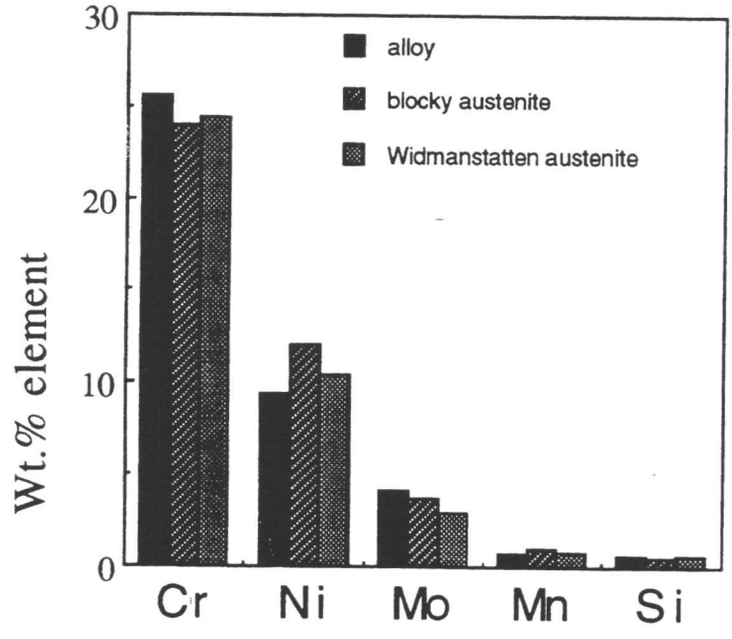

Figure 4.15. TEM EDX microanalysis data showing the measured alloying element concentration of blocky and Widmanstätten austenite in super duplex weld metal A219.

4.6.1 Inclusions

In MMA welding process the electrodes which produce the weld metal are flux covered consumables. Karlsson and Pak (1991) has studied the effect of the coating composition on the microstructure and properties of duplex MMA weld metals. They have reported that the austenite volume fractions of both rutile and basic weld metals are identical in the as-welded condition. However, the basic weld metal has a higher austenite fraction after heat treatment at 1300 °C and also the precipitation of intermetallic phases takes place much more rapidly

in the rutile weld metal than in the basic weld metal during heat treatment at 675 and 800 °C.

The chemical composition of the electrodes used to produce the weld metals investigated in this study are given in Table 4.2. All the electrodes had rutile coatings. The electrode covering has multiple usages. The combustion and decomposition of the electrode covering from the heat of the welding arc produces a gaseous shield that excludes the atmosphere from the weld area. The molten metal is further protected by materials in the electrode covering, that form a molten slag, which acts like a protective blanket until the metal has solidified. The slag is removed after the weld metal cools down to ambient temperature. However, numerous fine nonmetallic particles of the slag become trapped in the weld metal (Figure 4.16). Figure 4.17 shows the TEM micrographs of the carbon replica extracted from rutile weld metal A219. TEM EDX analysis of these inclusions (Table 4.6 and Figure 4.18) shows that (as it was expected) they are rich in silicon and manganese.

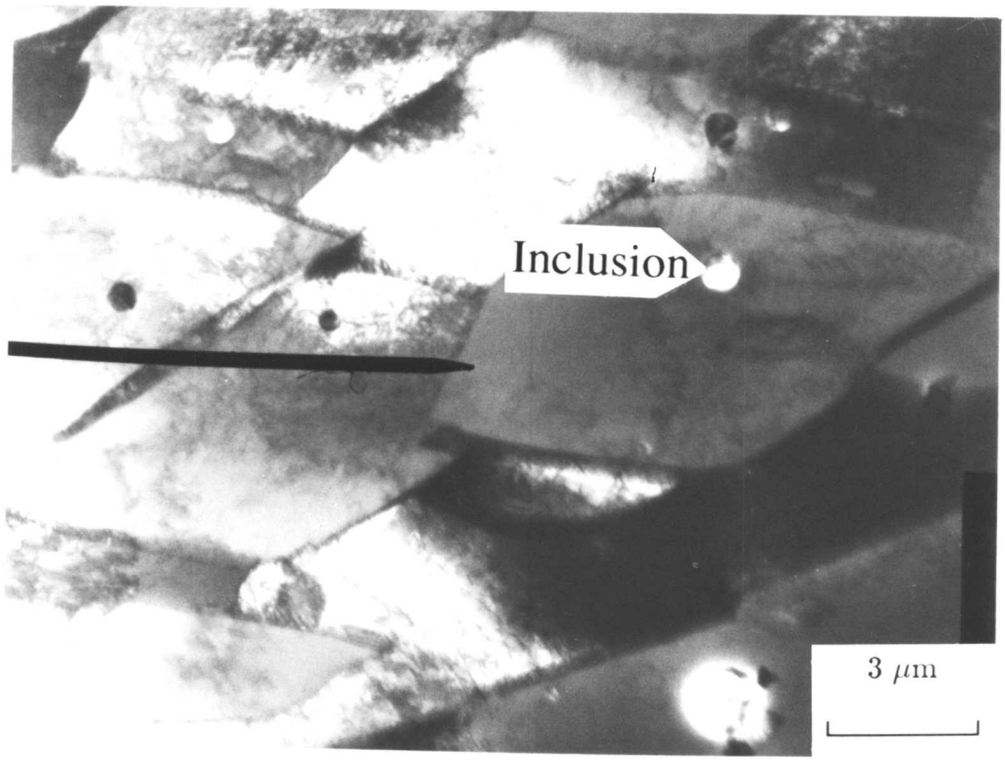

Figure 4.16. Bright field TEM micrograph showing the inclusions in rutile weld metal A219. The pointer identifies an austenite grain with an inclusion in it.

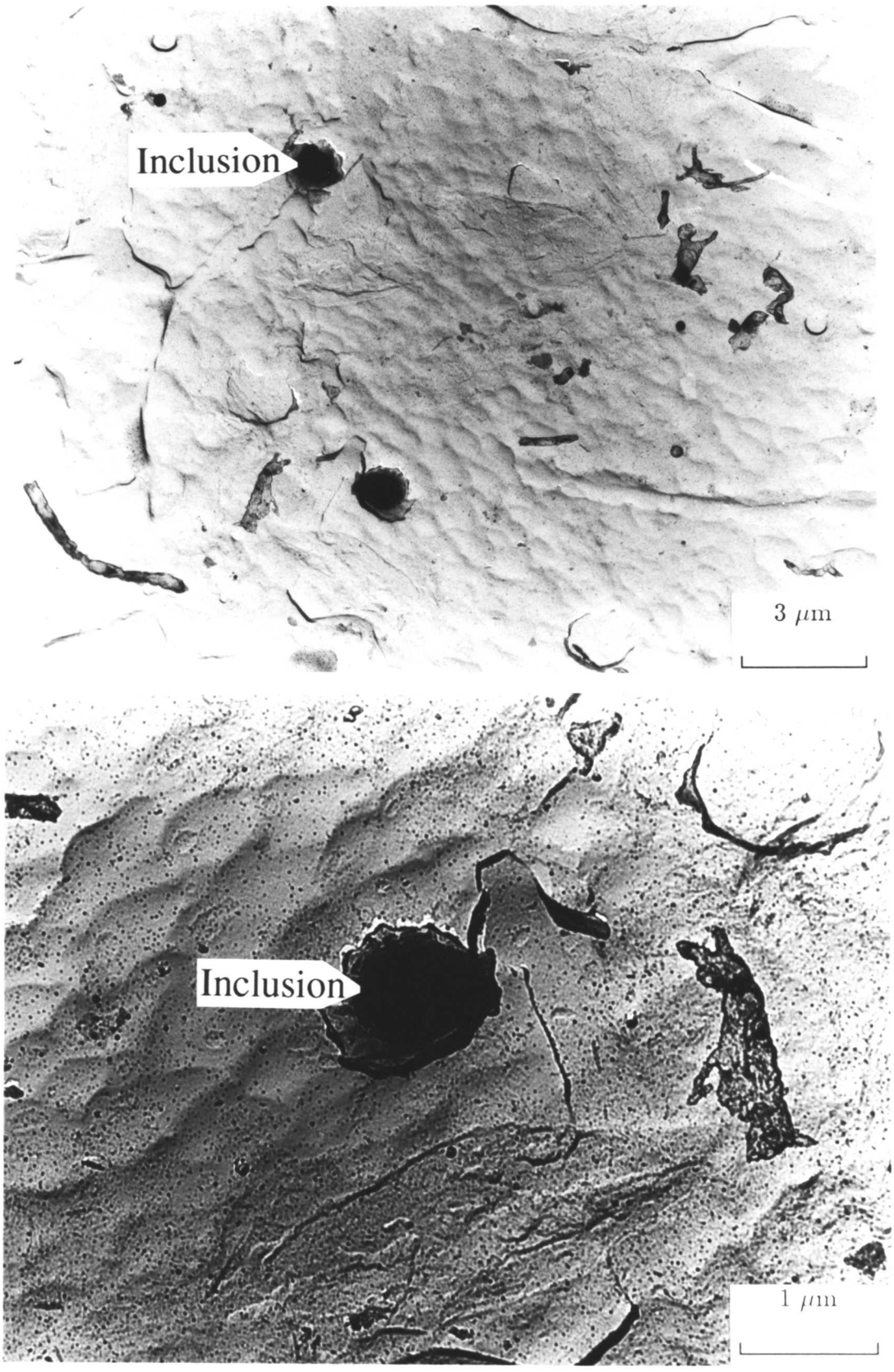

Figure 4.17. Bright field TEM micrographs of carbon extraction replica from rutile weld metal A219 showing inclusions in the weld metal.

Table 4.6. TEM EDX microanalysis data of inclusions in super duplex weld metal A219. All the concentrations are in wt.%.

Phase	Cr	Ni	Mo	Mn	Si
Inclusion	5.2±0.4	2.1±0.3	0.0±0.0	39.6±2.7	43.3±2.7

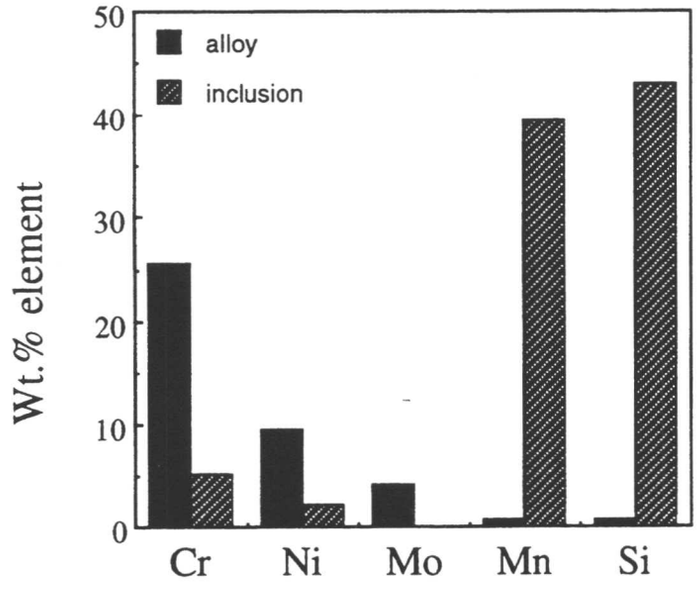

Figure 4.18. TEM EDX microanalysis data showing the measured chemical composition of the inclusions in Figure 4.17. Note that light elements such as oxygen are excluded from the analysis.

4.7 Reheated Weld Metal Microstructure

In multipass weldments the effect of fresh runs is to cause the underlying weld metal to be reheated. In the unmelted metal close to the fusion boundary, the rapid thermal cycle can cause structural transformations, if the maximum temperature attained is sufficiently high. Moreover, the material immediately adjacent to the weld metal, which is heated to a very high temperature, can be subjected to ferrite grain growth. Finally, the rapid cooling which follows welding produces effects which are analogous to quenching from different temperatures, and can leave non-equilibrium microstructures in the weld and HAZ at room temperature. The nature of these structures depends upon the composition of the duplex stainless steel being considered.

Our investigations on the microstructure of the reheated metal of super duplex stainless steel weld metals (see Table 4.2 for their chemical compositions

and Table 2.2 for the welding conditions) show that they consist of two different regions. Referritised and austenitised regions.

4.7.1 Referritised region

This region consists of the unmelted metal adjacent to the fusion boundary (Figure 4.19), and has been heated to very high temperatures (close to melting point). It is therefore subjected to ferrite formation. The striking feature is that there is more austenite in the as-deposited region when compared with the referritised zone in the reheated region. This is because the alloys solidify to a mixture of ferrite and austenite, the volume fraction of austenite in the solidified region is higher compared with that in the underlying reheated weld metal which ferritised. The microstructure can be seen in Figure 4.19 to consist of columnar grains of ferrite with intergranular and intra-granular plates of Widmanstätten austenite.

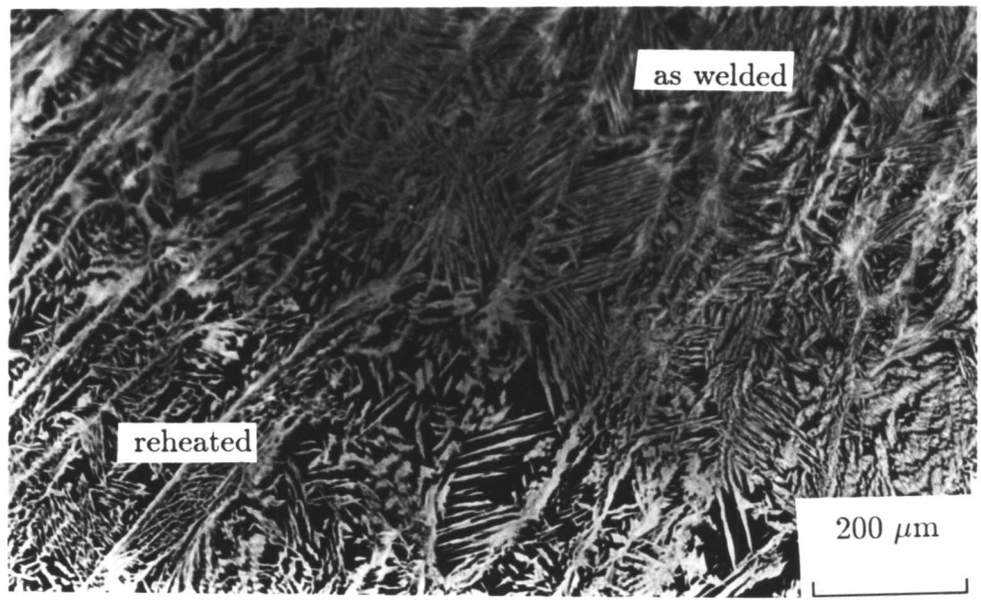

Figure 4.19. Light micrograph shows referritised region in reheated weld metal A219.

4.7.2 Austenitised region

This region of reheated metal experiences peak temperatures between 1100 and 800 °C and is immediately below the referritised region discussed above. In the microstructure of this region (Figure 4.20) fine intragranular plates of Widmanstätten can be seen inside the ferrite grains indicating that ferrite in this

region has been induced to decompose further to austenite. Moreover, a small amount of sigma phase was found to precipitate on the ferrite/austenite grain boundaries, confirming that the metal has been reheated over temperature range 800-1100 °C for long enough to permit ferrite to decompose to austenite plus sigma phase. Figure 4.21 shows the TEM EDX data from the sigma phase. As sigma phase is rich in chromium and molybdenum, its precipitation is expected to impair the corrosion properties. Sigma phase precipitation also increases the hardness and leads to a deterioration in toughness (for the mechanism of decomposition of ferrite to austenite plus sigma phase and effect of precipitation of sigma phase on corrosion and mechanical properties see chapter seven).

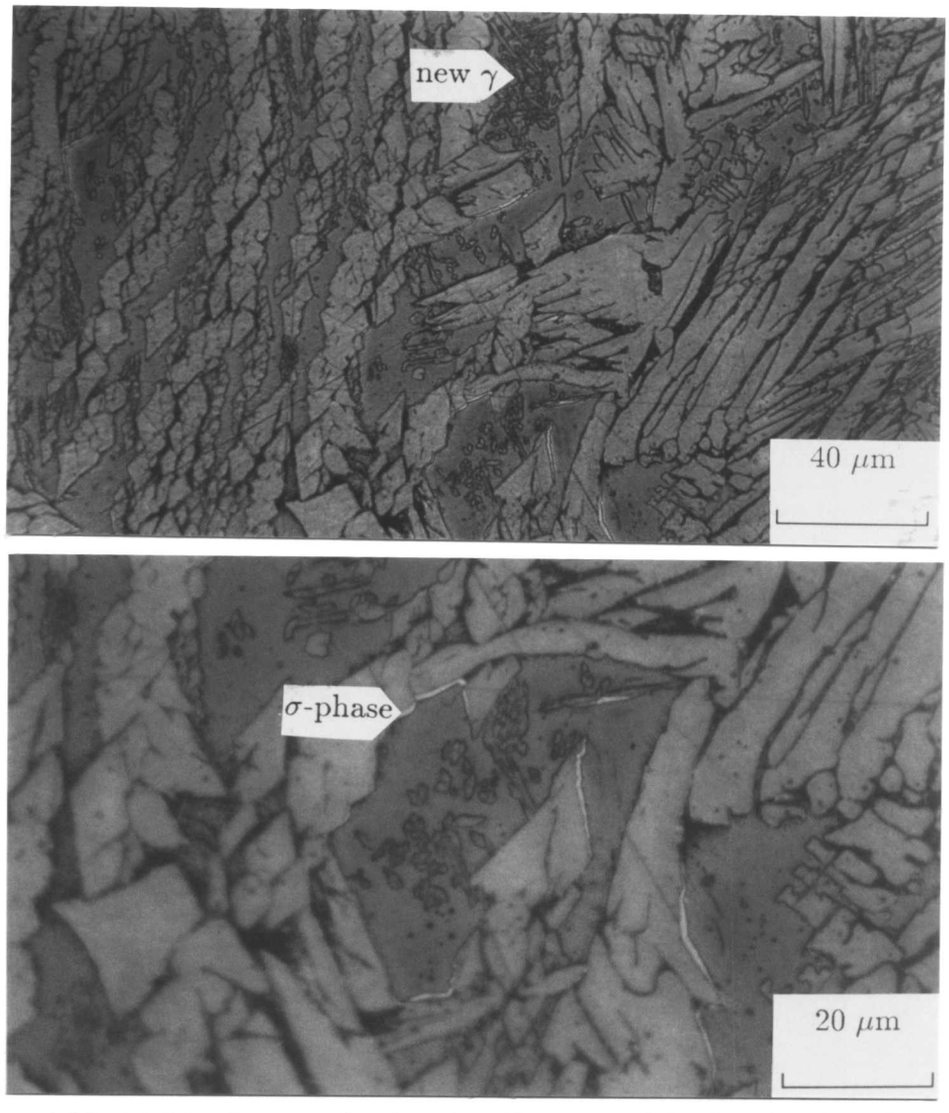

Figure 4.20. Light micrographs showing the austenitised region in reheated weld metal A219.

Table 4.7. TEM EDX microanalysis data of sigma phase found in austenitised region of reheated weld metal A219. All the concentrations are in wt.%.

Phase	Cr	Ni	Mo	Mn	Si
Sigma phase	37.4±2.7	3.3±0.6	10.7±0.9	2.8±0.4	2.2±0.3

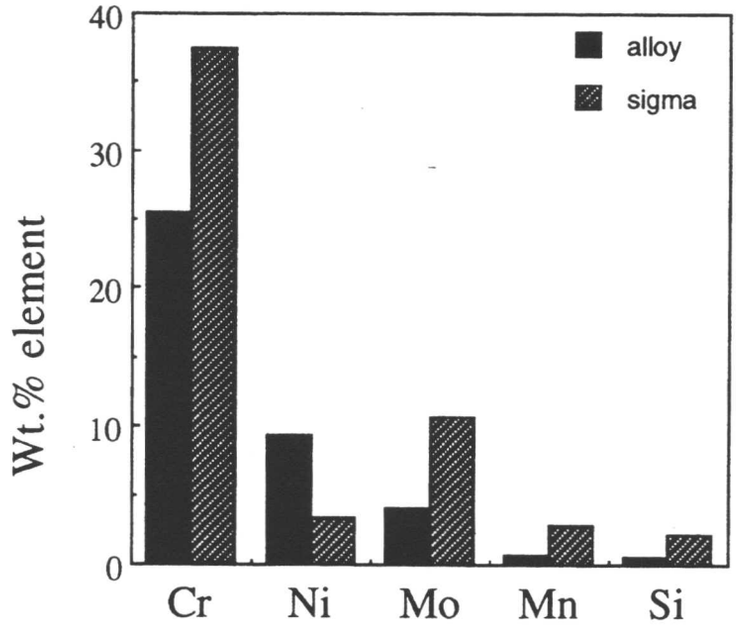

Figure 4.21. TEM EDX microanalysis data shows the chemical composition of sigma phase found in the reheated weld metal A219 (light elements are excluded).

4.8 Conclusions

1. The austenite in the as-solidified super duplex weld metal has two different morphologies; blocky and Widmanstätten. Blocky austenite is due to solidification directly from the liquid phase whereas Widmanstätten austenite is the product of the solid state transformation of δ-ferrite.

2. The reheated weld region in a multipass deposit consists of two distinct zones, the referritised and austenitised regions.

3. The volume fraction of austenite in the referritised region is much lower than in the as-deposited weld metal, presumably because it is solution treated at temperatures above 1300 °C.

4. The volume fraction of austenite in the austenitised region is much higher than in the as-deposited weld metal, presumably because it is annealed in the range 1100-800 °C during multipass welding.

5. A small amount of sigma phase precipitation was found in the austenitised region of the reheated weld metal A219. As expected this sigma phase was found to be rich in Cr and Mo.

6. The inclusions in rutile weld metal of super duplex stainless steel A219 was found to be rich in Si and Mn.

Chapter 5

SOLIDIFICATION OF SUPER DUPLEX STAINLESS STEEL WELD METALS

5.1 Introduction

The solidification mode in stainless steels is very important because it has an effect on the mechanical and corrosion properties of welded and cast components. The volume fraction of austenite as well as the partitioning of alloying elements between δ-ferrite and austenite in weld the metals are influenced by the solidification mode. As discussed in chapter four, the as-solidified austenite is richer in nickel compared with that which forms by solid state transformation. Completely ferritic solidification leads to columnar ferritic grains in the as-welded microstructure. Karlsson *et al.* (1991) have shown that a ferritic-austenitic mode of solidification in duplex stainless steel weld metal results in a microstructure in which the ferrite is enriched in elements such as chromium, and in addition the phase boundaries have relatively high energies compared with the δ/γ boundaries that occur during ferritic solidification. This makes the nucleation and growth of detrimental phases (such as sigma) more easy. This chapter deals with the different solidification modes that can occur in duplex stainless steels.

5.2 Previous Work

Suutala (1983) has shown that in austenitic stainless steels processed conventionally, the solidification mode depends essentially on the chemical composition of the steel and the effect of solidification conditions is of secondary importance. He used the Cr_{eq}/Ni_{eq} ratio to describe the effect of chemical composition. The Cr_{eq} and Ni_{eq} were calculated according to the Hammar and Svensson (1979) equation. Suutala showed that the morphology and location of the retained δ-ferrite enables the solidification mode to be determined metallographically. The transformation from δ-ferrite to austenite can start during or after solidification depending on the exact solidification sequence. Karlsson *et*

al. (1991) extended the Suutala work for application to duplex stainless steels. Figure 5.1 shows their model for the solidification of these steels. The solidification mode in duplex weld metal can be either fully ferritic or ferritic-austenitic or a mixture of both. Based on their model, duplex steels with Cr_{eq}/Ni_{eq} ratio of greater than 2.25 solidifies completely to ferrite. When the ratio is less than 2.05 the solidification mode is ferritic-austenitic. If the ratio falls between 2.05-2.25 then mixtures of fully ferritic and ferritic-austenitic regions grow from the liquid.

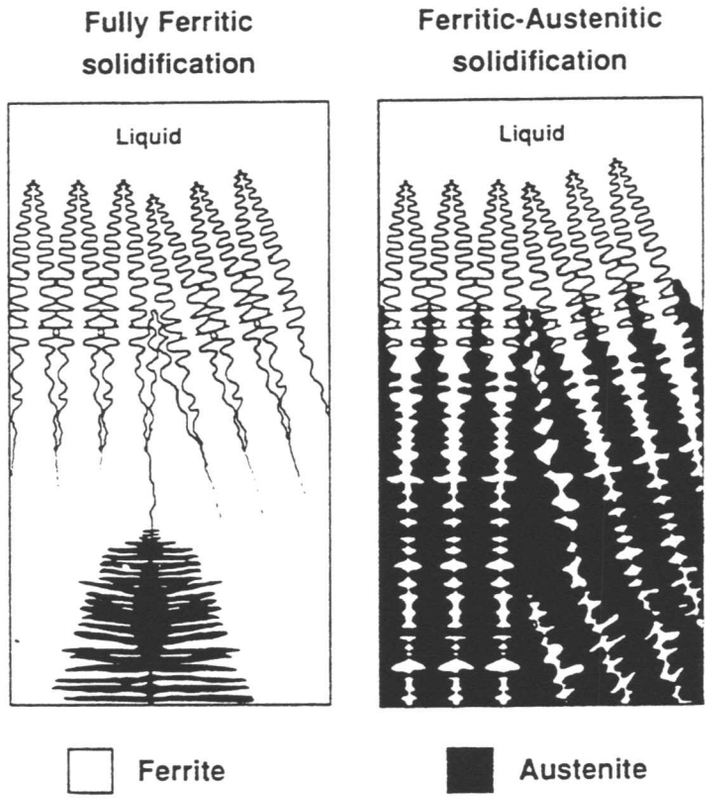

Figure 5.1. Schematic illustration of fully ferritic and ferritic-austenitic solidification (Karlsson *et al.*, 1991).

5.3 Thermodynamic assessment

Calculations of equilibrium phase diagram of duplex and super duplex steels and their weld metals were performed using the MTDATA package. The chemical compositions of the alloys used in these calculations are listed in Table 5.1. Table 5.2 shows their Cr_{eq}/Ni_{eq} ratios calculated according to the Hammar and Svensson (1979) equation. Figure 5.2 shows the calculated phase diagram of

duplex rolled metal IC381 in the temperature range of 1300-1500°C. It almost completely solidifies to ferrite, the volume fraction of ferrite at the solidus temperature (1384°C) being 0.97. Since the Cr_{eq}/Ni_{eq} is greater than 2.25, this is in accordance with the Karlsson model. nevertheless, the calculations do not reveal any temperature range in which δ-ferrite exists on its own. This is due to the presence of about 0.141 wt.% N that has stabilised the austenite phase up to the solidus temperature. In order to see the effect of a higher Cr content on the microstructure of duplex stainless steels, calculations were carried out for alloy IC373 in which the Cr concentration is 25.9 wt.%. The calculated phase diagram (Figure 5.3) shows a significant temperature range (1340-1380 °C) in which only δ-ferrite is stable, as might be expected from the higher Cr content. Figure 5.4 shows the effect of increasing the amount of Ni. Duplex stainless steel weld metal in general has an enhanced concentration of Ni when compared with wrought alloys. The solidification mode becomes ferritic-austenitic as the Cr_{eq}/Ni_{eq} ratio of duplex weld metal UNS31 is less than 2.25. The results of calculations for a nominal super duplex stainless steel alloy ZERON100 is shown in Figure 5.5. Although its Cr_{eq}/Ni_{eq} ratio is bigger than 2.25, its solidification mode is a mixture of fully ferritic and ferritic-austenitic type. Figure 5.6 shows the effect of increasing the amount of Ni in super duplex stainless steel. With a Cr_{eq}/Ni_{eq} ratio less than 2.25, the alloy (A219) solidifies to a mixture of ferrite and austenite.

Table 5.1. Chemical compositions (wt.%) studied using thermodynamic calculations.

Material	C	Si	Mn	P	S	Cr	Ni	Mo	V	Nb	Ti	Al	Cu	N	O
IC381	0.02	0.48	1.92	0.03	0.01	22.1	5.8	3.17	0.13	0.01	0.01	-	0.07	0.14	0.007
IC373	0.02	0.50	0.67	0.02	0.01	25.9	5.1	3.68	0.05	0.03	0.01	-	1.83	0.14	0.003
UNS31	0.03	0.38	1.16	0.02	0.001	22.0	9.0	3.0	-	-	-	-	-	0.17	-
ZERON100	0.03	1.0	1.0	0.02	0.01	26.0	7.0	4.08	-	-	-	-	1.0	0.27	-
A219	0.03	0.60	0.70	0.02	0.007	25.6	9.4	4.08	-	-	-	-	-	0.27	-

The striking feature of these calculations is that the suppression of the austenite in super duplex weld metal A219 would lead to the persistence of liquid to incredibly low temperatures. Figure 5.7 shows the results of these calculations with the suppression of ferrite. All the liquid solidifies as austenite at temperatures below 1310 °C. Figure 5.8 shows the similar data but this time with the suppression of austenite. Liquid persists at such unrealistically low temperatures that fully ferritic solidification must be considered impossible.

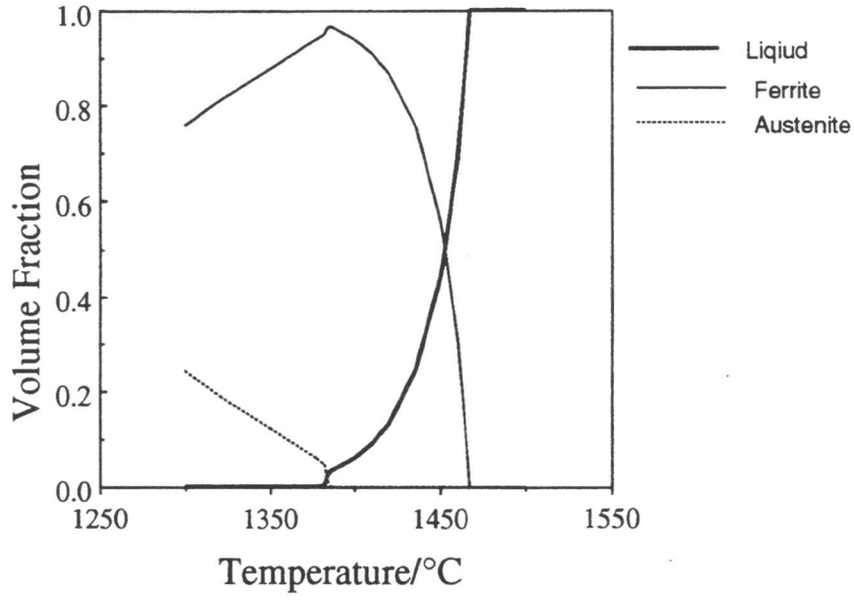

Figure 5.2. The calculated equilibrium phase fractions for conventional duplex stainless steel IC381.

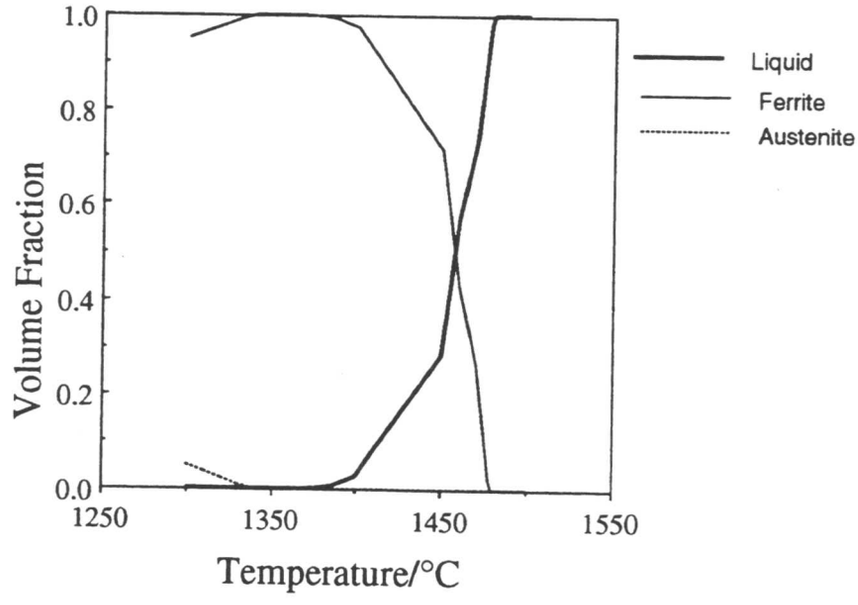

Figure 5.3. The calculated equilibrium phase fraction for a typical duplex stainless steel overalloyed with Cr (IC373).

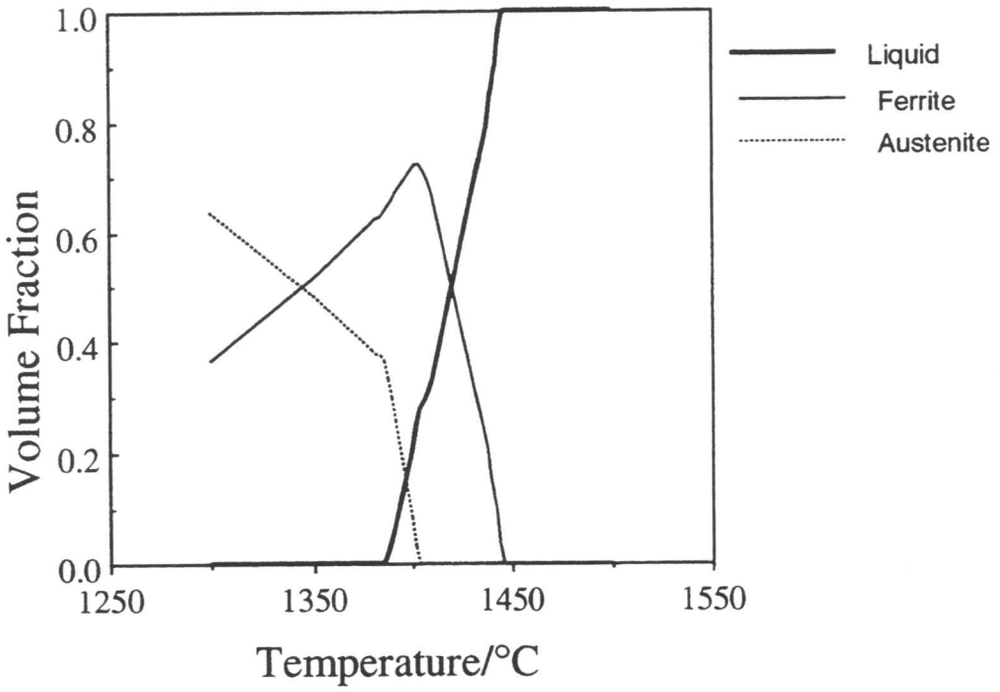

Figure 5.4. The calculated equilibrium phase fractions for a typical duplex stainless steel weld metal (UNS31).

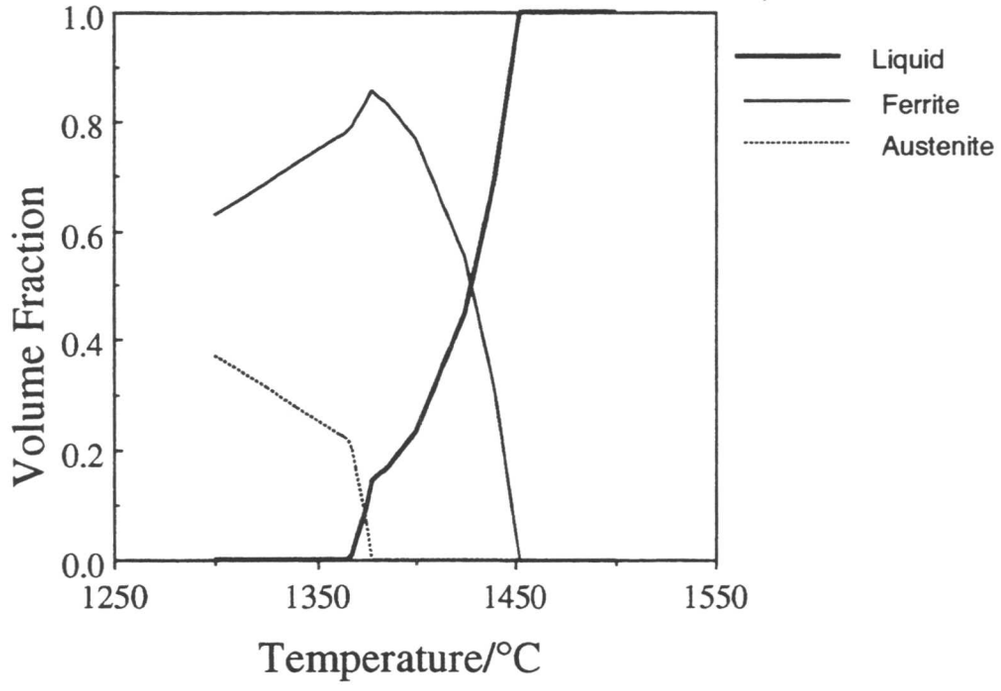

Figure 5.5. The calculated equilibrium phase fraction for a typical super duplex stainless steel rolled metal (ZERON100).

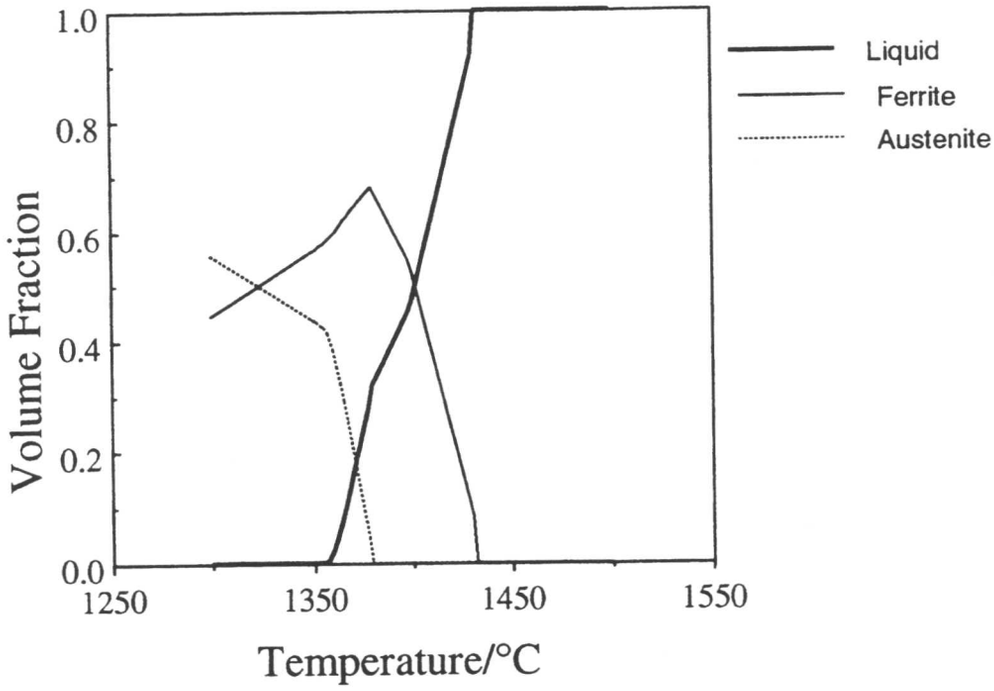

Figure 5.6. The calculated equilibrium phase fraction for a typical super duplex stainless steel weld metal (A219).

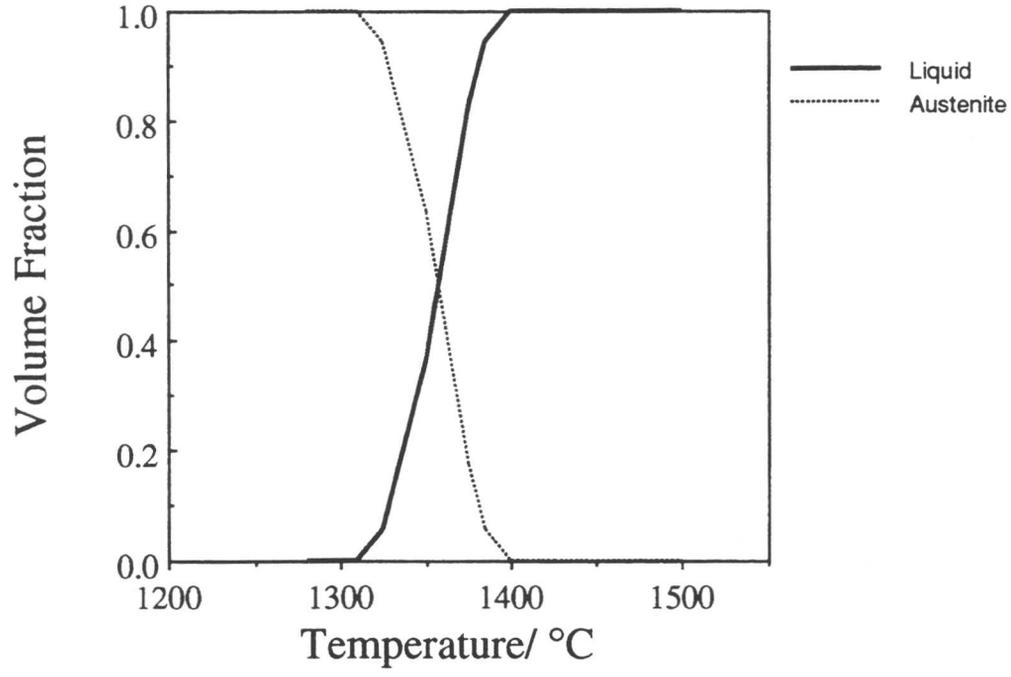

Figure 5.7. The calculated equilibrium phase fraction for a typical super duplex stainless steel weld metal (A219) assuming that the formation of ferrite can be suppressed.

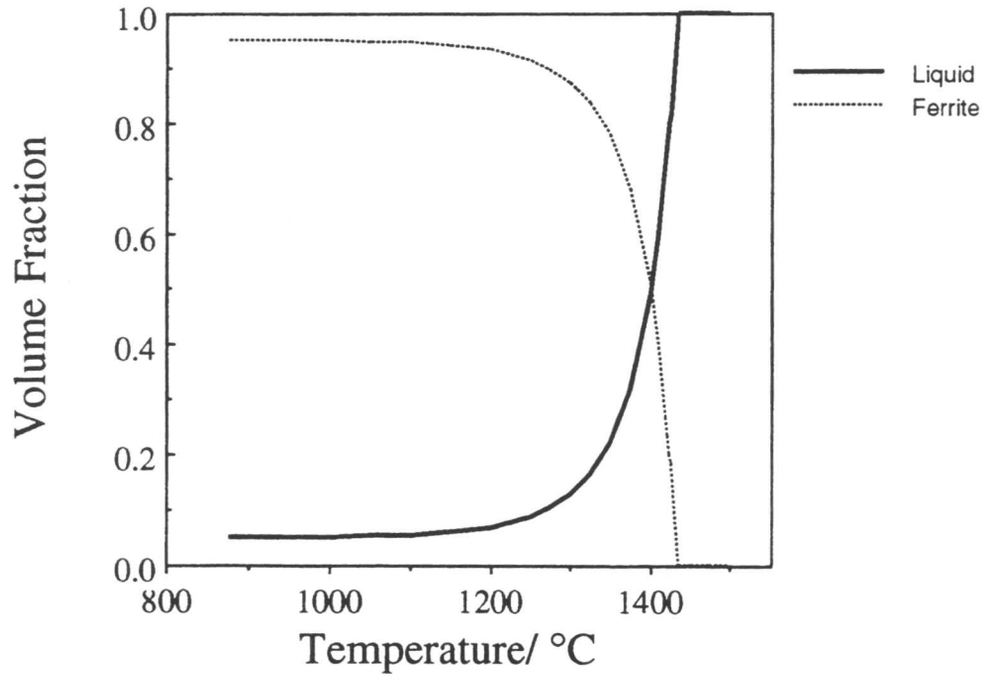

Figure 5.8. The calculated equilibrium phase fraction for a typical super duplex stainless steel weld metal (A219) assuming that the formation of austenite can be suppressed.

5.4 High Temperature DSC results

To measure the solidus temperatures and compare against calculations, and to investigate the effect of heating rate on the melting temperature, a series of experiments were carried out using a high temperature DSC (see chapter two). Table 2.1 shows the chemical compositions of the steels used. Super duplex weld metal A219 contains the highest concentration of alloying elements among the three stainless grades studied. In the first series of experiments the effect of chemical composition expressed by Cr_{eq} plus Ni_{eq} on the solidus temperature was studied, whereas the second series dealt with the effect of heating rate on the melting point. The heating and cooling segments over the temperature range of 1300-1480 °C for these steels are shown in Figures 5.9 to 5.11. The heating and cooling rates were 20 °C/min. Table 5.2 shows the calculated equilibrium, and measured (at 20 °C/min) solidus temperatures of these alloys. The Cr_{eq} and Ni_{eq} have been calculated using the Hammar and Svensson (1979) equation. As expected, both the solidus and liquidus temperatures are much lower during solidification than during melting. As the cooling rate increases this temperature difference will increase. With heating and cooling rate of 20 °C per minute this

difference is about 5°C for super duplex weld metal A219 (Figure 5.11) and 20 °C for duplex rolled metal IC373 (Figure 5.9). Figure 5.12 to 5.14 show the DSC curves covering the temperature range 900-1480°C. Alloy A219 shows another endothermic peak over the temperature range 1000-1100°C (Figure 5.12). This corresponds to the solid state transformation of δ-ferrite to austenite plus sigma phase (Chapter 7). This peak is less visible for the wrought alloys IC373 and IC381. This is in good agreement with the relative stability of the phases as suggested by their Cr_{eq}/Ni_{eq} ratio.

Table 5.2. Calculated (equilibrium) and measured solidus temperatures. The measurements are for samples heated at a rate of 20 °C per minute. The Cr_{eq} and Ni_{eq} are calculated according to the Hammar and Svensson (1979) equation.

Steel Grade	$Cr_{eq} + Ni_{eq}$	Cr_{eq}/Ni_{eq}	Calculated Solidus Temperature °C	Measured Solidus Temperature °C
IC373	39.32	4.15	1382	1440
IC381	36.09	3.04	1384	1435
A219	45.35	2.20	1358	1385

Figure 5.15 shows the heating and cooling DSC curves for weld metal A219 over the temperature range 1300-1480°C, with heating and cooling rates of 80°C/min. Comparing these results with Figure 5.11 indicates that the solidus temperature has increased from 1385°C to 1415°C due to the increase in the heating rate from 20°C/min to 80°C/min. The comparison also indicates that, as the heating rate increases, the superheating above the solidus temperature at the onset of transformation increases. Likewise, as cooling rate increases, there is a similar increase in undercooling below the solidus. Another interesting fact is the disappearance of the solid state transformation peak due to the increase in the heating rate, as can be seen by comparing Figure 5.16 with Figure 5.12. This is presumably because the transformation is spread over a wider temperature range during faster heating.

Figure 5.9. DSC heating and cooling curves for duplex rolled metal IC373 with a heating rate of 20 °C/min.

Figure 5.10. DSC heating and cooling curves for duplex rolled metal IC381 with a heating rate of 20 °C/min.

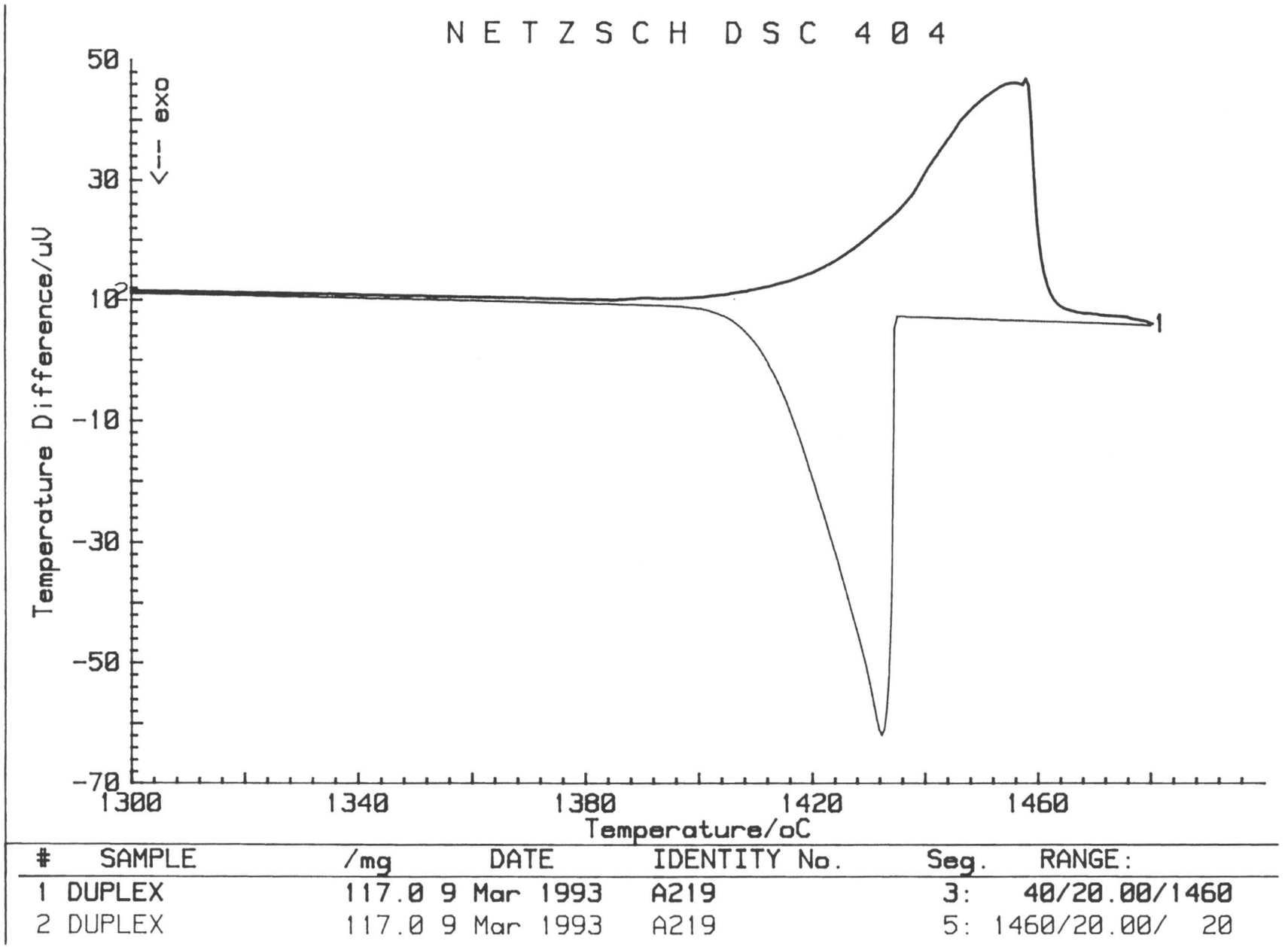

#	SAMPLE	/mg	DATE	IDENTITY No.	Seg.	RANGE:
1	DUPLEX	117.0	9 Mar 1993	A219	3:	40/20.00/1460
2	DUPLEX	117.0	9 Mar 1993	A219	5:	1460/20.00/ 20

Figure 5.11. DSC heating and cooling curves for super duplex weld metal A219 with a heating rate of 20 °C/min.

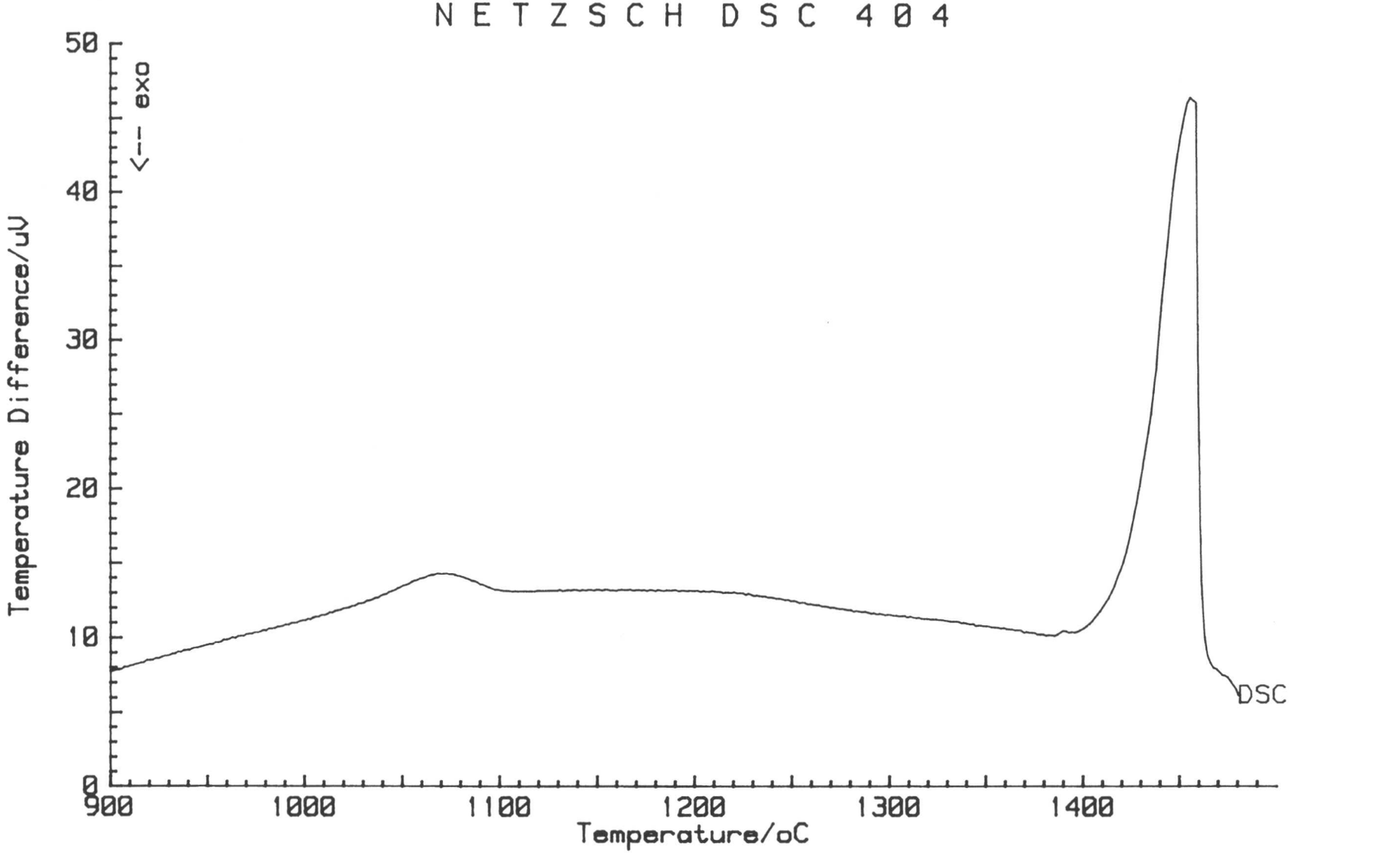

Figure 5.12. DSC heating curve for super duplex weld metal A219 with a heating rate of 20 °C/min.

Figure 5.13. DSC heating curve for duplex rolled metal IC381 with a heating rate of 20 °C/min.

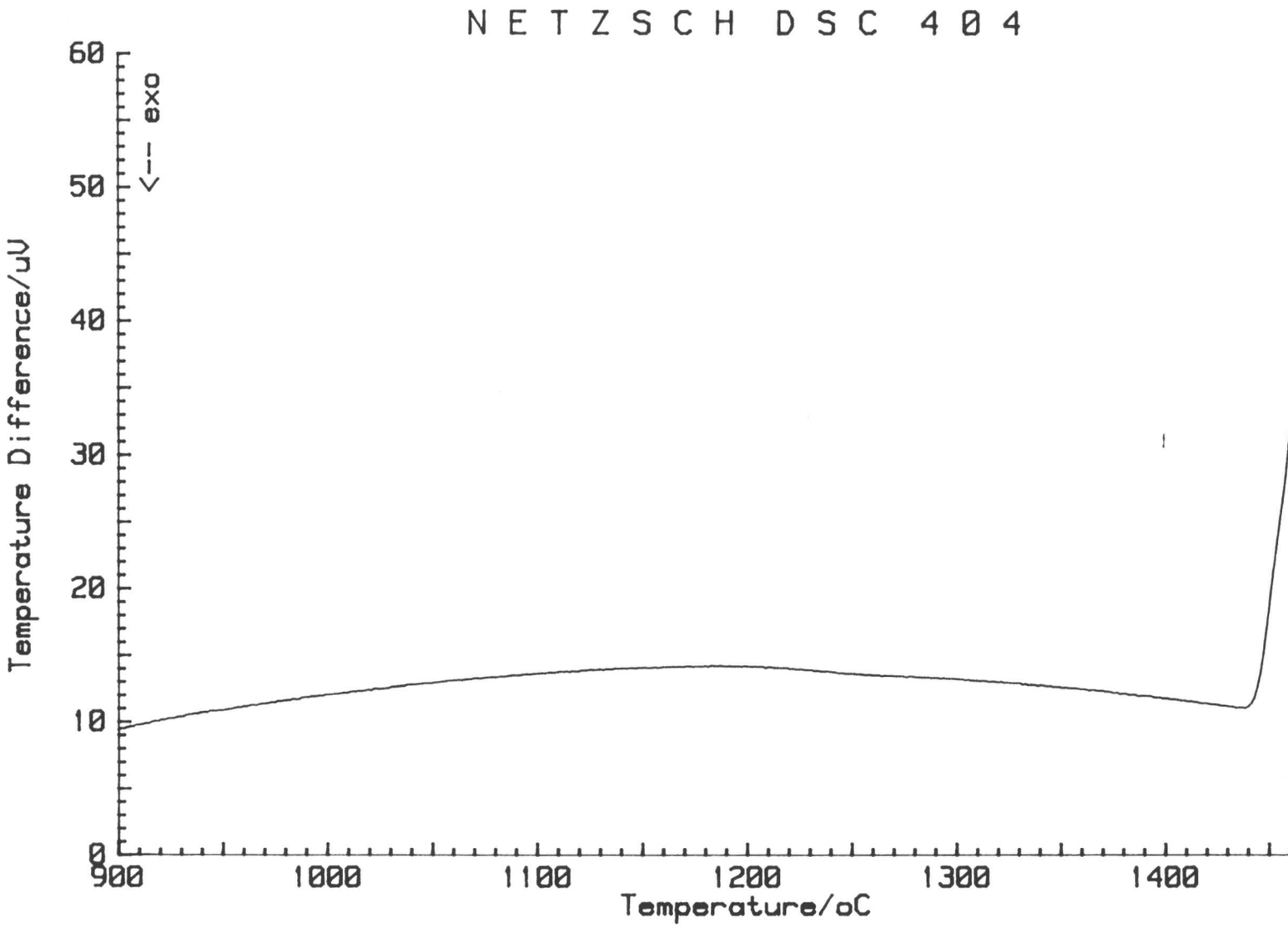

IDENTITY No.	IC373	SAMPLE	DUPLEX	112.80	DSC
DATE	9 Mar 1993	REFERENCE	NON	0.00	
OPERATOR	K.MURAKAMI	ATMOSPHERE	HE / 50		
NETZSCH		CRUCIBLE	AL203		

Seg. 3: 40oC/20

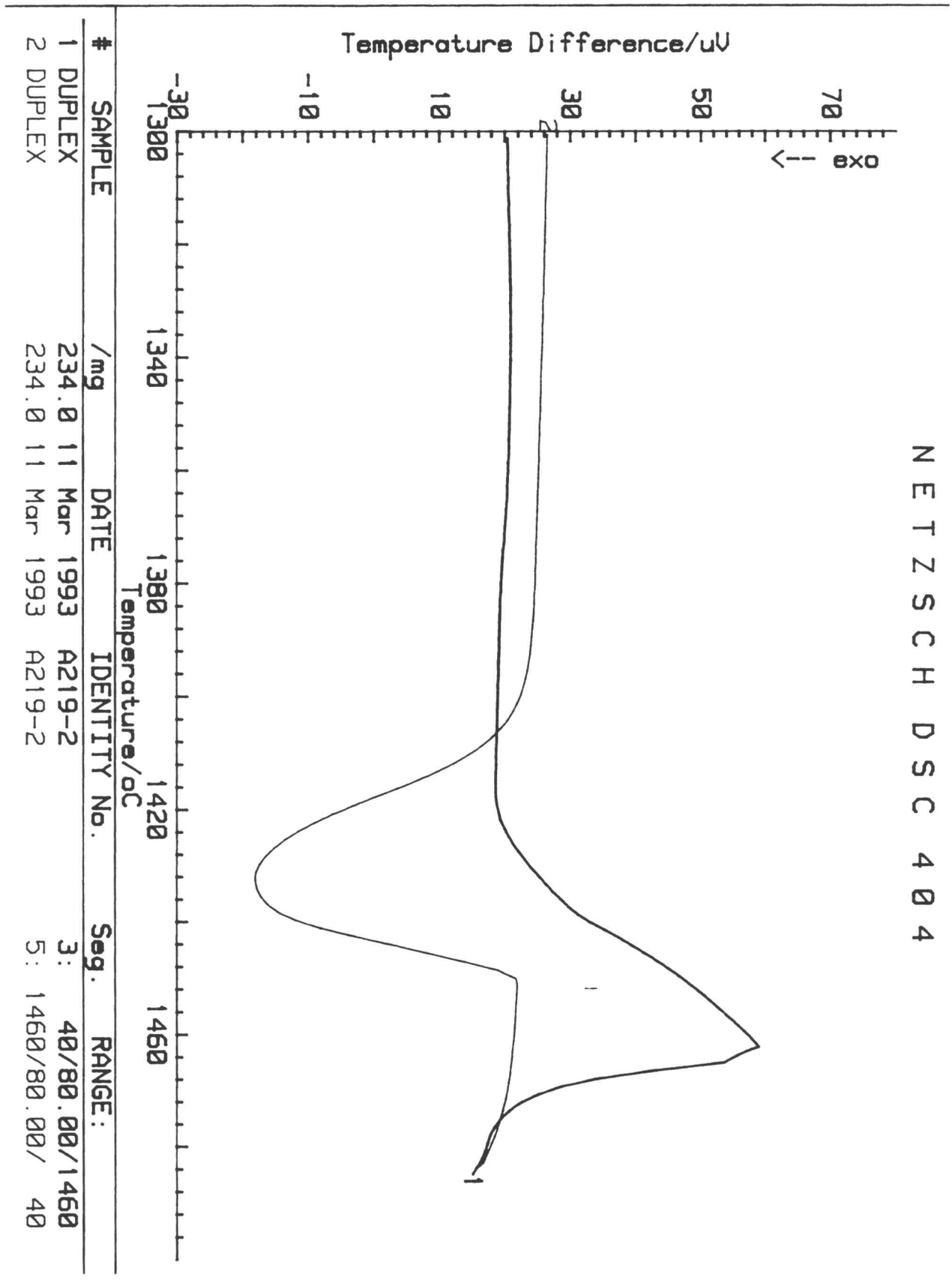

Figure 5.15. DSC heating and cooling curves for super duplex weld metal A219 with a heating rate of 80 °C/min.

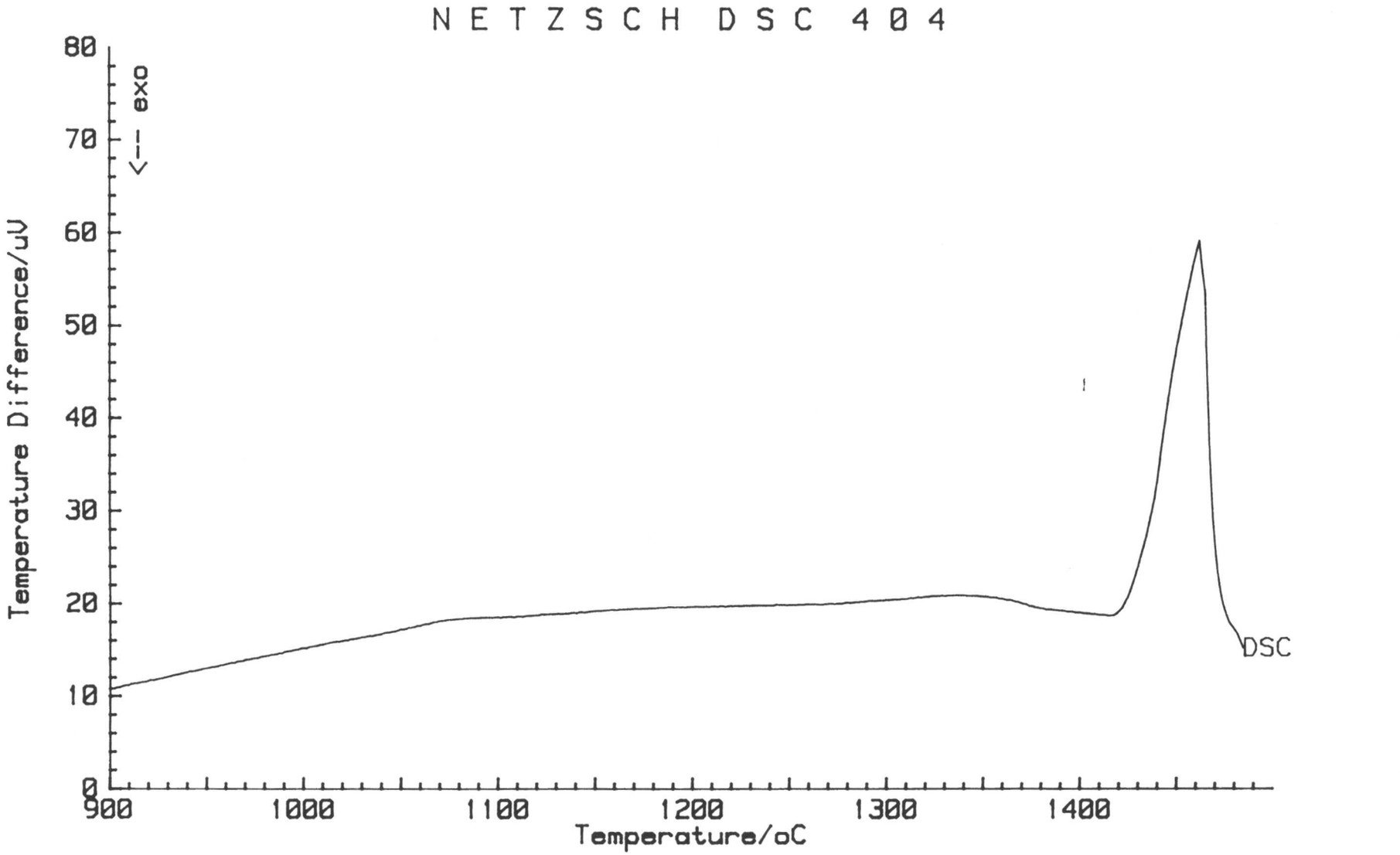

Figure 5.16. DSC heating curve for super duplex weld metal A219 with a heating rate of 80 °C/min.

Figure 5.17 shows the measured and calculated solidus temperatures for different steel grades against their chemical compositions, expressed in terms of the Cr_{eq} + Ni_{eq}. The calculated equilibria were obtained using the MT-DATA package and the experimental values were measured at a heating rate of 20°C/min. As expected, the equilibrium values are much lower than those measured under non-equilibrium heating conditions. Figure 5.17 also illustrates how the solidus temperature decreases as the solute content increases. Figure 5.18 shows the effect of heating rate on the solidus temperature of weld metal A219. As expected, the solidus temperature increased with increasing heating rate.

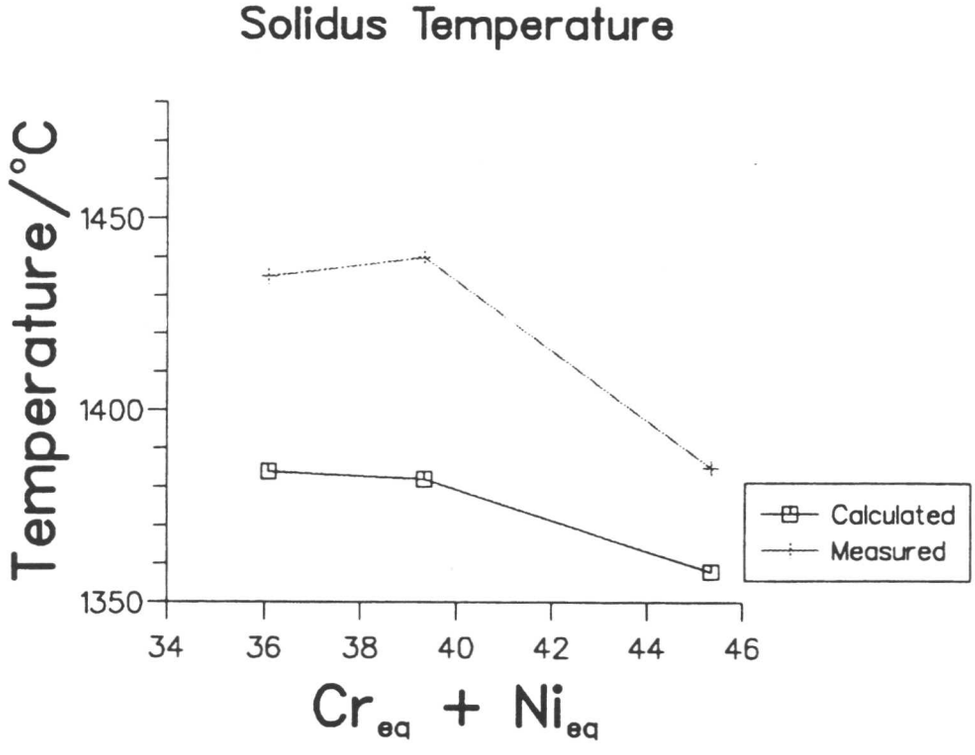

Figure 5.17. Measured and calculated solidus temperature against chemical composition of different steel grades. The heating rate in the experiments is 20 °C/min.

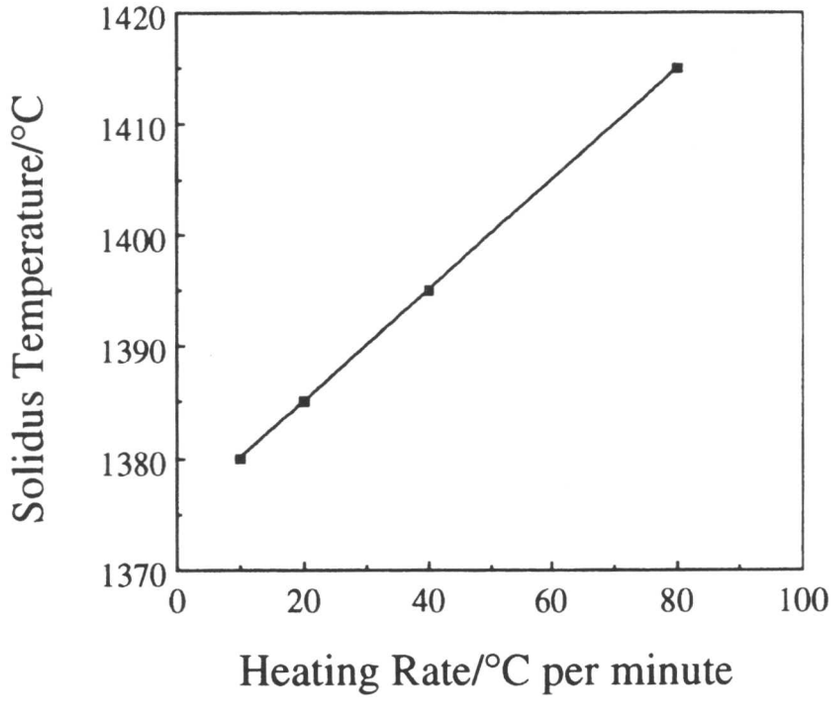

Figure 5.18. Solidus temperature against heating rate in super duplex stainless steel weld metal A219.

5.5 Microstructural Observations

Metallographic observations were conducted on steels solution treated for long times at 1300 °C and then quenched into water. The microstructure of alloy IC373 becomes almost completely ferritic with the volume fraction of austenite less than 0.05 above 1300 °C. Austenite has precipitated mainly at grain boundaries and on the inclusions (Figure 5.20). On the other hand, the microstructures of IC381 and A219 was confirmed to be ferritic-austenitic. These results are in a good agreement with the thermodynamic calculations presented previously (Figures 5.2-5.6). The very fine intragranular precipitates inside the δ-ferrite grains are austenite particles formed during quenching. In the case of alloy A219 (Figure 5.21) the measured volume fraction of austenite at 1300 °C was about 0.53 whereas for IC381 (Figure 5.19) it was only 0.19. The fraction was measured using both point counting and image analysis. It should be noted that the fine austenite which forms during the quench is not included in the stated volume fractions.

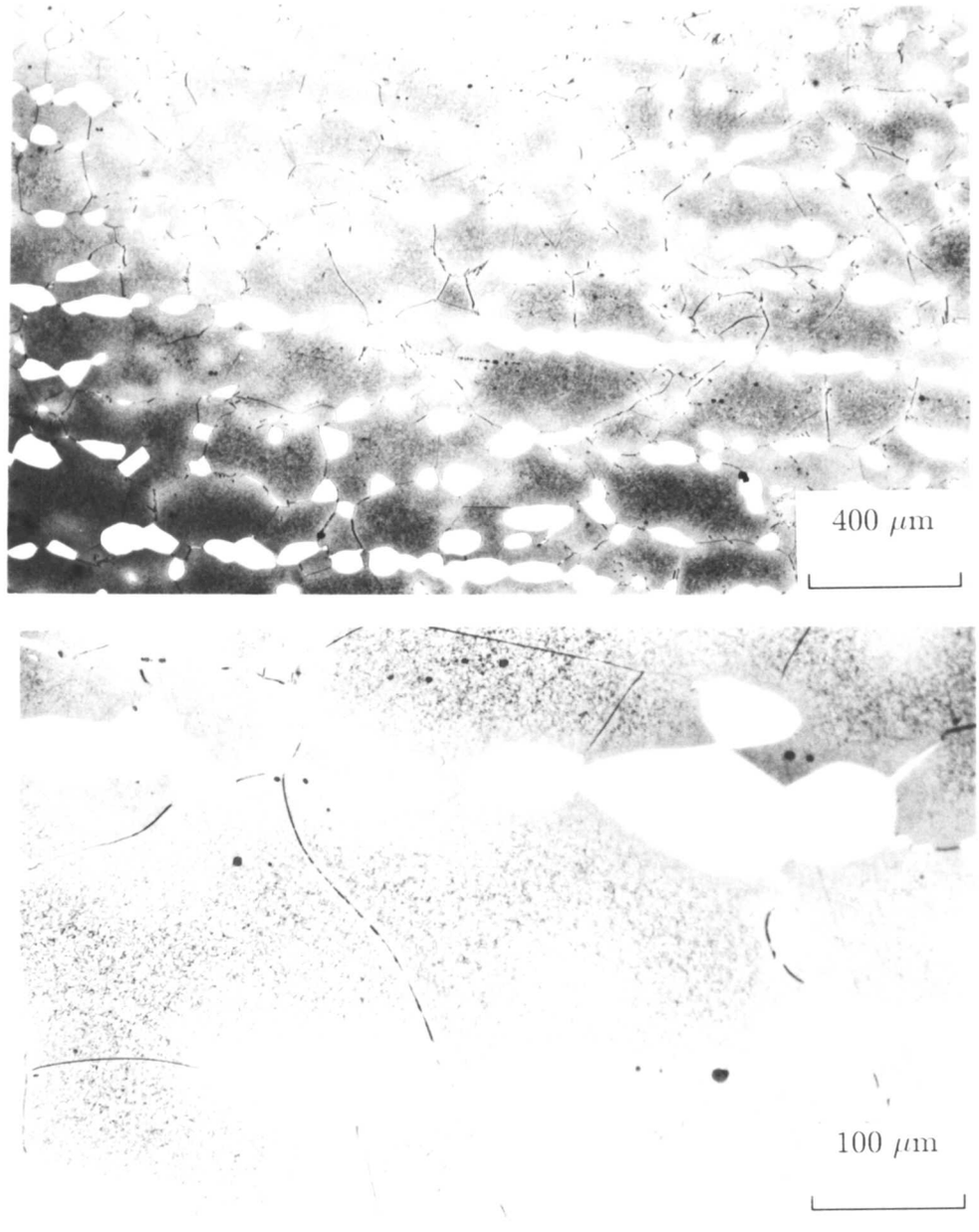

Figure 5.19. Light micrographs showing the microstructure of duplex rolled metal IC381 solution treated at 1300 °C for 26 hours and then quenched into water. The light phase is austenite and the dark one is ferrite. TEM observations (Figure 5.22) show that the fine particles inside the ferrite grains are austenite formed during quenching. The measured volume fraction of austenite (excluding fine particles) is about 0.19.

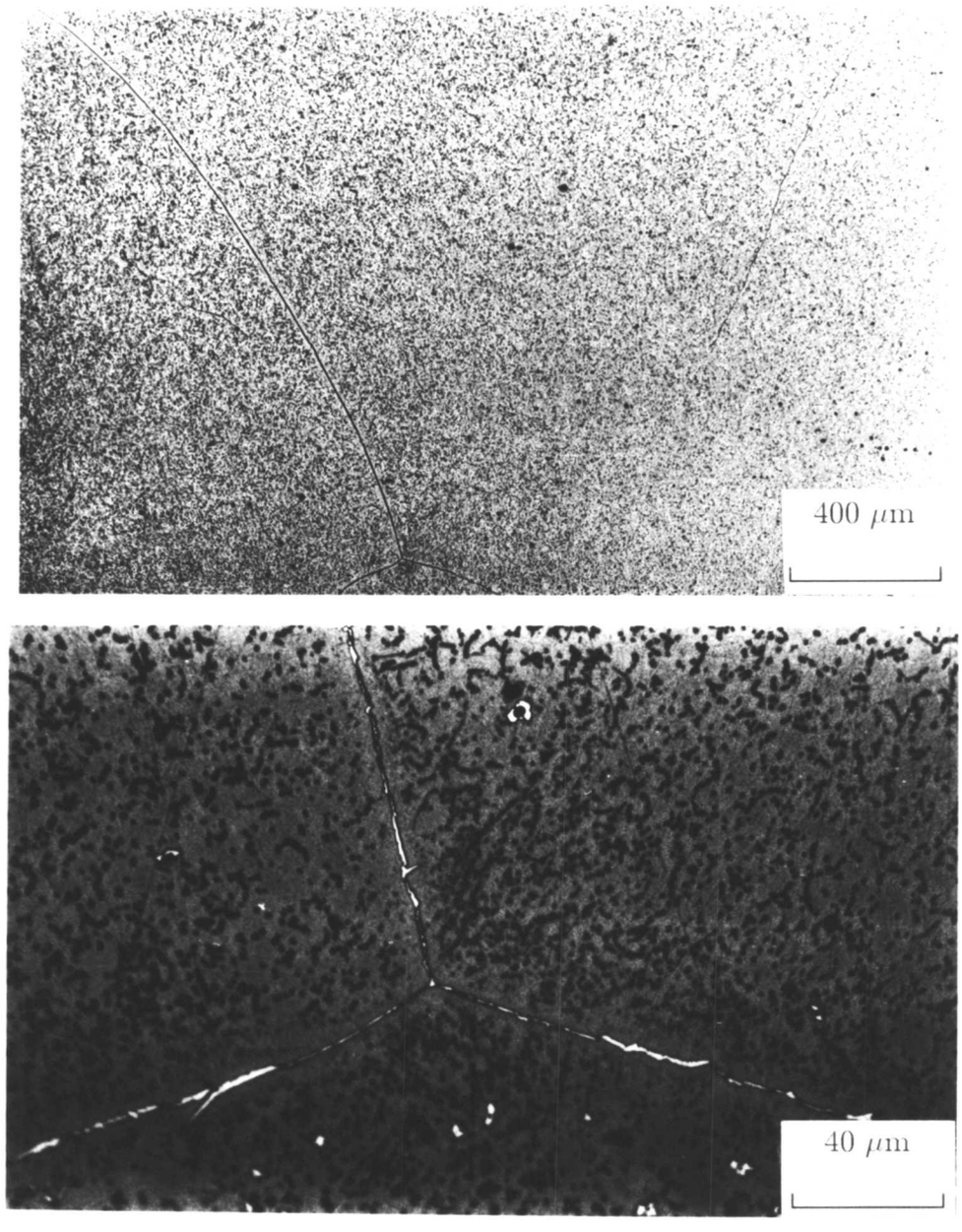

Figure 5.20. Light micrographs showing the microstructure of duplex rolled metal IC373 solution treated at 1300 °C for 26 hours and then quenched into water. Austenite has precipitated mainly at grain boundaries and on inclusions at the elevated temperature. The fine particles inside the ferrite grains are austenite formed during quenching. The measured volume fraction of austenite (excluding fine particles) is less than 0.05.

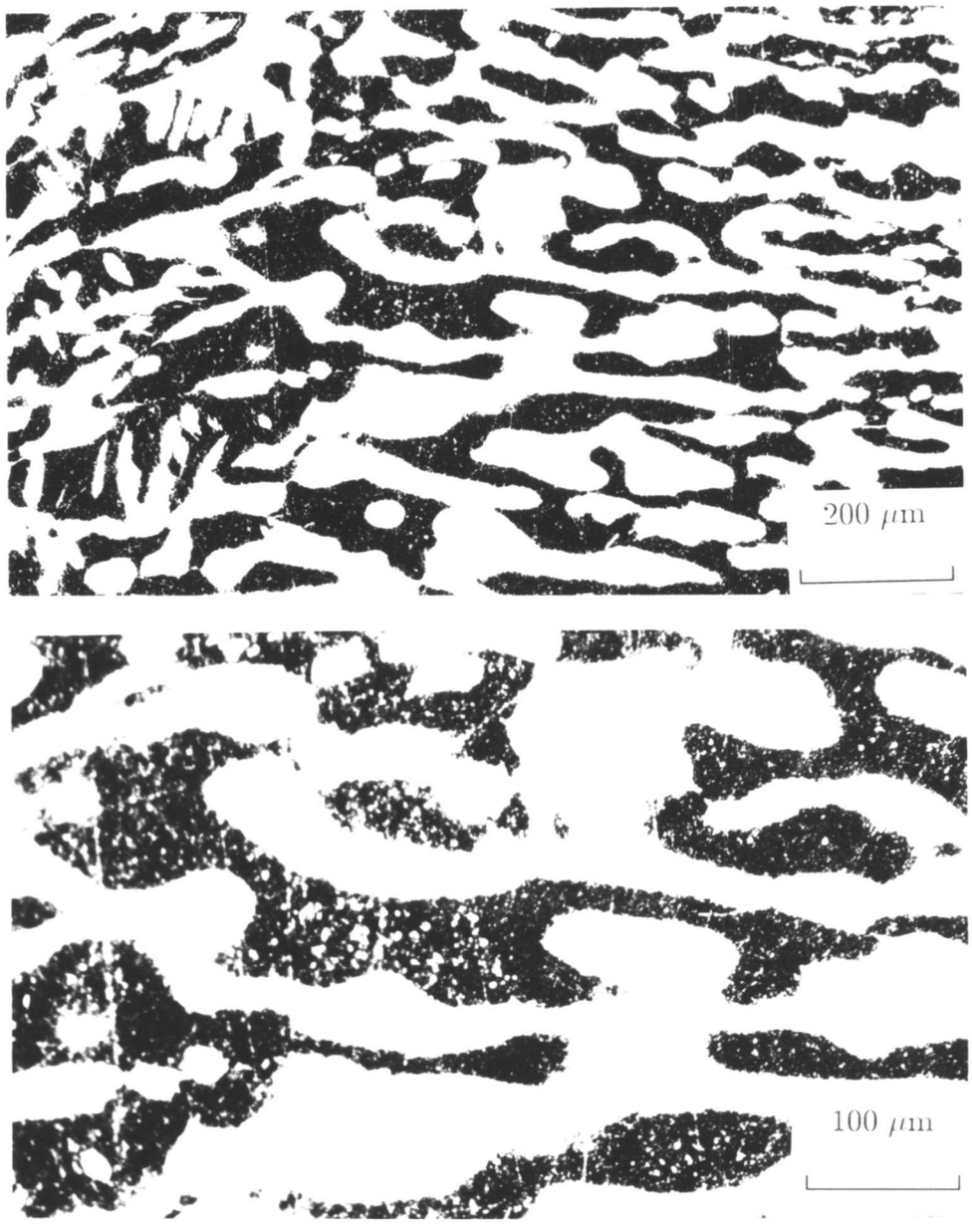

Figure 5.21. Light micrographs showing the microstructure of super duplex weld metal A219 solution treated at 1300 °C for 26 hours and then quenched into water. The measured volume fraction of austenite (excluding fine particles) is less than 0.53.

Figure 5.20 shows the microstructure of duplex rolled metal IC373 is almost wholly ferritic at 1300 °C. Note again that the TEM observations (Figure 5.22) show that the fine precipitates inside the ferrite grains are austenite formed during quenching. Figure 5.23 confirms that the matrix has a b.c.c crystal structure whereas the particle (Figure 5.24) has an f.c.c crystal structure. Figure 5.25 shows clusters of fine austenite particles in the same specimen, the clusters presumably being due to autocatalytic nucleation in which the formation of one particle stimulates others. TEM EDX microanalysis shows that the chemical composition of these precipitates (Table 5.3) is the same as the matrix as far as the substitutional alloying elements are considered. This contrasts with the partitioning of alloying elements between the coarser ferrite and austenite grains (see chapter six).

Table 5.3. TEM EDX microanalysis of δ-ferrite matrix and fine austenite in duplex rolled metal IC373 solution treated for 26 hour (concentrations are in wt.%).

Phase	Fe	Cr	Ni	Mo	Mn	Si
δ-ferrite	62.40±0.94	27.50±0.95	5.13±0.27	2.85±0.64	1.69±0.82	0.43 ±0.11
fine austenite	62.20±0.46	27.24±0.25	5.48±0.24	2.04±0.46	2.50±0.26	0.54 ±0.17

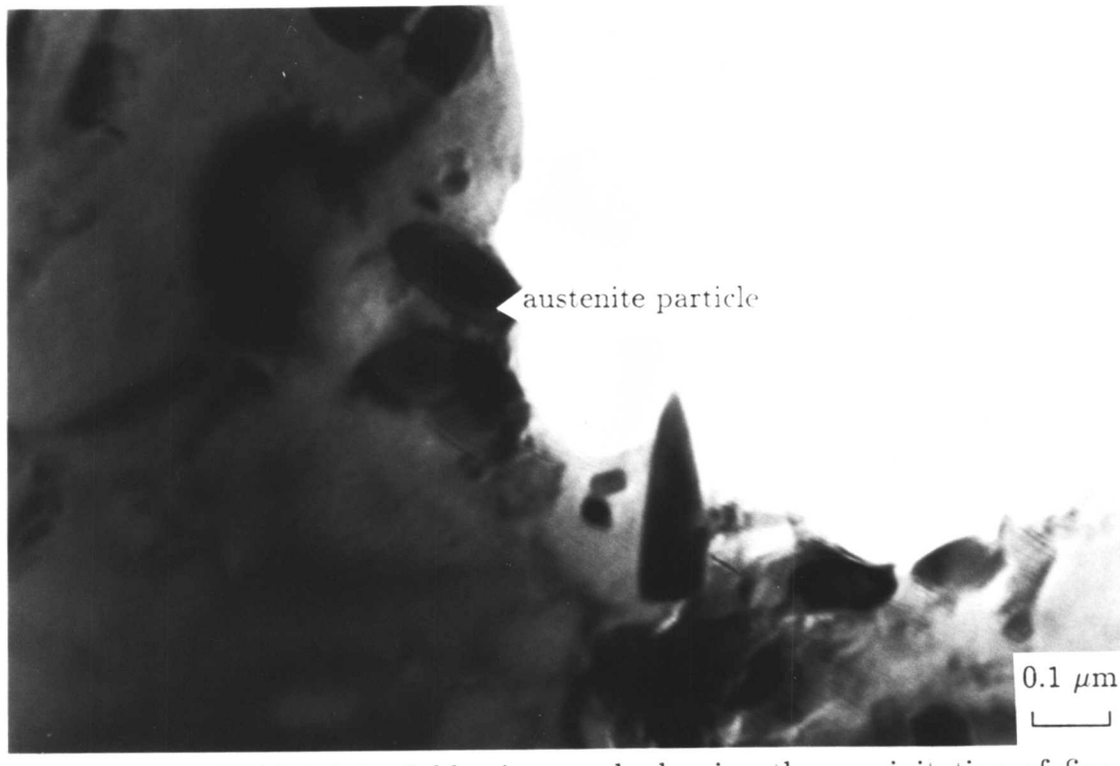

Figure 5.22. TEM bright field micrograph showing the precipitation of fine austenite particles inside δ-ferrite grain in duplex rolled metal IC373 solution treated at 1300 °C for 26 hours.

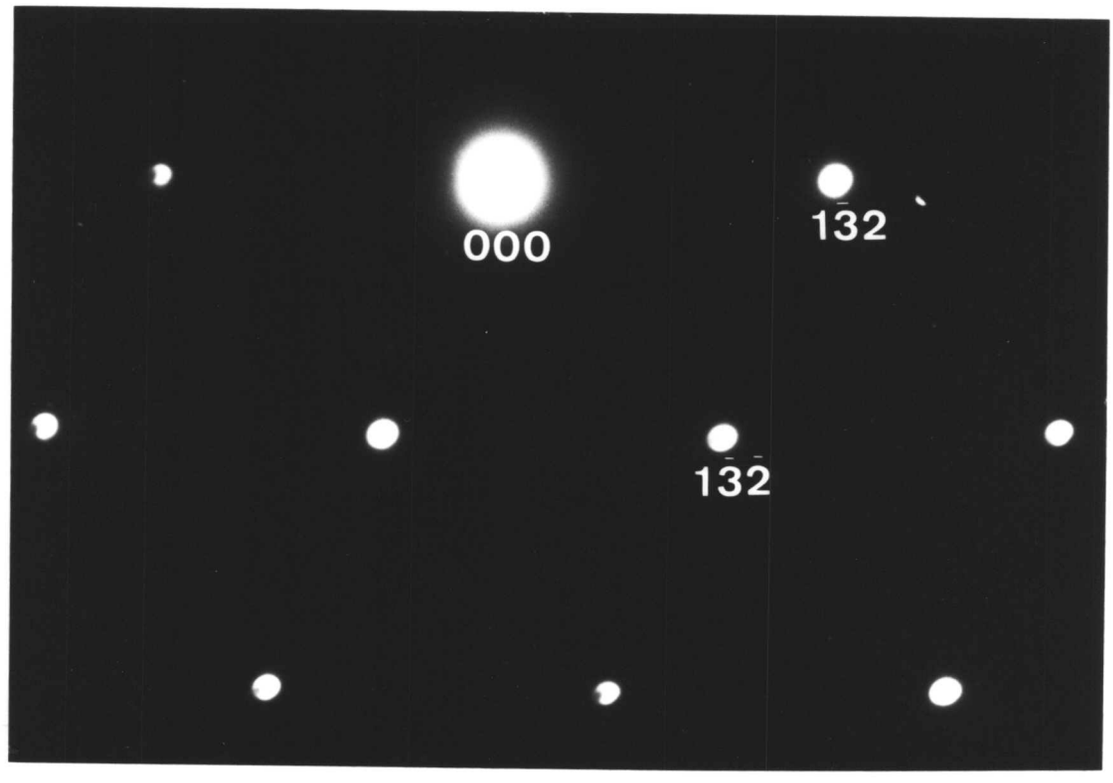

Figure 5.23. SADP of the matrix (δ-ferrite grain in Figure 5.22) showing that its crystal structure is b.c.c. The zone direction of diffraction pattern is [310].

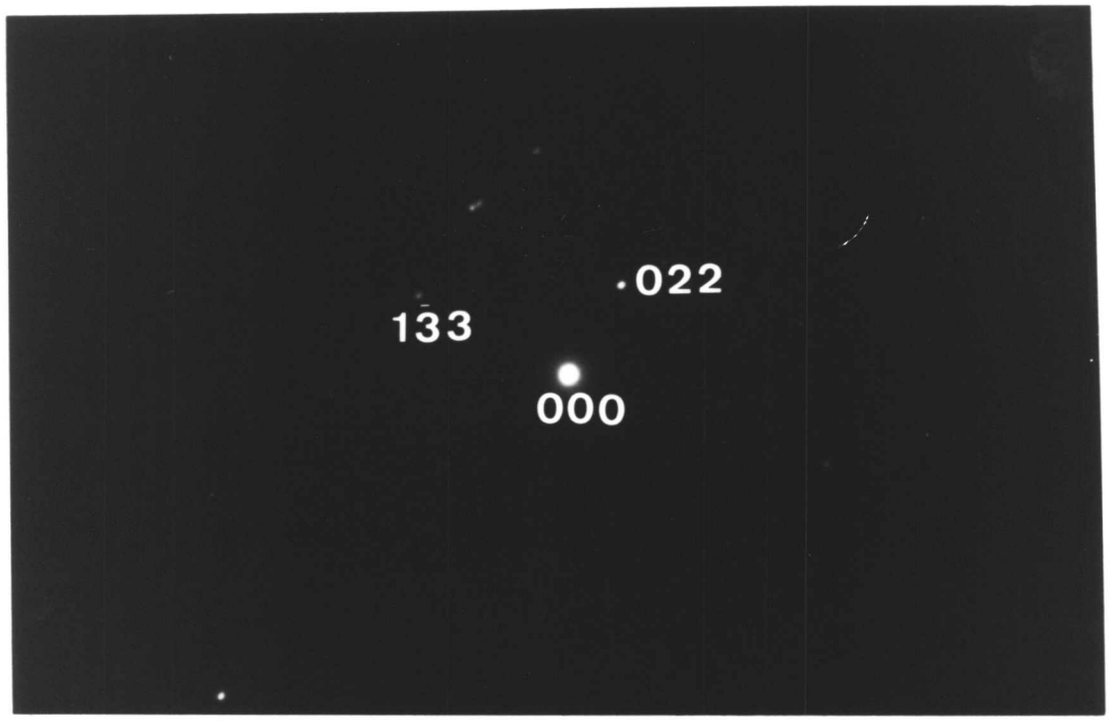

Figure 5.24. SADP of the particle (indicated in Figure 5.22) showing that it has an f.c.c. crystal structure. The zone direction of diffraction pattern is $[61\bar{1}]$.

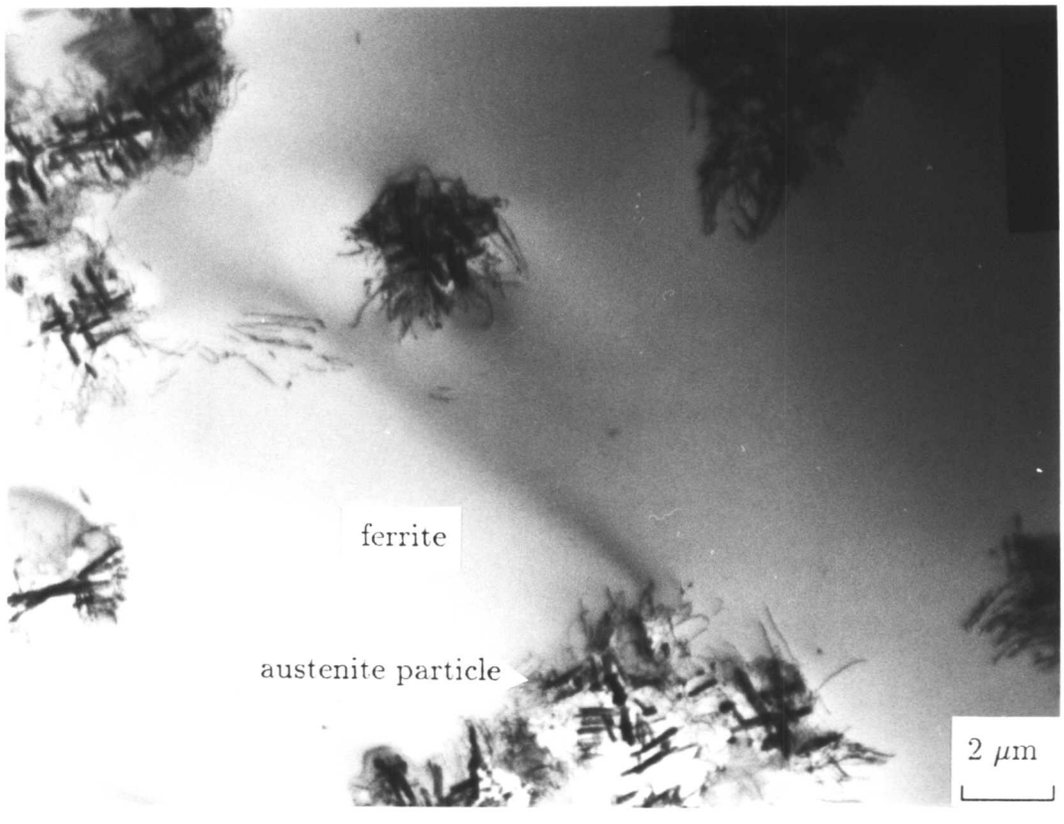

Figure 5.25. TEM bright field micrograph showing the precipitation of fine austenite in cluster form in duplex rolled metal IC373 solution treated at 1300 °C.

5.6 Laser Welding

To investigate the solidification mode of different types of stainless steels and to elucidate the role of austenite and ferrite nucleation on the solidification behaviour a series of laser welds traversing stainless steels of different chemical compositions was studied. Table 5.4 shows the steel grades used in this investigation. The solidification modes shown in the table are those predicted according to the Suutala (1983) model. The chemical compositions of the steels are listed in Table 2.1 and the welding conditions are presented in section 2.3. To ensure full penetration during welding the thickness of the plates was reduced to 0.5 mm by rolling. The welds were made on thin sheet couples of stainless steels of two different compositions butted together (e.g. 904L/IC373), the weld starting on a sheet of one composition and running into the other across the junction (Figure 2.1).

Figure 5.26 to 5.28 show the microstructures of laser weld metals of these alloys in the undiluted regions far from the junctions. The microstructure of laser weld metal of 904L (Figure 5.26) consists of austenite dendrites with interdendritic δ-ferrite showing that the solidification mode is austenitic-ferritic. Figure 5.27 shows that the microstructure of laser weld metal of A219 consists of dendritic and Widmanstätten austenite and ferrite grains. This confirms that the solidification mode is ferritic-austenitic. The ferrite dendrites are invisible as the result of solid state transformation (δ-ferrite to austenite). The microstructure of laser weld metal of IC373 (Figure 5.28) consists of elongated ferrite grains in the weld direction with precipitation of austenite mainly at the grain boundaries. This confirms that the solidification mode is fully ferritic.

5.6.1 Dilution

For the dissimilar joint configuration examined in this study, in which the weld starts from alloy A (Figure 2.1) and the weld direction is normal to the metal junction, dilution in weld pool will start as the front of the weld pool crosses the interface between alloys A and B. To measure the variation of composition with distance from the metal junction a scanning electron microscope

equipped with an energy dispersive X-ray analysis system was used (see section 2.10). The differences in composition of the individual phases present in the microstructure did not influence the measurements since the compositions were evaluated over a rastered area (about 0.9×0.12 mm) that was very large compared with the scale of the microstructure (a few micrometres). Measurements were made along the welding direction at the centre of the weld. Only the major constituents were analysed, namely Fe, Cr, Ni, Mo, Mn and Si, and the concentrations of these elements were normalised to 100 wt.%. In addition, limited measurements were also made on the individual phases present in microstructure in order to identify them. The variation of composition with distance for different welds are plotted in Figure 5.29 to 5.31. All the profiles show a rather steep initial change in composition followed by a more gradual decline to the composition of the undiluted alloy (alloy B). With the welding conditions used (see section 2.3) the length of the transition zone (the zone that the composition changes completely from alloy A to alloy B) was found to be not greater than 5-6 mm.

Table 5.4. Steel grades used in this investigation and their solidification modes predicted according to Suutala (1983) model. The Cr_{eq}/Ni_{eq} ratios are calculated according to Hammar and Svensson (1979) equation.

Steel Grade	Cr_{eq}/Ni_{eq}	Solidification mode
IC373	4.15	fully ferritic
A219	2.20	mixture of fully ferritic and ferritic-austenitic
904L	0.98	austenitic-ferritic

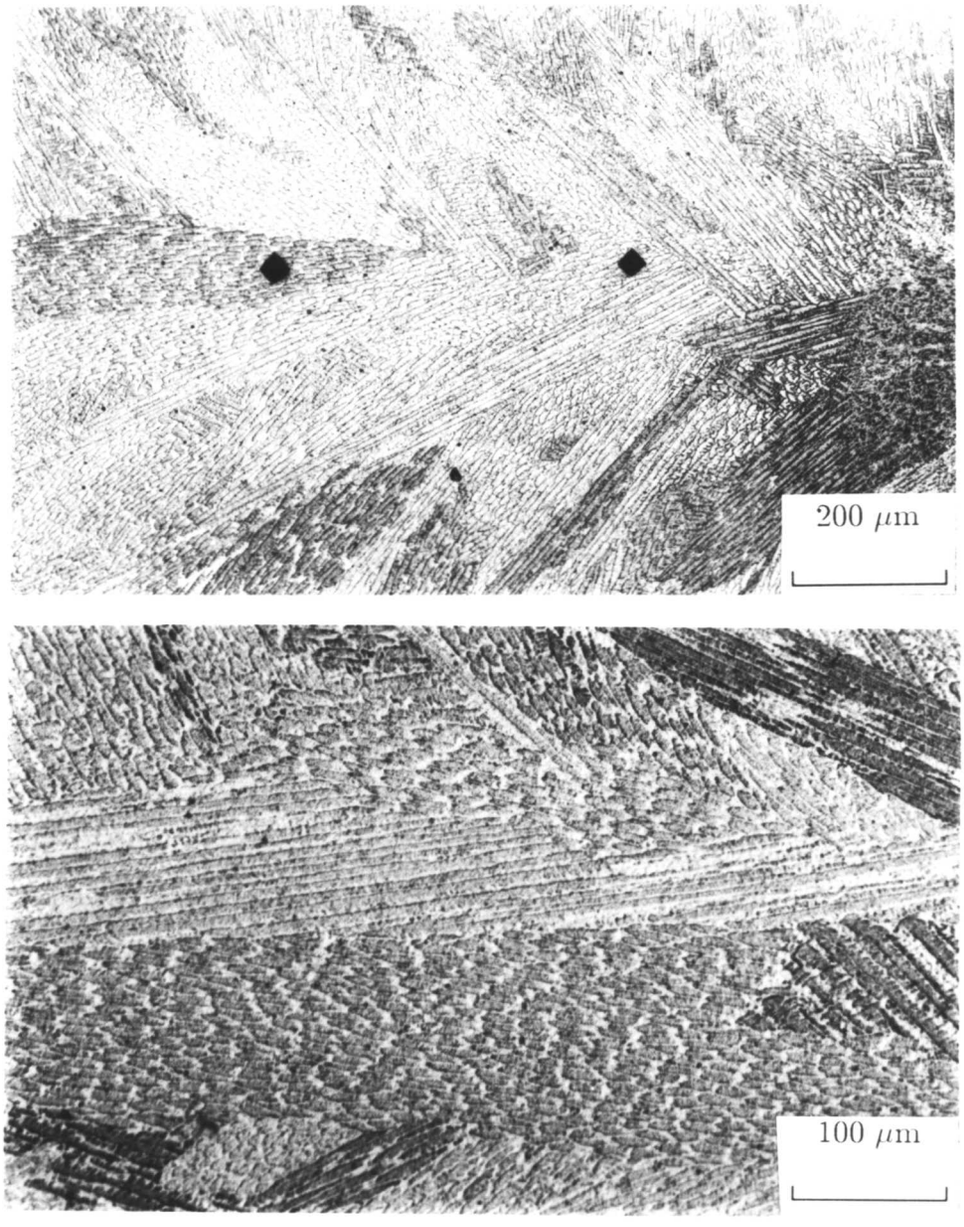

Figure 5.26. Microstructure of laser weld metal of alloy 904L showing the austenite dendrites with interdendritic δ-ferrite. The solidification mode is austenitic-ferritic.

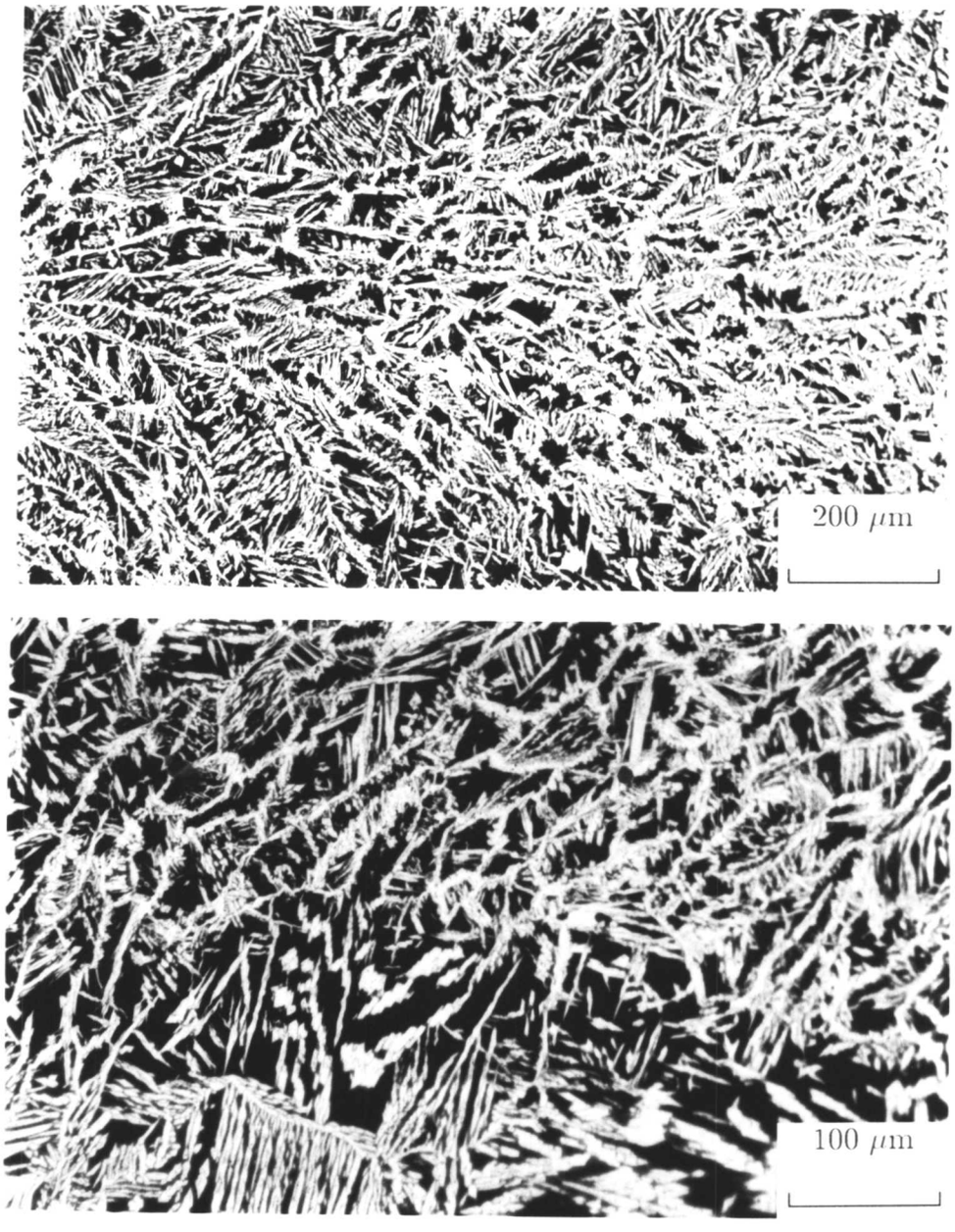

Figure 5.27. Microstructure of laser weld metal of alloy A219. It consists of dendritic and Widmanstätten austenite plus ferrite grains. This confirms that the solidification mode is ferritic-austenitic. The ferrite dendrites are invisible as the result of solid state transformation (δ-ferrite to austenite).

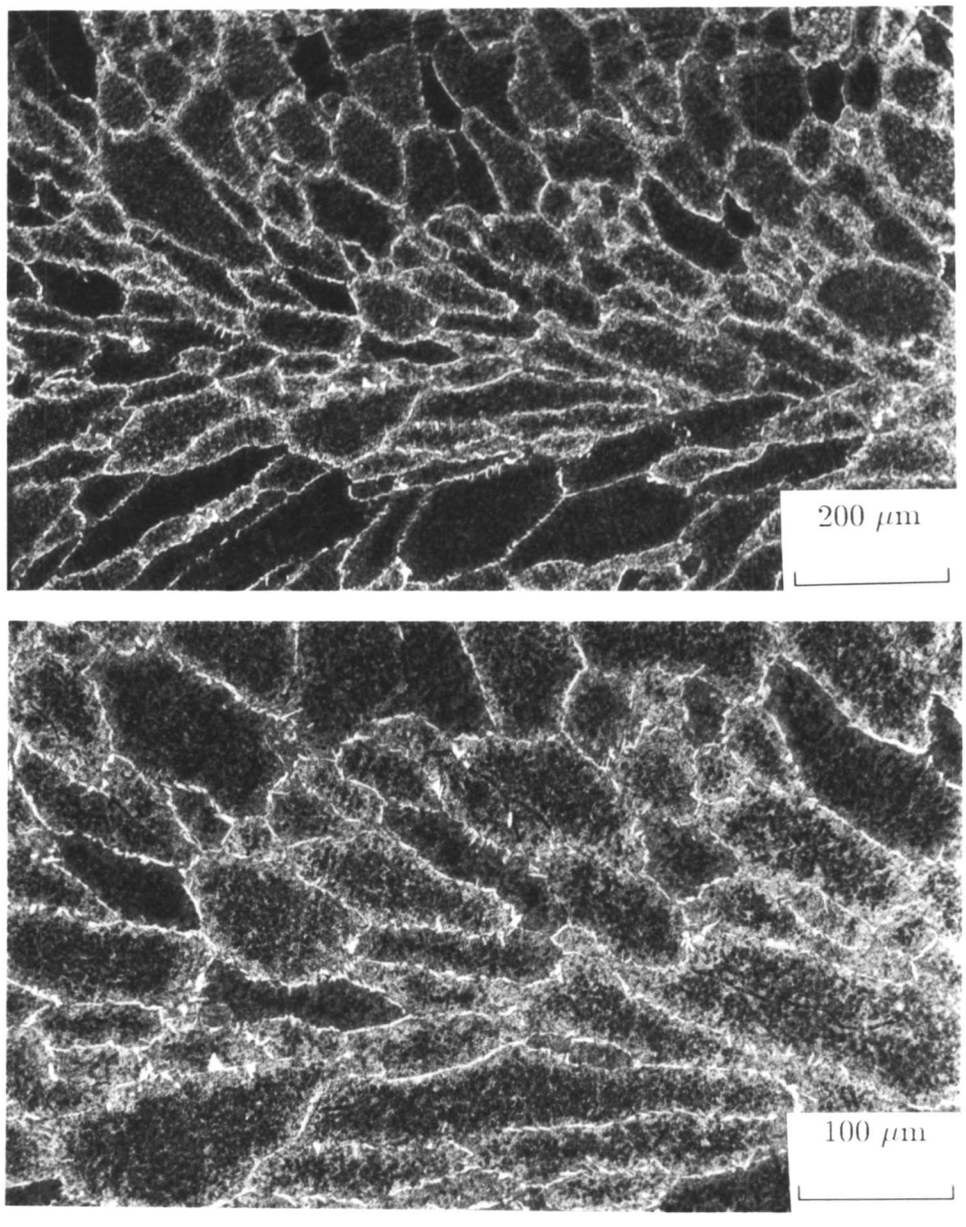

Figure 5.28. Microstructure of laser weld metal of alloy IC373. It consists of ferrite grains elongated in the weld direction with precipitation of austenite mainly at grain boundaries. This confirms that the solidification mode is fully ferritic.

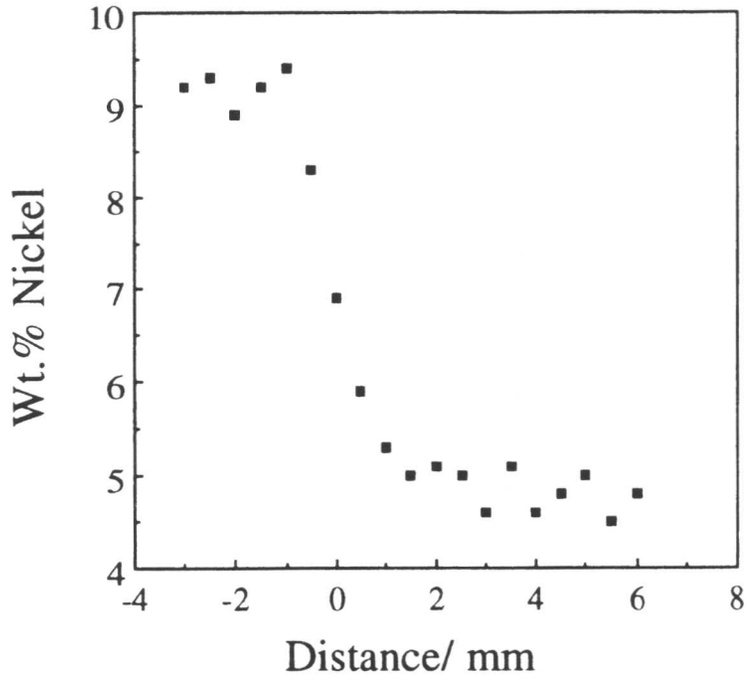

Figure 5.29. SEM EDX data illustrating the extent of dilution associated with dissimilar metal joint between alloys A219 and IC373, as a function of distance normal to dissimilar metal junction. The data show the change in Ni concentration at the centre of the weld. The welding direction is from alloy A219 (wt.%Ni=9.4) to alloy IC373 (wt.%Ni=5.1).

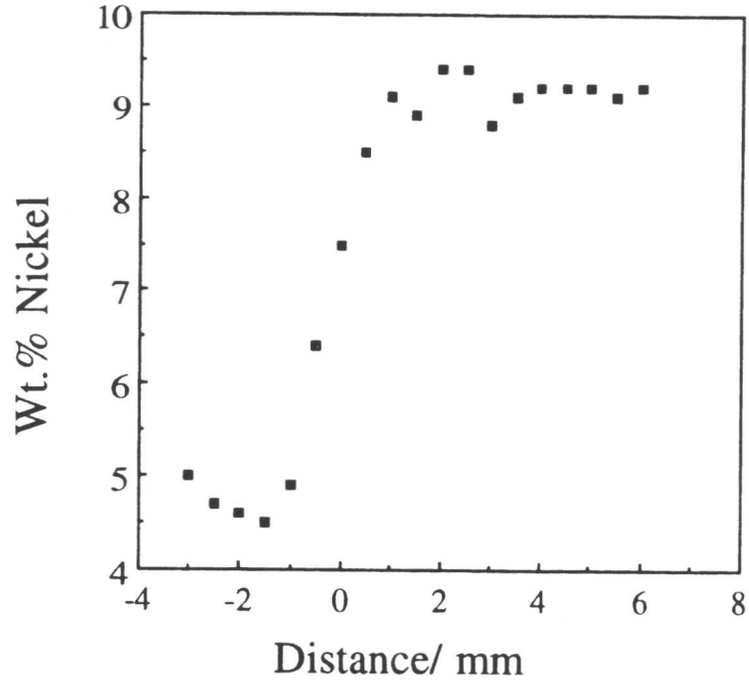

Figure 5.30. Same as Figure 5.29 except that the welding direction is from alloy IC373 to alloy A219.

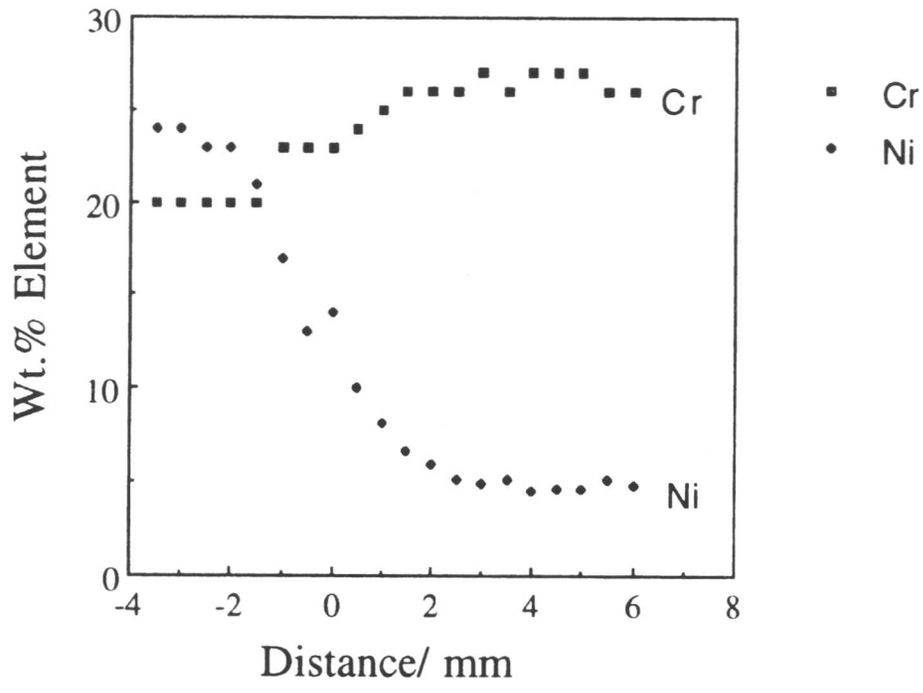

Figure 5.31. SEM EDX data illustrating the extent of dilution associated with dissimilar metal joint between alloys 904L and IC373, as a function of distance normal to dissimilar metal junction. The data show the changes in Ni and Cr concentrations at the centre of the weld. The welding direction is from alloy 904L (24.7 wt.%Ni, 20.0 wt.%Cr) to alloy IC373 (5.1 wt.%Ni, 25.9 wt.%Cr).

5.6.2 Variation of solidification mode in the transition zone

As the solidification front of the weld pool crosses the interface between dissimilar alloys A and B, the chemical composition of the weld pool will change. This obviously can affect the solidification mode, depending on the degree of dilution in the transition zone. Bhadeshia *et al.* (1991) have reported a change of solidification mode from ferritic-austenitic (FA) to austenitic-ferritic (AF) in the transition zone. When the Cr_{eq}/Ni_{eq} ratios for the two alloys do not differ much this change was found to persist far from the transition zone. The Cr_{eq}/Ni_{eq} ratios of alloys that they have used were in the range of 1.30-1.75, which makes the degree of dilution low. Starting the laser weld from the steel with the lower Cr_{eq}/Ni_{eq} ratio (AF solidification mode) they removed the need for the nucleation of austenite in the transition zone and even in undiluted metal of alloy with higher Cr_{eq}/Ni_{eq}. As the result austenite dendrites penetrated into undiluted regions and the alloy solidified to metastable austenite rather than the

thermodynamically stable δ-ferrite.

In the present work the difference between the Cr_{eq}/Ni_{eq} of the steels used (Table 5.4) is much greater than those studied by Bhadeshia *et al.* (1991) and no change of solidification mode was observed beyond the transition zone. This confirms that the solidification mode of stainless steels depends essentially on the composition of steel and the effect of solidification conditions is of secondary importance in the present context.

Figure 5.32 shows the microstructure of a dissimilar metal junction between alloys 904L and IC373. The welding direction is from alloy 904L with austenitic-ferritic solidification mode (Cr_{eq}/Ni_{eq}=0.98) to alloy IC373 with fully ferritic solidification mode (Cr_{eq}/Ni_{eq}=4.15). Austenite dendrites penetrated into the transition zone. As the difference between the Cr_{eq}/Ni_{eq} is very high solidification mode changed from austenitic-ferritic to ferritic-austenitic and then to fully ferritic as soon as the transition zone was exceeded.

Figure 5.33 shows the microstructure of a dissimilar metal junction between alloys A219 and IC373. The welding direction is from alloy A219 with ferritic-austenitic solidification mode (Cr_{eq}/Ni_{eq}=2.20) to alloy IC373. Again austenite dendrites penetrated into the transition zone but failed to penetrate undiluted regions of IC373. Figure 5.34 shows the microstructure of dissimilar metal junctions between the same alloys as in Figure 5.33 but with the opposite welding direction. Again the change in solidification mode (this time from fully ferritic to ferritic-austenitic) only occurred in the transition zone.

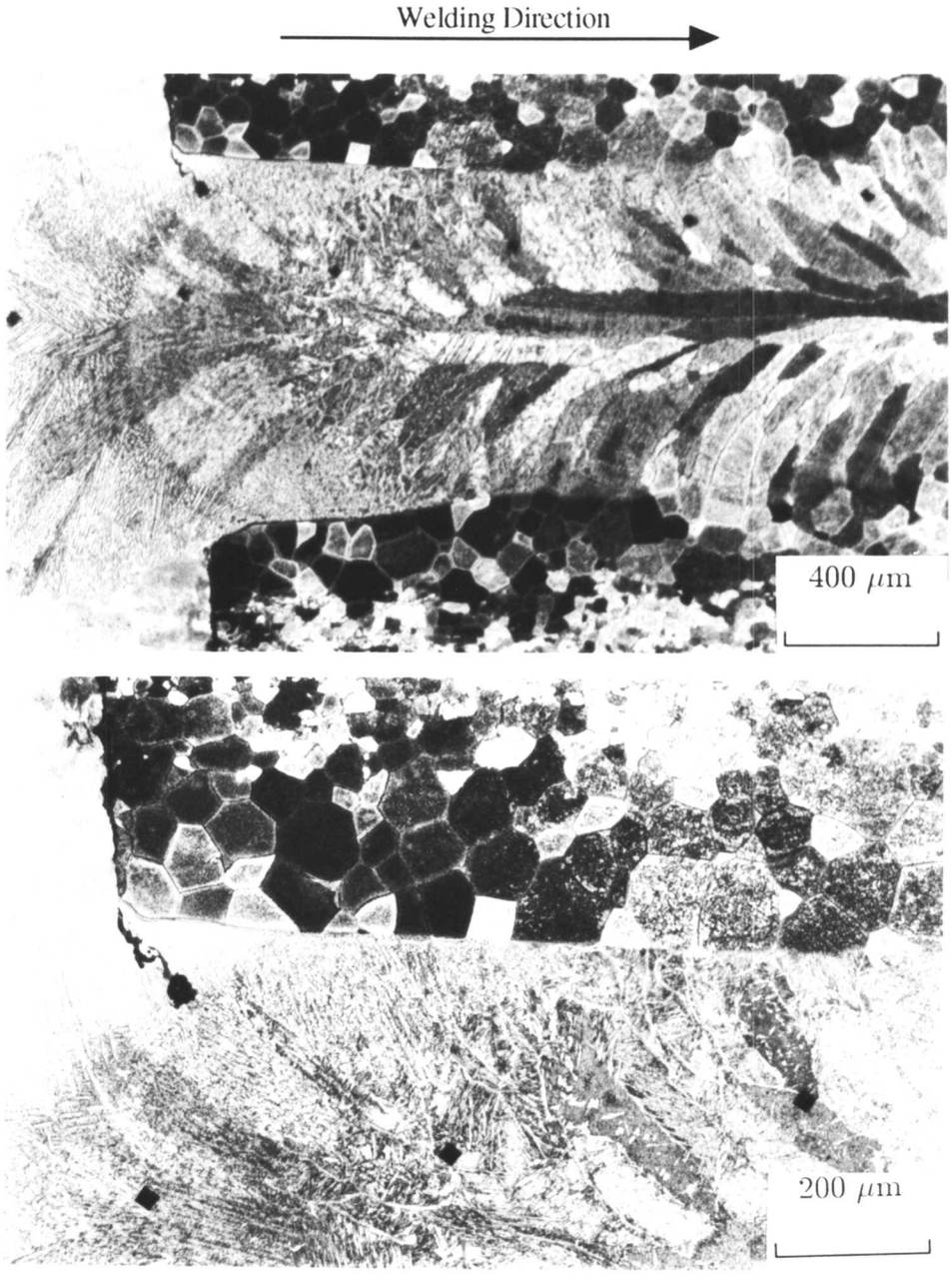

Figure 5.32. microstructure of dissimilar metal junction between alloys 904L and IC373. The weld direction is from alloy 904L (AF solidification mode) to alloy IC373 (fully ferritic solidification mode). A change of solidification mode from AF to FA and then to fully ferritic can be seen in transition zone due to dilution effect.

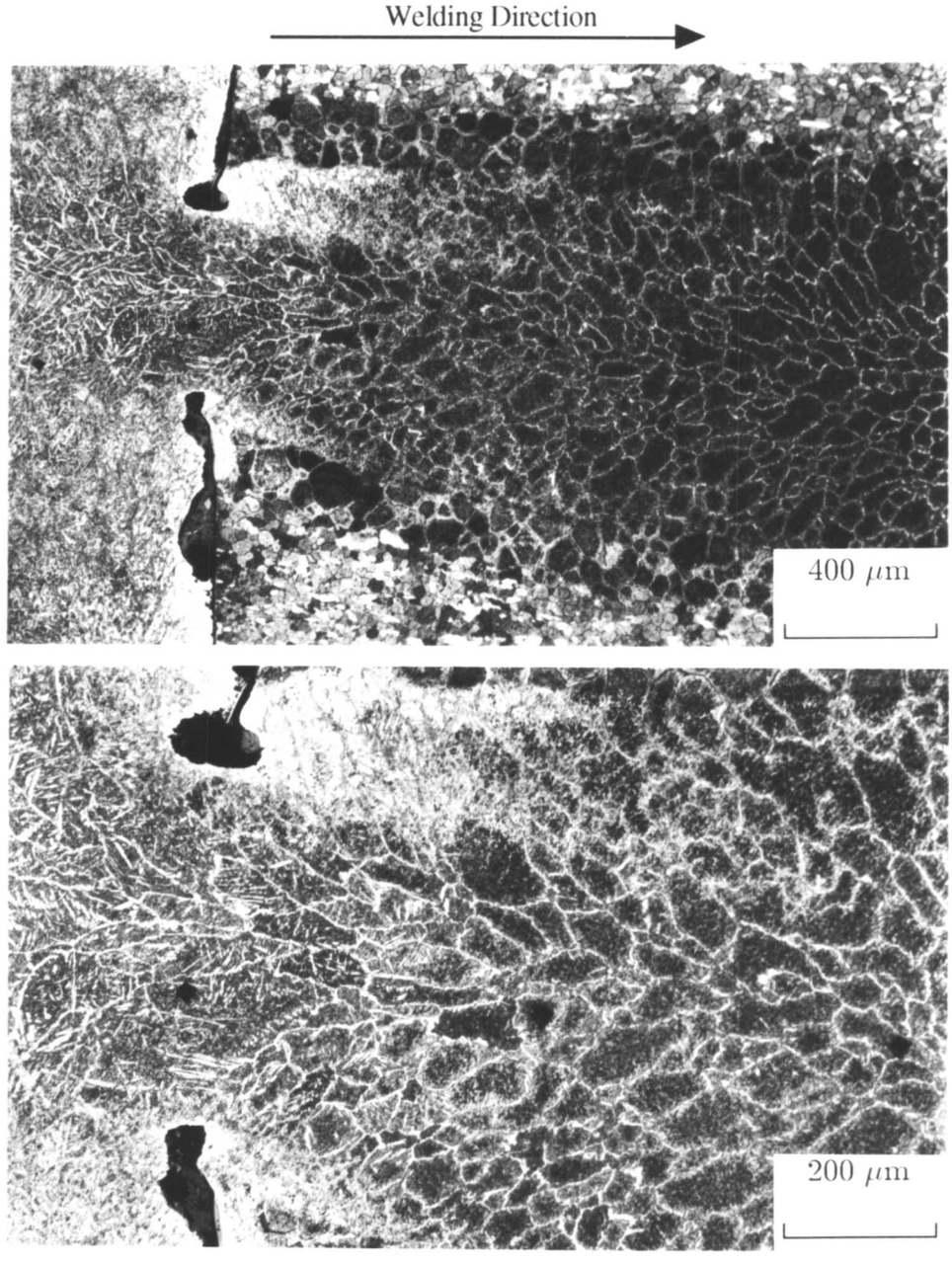

Figure 5.33. microstructure of dissimilar metal junction between alloys A219 and IC373. The weld direction is from alloy A219 (FA solidification mode) to alloy IC373 (fully ferritic solidification mode). A change of solidification mode from FA to fully ferritic can be seen in transition zone due to dilution effect.

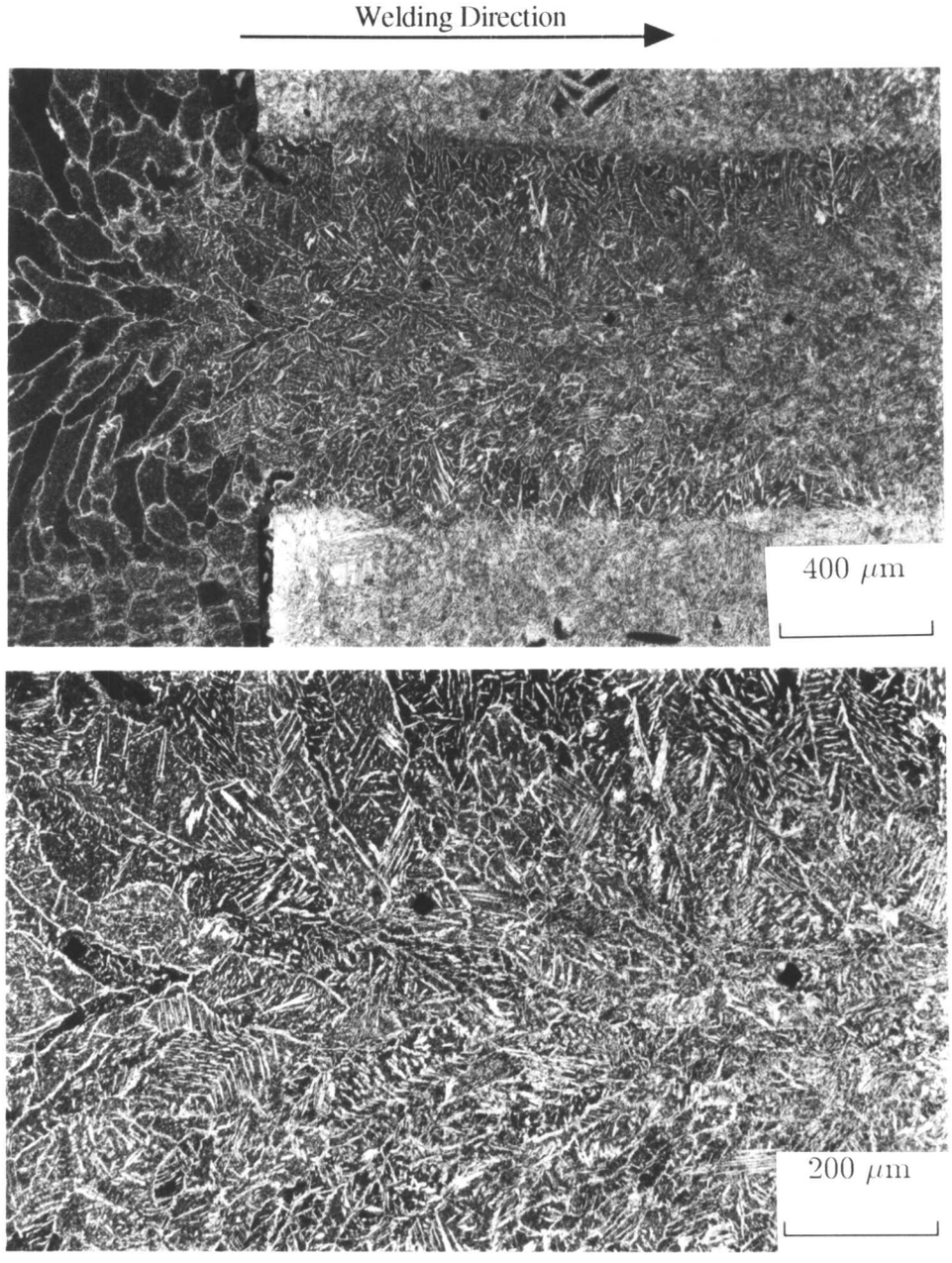

Figure 5.34. microstructure of dissimilar metal junction between alloys IC373 and A219. The weld direction is from alloy IC373 (fully ferritic solidification mode) to alloy A219 (FA solidification mode). A change of solidification mode from fully ferritic to FA can be seen in transition zone due to dilution effect.

5.7 Conclusions

1. Phase diagram calculations of the solidification mode have been found to be consistent with estimates using the Cr_{eq}/Ni_{eq} approach of the Suutala model. Of the five different steel grades investigated only one (ZERON100) shows different solidification mode other than predicted by model. This indicates that the model needs some modification for super duplex stainless steels.

2. Thermodynamic calculations indicate that the suppression of the austenite phase in super duplex weld metal A219 would lead to the persistence of liquid to incredibly low temperatures showing that fully ferritic solidification of this alloy is impossible. This was confirmed experimentally by the failed attempts to induce the alloy to solidify into a fully ferritic state using laser welds which traverse dissimilar metal junctions.

3. The results of long time solution treatments at 1300 °C show that duplex rolled metal IC373 has a wholly ferritic microstructure above this temperature indicating that the solidification mode is fully ferritic as predicted by calculations. In the case of steel grades IC381 and A219 the microstructure is a mixture of ferrite and austenite at 1300 °C . The volume fraction of austenite that forms at all temperatures in grade A219 is much larger than in grade IC381 as predicted by calculations.

4. The melting point of steel decreases with increasing the amount of alloying elements.

5. The melting point of steel increases with increasing heating rate.

6. The solidus temperature on heating is much higher than on cooling and this difference increases with increasing the heating and cooling rates. This is due to the superheating of solid and undercooling of liquid.

7. During the quenching of these steels from an elevated temperature (i.e. 1300 °C) very fine austenite particles (some of them in cluster forms) will precipitate inside the δ-ferrite grains. These fine austenite particles have the same chemical composition as far as substitutional alloying elements are concerned. This is presumably because they form at a low temperature during the quench, where diffusion becomes sluggish.

8. Although from published data (e.g. Bhadeshia *et al.*, 1991) the solidifi-

cation conditions can change the solidification mode from ferritic-austenitic to austenitic-ferritic when the Cr_{eq}/Ni_{eq} of steel be near to the critical value corresponding to the mode change, but the solidification mode depends essentially on the chemical composition of steel (present by Cr_{eq}/Ni_{eq}) and the effect of solidification conditions is of secondary importance.

Chapter 6

ISOTHERMAL HEAT TREATMENT AND ITS EFFECT ON THE FERRITE/AUSTENITE BALANCE

6.1 Introduction

The essential reason for the success of duplex stainless steels is their higher strength and better corrosion resistance when compared with austenitic stainless steels. Moreover, they also have a good weldability. These good properties are to some extent attributable to the microstructure which contains approximately 50 vol.% each of ferrite and austenite (the super duplex grades might have about 60 vol.% austenite). The relative fractions of the phases can be controlled both by the composition of the steel or by heat treatment. The effect of chemical composition on the balance between ferrite and austenite was discussed in chapter three. The influence of heat treatment is presented in this chapter.

6.2 Thermodynamic calculations

Phase calculations using MTDATA are present in Figure 6.1. The calculations take into account the phases liquid, ferrite, austenite, sigma and the carbides $M_{23}C_6$ and M_7C_3. They cover a temperature range over which only liquid, ferrite and austenite coexist. The purpose of these calculations was to enable a comparison against experimental measurements presented in the subsequent sections. The calculations have been done for a typical duplex wrought metal (IC381), duplex composition overalloyed with Cr (IC373), duplex weld metal (UNS31), super duplex wrought metal (ZERON100) and super duplex weld metal (A219). Their chemical compositions are listed in Table 5.1 and Table 5.2 shows their Cr_{eq}/Ni_{eq} ratios calculated according to the Hammar and Svensson (1979) equation. Comparing the results of these calculations shows that duplex weld metal UNS31 (which has the lowest Cr_{eq}/Ni_{eq}) has the highest volume fraction of austenite.

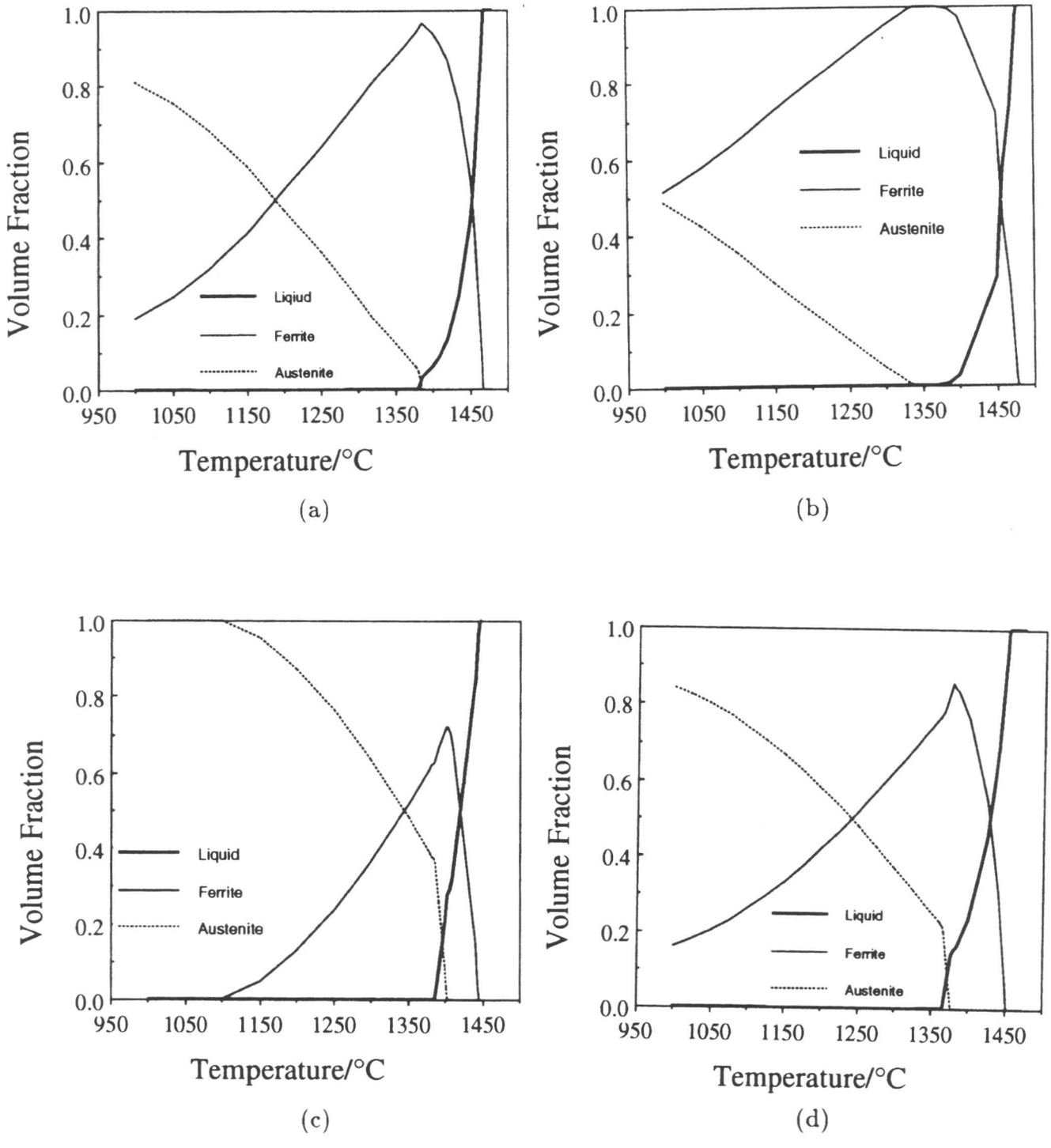

Figure 6.1. The calculated equilibrium phase diagrams for alloys a) typical duplex wrought metal (IC381); b) duplex composition overalloyed with Cr (IC373); c) duplex weld metal (UNS31); d) super duplex wrought metal (ZERON100); e) super duplex weld metal (A219).

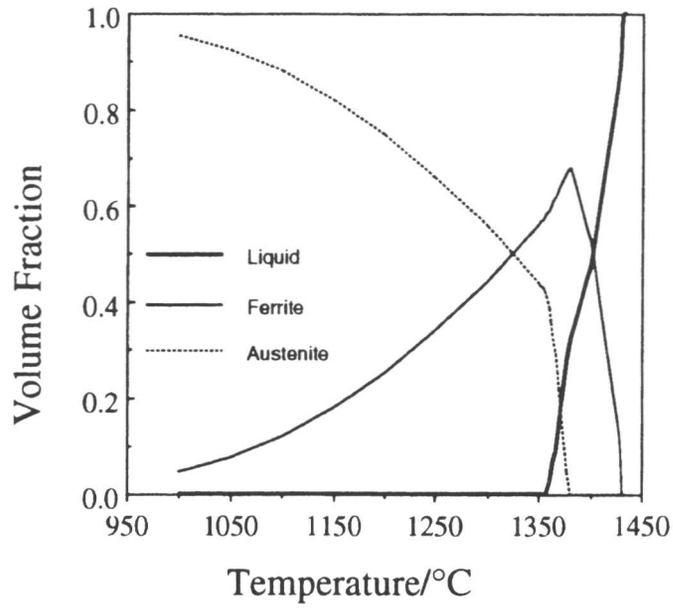

(e)

Figure 6.1. (Continued)

6.3 Equilibrium isothermal heat treatments

Equilibriation heat treatments were carried out on duplex stainless steel rolled metals IC373, IC381 and super duplex weld metal A219 (Table 5.1); the heat treatment conditions are summarised in Table 6.1. To avoid oxidation, decarburisation and the escape of nitrogen, all the specimens were sealed in silica-quartz tubes containing a partial pressure of argon (about 100 mm Hg). The minimum temperature of the heat treatments is 1100 °C to avoid the precipitation of sigma-phase, especially in alloy A219. Figure 6.2 shows the precipitation of sigma-phase at 1050 °C in super duplex weld metal A219. The maximum heat treatment temperature used was 1300 °C as the silica-quartz tube is not stable at temperatures higher than that.

Table 6.1. Heat treatments.

Temperature (°C)	1100	1150	1200	1250	1300
Time (h)	315	165	65	48	26

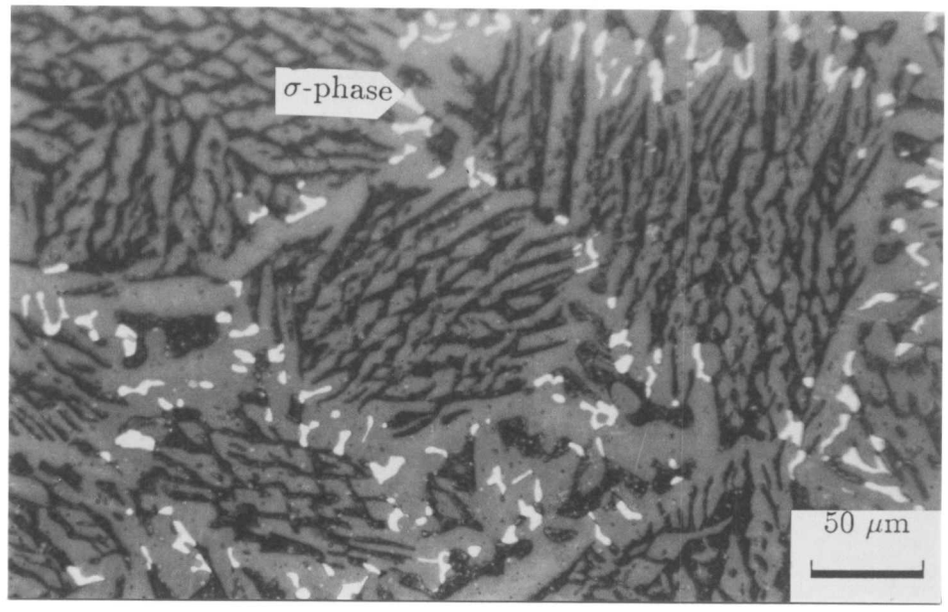

Figure 6.2. The microstructure of super duplex stainless steel alloy A219 solution treated at 1150 °C for 2.5 hours before quenching in water. Sigma-phase (bright white) has been precipitated on the grain boundaries between austenite (yellow) and ferrite (dark colour).

Figures 6.3-6.6 show the microstructures of duplex alloy IC381 after heat treated at different temperatures. The light phase is austenite and the dark one is ferrite. The fine particles inside the ferrite grains are austenite formed during quenching. The volume fraction of austenite (excluding the fine particles) was measured using both the linear point counting and image analysing techniques. As the temperature was reduced from 1300 (Figure 5.19) to 1100 °C (Figure 6.6) the measured volume fraction of austenite (excluding fine austenite which has precipitated during quenching) increased from about 0.19 to 0.65.

Duplex rolled metal IC373 has a Cr_{eq}/Ni_{eq} ratio which is much higher so that the formation of austenite is retarded to a much lower temperature compared with IC381 (Figure 6.7-6.10). Figure 6.9 shows allotriomorphic austenite at δ-ferrite grain boundaries after heat treatment at 1150 °C for 165 hours. The volume fraction of austenite (excluding the fine particles) is less than 0.05. By comparison, the specimen which was heat treated at 1100 °C, contained about 0.28 volume fraction of austenite (excluding the fine particles).

In the case of super duplex weld metal A219 (Figures 6.11 to 6.14) with a Cr_{eq}/Ni_{eq} ratio of 2.20 (Table 5.2) the solidification mode is ferritic-austenitic

(chapter 5), so the volume fraction of austenite at all temperatures is much higher compared with IC373 and IC381. As the temperature was reduced from 1300 (Figure 5.21) to 1100 °C (Figure 6.14) the measured volume fraction of austenite (excluding fine austenite which has precipitated during quenching) increased from 0.53 to 0.70. The microstructure of specimen heat treated at 1100 °C (Figure 6.14) shows that δ-ferrite has decomposed to austenite plus sigma phase. This confirms that sigma phase in super duplex stainless steel weld metal A219 forms at higher temperatures compared with duplex stainless steel wrought metals IC381 and IC373. This is due to higher amount of Cr and Mo in the super grade (these two elements are strong sigma formers).

The measured volume fractions of austenite for different specimens are listed in Table 6.2. Figures 6.15-6.17 shows the variations of equilibrium (calculated and measured) volume fraction of austenite with temperature for alloys IC381, IC373 and A219 respectively. The agreement is good in all cases except for IC373 which contains a less austenite at high temperatures than is predicted. This is the only alloy which solidifies completely to ferrite. The nucleation of austenite must therefore be difficult. The situation would be worse by the fact that elevated temperature heat treatments lead to excessively coarse δ grain structures, so that the number density of haterogenous nucleation sites is drastically reduces. Consequently, the observed discrepancies at elevated temperatures are attributed to the kinetic hindrance of transformations. The fact that agreement with the phase calculations is recovered for the heat treatment at 1100 °C (fine δ grain structure, larger nucleation site) confirms this hypothesis.

Table 6.2. Equilibrium volume fraction of austenite measured using both the linear point counting and image analysis techniques.

Steel Grade	Temperature °C				
	1100	1150	1200	1250	1300
IC381	0.65±0.07	0.60±0.05	0.34±0.03	0.29±0.03	0.19±0.03
IC373	0.28±0.04	<0.05	<0.05	<0.05	<0.05
A219	0.70±0.06	0.75±0.05	0.68±0.06	0.57±0.05	0.53±0.06

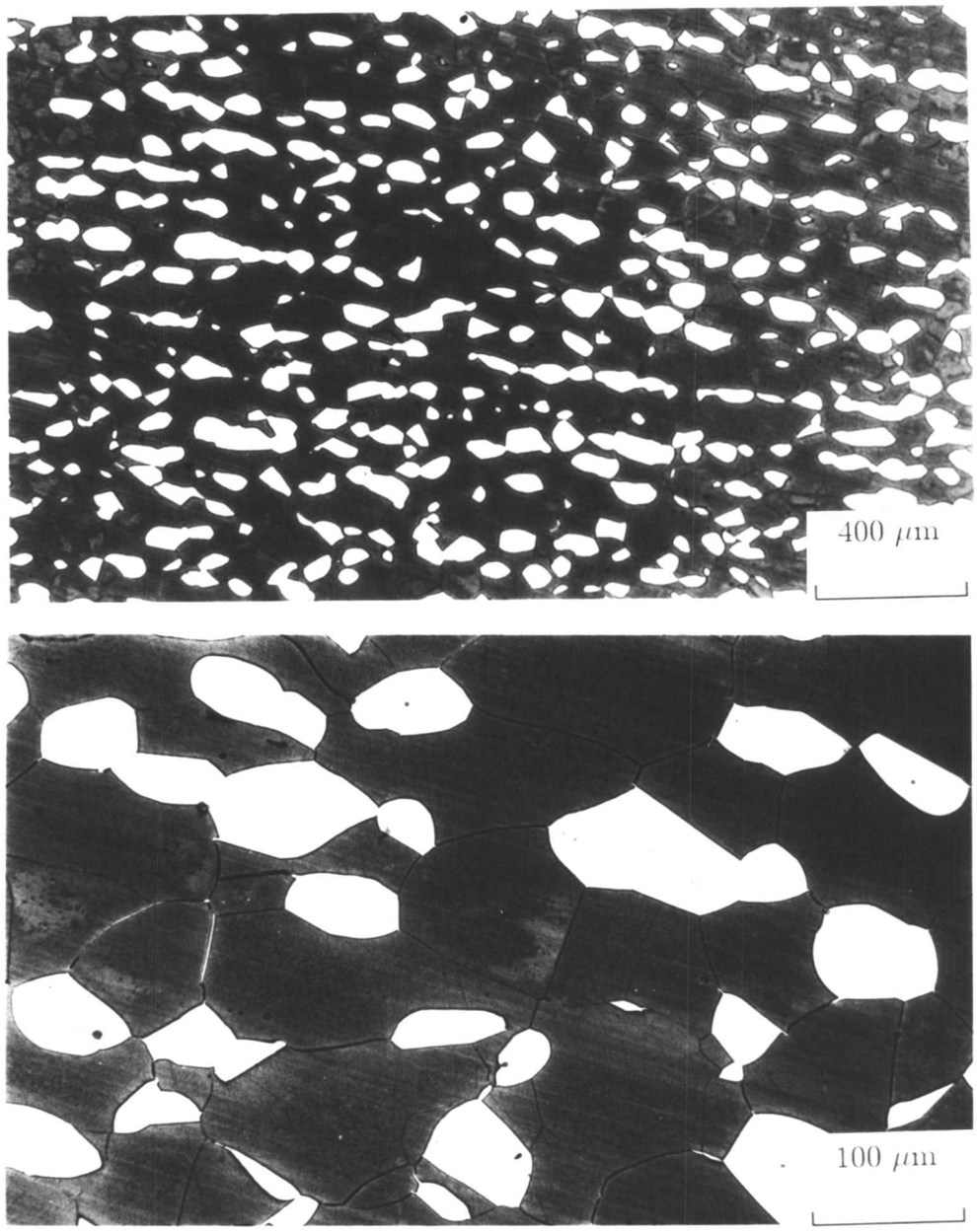

Figure 6.3. Light micrographs showing the microstructure of duplex rolled metal IC381 heat treated at 1250 °C for 48 hours and then quenched into water. The light phase is austenite and the dark one is ferrite. The fine particles inside the ferrite grains are austenite formed during quenching. The measured volume fraction of austenite (excluding the fine particles) is about 0.29.

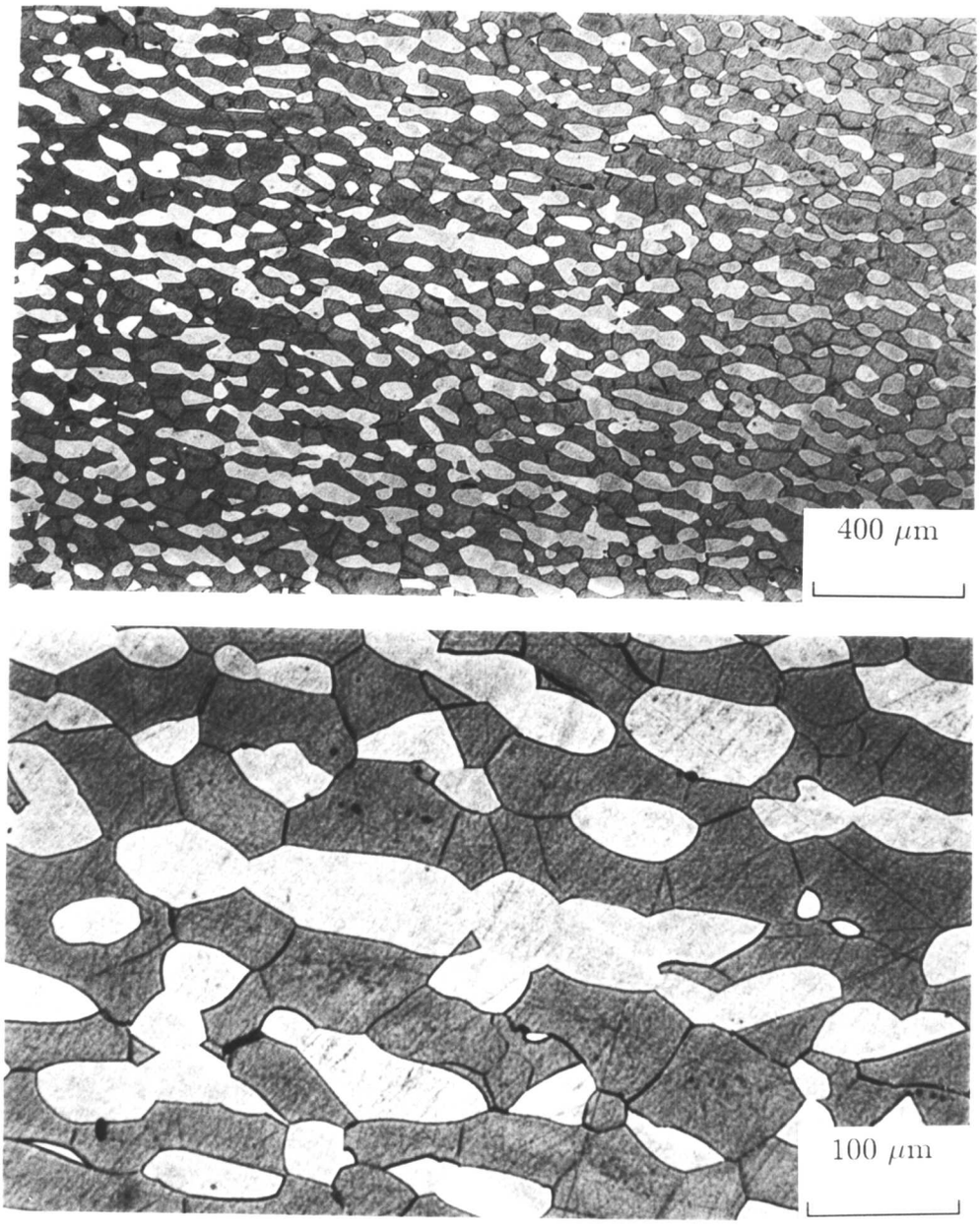

Figure 6.4. Light micrographs showing the microstructure of duplex rolled metal IC381 heat treated at 1200 °C for 65 hours and then quenched into water. The light phase is austenite and the dark one is ferrite. The fine particles inside the ferrite grains are austenite formed during quenching. The measured volume fraction of austenite (excluding the fine particles) is about 0.34.

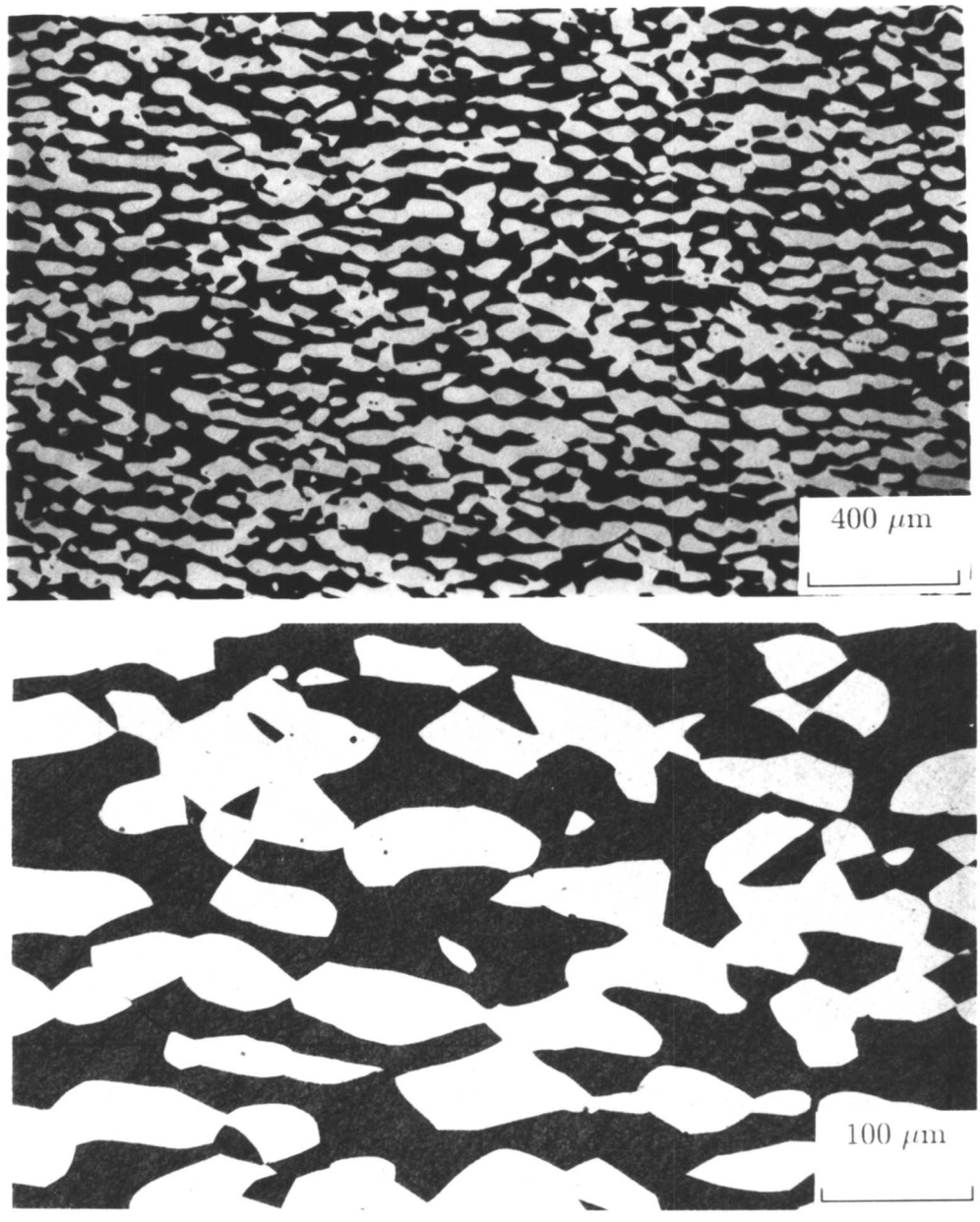

Figure 6.5. Light micrographs showing the microstructure of duplex rolled metal IC381 heat treated at 1150 °C for 165 hours and then quenched into water. The light phase is austenite and the dark one is ferrite. The fine particles inside the ferrite grains are austenite formed during quenching. The measured volume fraction of austenite (excluding the fine particles) is about 0.60.

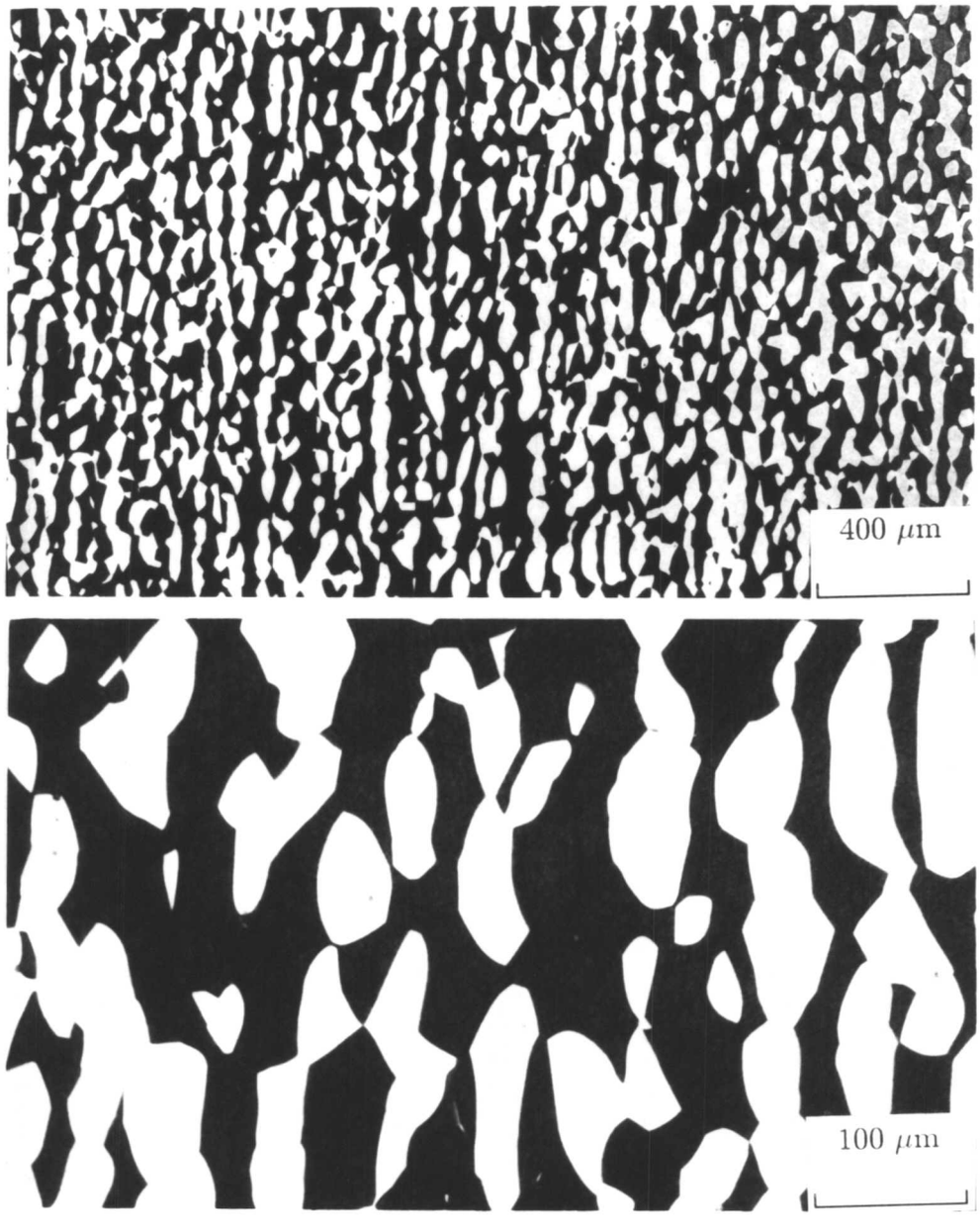

Figure 6.6. Light micrographs showing the microstructure of duplex rolled metal IC381 heat treated at 1100 °C for 315 hours and then quenched into water. The light phase is austenite and the dark one is ferrite. The fine particles inside the ferrite grains are austenite formed during quenching. The measured volume fraction of austenite (excluding the fine particles) is about 0.65.

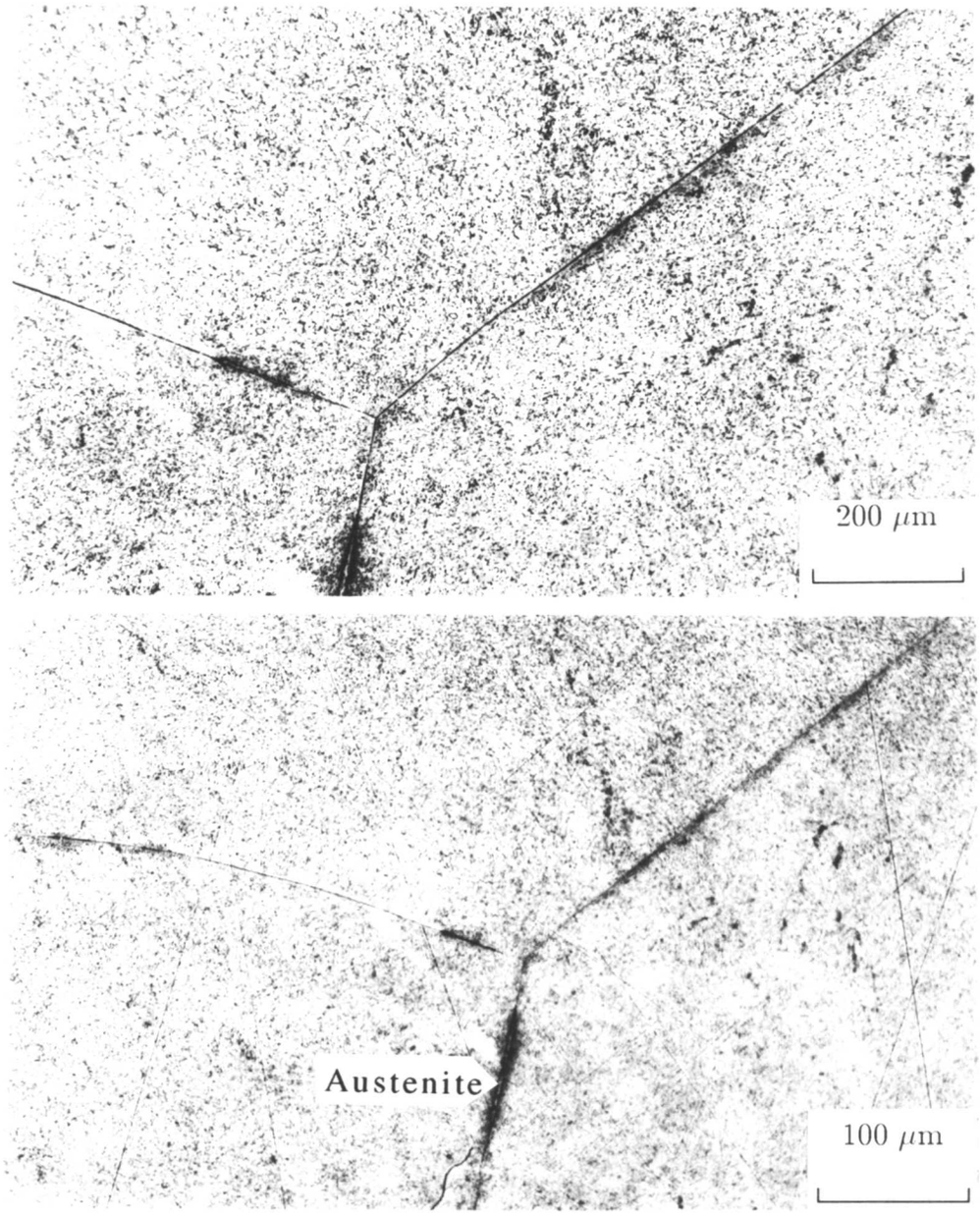

Figure 6.7. Light micrographs showing the microstructure of duplex rolled metal IC373 heat treated at 1250 °C for 48 hours and then quenched into water. This figure shows that the equilibrium microstructure at the elevated temperature consists of huge δ-ferrite grains with a small amount of austenite formed mainly at the grain boundaries. The fine particles inside the ferrite grains are austenite formed during quenching. The measured volume fraction of austenite (excluding the fine particles) is less than 0.05.

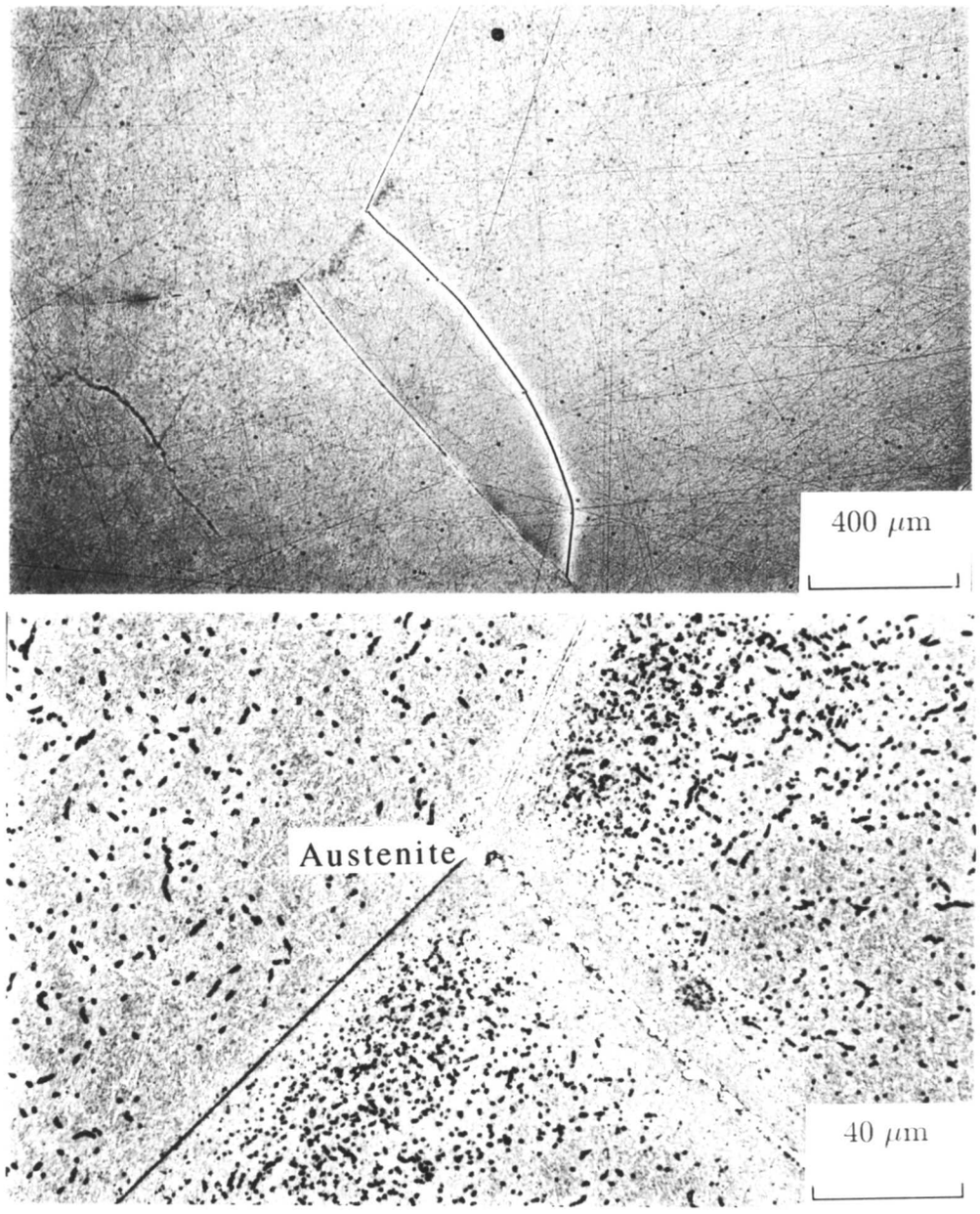

Figure 6.8. Light micrographs showing the microstructure of duplex rolled metal IC373 heat treated at 1200 °C for 65 hours and then quenched into water. This figure shows that the equilibrium microstructure at the elevated temperature consists of huge δ-ferrite grains with a small amount of austenite formed mainly at the grain boundaries. The fine particles inside the ferrite grains are austenite formed during quenching. The measured volume fraction of austenite (excluding the fine particles) is less than 0.05.

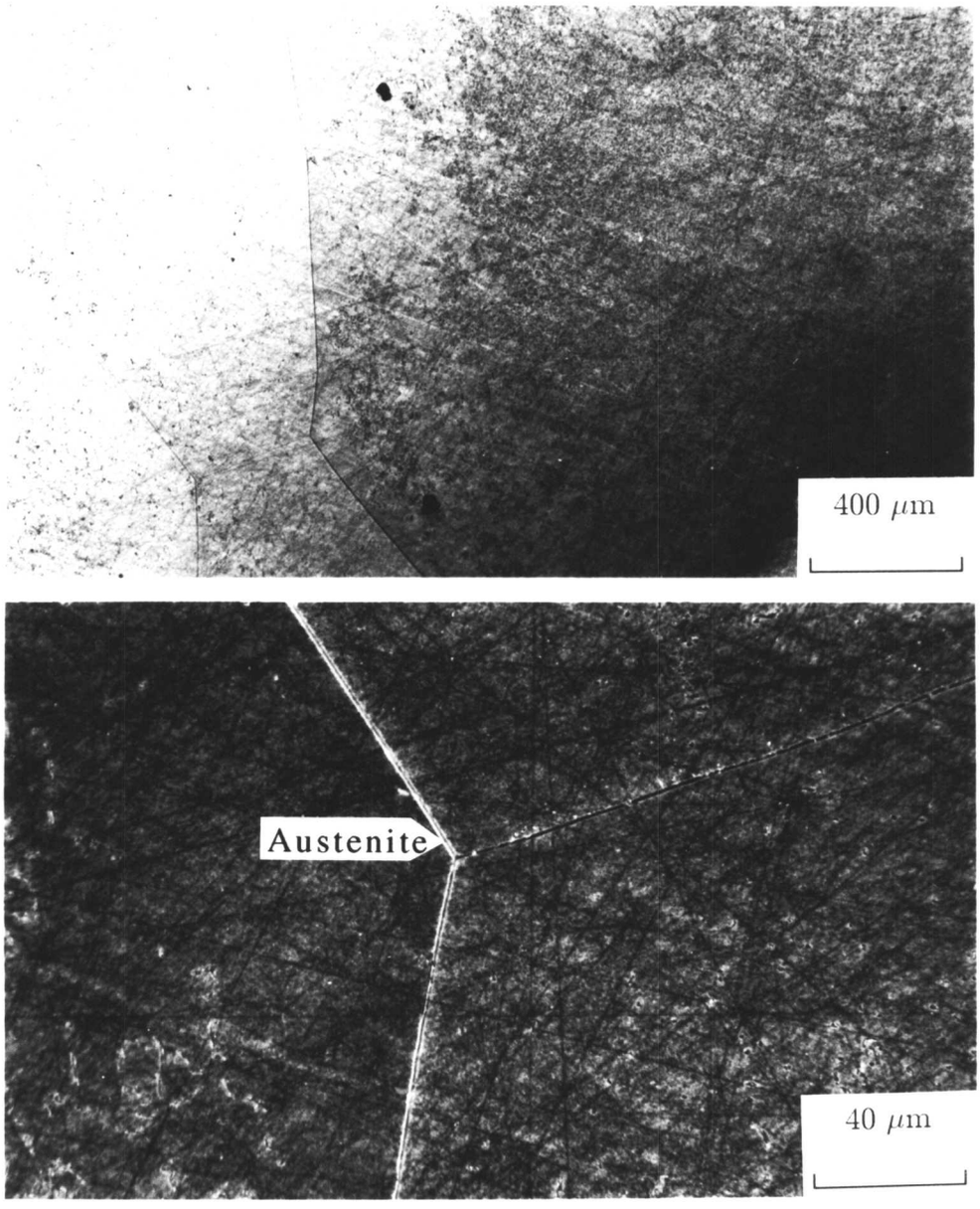

Figure 6.9. Light micrographs showing the microstructure of duplex rolled metal IC373 heat treated at 1150 °C for 165 hours and then quenched into water. This figure shows that the equilibrium microstructure at the elevated temperature consists of huge δ-ferrite grains with a small amount of austenite formed mainly at the grain boundaries. The fine particles inside the ferrite grains are austenite formed during quenching. The measured volume fraction of austenite (excluding the fine particles) is less than 0.05.

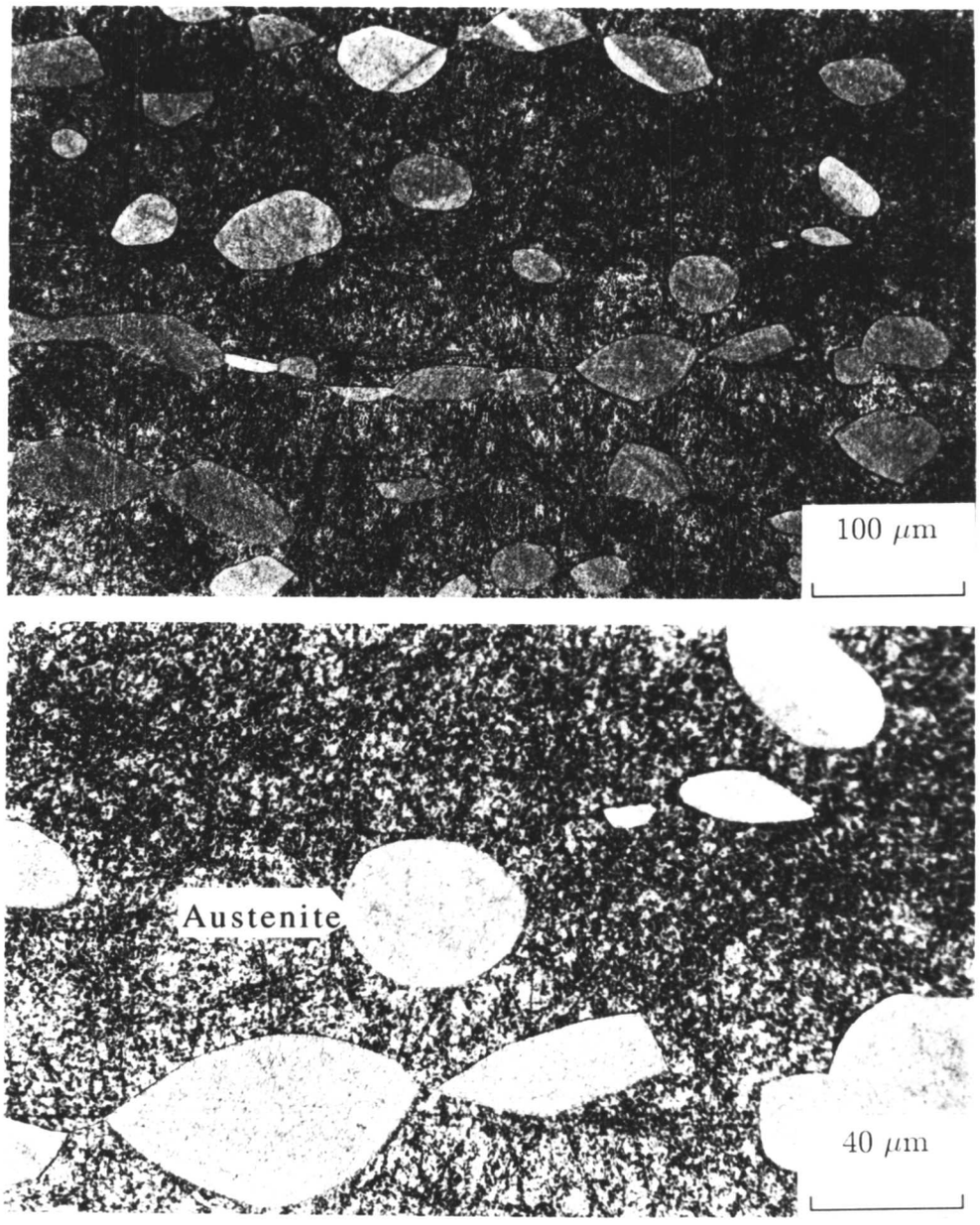

Figure 6.10. Light micrographs showing the microstructure of duplex rolled metal IC373 heat treated at 1100 °C for 315 hours and then quenched into water. The light phase is austenite and the dark one is ferrite. The fine particles inside the ferrite grains are austenite formed during quenching. The measured volume fraction of austenite (excluding the fine particles) is about 0.28.

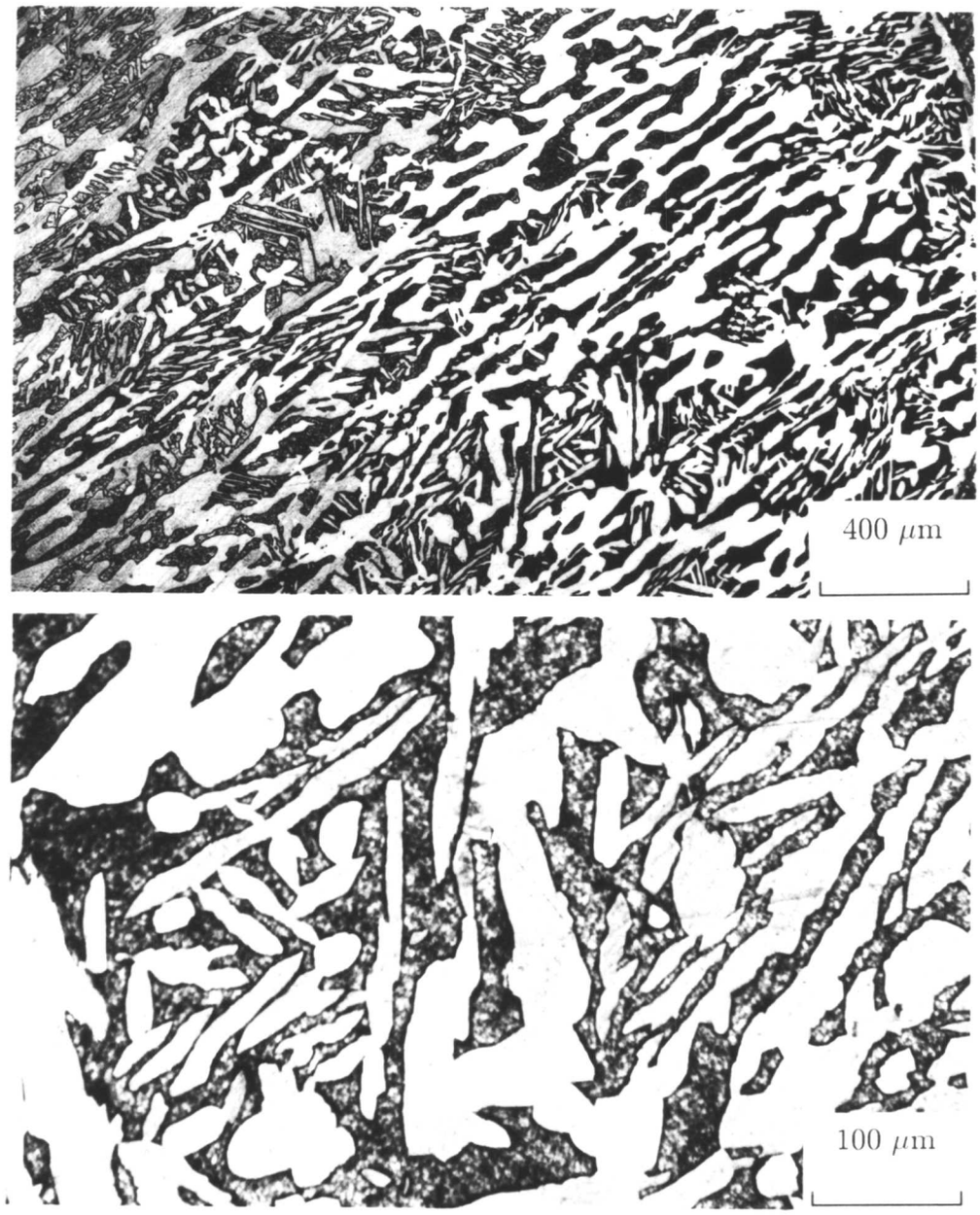

Figure 6.11. Light micrographs showing the microstructure of super duplex weld metal A219 heat treated at 1250 °C for 48 hours and then quenched into water. The light phase is austenite and the dark one is ferrite. The fine particles inside the ferrite grains are austenite formed during quenching. The measured volume fraction of austenite (excluding the fine particles) is about 0.57.

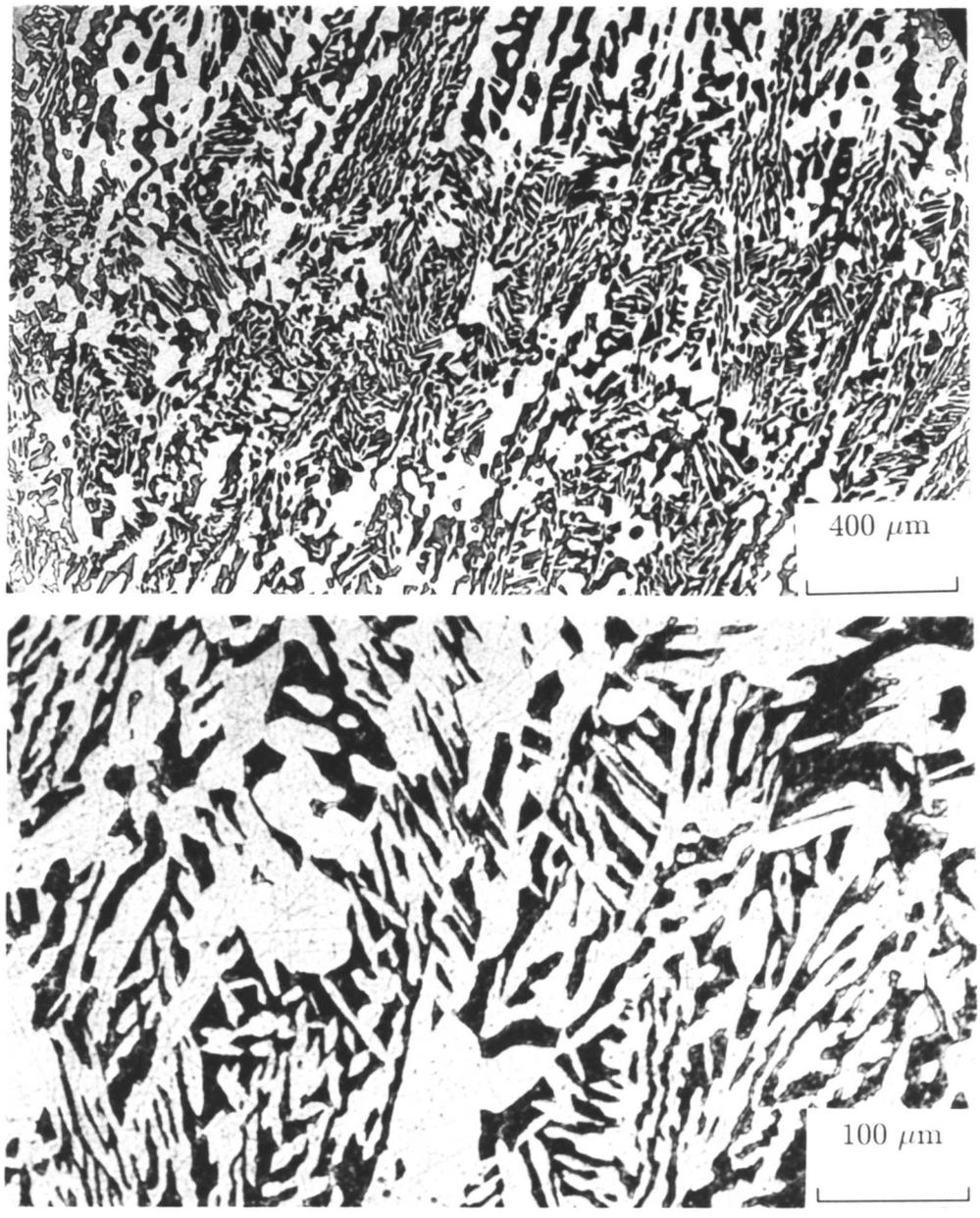

Figure 6.12. Light micrographs showing the microstructure of super duplex weld metal A219 heat treated at 1200 °C for 65 hours and then quenched into water. The light phase is austenite and the dark one is ferrite. The fine particles inside the ferrite grains are austenite formed during quenching. The measured volume fraction of austenite (excluding the fine particles) is about 0.68.

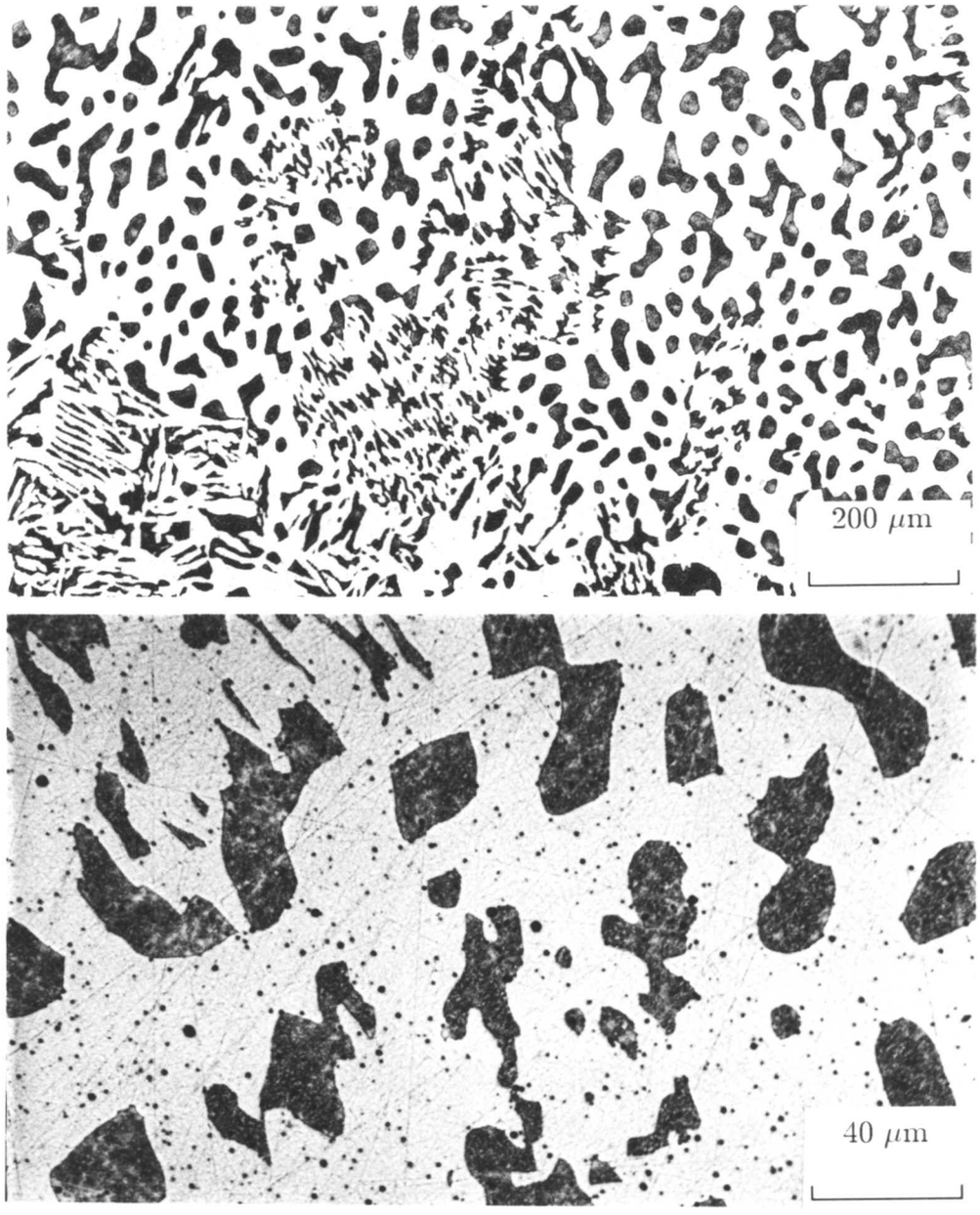

Figure 6.13. Light micrographs showing the microstructure of super duplex weld metal A219 heat treated at 1150 °C for 165 hours and then quenched into water. The light phase is austenite and the dark one is ferrite. The fine particles inside the ferrite grains are austenite formed during quenching. The measured volume fraction of austenite (excluding the fine particles) is about 0.75.

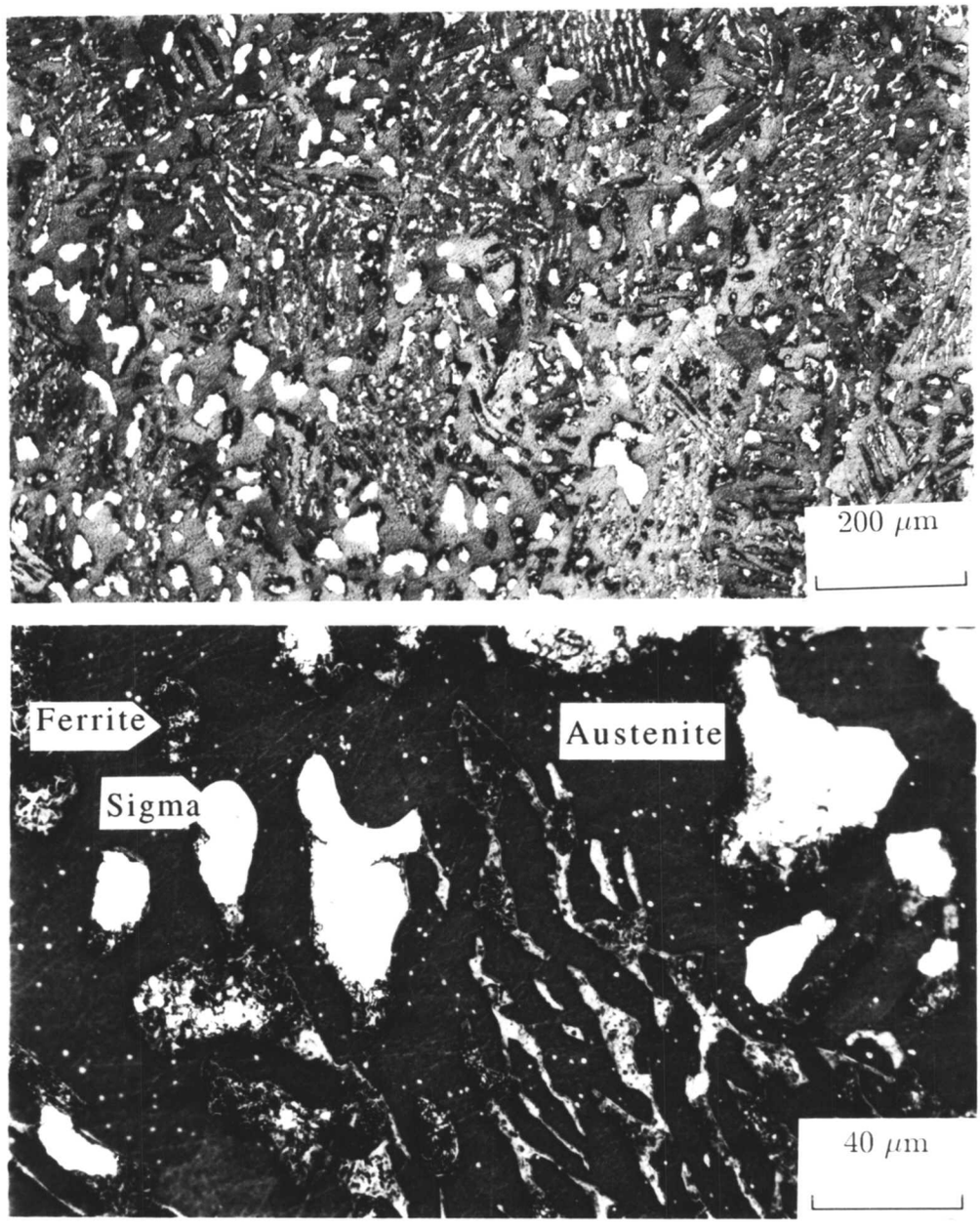

Figure 6.14. Light micrographs showing the microstructure of super duplex weld metal A219 heat treated at 1100 °C for 315 hours and then quenched into water. This figure shows that ferrite (dark phase) has decomposed to austenite (gray phase) plus sigma (bright phase). is austenite. The measured volume fraction of austenite is about 0.70.

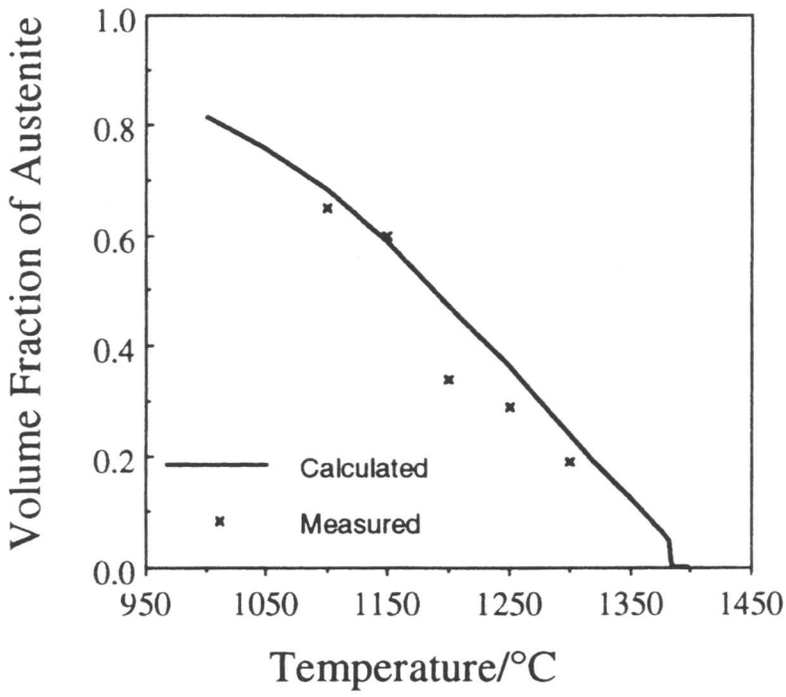

Figure 6.15. Calculated and measured equilibrium volume fractions of austenite as a function of temperature in duplex alloy IC381.

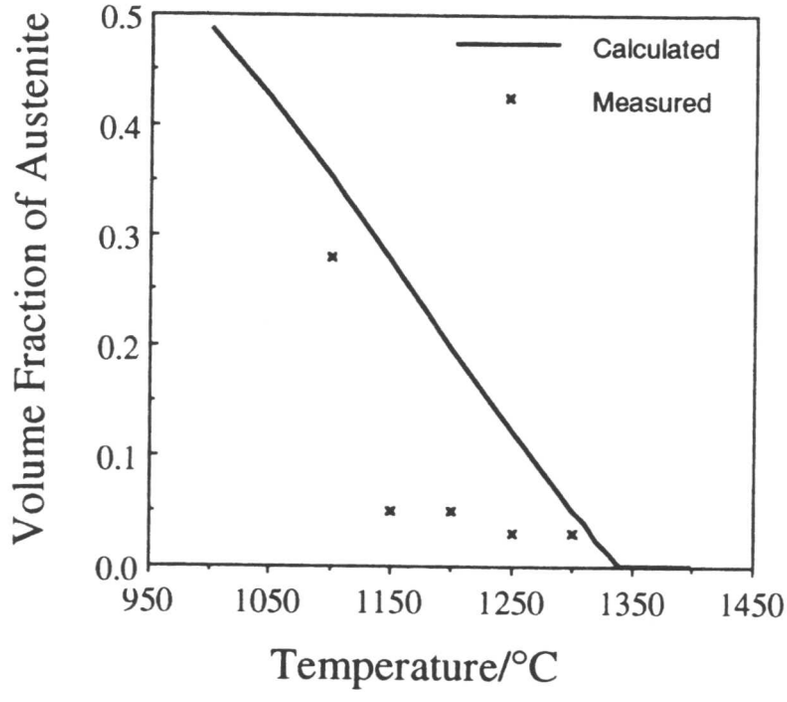

Figure 6.16. Calculated and measured equilibrium volume fractions of austenite as a function of temperature in duplex alloy IC373.

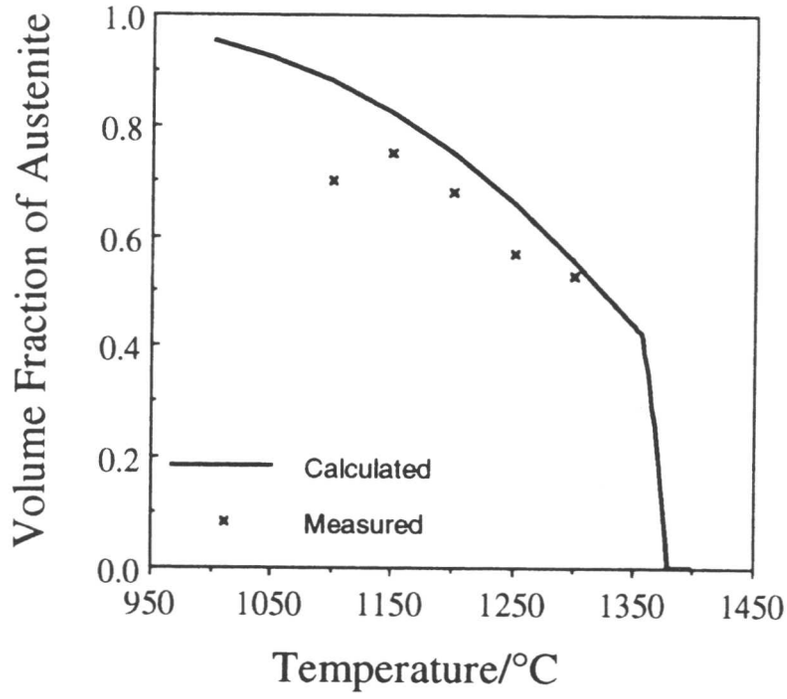

Figure 6.17. Calculated and measured equilibrium volume fractions of austenite as a function of temperature in super duplex weld metal A219.

6.4 Effect of Ferrite/Austenite Balance on Hardness

The experiments show that the hardness has a close relation with the volume fraction of δ-ferrite in duplex stainless steels. Figure 6.18 shows the measured hardness against the heat treatment temperature over the temperature range 1100-1300 °C. In this temperature range, the microstructure is ferritic-austenitic and almost free from other precipitation (except for alloy A219 heat treated at 1100 °C that microstructure consists of three phases austenite, ferrite and sigma phase). The hardness was found to increase with increasing heat treatment temperature. This is expected because of the accompanying increase in the volume fraction of δ-ferrite which is the harder of the two phases. For temperatures below 1200 °C, super duplex weld metal A219 is harder than duplex rolled metal IC381 although its volume fraction of austenite is higher. This is due to the formation of sigma phase at 1100 °C in alloy A219 (Figure 6.14). In the case of 1150 °C this can be due to precipitation of chromium nitride as the nitrogen and chromium content of A219 is larger than in IC381 (see section 6.6).

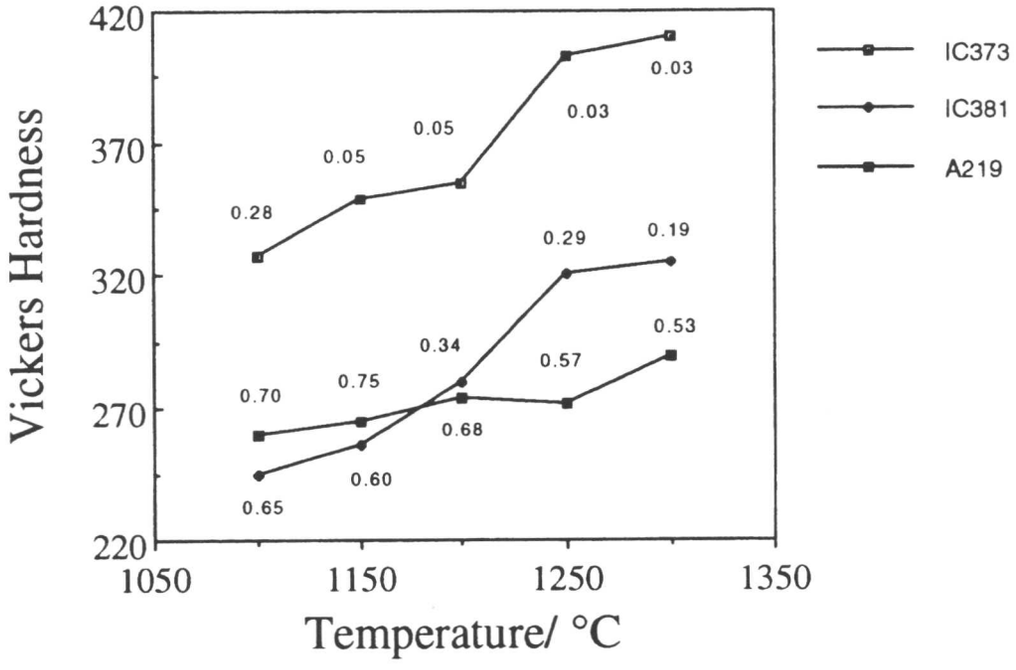

Figure 6.18. Measured hardness values as a function of the heat treatment temperatures. The measured fractions of austenite (excluding fine particles) are also included.

6.5 Equilibrium partitioning of alloying elements

The concentrations of different elements in each phase were measured using an EDX analyser on a scanning electron microscope (see section 2.10). Only the major constituents were analysed, namely Fe, Cr, Ni, Mo, Mn and Si. The concentrations of these elements were normalised to 100 wt.%. Between these elements molybdenum has a much larger atomic mass compared with the others. Since the microanalytic measurements are carried out assuming that all the elements absorb X-rays to a similar degree, the molybdenum data are likely to be flawed, the extent of the error depending on the thickness of the particle along the electron beam direction (a parameter which is very difficult to determine). The chemical composition of each phase was analysed twenty times in each heat treated specimen (Tables 6.3 to 6.6), the error bars show the standard

deviation. Figures 6.19 to 6.24 show the calculated and measured partitioning of different alloying elements in duplex rolled metal IC381 and super duplex weld metal A219 as a function of temperature. As the temperature increases the equilibrium concentration of chromium in ferrite decreases while its nickel content increases (Figures 6.19 and 6.20). The equilibrium nickel content of austenite also increases with temperature (Figures 6.20 and 6.23). There is broad agreement between calculations and measurements, except for molybdenum where the discrepancies are large.

Table 6.3. TEM EDX microanalysis of δ-ferrite in duplex rolled metal IC381 heat treated at different temperatures (all concentrations in wt.%).

Temperature °C	Fe	Cr	Ni	Mo	Mn	Si
1300	64.30±0.47	24.30±0.47	5.47±0.09	3.37±0.19	1.97±0.05	0.47 ±0.02
1250	65.00±0.82	24.67±0.47	4.97±0.17	3.30±0.14	1.80±0.22	0.43 ±0.02
1200	64.67±0.47	24.67±0.47	5.00±0.14	3.47±0.12	1.87±0.25	0.47 ±0.05
1150	64.00±0.62	26.00±0.35	4.60±0.27	3.71±0.23	1.43±0.21	0.49 ±0.02
1100	63.67±0.47	25.67±0.47	4.47±0.17	3.87±0.12	1.83±0.05	0.46 ±0.04

Table 6.4. TEM EDX microanalysis of austenite in duplex rolled metal IC381 heat treated at different temperatures (all concentrations in wt.%).

Temperature °C	Fe	Cr	Ni	Mo	Mn	Si
1300	64.67±0.47	23.20±0.47	7.00±0.22	2.90±0.73	2.13±0.05	0.45 ±0.07
1250	65.67±0.47	22.67±0.47	7.00±0.22	2.27±0.12	2.13±0.26	0.40 ±0.04
1200	66.00±0.87	22.00±0.57	7.23±0.19	2.37±0.05	2.10±0.08	0.41 ±0.03
1150	66.10±0.43	22.10±0.63	7.31±0.23	2.33±0.13	1.70±0.16	0.33 ±0.05
1100	65.00±0.61	22.00±0.72	7.20±0.33	2.60±0.67	2.40±0.15	0.46 ±0.06

Table 6.5. TEM EDX microanalysis of δ-ferrite in super duplex weld metal A219 heat treated at different temperatures (all concentrations in wt.%).

Temperature °C	Fe	Cr	Ni	Mo	Mn	Si
1300	58.00±0.97	28.75±0.43	8.27±0.25	4.15±0.17	0.63±0.07	0.48 ±0.06
1250	57.33±0.47	29.33±0.47	7.73±0.15	4.43±0.41	0.67±0.13	0.56 ±0.04
1200	58.00±0.50	29.00±0.50	7.17±0.26	4.73±0.29	0.66±0.06	0.55 ±0.06
1150	57.00±0.50	30.10±0.63	6.95±0.25	4.45±0.55	0.99±0.01	0.43 ±0.07
1100	57.00±0.50	30.00±0.20	6.80±0.20	4.85±0.05	0.77±0.11	0.62 ±0.02

Table 6.6. TEM EDX microanalysis of austenite in super duplex weld metal A219 heat treated at different temperatures (all concentrations in wt.%).

Temperature °C	Fe	Cr	Ni	Mo	Mn	Si
1300	59.00±0.50	26.50±0.50	10.25±0.43	2.60±0.25	0.68±0.13	0.45 ±0.10
1250	58.50±0.50	27.00±0.50	10.00±0.50	3.20±0.40	0.76±0.06	0.48 ±0.09
1200	59.00±0.50	27.00±0.82	9.90±0.14	2.35±0.55	0.85±0.19	0.39 ±0.17
1150	58.00±0.82	27.33±0.47	9.87±0.12	3.00±0.08	1.5±0.64	0.40 ±0.08
1100	59.00±0.50	26.00±0.50	11.00±0.50	3.05±0.25	0.70±0.11	0.47 ±0.05

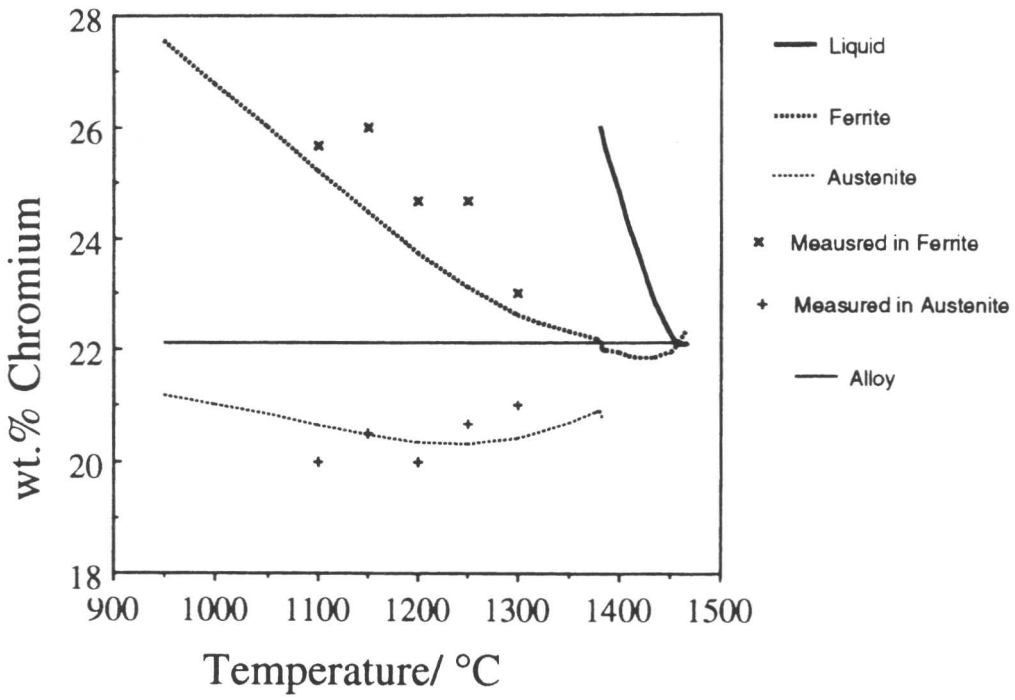

Figure 6.19. The calculated and measured partitioning of chromium in duplex rolled metal IC381 as a function of temperature.

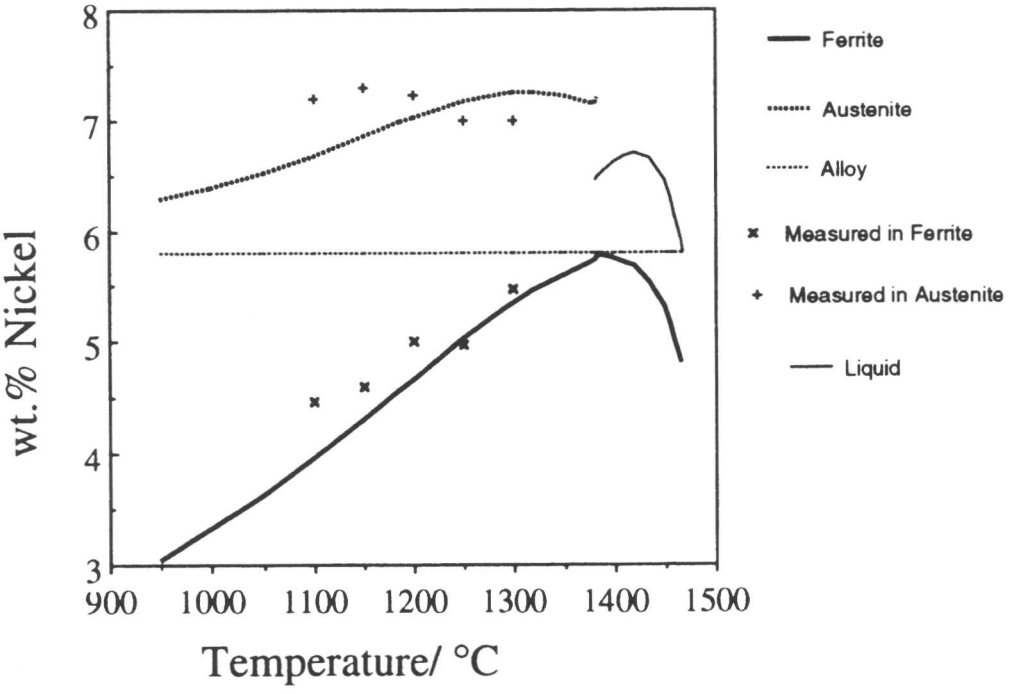

Figure 6.20. The calculated and measured partitioning of nickel in duplex rolled metal IC381 as a function of temperature.

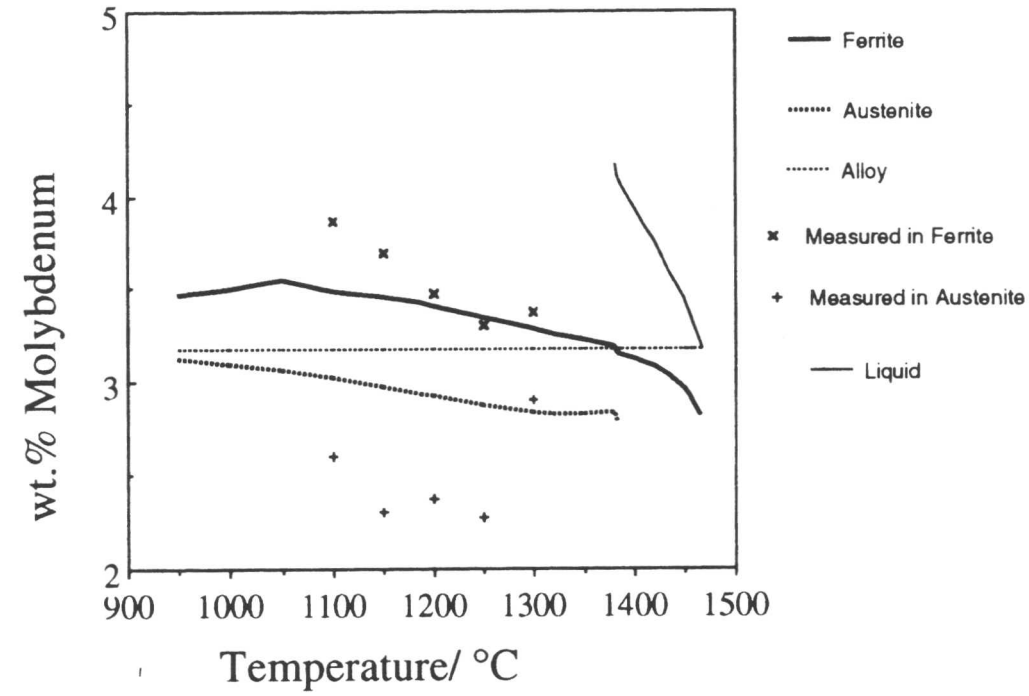

Figure 6.21. The calculated and measured partitioning of molybdenum in duplex rolled metal IC381 as a function of temperature.

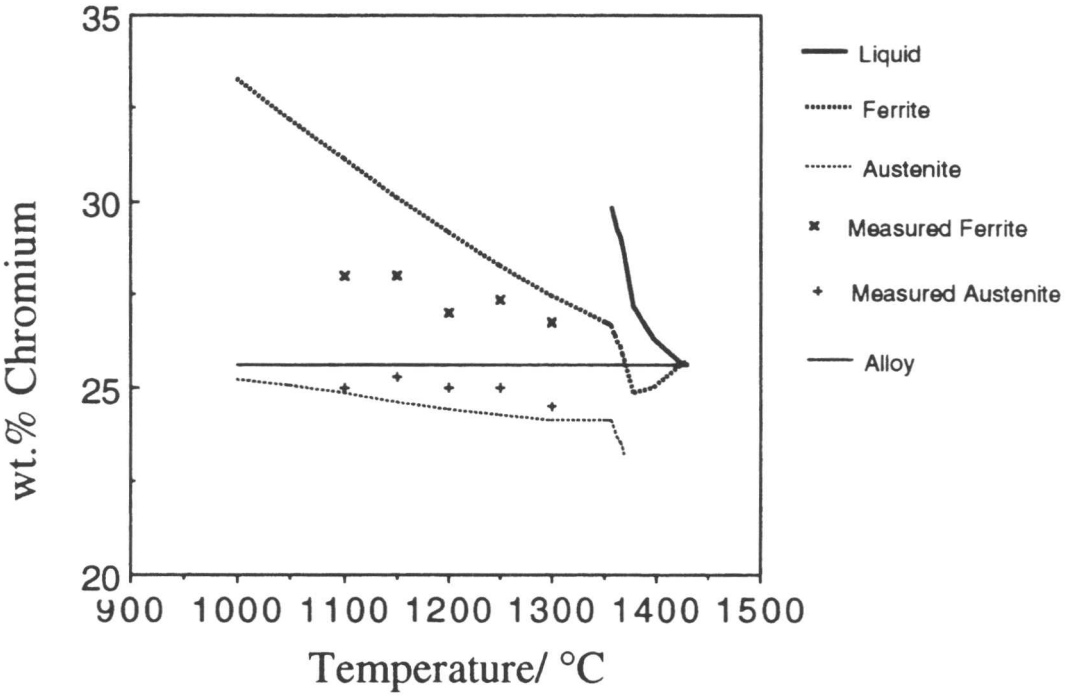

Figure 6.22. The calculated and measured partitioning of chromium in super duplex weld metal A219 as a function of temperature.

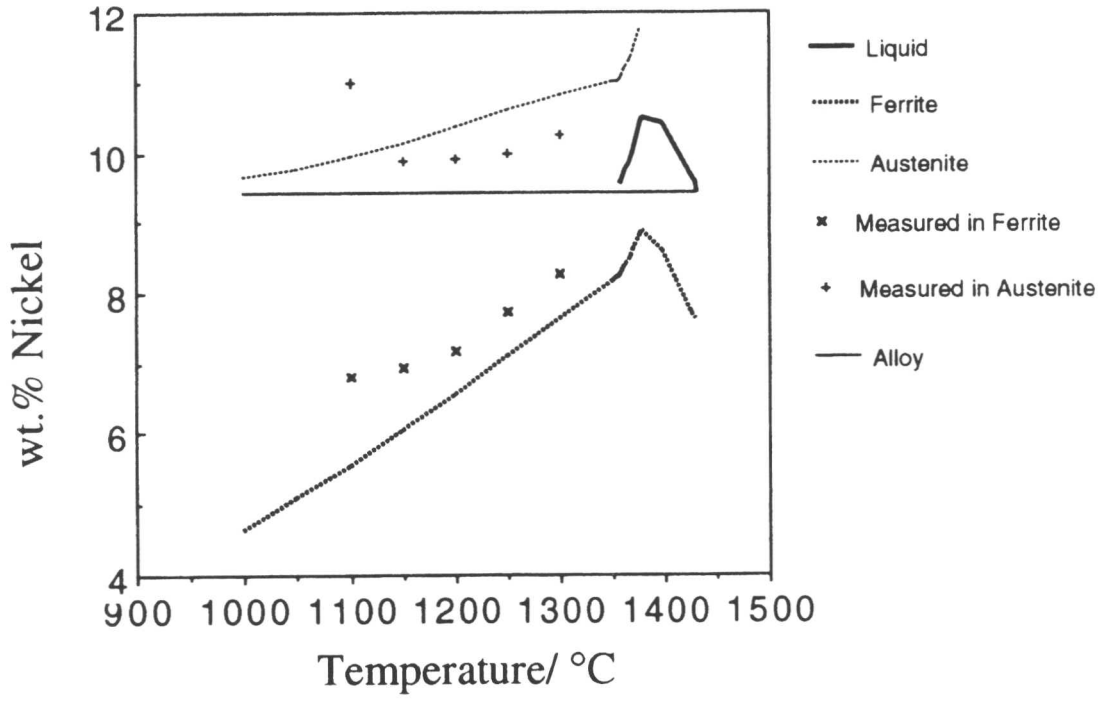

Figure 6.23. The calculated and measured partitioning of nickel in super duplex weld metal A219 as a function of temperature.

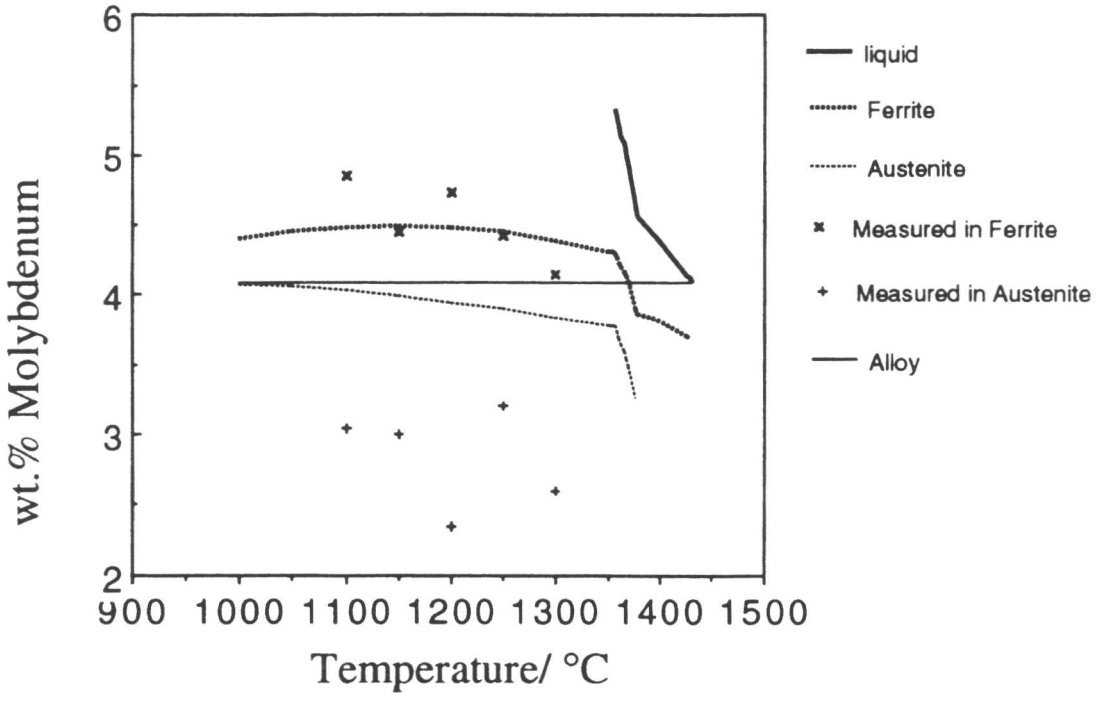

Figure 6.24. The calculated and measured partitioning of molybdenum in super duplex weld metal A219 as a function of temperature.

6.6 Precipitation of Cr_2N

With increased use of N as an alloying element in duplex and super duplex stainless steels, the tendency for the precipitation of chromium nitrides of type Cr_2N in the temperature range 700-900 °C has been enhanced (Hochmann *et al.*, 1974). The precipitate can even form during quenching from solution treatment temperatures. Nilsson and Liu (1988) have observed Cr_2N of 200-500 Å diameter at δ/δ boundaries after quenching in water from 1150 °C in some super duplex steels. Roscoe *et al.*, (1985) have shown that precipitation of Cr_2N is more likely when solutionising is performed at higher temperatures, for instance 1300 °C. However, the effect of Cr_2N on the mechanical and corrosion properties has not been separated from that of sigma, since Cr_2N and sigma often coexist.

In this study, chromium nitride was found to precipitate intragranularly inside the δ-ferrite grains during quenching from solution temperatures higher than 1100 °C in super duplex weld metal A219. Their precipitation was not observed in duplex rolled metals IC381 and IC373. This is due to the fact that the nitrogen content of A219 is more than twice that of IC381 and IC373. Specimens of alloy A219 heat treated at 1150 °C were found to be harder than specimens of alloy IC381 even though the ferrite volume fraction of IC381 is higher (Figure 6.18). This may be due to the precipitation of chromium nitride in alloy A219. Figure 6.25 shows the very fine precipitations of chromium nitride particles inside δ-ferrite grain which have formed during quenching from 1300 °C in A219. Figure 6.26 shows the dark field image of the same particles and Figure 6.27 shows the diffraction pattern of the matrix confirming that matrix has a b.c.c. crystal structure and chromium nitride precipitation do occur in ferrite. Figure 6.28 shows TEM micrographs of carbon replica extract from same sample. The electron diffraction pattern shown in Figure 6.29 confirms that particles have a structure which is trigonal, consistent with that reported by Eriksson (1934). The EDX microanalysis of the carbon replica samples shows that the particles are very rich in chromium (Table 6.7). These results confirm that the particles are likely to be chromium nitrides.

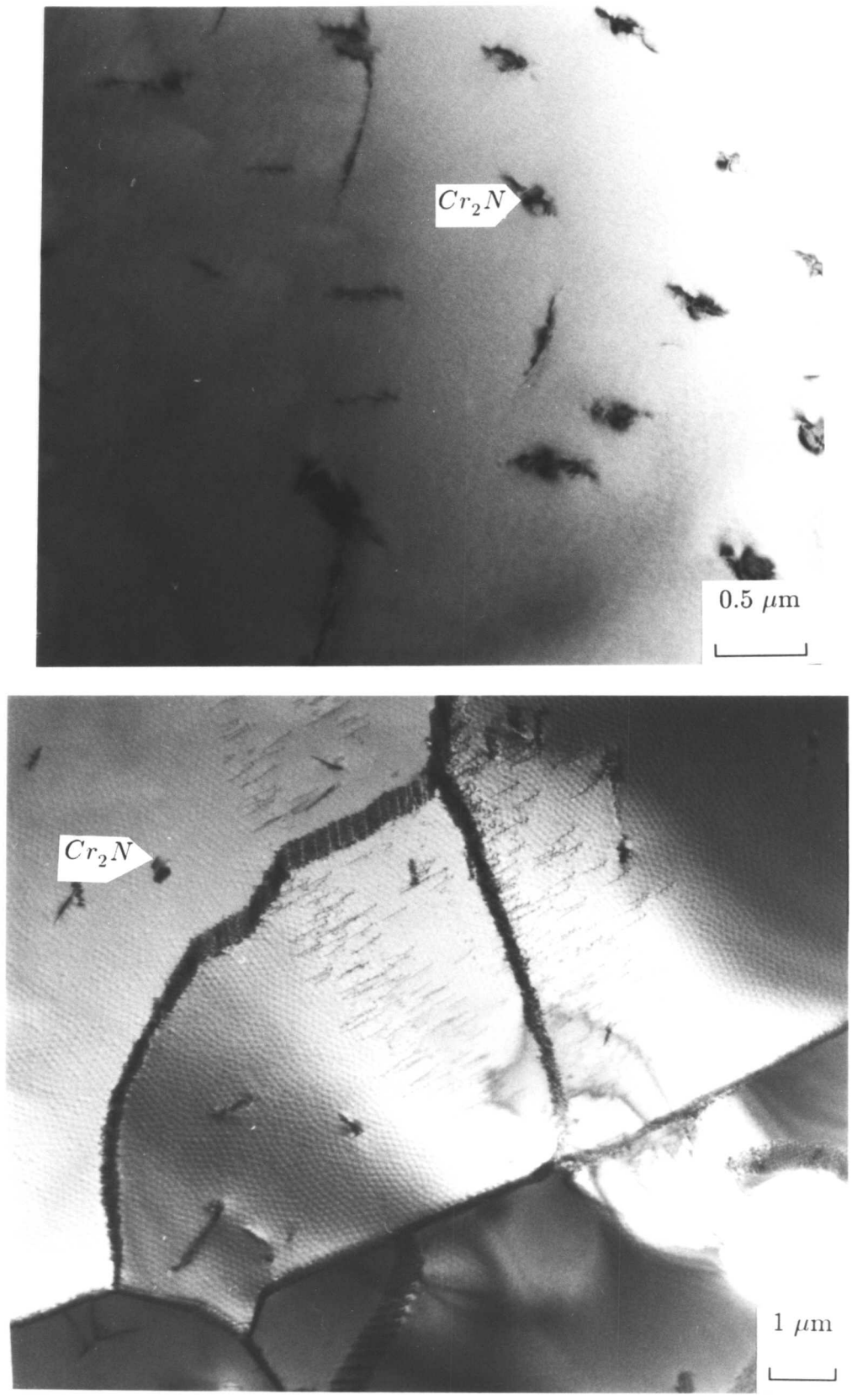

Figure 6.25. Bright field TEM micrographs from thin foils showing the intragranular precipitation of Cr_2N in δ-ferrite formed in A219 during quenching from 1300 °C.

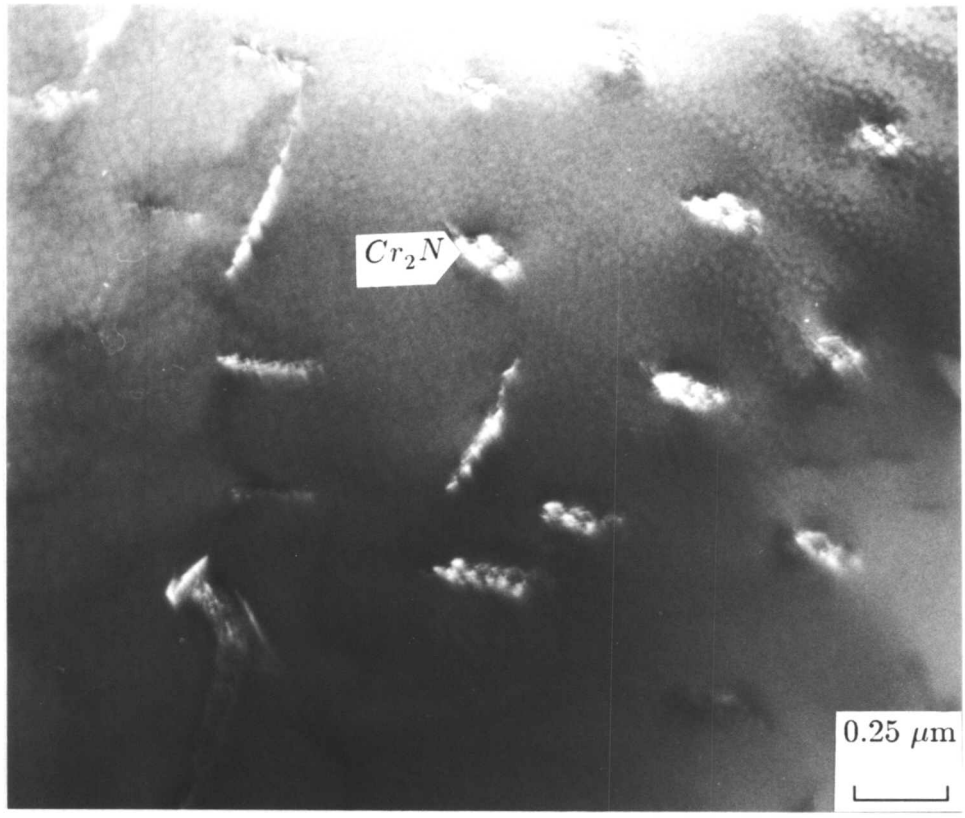

Figure 6.26. Dark field TEM micrographs from thin foils showing the intragranular precipitation of Cr_2N in δ-ferrite formed in A219 during quenching from 1300 °C.

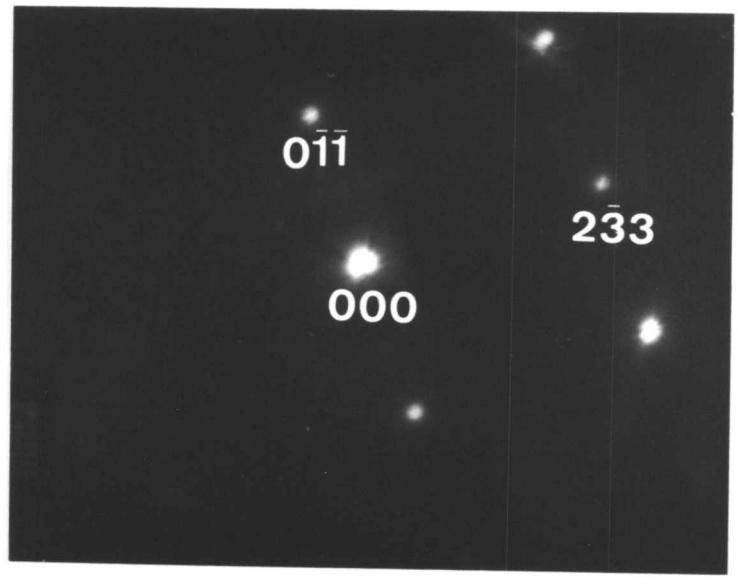

Figure 6.27. SADP of the matrix of Figure 6.25. The zone direction of the diffraction pattern is $[\overline{3}\overline{1}1]$.

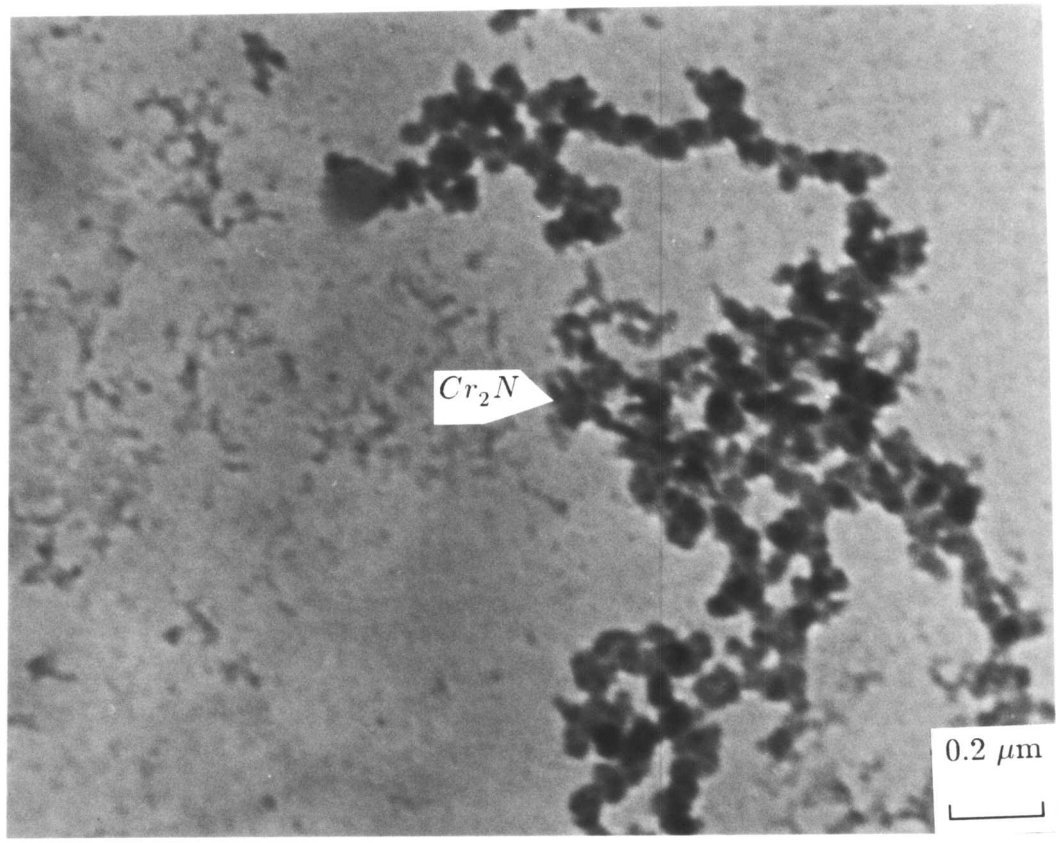

Figure 6.28. Bright field TEM micrographs from carbon replica extracted from A219 sample quenched from 1300 °C showing the Cr_2N particles formed during quenching.

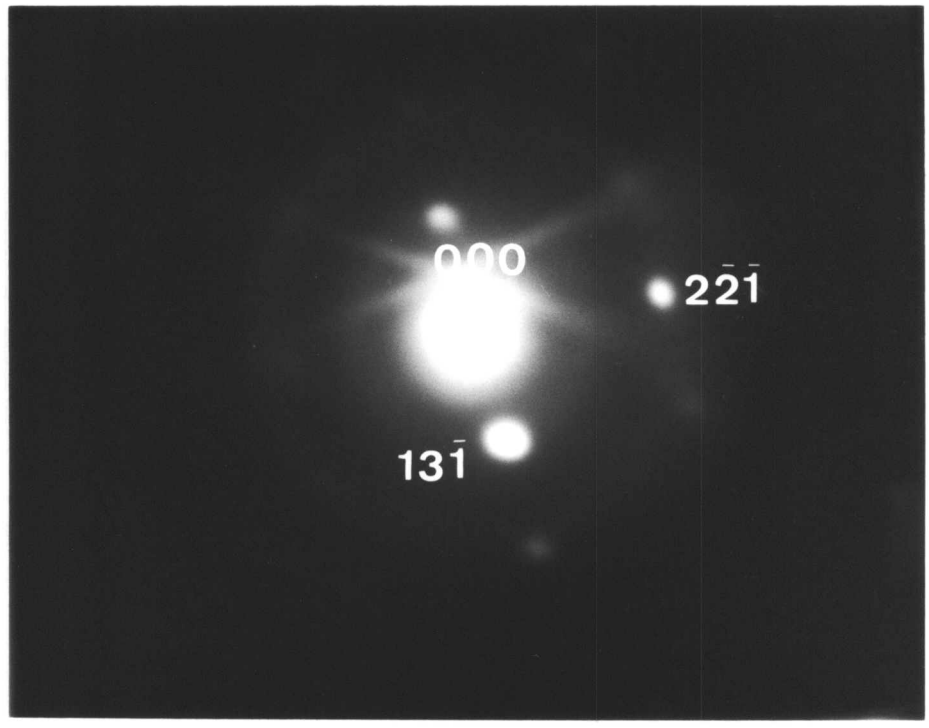

Figure 6.29. SADP of the Cr_2N particles. The zone direction of the diffraction pattern is [518].

Table 6.7. TEM EDX microanalysis of chromium nitride particles formed during quenching from 1300 °C in A219 (all concentrations in wt.%).

Fe	Cr	Ni	Mo	Mn	Si
7.25±0.43	84.57±0.61	0.51±0.09	0.12±0.03	2.72±0.05	-

6.7 Modelling of T_δ

Computer programs have been used to estimate the ferritisation temperature (the temperature where the microstructure is wholly ferritic, T_δ) and volume fractions of austenite. The aim was to provide a simple way of estimating these values. MTDATA therefore provided the raw data which were fitted using regression analysis. These computer programs are presented in appendices A, B and C respectively.

The first program calculates the Ni_{eq} and Cr_{eq} using the Pickering equation (see section 3.4). It then employs regression analysis using values of T_δ calculated by the MTDATA package as actual values, in order to determine an empirical formula for T_δ as a function of Ni_{eq} and Cr_{eq}. In some cases, the calculation of T_δ by MTDATA required the liquid phase to be suppressed. These calculations have produced the following empirical equation where T_δ in degree °C.

$$T_\delta = 1201 + 30.59 \times Ni_{eq} - 3.62 \times Cr_{eq} \qquad (6.1)$$

Figure 6.30 shows calculated and actual T_δ against Ni_{eq}/Cr_{eq} for the steels presented in Table 2.1.

The second computer program is written to calculate the coefficients of the elements in Cr_{eq} and Ni_{eq}, in order to design a new equation for super duplex stainless steels. These calculations have produced the following empirical equation where all the concentrations are in wt.%.

$$Cr_{eq} = Cr + 2Si + 4Mo + 5V + 5.5Al + 0.75Nb + 1.5Ti + 0.75W$$
$$Ni_{eq} = Ni + Co + 0.5Mn + 0.3Cu + 15C + 11N$$

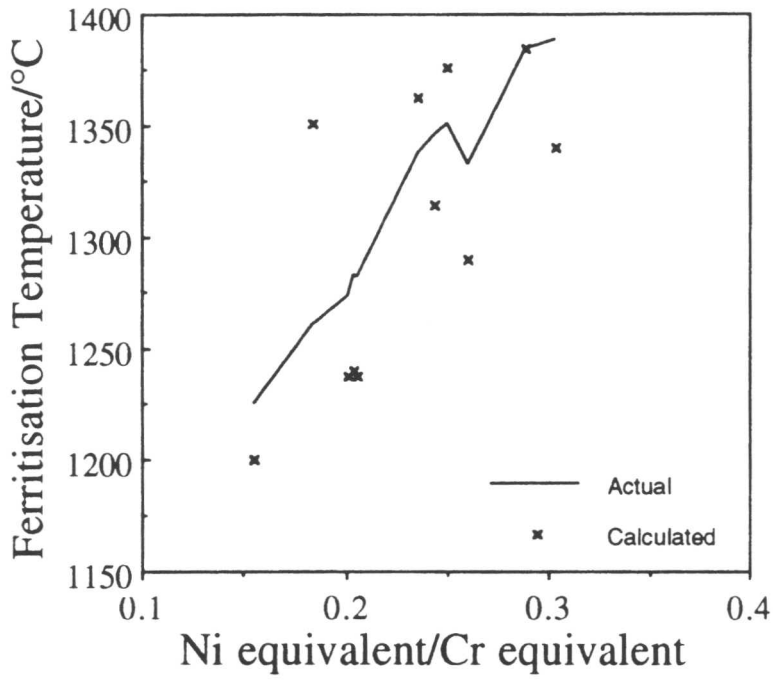

Figure 6.30. Calculated and actual T_δ of different types of duplex stainless steels listed in Table 2.1.

The third computer program is designed to predict the volume fraction of austenite using two dimensional regression analysis on input values of austenite fraction (calculated by MTDATA) against undercooling below T_δ. The following empirical formula is the result of these calculations where T and T_δ are in degree °C and V_γ is the volume fraction of austenite (T_δ can be calculated from equation 6.1).

$$\ln(V_\gamma + 0.0194) = 1.393\ln(T_\delta - T + 1) - 3.945 \qquad (6.2)$$

Where T is less than T_δ. It is important to know that the application of equation 6.2 to predict the equilibrium volume fraction of austenite is limited over the temperature range where the microstructure is duplex (i.e. where sigma phase and other precipitates are unstable). This means for the steels that we studied in this chapter this equation can be used only where $1100<T<T_\delta$. Secondly, this equation gives the equilibrium volume fraction of austenite at the

desired temperature. But since austenite always forms during quenching in order to obtain the desired balance between austenite and ferrite at room temperature, a heat treatment should be designed which produces lower fractions of austenite than that required. Figure 6.31 shows the variation of calculated volume fraction of austenite (predicted by equation 6.2) and actual values (calculated by MTDATA) with temperature for super duplex weld metal A201.

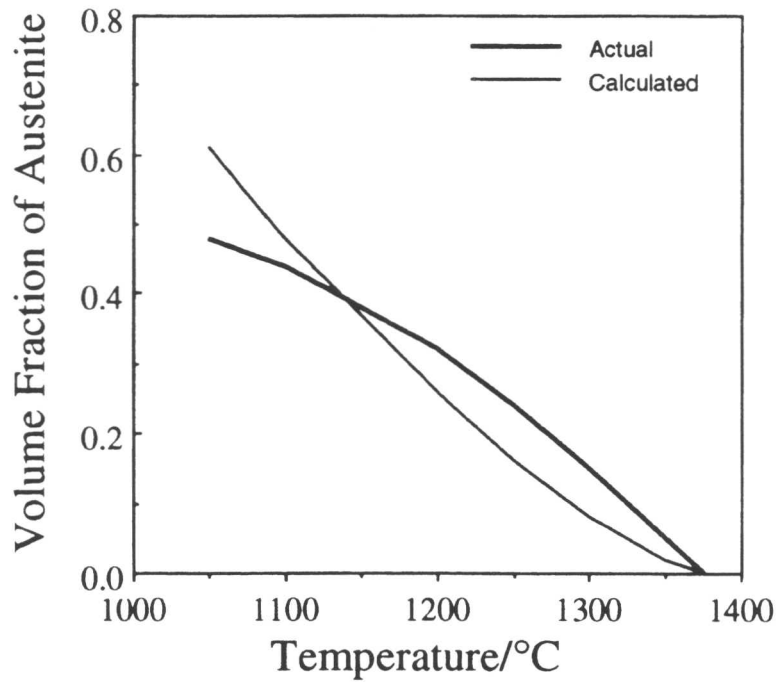

Figure 6.31. The variation of volume fraction of austenite (predicted and actual) with temperature for super duplex stainless steel weld metal A201 (Table 2.1).

6.8 Conclusions

1. Both the thermodynamic calculations and experimental measurements show that within the temperature range 1100-1300 °C, ferrite and austenite are the only phases which are present in duplex and super duplex stainless steels studied (except in super duplex A219 that sigma phase was found to form at 1100 °C).
2. The agreement between thermodynamic calculations and experimental volume fractions of austenite for samples which underwent prolonged isothermal heat treatments is good in all cases where the nucleation of austenite is rela-

tively easy.

3. As the temperature decreases the volume fraction of austenite in duplex and super duplex increases, causing the hardness to decrease.

4. Sigma phase does form at higher temperatures in super duplex stainless steel compared with the duplex grades. This is the effect of the higher Cr and Mo content (which are the strong sigma-phase formers) in the super duplex grades.

5. Chromium nitride was found to form during quenching from elevated solution temperature in super grade A219 (which has higher nitrogen content). The precipitation of these particles increases the hardness.

Chapter 7

PRECIPITATION IN SUPER DUPLEX STAINLESS STEELS

7.1 Introduction

Duplex stainless steels have better mechanical and corrosion properties compared with austenitic and/or ferritic stainless steels, because they combine the favourable properties of ferrite (δ) and austenite (γ), which are present in approximately equal amounts. However, a variety of undesired phases and precipitates may also appear if the steel is improperly treated at elevated temperatures. The presence of these precipitates can spoil the mechanical and corrosion properties. This chapter deals with an experimental characterisation of these undesired phases.

7.2 Previous Work

Josefsson *et al.* (1991) have reviewed the work which has been done by many researchers on phase transformation in duplex stainless steels, as summarised in Table 7.1. Solomon *et al.* (1979) have studied the phase transformations for the duplex alloy U50 and have proposed a TTT diagram which is presented in Figure 7.1.

Table 7.1. Precipitates and phases which have been observed in duplex stainless steels (Josefsson *et al.*, 1991).

Type of precipitate	Nominal chemical formula	Temperature range (°C)	Lattice parameter (Å)	Reference
δ	-	-	a=2.86-2.88	-
γ	-	-	a=3.58-3.62	-
σ	$Fe-Cr-Mo$	600-1000	a=8.79, c=4.54	Hall and Algie, 1966
Cr_2N	Cr_2N	-900	a=4.795, c=4.469	Eriksson, 1934
χ	$Fe_{36}Cr_{12}Mo_{10}$	700-850	a=8.92	Kasper, 1954
R	$Fe-Cr-Mo$	550-650	a=10.903, c=19.342	Rideout *et al.*, 1951
π	$Fe_7Mo_{13}N_4$	550-600	a=6.47	Evans and Jack, 1957
M_7C_3	M_7C_3	950-1050	a=4.52, b=6.99 c=12.11	Rouault *et al.*, 1970
$M_{23}C_6$	$M_{23}C_6$	600-950	a=10.56-10.65	Bowman *et al.*, 1972

7.2.1 Secondary austenite

Secondary austenite is the austenite produced by transformation from ferrite. The ferrite to austenite transformation can happen over a wide temperature range and via different mechanisms depending on the transformation temperature.

7.2.1.1 Transformation temperatures greater than 650 °C

At temperatures above 650 °C austenite will form as Widmanstätten precipitates in various morphologies (Southwick and Honeycombe, 1980). Because of the high temperature, diffusion accompanies transformation and the austenite has a higher content of Ni than the ferrite matrix from which it grows.

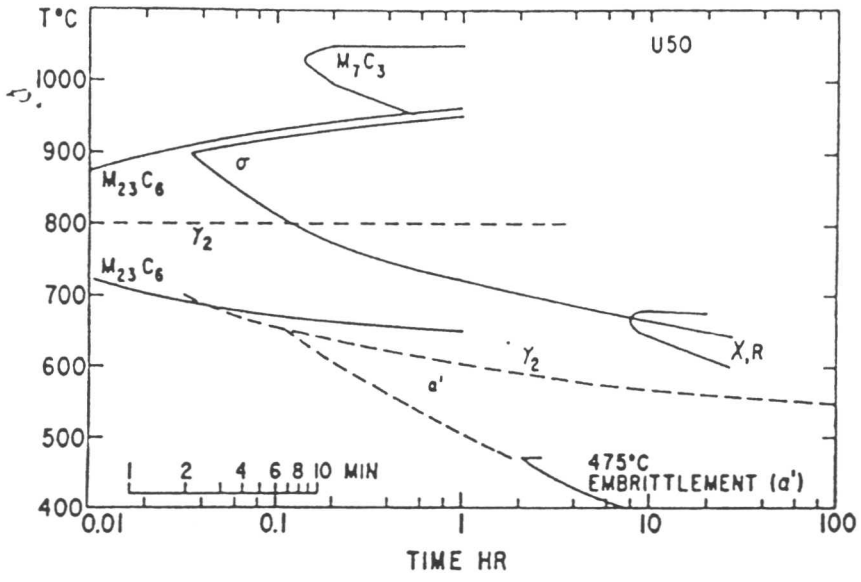

Figure 7.1. TTT diagram of a duplex stainless steel alloy U50 after Solomon *et al.*, 1979.

7.2.1.2 Transformation temperature in the range 700-900 °C

In this temperature range the transformation of δ-ferrite to austenite tends to occur by a eutectoid reaction

$$\delta_{\text{ferrite}} \rightarrow \sigma + \gamma_{\text{austenite}} \tag{7.1}$$

because the δ-ferrite becomes destabilised by the precipitation of σ which reduces the Cr and Mo concentrations in ferrite. The δ-ferrite grains therefore change into intimate mixtures of austenite and σ.

7.2.1.3 Transformation temperatures less than 650 °C

At temperatures less than 650 °C the mobility of substitutional elements such as Cr, Ni and Mo is very small. Ferrite will transform to austenite via a mechanism that shows great similarities with martensite formation. The precipitation of austenite is isothermal and there is no difference in the composition of austenite and ferrite matrix with respect to the substitutional solutes. Southwick *et al.* (1980) have shown that the γ/δ orientation relationship is of the Nishiyama-Wasserman type. This form of austenite precipitates inside the ferrite grains independently of the precipitation of other phases and has been called γ_2 in some literature (Southwick and Honeycombe, 1980).

7.2.2 Sigma phase

Sigma phase is an intermetallic compound with a body centred tetragonal (b.c.t.) crystal structure, occurring mostly in the Fe-Cr and Fe-Cr-Mo systems. In Fe-Cr alloys containing more than 22 wt.% Cr, sigma phase has a composition centred on a Cr content of about 45 wt.%, and can appear during prolonged heat treatment at temperatures above 550 °C (Castro and de Candenet, 1968). In Fe-Cr-Mo systems the temperature range of stability is extended as Mo stabilises sigma. Maehara *et al.* (1983) have shown that Cr, Mo and Si increase both the precipitation rate and volume fraction of sigma in a large number of duplex steels. Ni on the other hand reduces the equilibrium volume fraction of sigma. However, it accelerates precipitation kinetics by reducing the δ-ferrite fraction, and increasing the partitioning of σ-promoting elements to ferrite.

Strutt and Lorimer (1984) have investigated the structure property relationships of ZERON 100 which is a super duplex stainless steel of nominal composition 25 Cr, 7.5 Ni, 3.5 Mo and 0.25 N wt.%. Their measured C-curve for 5 vol.% sigma is shown in Figure 7.2. They found that the nucleation of sigma-phase occurs on ferrite/austenite boundaries, presumably due to the good crystallographic match of the {111} plane of sigma and the {111} plane of austenite.

Preferential growth of sigma-phase into ferrite occurs because the ferrite is Cr-rich. The ferrite near the sigma naturally becomes depleted in Cr and Mo, and hence sometimes tends to partially transform to austenite.

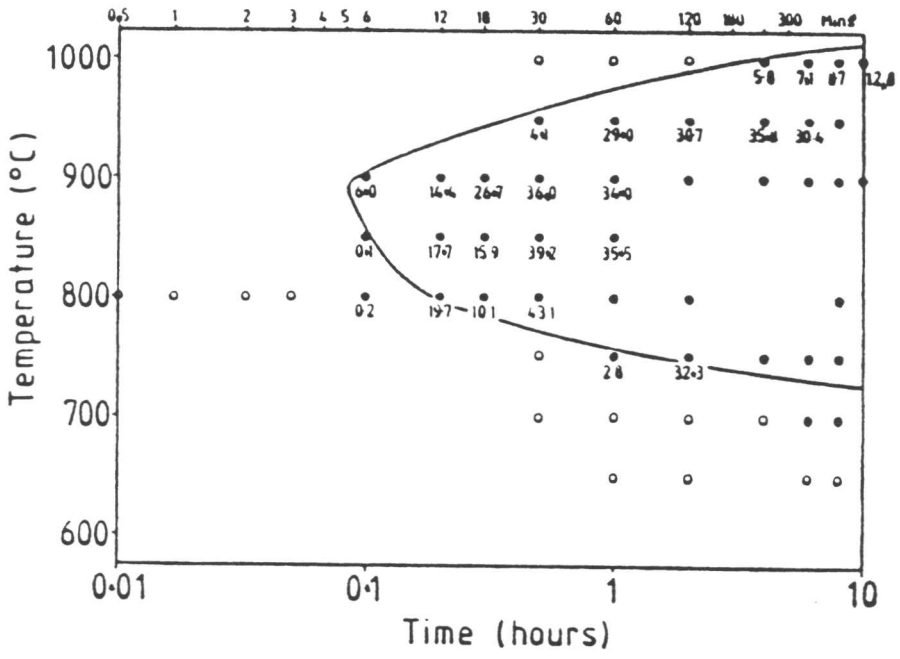

Figure 7.2. The measured C-curve for 5 vol.% sigma-phase formation in forged ZERON100 based on quantitative metallographic data (Strutt and Lorimer, 1986).

As sigma phase is hard and brittle, its presence in welds can cause embrittlement and its absorption of chromium can sensitise the alloy to corrosion (Hevbsleb and Schwabb, 1984).

7.2.3 Cr_2N

See chapter six.

7.2.4 Chi phase

Chi phase is another intermetallic compound which can precipitate in duplex and super duplex steels which precipitates in the temperature range 700-900 °C (Thorvaldsson *et al.*, 1985). As it is brittle it has an adverse effect on toughness, but owing its much lower volume fraction, it is much less important than sigma phase.

7.2.5 R phase

R phase is a Mo-rich compound which appears to be detrimental to toughness. Nilsson *et al.* (1991) have investigated its precipitation in a Fe-22Cr-8Ni-3Mo wt.% weld metal. It precipitates in temperature interval 550-650 °C and has an approximate composition of Fe-25Cr-6Ni-34Mo-4Si wt.%. These data must obviously depend on alloy chemistry as well, although the details are not known.

7.2.6 Carbides

Carbides of type M_7C_3 precipitate in the temperature range 950-1050 °C and $M_{23}C_6$ below about 950 °C. Thorvaldsson *et al.* (1985) have observed precipitation of both types of carbide at δ/δ, γ/γ and δ/γ boundaries. However, due to the low carbon content of duplex and super duplex steels carbides play a less important role compared with other types of stainless steels with higher carbon contents.

7.2.7 π-nitride

π-nitride is a detrimental intermetallic compound that may precipitate intragranularly in duplex and super duplex stainless steels (Thorvaldsson *et al.*, 1991). It can easily be confused with sigma phase with a chemistry of approximately Fe-35Cr-3Ni-34Mo wt.% (ideally $Fe_7Mo_{13}N_4$).

7.2.8 Low temperature ageing

Iron–chromium ferritic solid solutions have a tendency to show the clustering of atoms, rather than a random distribution. The clustering manifests at low temperatures since at elevated temperatures, entropy effects tend to randomise the solution. There are severe embrittling effects which occur as a consequence during prolonged low temperature ageing, at temperatures in the vicinity of 430-470 °C. A chromium rich α' "phase" precipitates on a very fine scale, probably by a mechanism involving spinodal decomposition. These effects are not explored in the present work, but could be quite important if duplex and super duplex alloys are used in the appropriate service conditions (Strangwood and Druce, 1990).

7.3 Thermodynamic calculations

The purpose here was to investigate the carbide and sigma phases using the MTDATA package for super duplex weld metal A219 (Table 5.1). Figure 7.3 shows the calculated phase diagram of the alloy. In addition to δ-ferrite and austenite, sigma phase and $M_{23}C_6$ also precipitate. Note that other carbides (M_7C_3 and M_2C) were also included in the analysis but do not form in the equilibrium state.

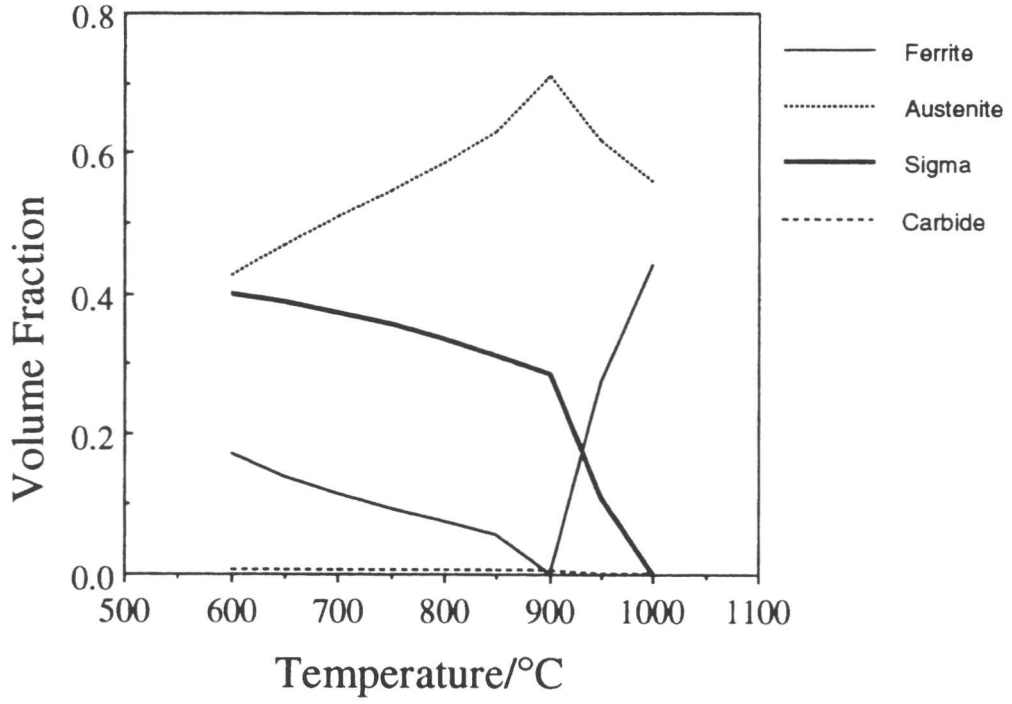

Figure 7.3. The equilibrium phase fractions for super duplex weld metal A219.

7.3.1 Discussion

The above calculations are in good agreement with literature data which indicate the only important precipitation in duplex and super duplex stainless steels in temperature range 600-1000 °C is sigma-phase and $M_{23}C_6$, although the maximum volume fraction of the latter phase is only about 0.006, negligible when compared with sigma phase. This is because new duplex and super duplex alloys contain little carbon (less than 0.03 wt.%). Further calculations therefore neglect any phases other than δ, γ and σ.

7.3.2 Calculations assuming only δ, γ and σ exist

Thermodynamic calculations have been done for duplex and super duplex

alloys IC381, IC373, UNS31, ZERON100 and A219 (Table 5.1) in the temperature range of 600-1000 °C. the results are presented in Figure 7.4. Figure 7.4a shows the equilibrium precipitation of sigma-phase in an ordinary duplex stainless steel IC381. The sigma-phase begins to precipitate at 865 °C and its volume fraction increases as the temperature drops. At about 680 °C its equilibrium volume fraction reaches a maximum of about 0.18. At temperatures below 680 °C the austenite should transform to ferrite.

Figure 7.4b shows that the σ_s temperature is much higher for alloy IC373 which has been overalloyed with Cr compared with TIC381. The sigma-phase volume fraction is also much higher (its maximum is about 0.32 at 680 °C). In the duplex weld metal UNS31 as Mo and Cr are lower in concentration compared with IC381 σ_s is lowered to 820 °C with correspondingly smaller volume fraction. Super duplex alloy ZERON100 (Figure 7.4d) contains a larger Cr and Mo content compared with TIC381 leading to a higher σ_s temperature and volume fraction. The interesting result is that the calculated phase diagram for super duplex weld metal A219, shows the highest σ_s temperature (about 990 °C). However, due to its higher Ni content the volume fraction of σ-phase is smaller than in ZERON100. With large Ni concentrations (UNS31 and A219) ferrite does not form at low temperatures at all until σ precipitation is completed. Consequently there is no δ-ferrite phase available to decompose to austenite plus sigma. Hence, the calculated fraction of sigma-phase is in such alloys always rather small.

7.3.3 Partitioning

Sigma-phase is a brittle phase rich in chromium, and in the alloys such as A219, exists in equilibrium with austenite for temperatures below 990 °C. Figures 7.5 to 7.7 show the expected equilibrium partitioning of Cr, Mo and Ni respectively between austenite and sigma over temperature range of 600-990 °C. It is interesting that the Cr concentration in sigma-phase is about twice that in austenite with the partitioning becoming more pronounced at lower temperatures.

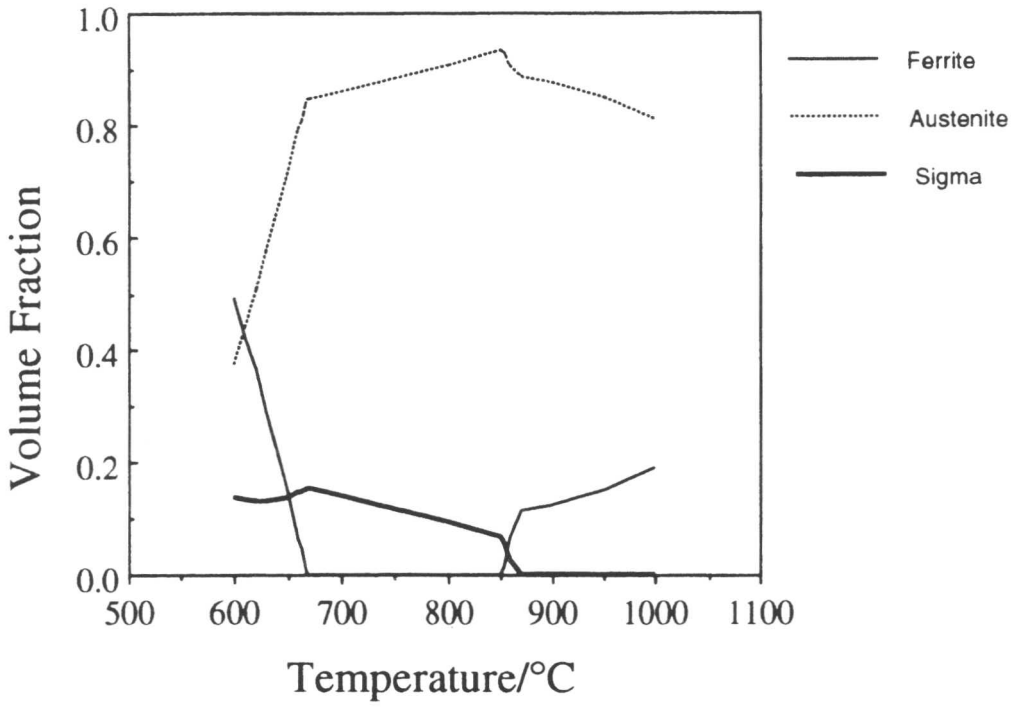

(a)

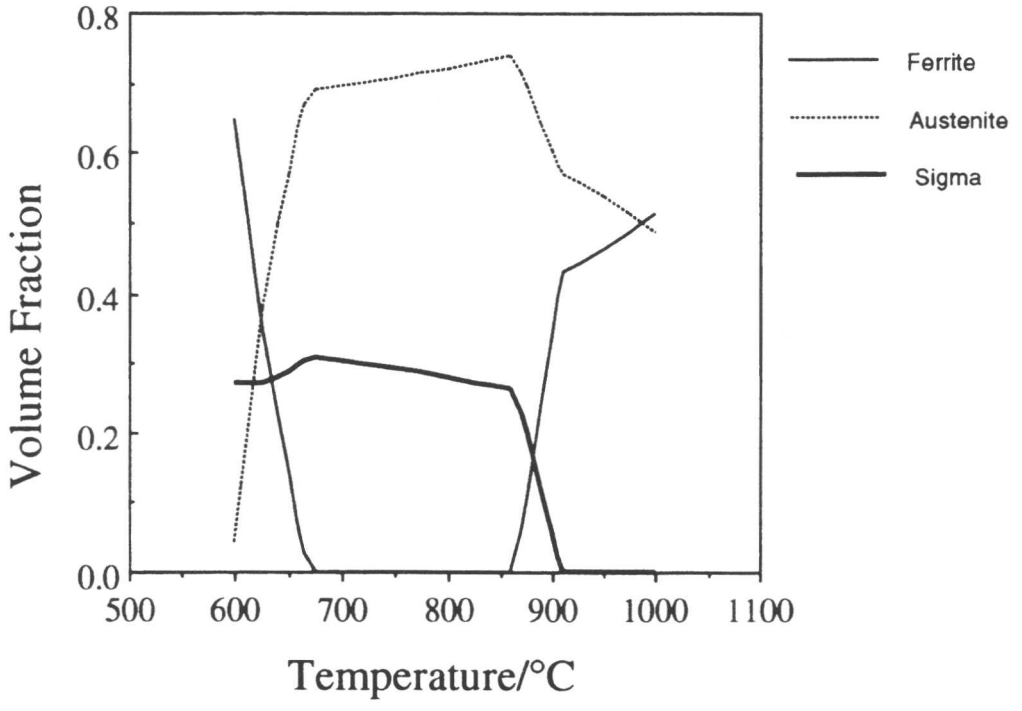

(b)

Figure 7.4. The calculated equilibrium phase fractions. a) duplex stainless steel IC381; b) overalloyed with Cr, IC373; c) duplex weld metal UNS31; d) super duplex stainless steel ZERON100; e) super duplex weld metal A219.

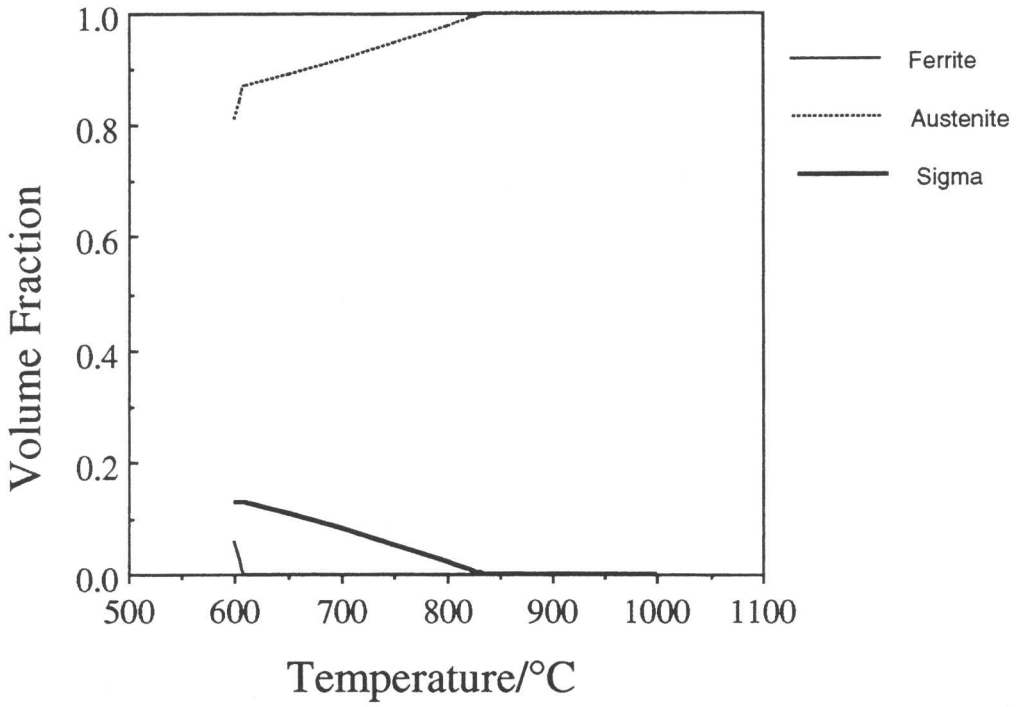

(c)

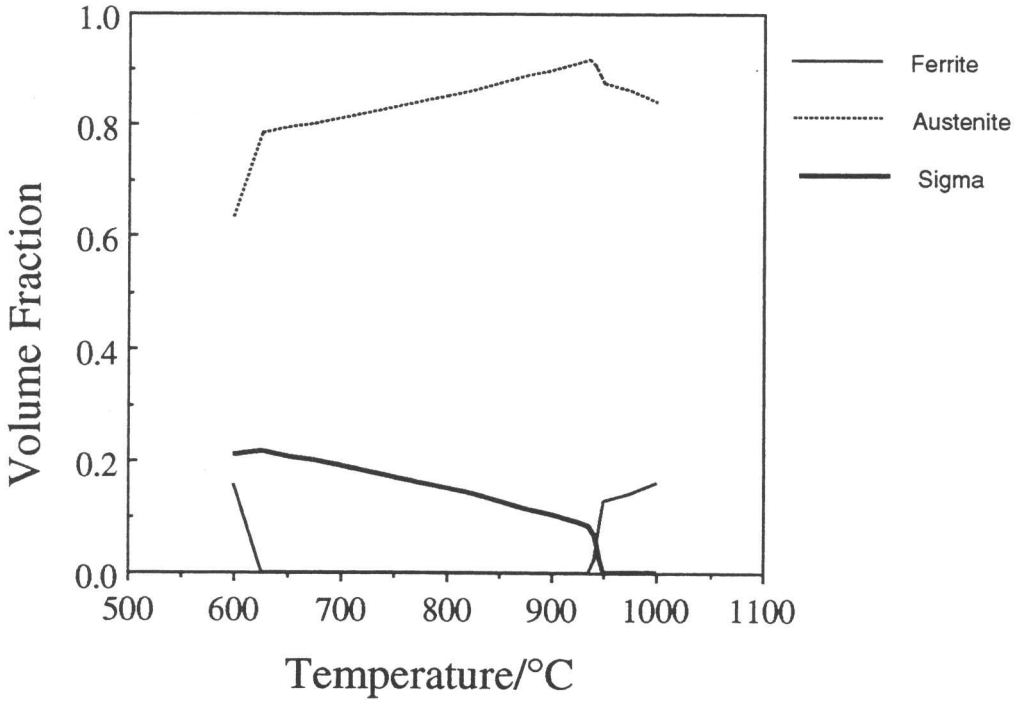

(d)

Figure 7.4. (Continued)

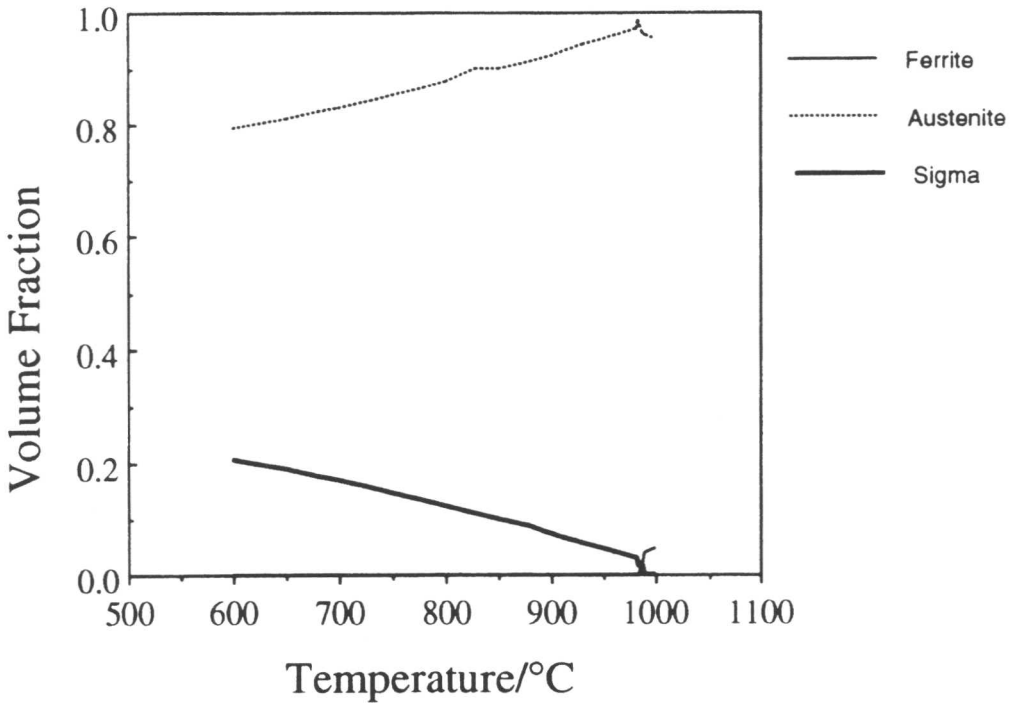

(e)

Figure 7.4. (Continued)

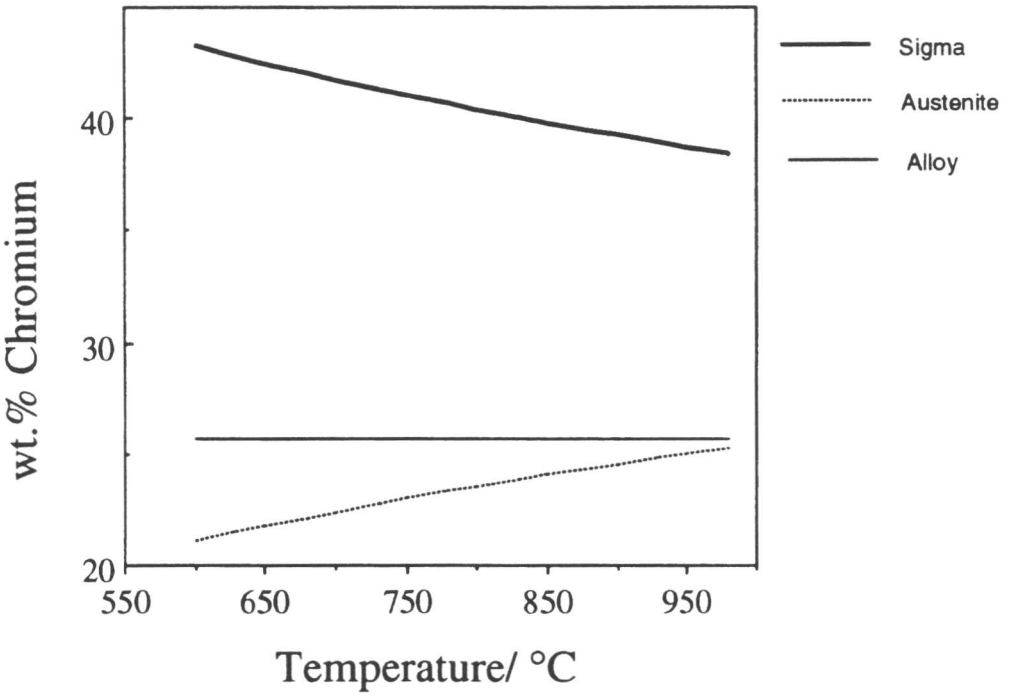

Figure 7.5. The calculated equilibrium partitioning of chromium between sigma phase and austenite in super duplex weld metal A219.

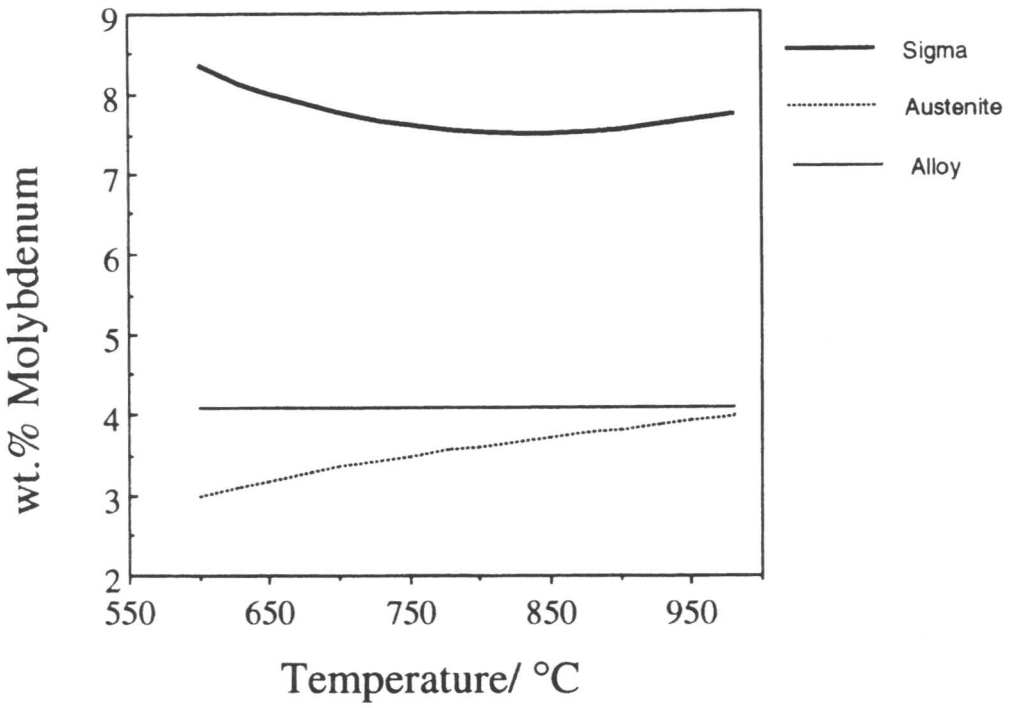

Figure 7.6. The calculated equilibrium partitioning of molybdenum between sigma phase and austenite in super duplex weld metal A219.

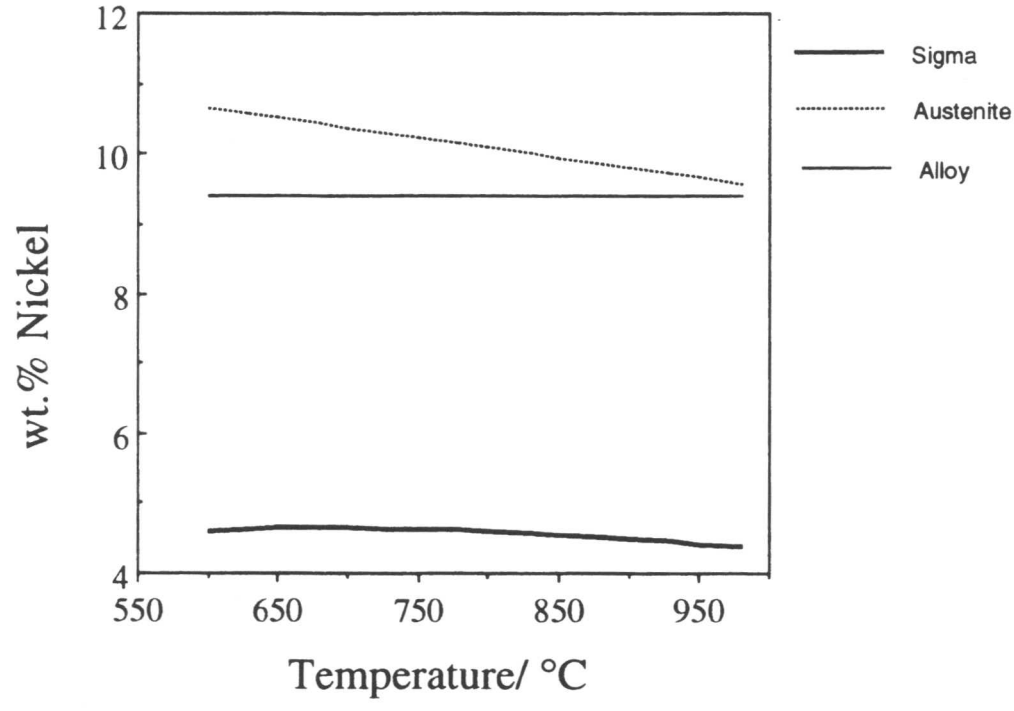

Figure 7.7. The calculated equilibrium partitioning of nickel between sigma phase and austenite in super duplex weld metal A219.

7.8.4 The equilibrium sigma-start temperature

The previous work has shown that most of the elements which are ferrite formers (for example Cr and Mo), also promote sigma-phase formation and widen the temperature range where sigma phase is stable. The calculations show that as the Cr_{eq} increases, so does the equilibrium σ_s temperature (Figure 7.8).

There is a strong effect of Mo on the precipitation of sigma-phase (Figure 7.9), the correlation of the σ_s temperature against Mo content being better than against the Cr_{eq}. These results lead to the conclusion that although the Cr_{eq} of the alloy is important in determining the precipitation of sigma phase (specially on the volume fraction of the phase), but the most important factor on this precipitation is the Mo content of the alloy (specially on the temperature range where the sigma-phase is thermodynamically stable).

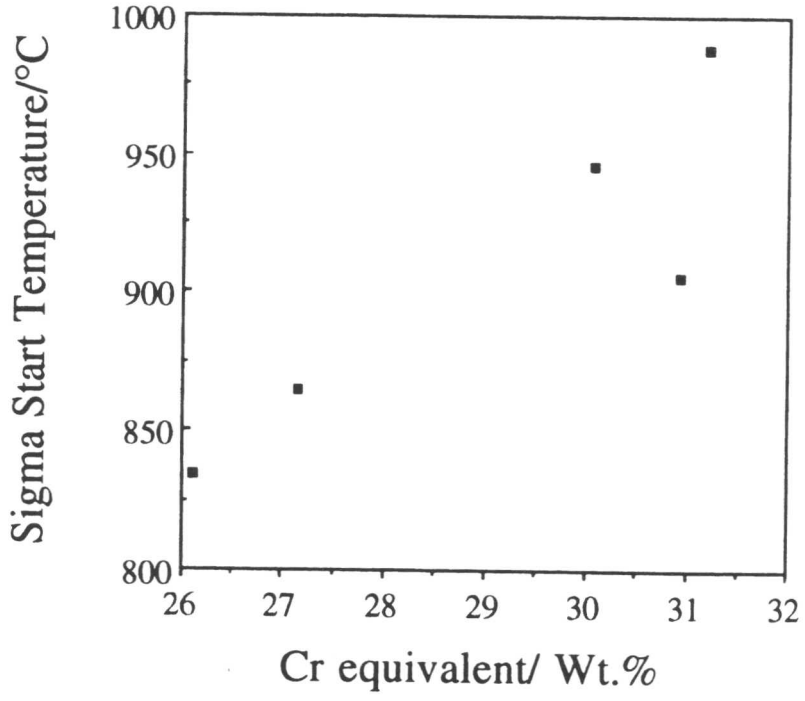

Figure 7.8. The calculated equilibrium sigma start temperature against Cr_{eq} of the different duplex and super duplex stainless steel alloys as listed in Table 5.1. The chromium equivalents are calculated according to Hammar and Svensson (1979).

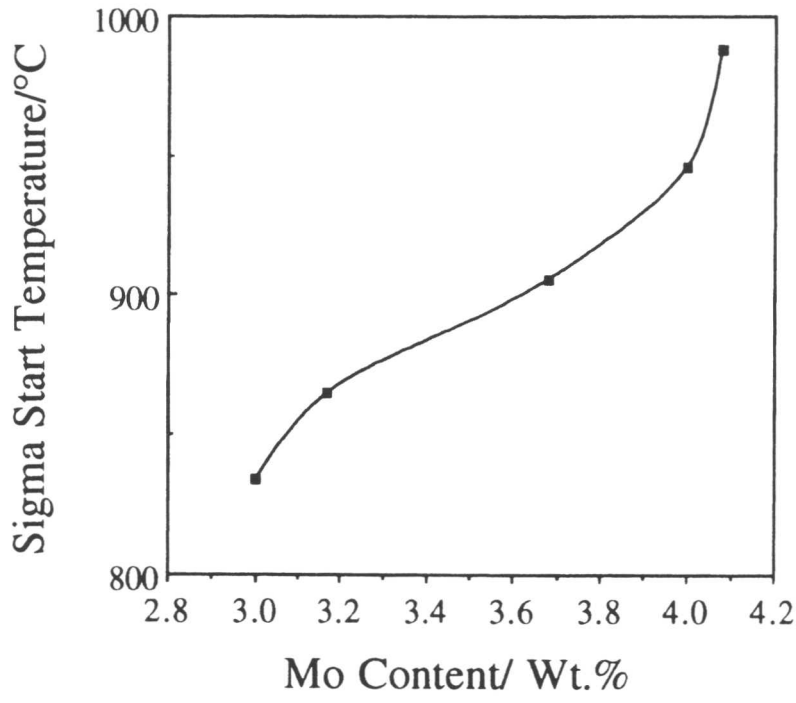

Figure 7.9. The calculated equilibrium sigma start temperature against Mo content of the different duplex and super duplex stainless steel alloys as listed in Table 5.1.

7.4 Isothermal aging Heat Treatments

To construct the TTT diagrams for sigma phase precipitation in super duplex stainless steel alloy A219, specimens were isothermally heat treated in the range 600-1100 °C. To prevent oxidation and decarburisation, they were sealed in silica tubes under partial pressure of argon (about 100 mm Hg). An electric furnace with an even temperature distribution was used for the heat treatments with an accuracy of ±5 °C. After an appropriate time interval, the specimens in their capsules were dropped into and broken under water. Sigma phase formation causes a sharp increase in the hardness (Table 7.2).

The Vickers hardness number (VHN) of the as-received material is 293. Figure 7.10 shows the hardness of specimens aged for 2 hours at different temperatures. The hardness peaks at about 850 °C, indicating that the amount of sigma phase formed at this temperature is a maximum compared with other

ageing temperatures. Up to 30 vol% of σ- phase was observed in specimens aged at 900 and 800 °C.

Table 7.2. Vickers hardness for aged specimens of super duplex stainless steel weld metal A219 (see Table 5.1 for chemical compositions and Table 2.2 for welding conditions).

Temp°C	1 min	5 min	10 min	.5 hr	1 hr	2 hr	4 hr	8 hr	16 hr
1100	291	293	287	292	287	283	285	285	282
1000	298	301	318	320	360	360	366	366	382
900	278	314	341	345	398	411	433	415	389
800	294	306	323	332	400	397	385	418	384
700	292	291	291	294	296	342	356	362	392
600	288	291	286	295	294	293	309	314	305

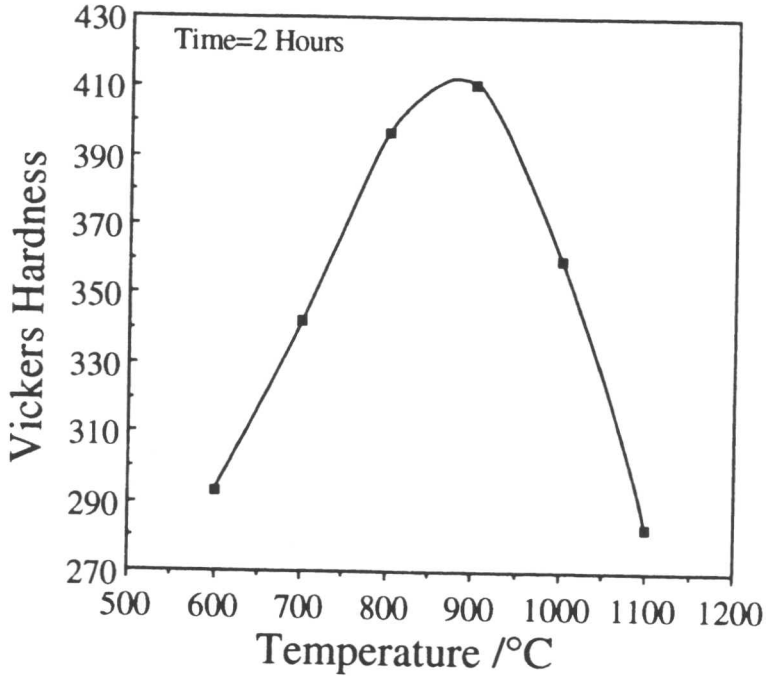

Figure 7.10. Vickers hardness of specimens of weld metal A219 (see Table 5.1 for composition and Table 2.2 for welding conditions) aged for two hours at each temperatures.

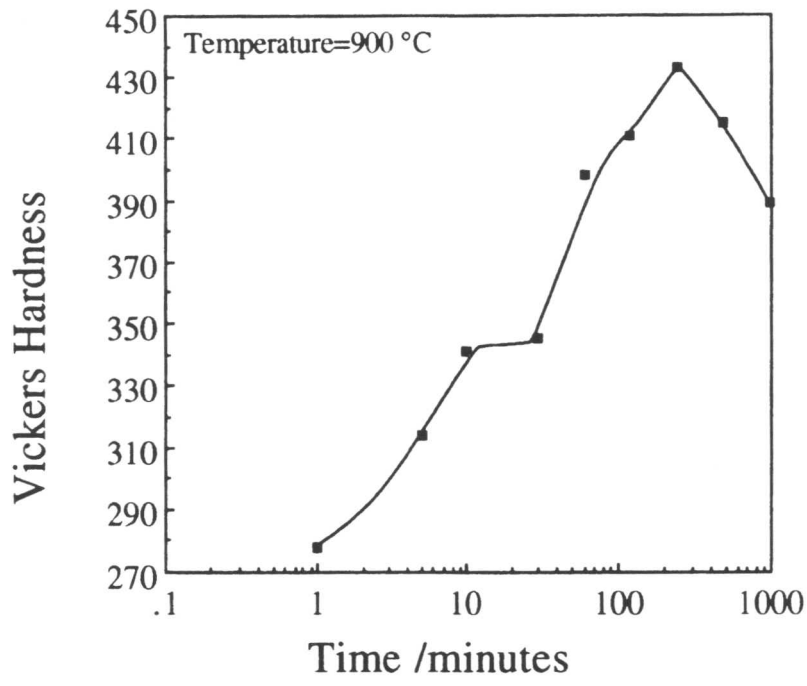

Figure 7.11. Hardness of weld metal A219 (see Table 5.1 for composition and Table 2.2 for welding conditions) aged at 900 °C for different times.

Figure 7.11 shows the hardness of specimens aged at 900 °C, as a function of ageing time. The hardness peaks at 433 VHN after four hours of aging. Metallography indicates that the fraction of sigma almost does not increase beyond an ageing time of four hours, but the precipitates coarsen with continued ageing. However, the drop of hardness probably was more to do with the fact that almost all of ferrite transformed into softer austenite.

7.5 Microstructural Observations

Optical, SEM, TEM electron diffraction and EDX analysis were used to characterise the aged specimens. Sigma phase was not found for the specimens aged at or below 600 °C and above 1050 °C. The different phases were identified by their electron diffraction patterns and also by EDX analysis on SEM or TEM. The volume fraction of sigma phase was measured both by point counting and image analysis techniques. Figure 7.12 is an optical micrograph showing the microstructure of super duplex stainless steel alloy A219 aged at 600 °C for 16 hours. The phases in this specimen were identified by TEM EDX microanalysis (Table 7.3) and TEM SADP. From this information it was found out that the light etching phase is austenite and the dark one is ferrite. Although the speci-

men has been aged at this temperature for a long time but there is still no sign of sigma phase precipitation.

The sigma phase volume fraction was found to be more than 0.01 in the specimens aged at 700 °C whenever the ageing time was more than 10 minutes. Figure 7.13 shows the microstructure of the alloy aged at 700 °C for 10 minutes. The fraction of sigma is estimated to be less than 0.01. Very fine particles of sigma phase precipitated on δ/γ grain boundaries. At 800 °C sigma phase was found to form more rapidly (Figure 7.14). With increasing ageing time, sigma phase was observed to grow inside the δ-ferrite grains (Figure 7.15). Figures 7.16 to 7.18 show the microstructures of specimens aged at 900 °C for 1, 5 and 10 minutes respectively. As sigma phase grows inside ferrite the surrounding area becomes depleted of Cr and Mo, and hence unstable with respect to austenite formation. These new austenite particles have a very fine Widmanstätten morphology (Figure 7.17). Table 7.4 shows the TEM EDX results for specimen aged at 900 °C for 5 minutes. As the ageing time increases, so does the sigma fraction until almost all ferrite decomposes to sigma plus austenite (Figure 7.20). Figure 7.19 shows that the decomposition of ferrite is slower at 1000 °C compared with at 900 °C. However after a long aging time (16 hours) again all ferrite transformed to sigma plus austenite at this temperature (Figure 7.20).

Table 7.3. TEM EDX microanalysis of the ferrite and austenite phases in super duplex weld metal A219 aged at 600 °C for 16 hours (all concentrations are in wt.%).

Phase	Fe	Cr	Ni	Mo	Mn	Si
Ferrite	57.7±0.3	28.5±0.7	7.9±0.6	4.9±0.3	0.4±0.1	0.5±0.1
Austenite	58.4±0.5	24.9±0.2	10.1±0.2	3.2±0.1	0.4±0.1	1.0±0.1

For short ageing times, sigma phase was observed to precipitate mostly at the austenite/ferrite grain boundaries and then grow into the ferrite grains. As the fraction of sigma phase increased (to values greater than $\simeq 0.2$) at the

and the remainder is austenite.

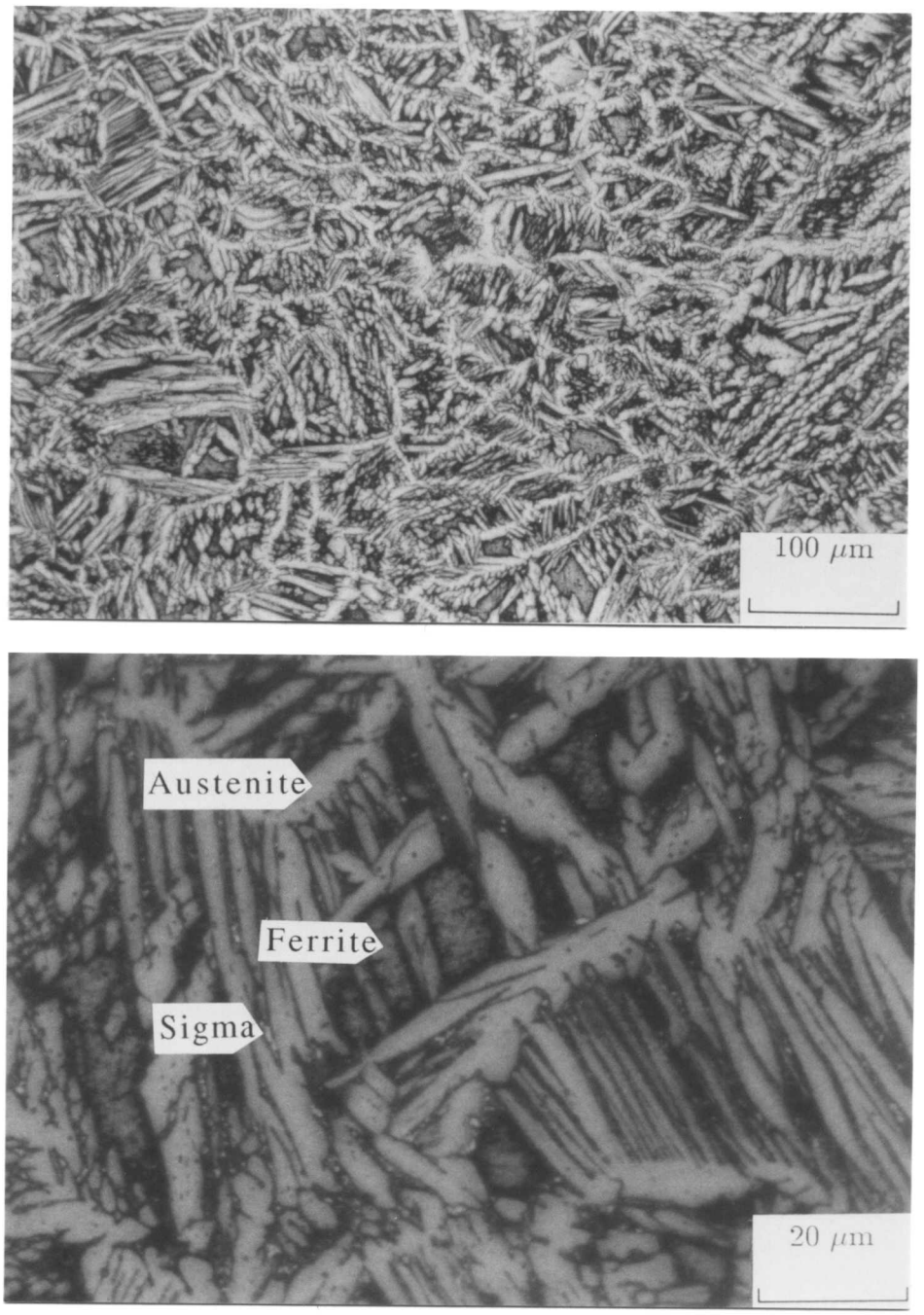

Figure 7.13. The microstructure of super duplex stainless steel A219 aged at 700 °C for 10 minutes. Note the bright fine sigma precipitations mostly at austenite/ferrite grain boundaries. The sigma fraction is probably less than 0.01.

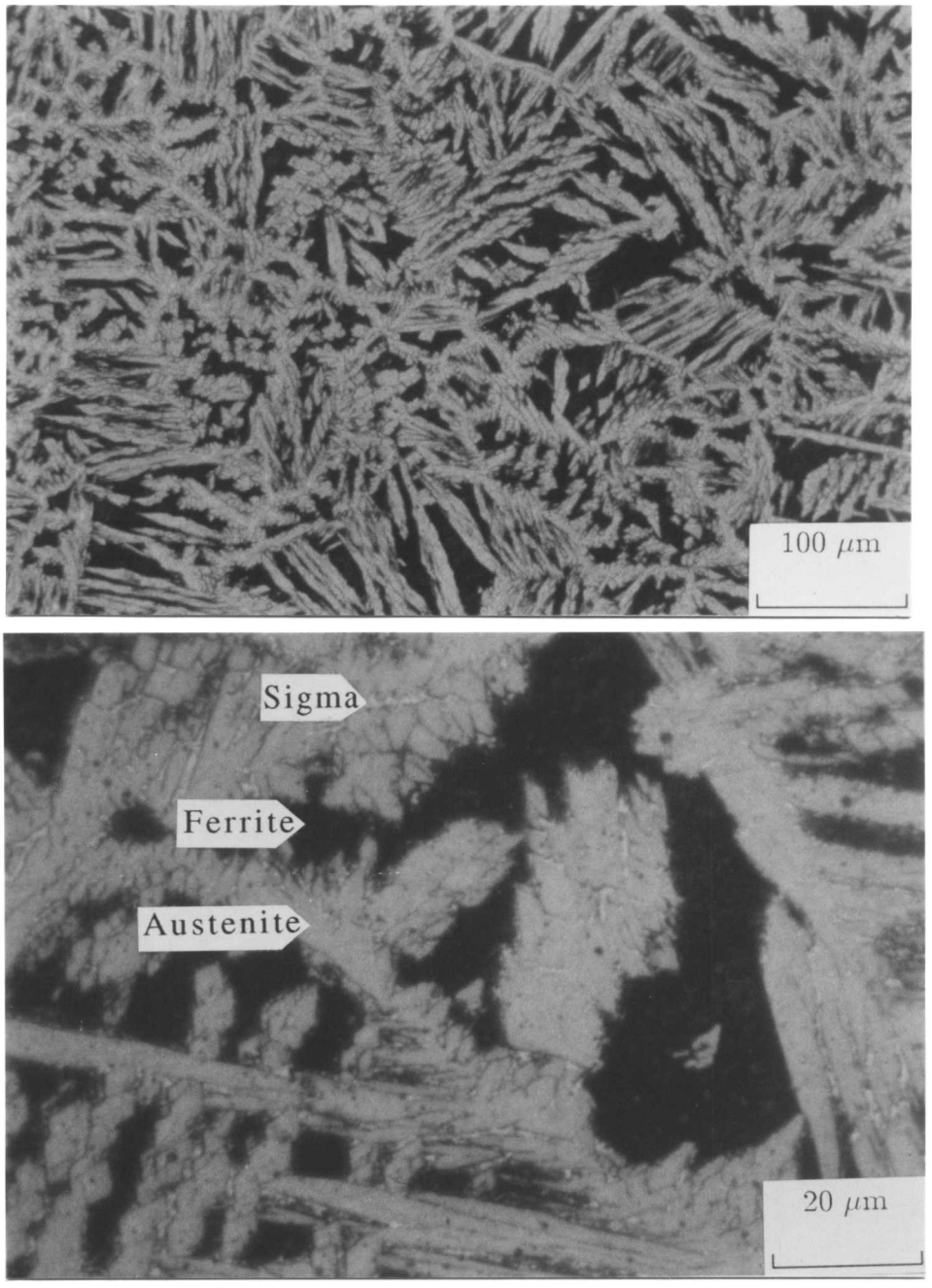

Figure 7.14. The microstructure of super duplex stainless steel A219 aged at 800 °C for 1 minute. Note the bright fine sigma precipitations mostly at austenite/ferrite grain boundaries. The sigma fraction is probably less than 0.01.

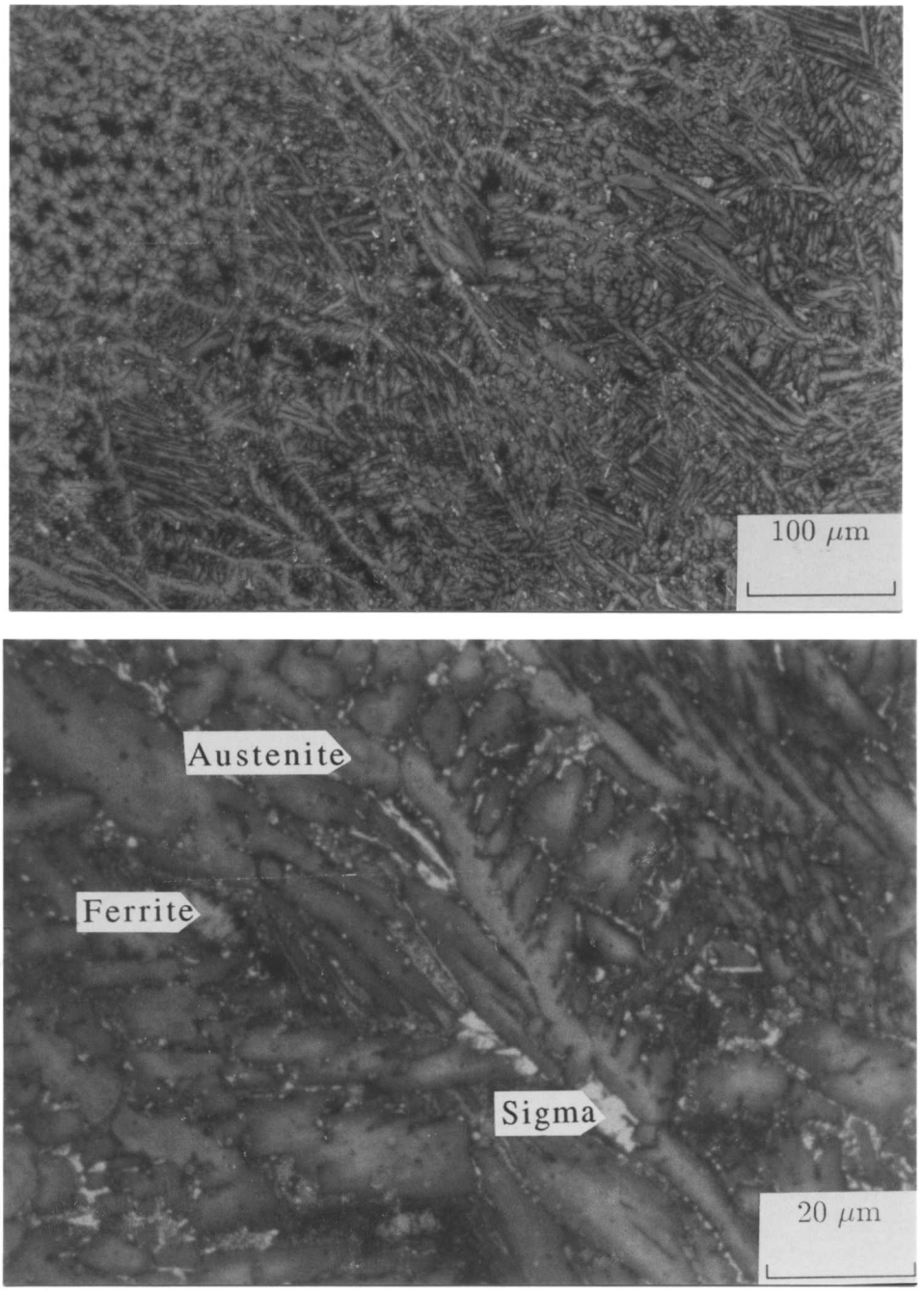

Figure 7.15. The microstructure of super duplex stainless steel A219 aged at 800 °C for 10 minutes. Note the growth of sigma phase inside ferrite grains. The sigma fraction is about 0.08.

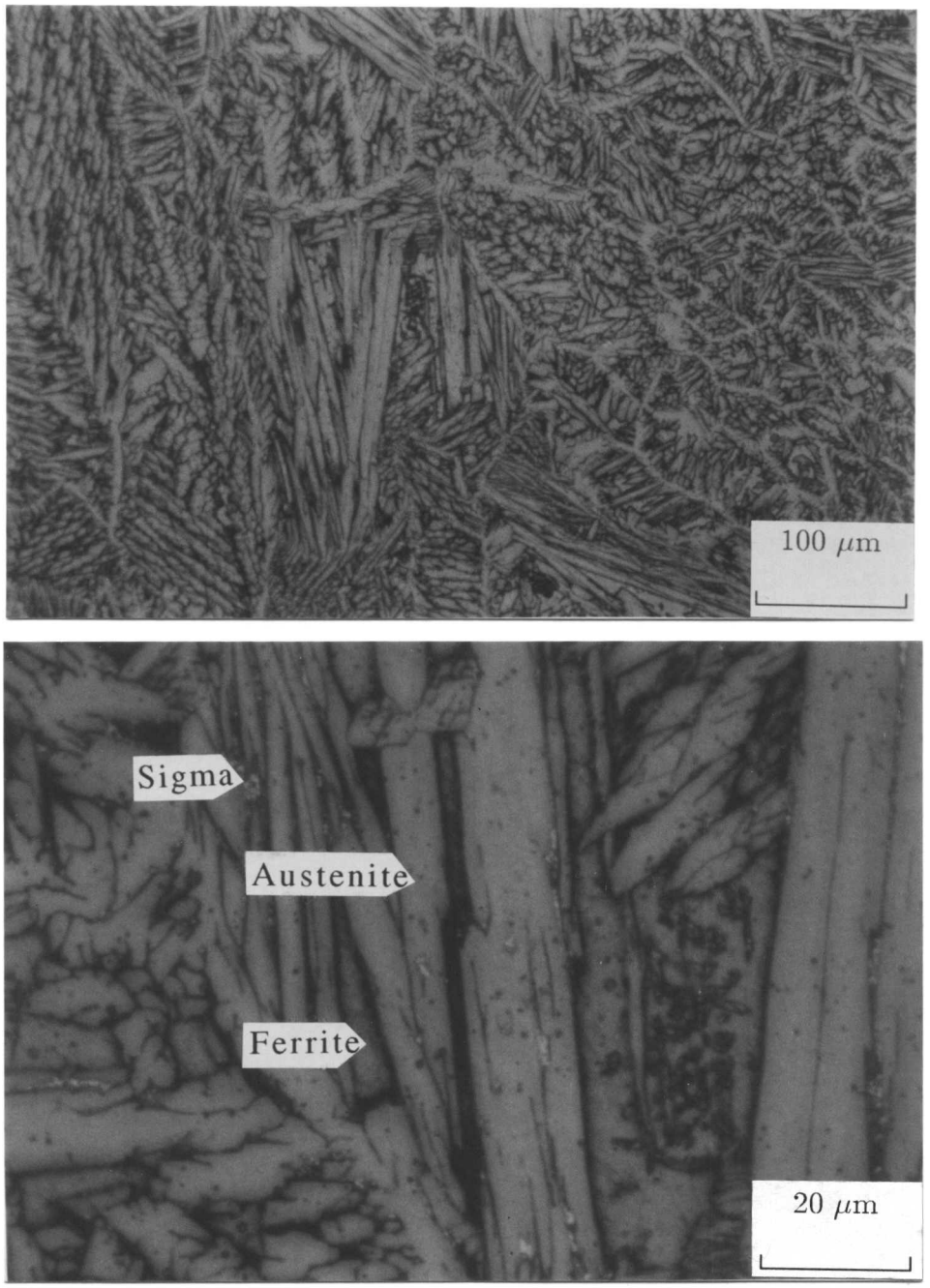

Figure 7.16. The microstructure of super duplex stainless steel A219 aged at 900 °C for 1 minute. The bright phase which has precipitated mainly in grain boundaries is sigma with fraction probably less than 0.01.

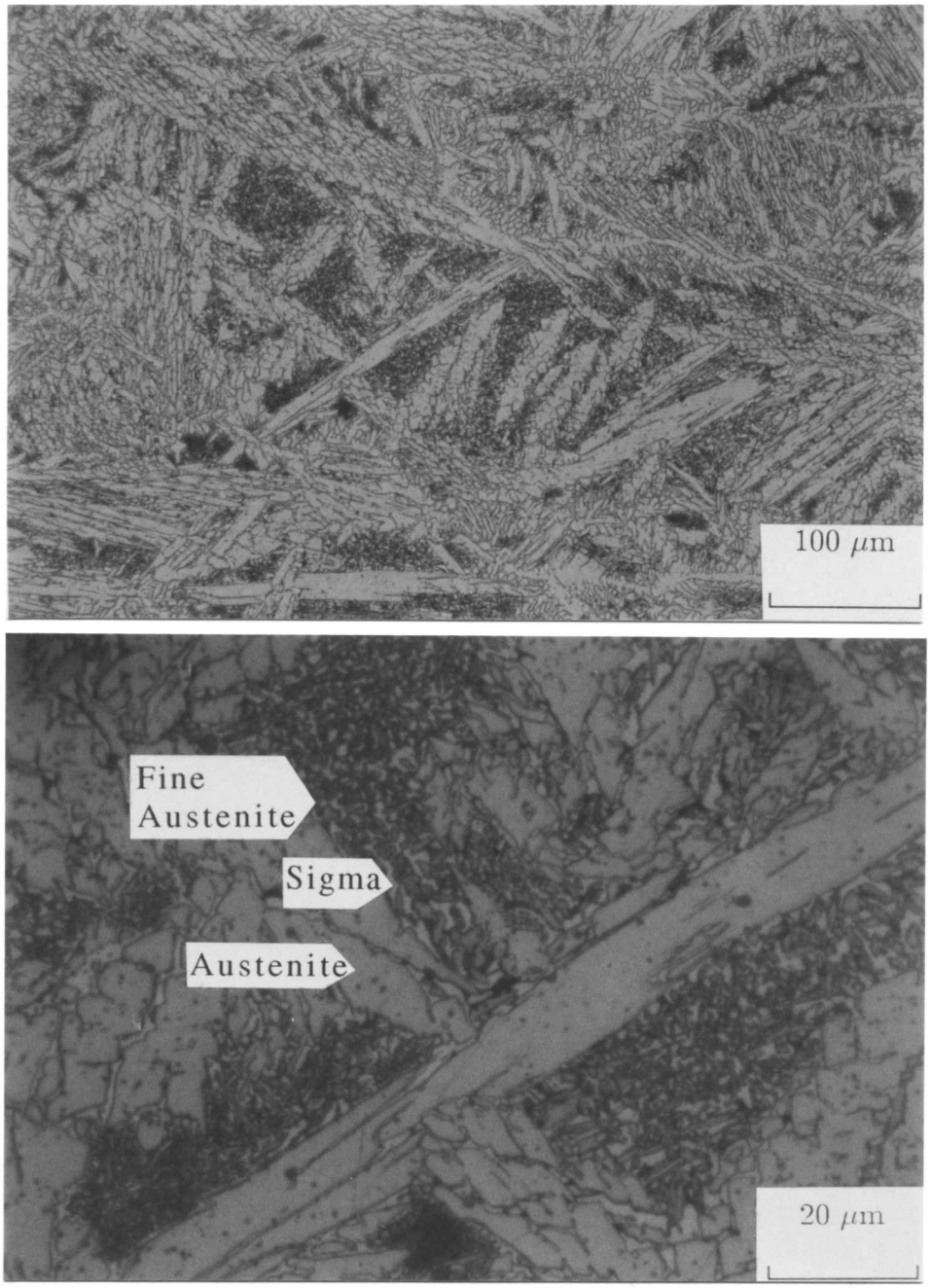

Figure 7.17. The microstructure of super duplex stainless steel A219 aged at 900 °C for 5 minutes. Ferrite grains have decomposed to sigma and austenite. The new austenite has a very fine Widmanstätten morphology. The measured volume fraction of sigma is about 0.07.

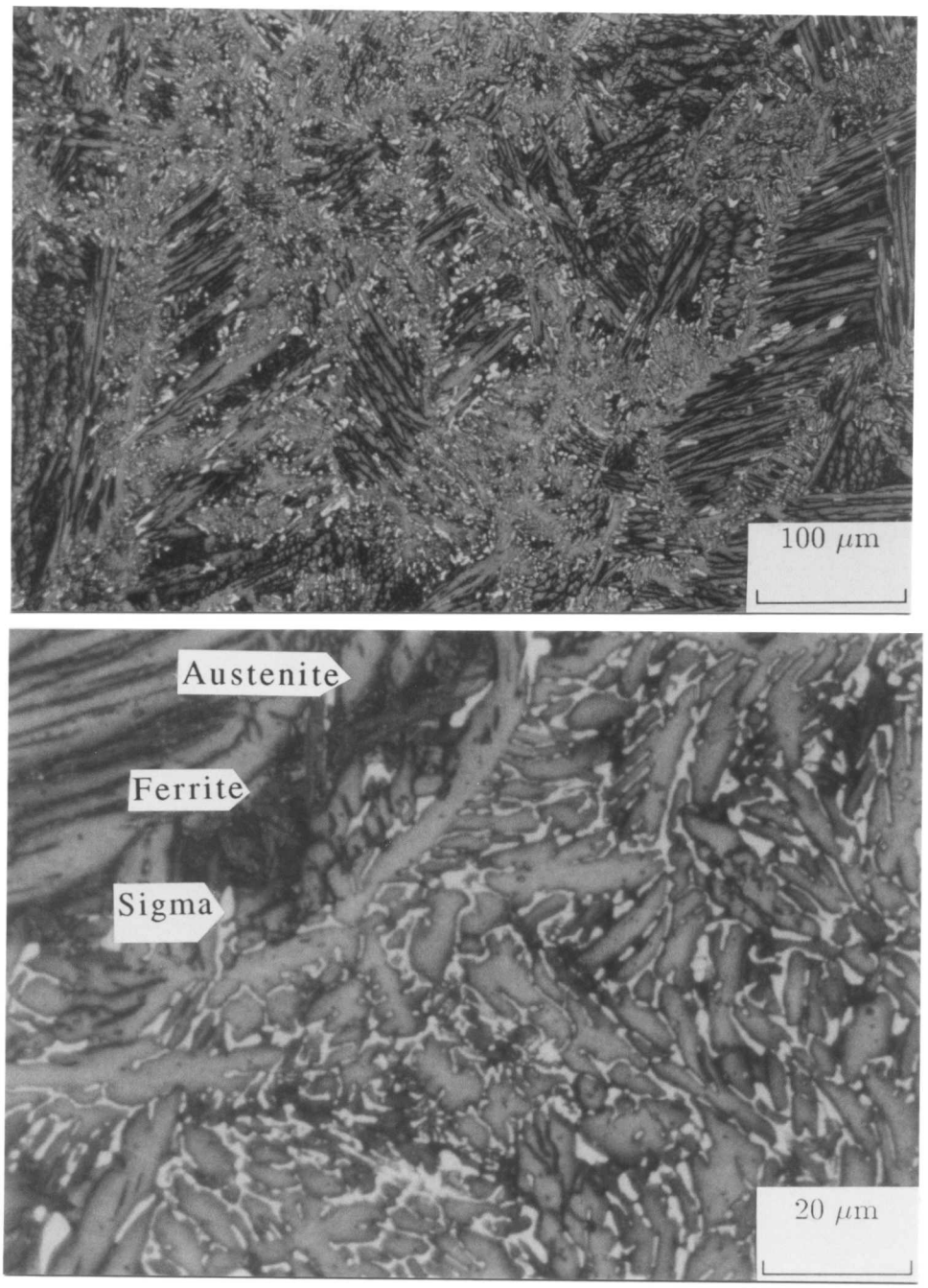

Figure 7.18. The microstructure of super duplex stainless steel A219 aged at 900 °C for 10 minutes. The measured volume fraction of sigma is about 0.21.

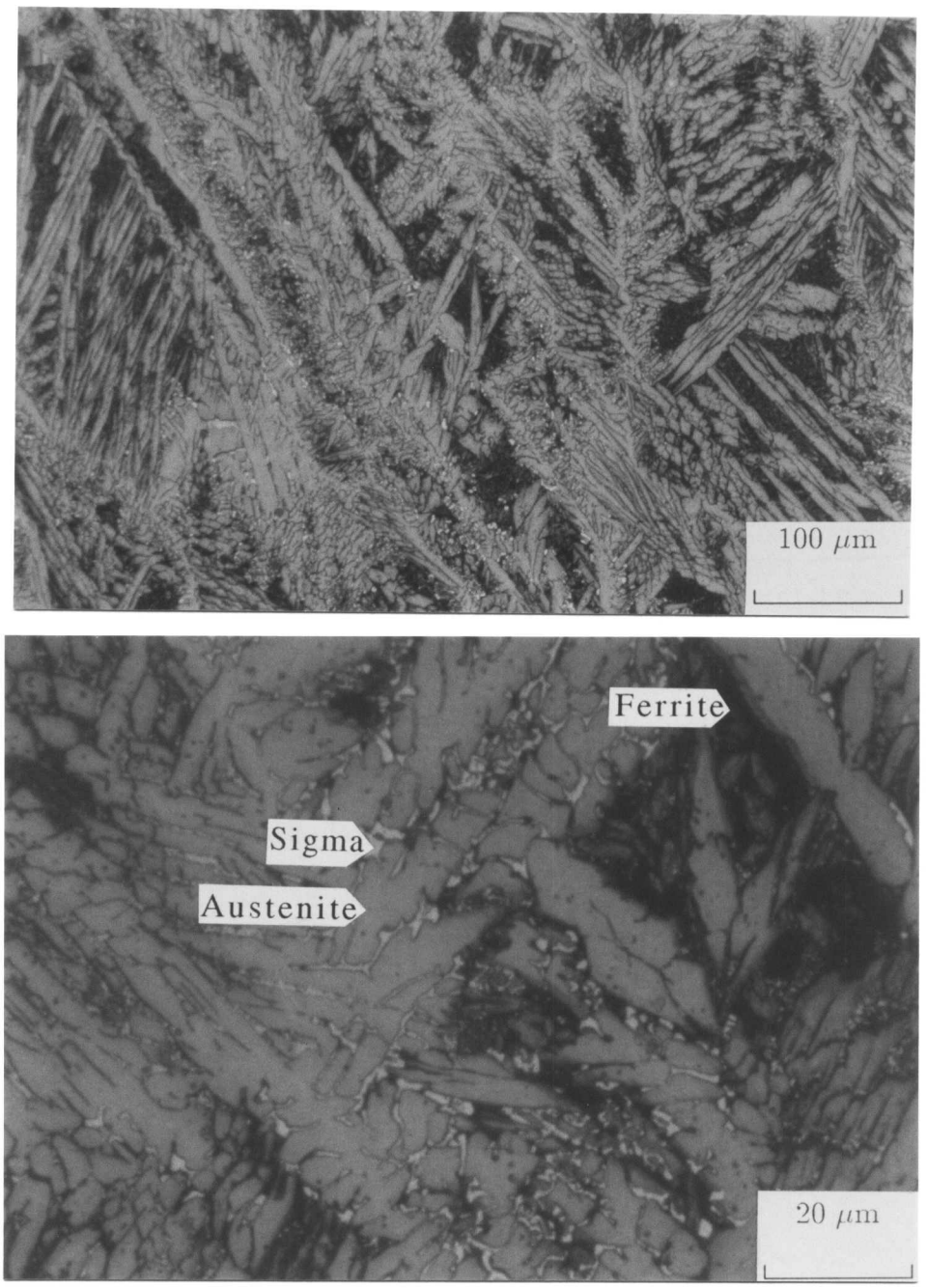

Figure 7.19. The microstructure of super duplex stainless steel A219 aged at 1000 °C for 5 minutes. The measured volume fraction of sigma is about 0.03.

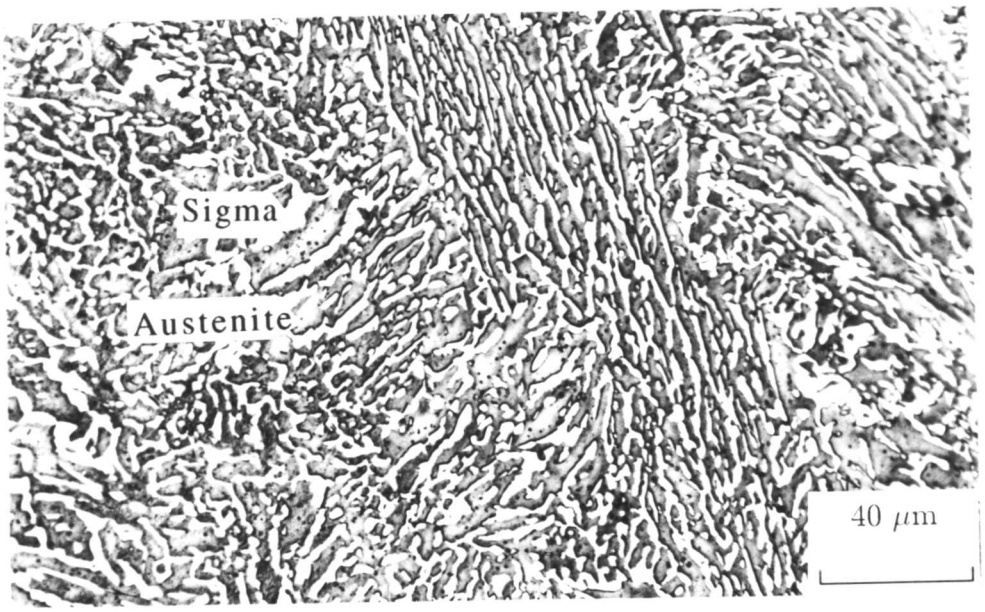

(a)

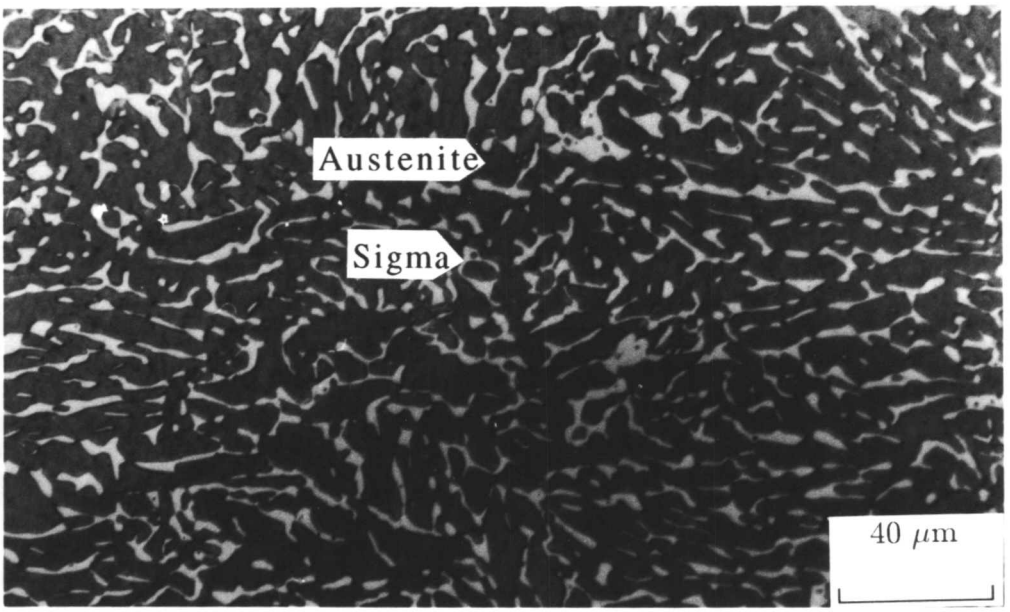

(b)

Figure 7.20. The microstructure of super duplex stainless steel A219 aged for 16 hours a) at 900 °C with about 0.30 volume fraction of sigma b) at 1000 °C with about 0.31 volume fraction of sigma. Sigma phase has become the prominent second phase and there is almost no sign of ferrite.

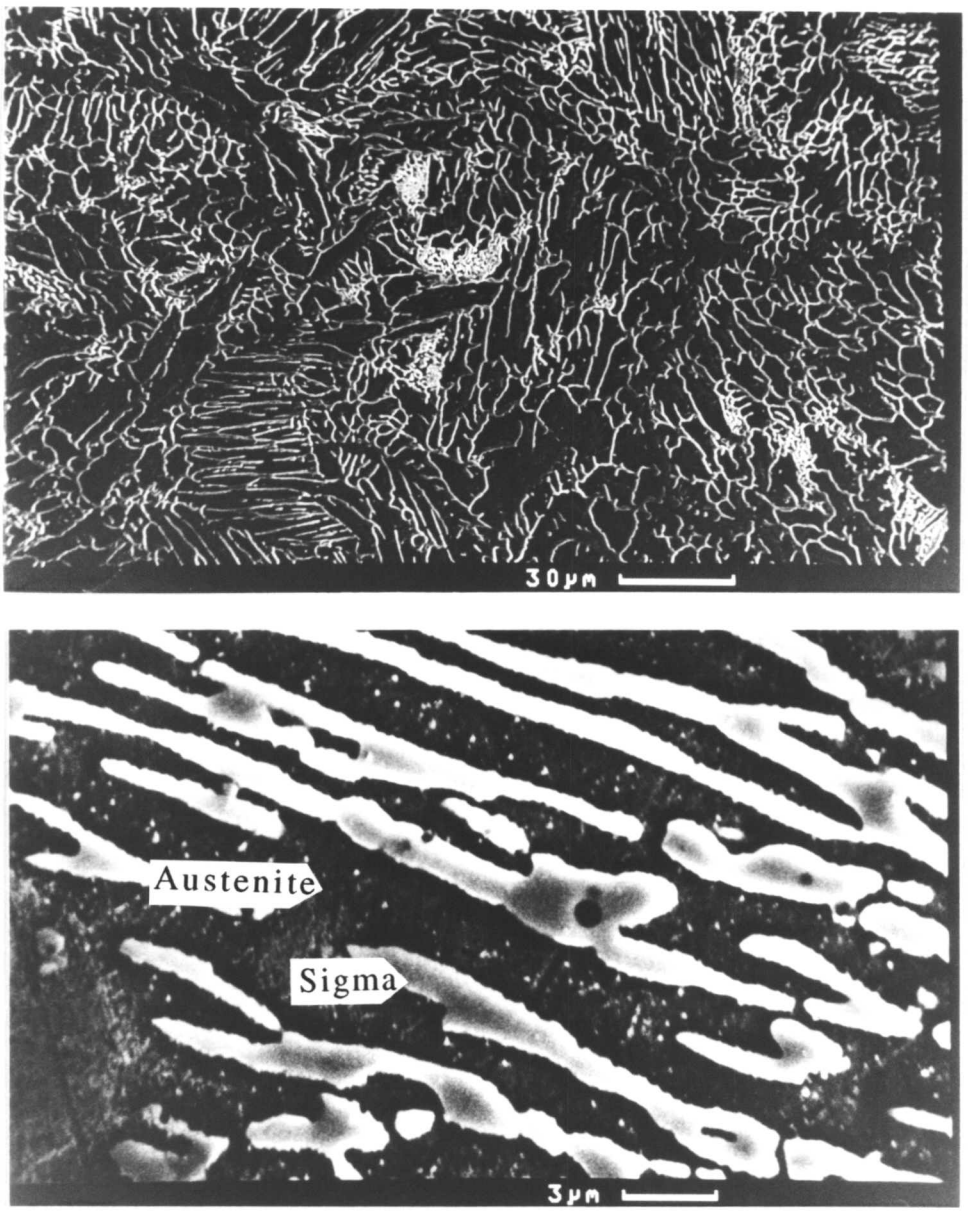

Figure 7.21. SEM micrographs showing the microstructure of super duplex stainless steel A219 aged at 900 °C for four hours. The bright phase is sigma and the dark one is austenite. Note that the sigma phase has almost formed a network.

TEM confirmed that in specimens aged for short time periods in temperature range 700-1050 °C sigma phase precipitated mostly at austenite/ferrite grain boundaries and grew into the ferrite grains. Figure 7.22 shows the microstructure of specimen aged at 900 °C for 5 minutes and Figures 7.23 to 7.25 show the SADP of different phases found in this specimen. In the samples aged for a long time, large volume fractions of sigma phase were found. Correspondingly, the volume fraction of δ-ferrite phase which was about 0.35 in the original weld microstructure, had become very low hardly detectable. It seems that all of the ferrite transformed into sigma plus austenite. Figures 7.26 to 7.31 show the microstructures of the specimens aged for 16 hours.

7.6 Measurement of Sigma Phase Volume Fraction

The volume fractions of sigma phase in different aged specimens were measured both by point counting and image analysis. Light micrographs were used to do these measurements. Table 7.5 shows the results of these measurements.

Table 7.5. Measured volume fraction of sigma phase for different aged specimens of super duplex stainless steel weld metal A219.

Temp°C	1 min	5 min	10 min	.5 hr	1 hr	2 hr	4 hr	8 hr	16 hr
1100	-	-	-	-	-	-	-	-	-
1000	-	0.03	0.04	0.06	0.29	0.22	0.21	0.20	0.25
900	-	0.07	0.21	0.28	0.38	0.36	0.38	0.35	0.30
800	-	0.01	0.08	0.31	0.35	0.32	0.33	0.31	0.31
700	-	-	-	0.01	0.04	0.33	0.35	0.34	0.31
600	-	-	-	-	-	-	-	-	-

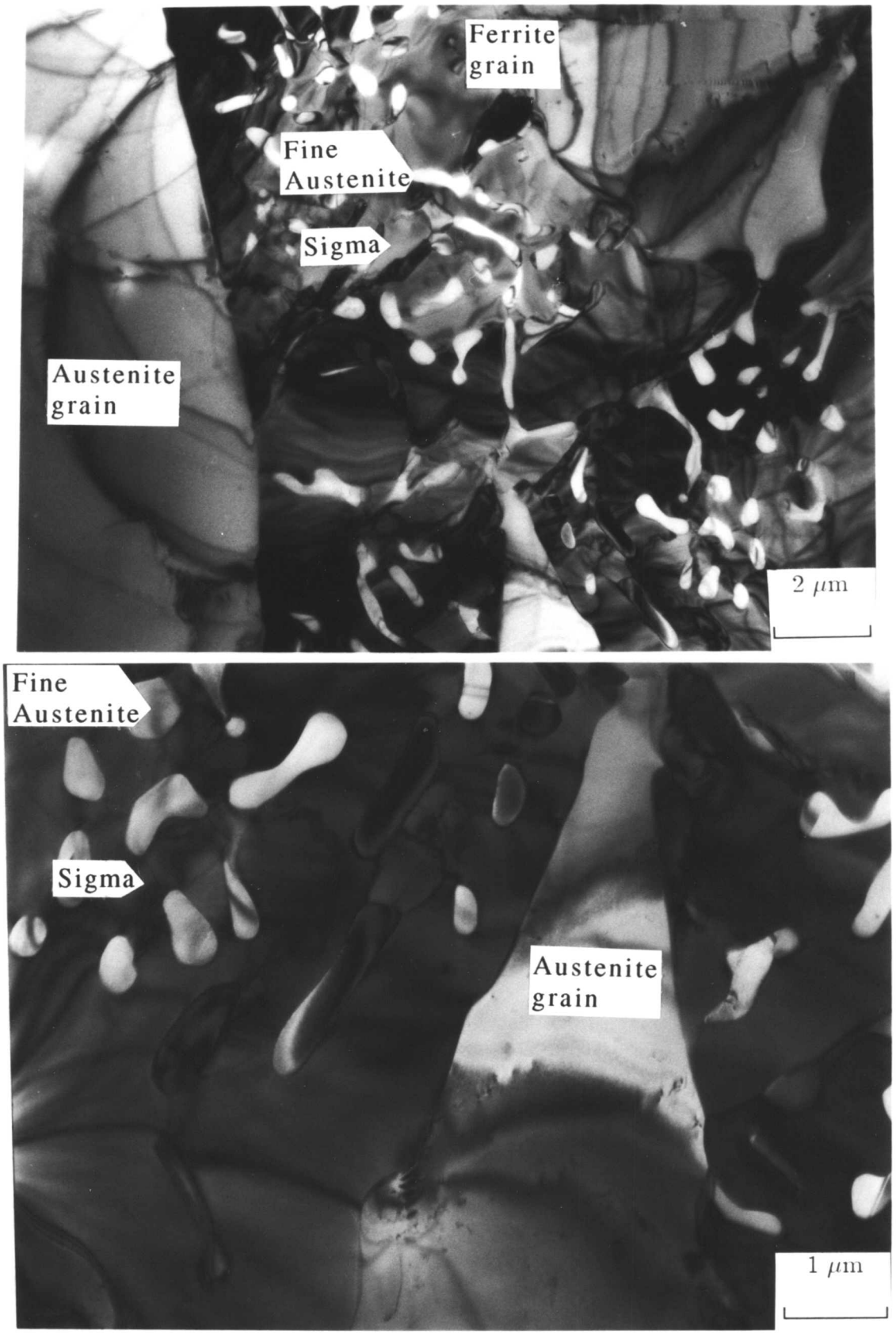

Figure 7.22. Bright field TEM micrographs showing the microstructure of super duplex stainless steel A219 aged at 900 °C for 5 minutes. Ferrite grains have decomposed to sigma plus austenite.

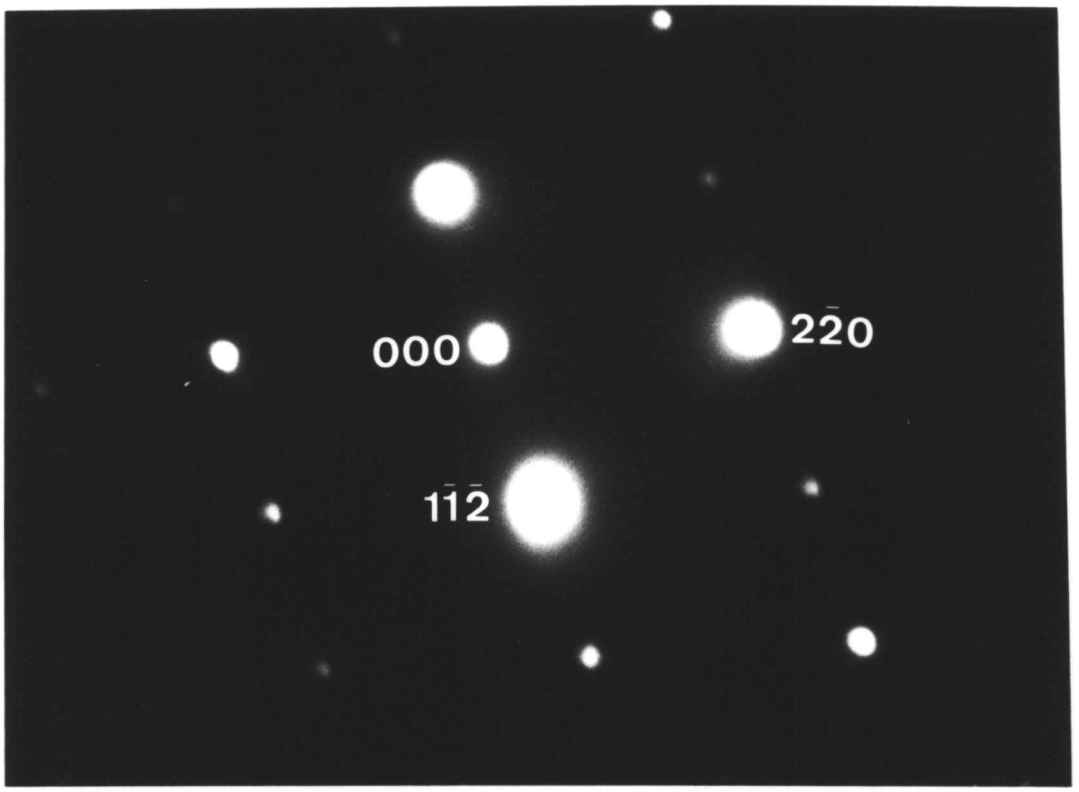

Figure 7.23. Diffraction pattern of the dark phase in figure 7.22 (sigma phase) confirms that it has a b.c.t. crystal structure. The zone axis is [110].

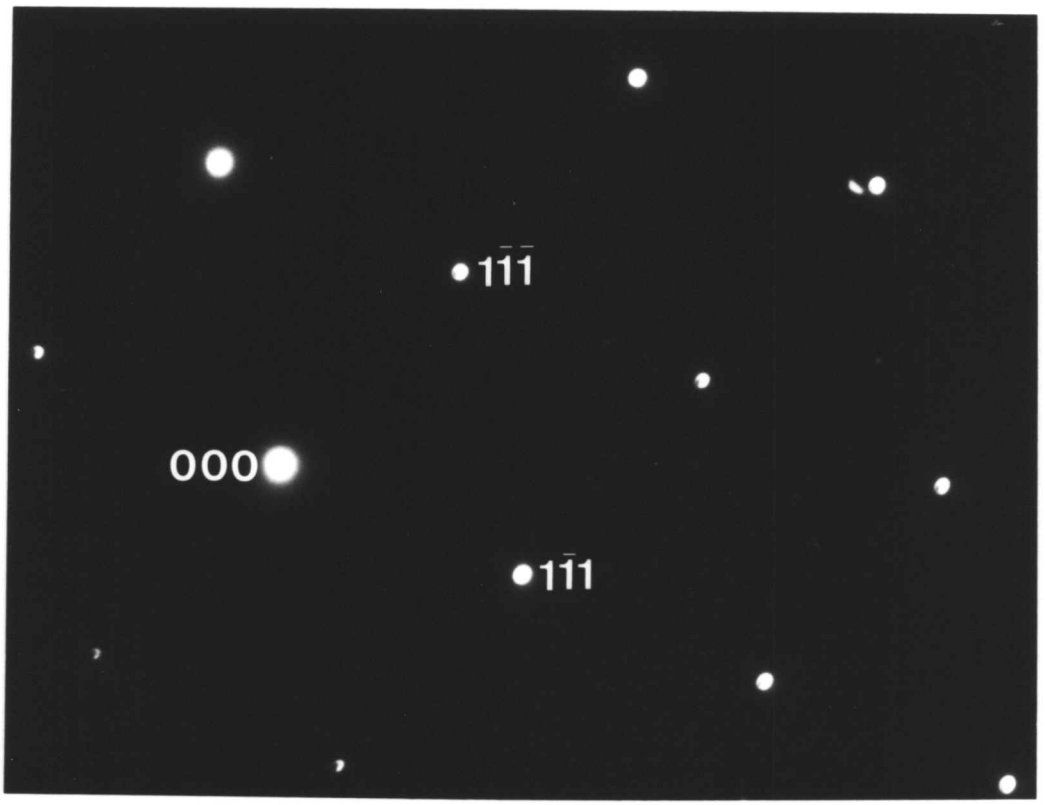

Figure 7.24. Diffraction pattern of the small light particles in figure 7.22 (austenite) confirms that they have a f.c.c. crystal structure. The zone axis is [110].

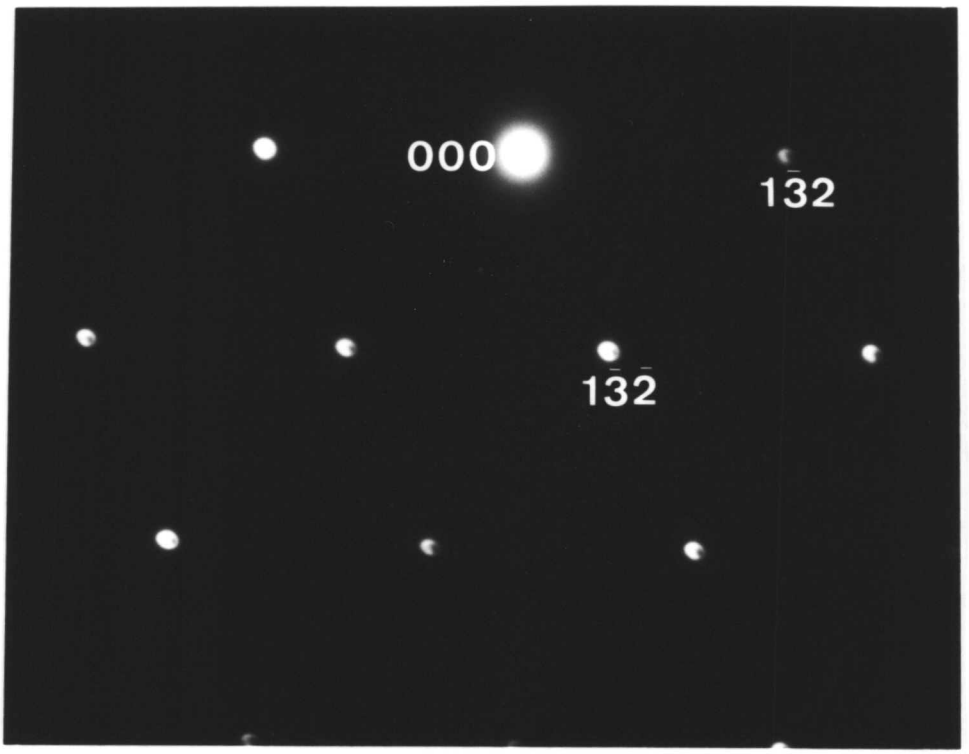

Figure 7.25. Diffraction pattern of the grain point out in figure 7.22 (ferrite) confirms that it has an b.c.c. crystal structure. The zone direction is [310].

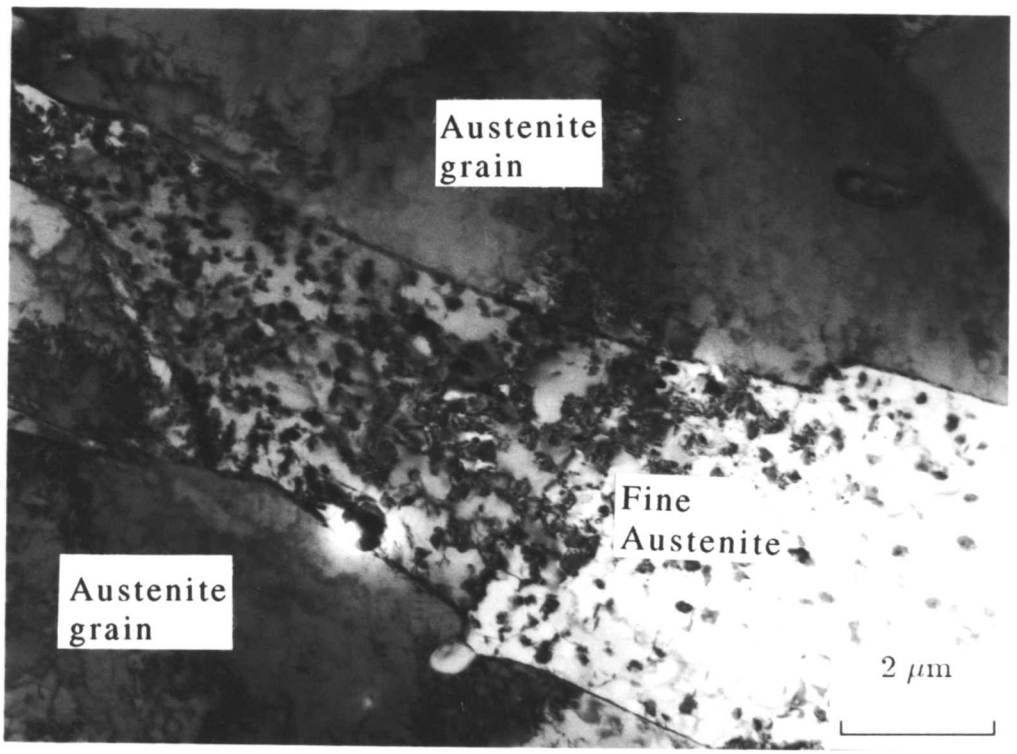

Figure 7.26. Bright field TEM micrograph showing the microstructure of super duplex stainless steel A219 aged at 600 °C for 16 minutes. Note the precipitation of fine austenite particles inside δ-ferrite grain. Microstructure consists of ferrite and austenite and there is no sign of sigma.

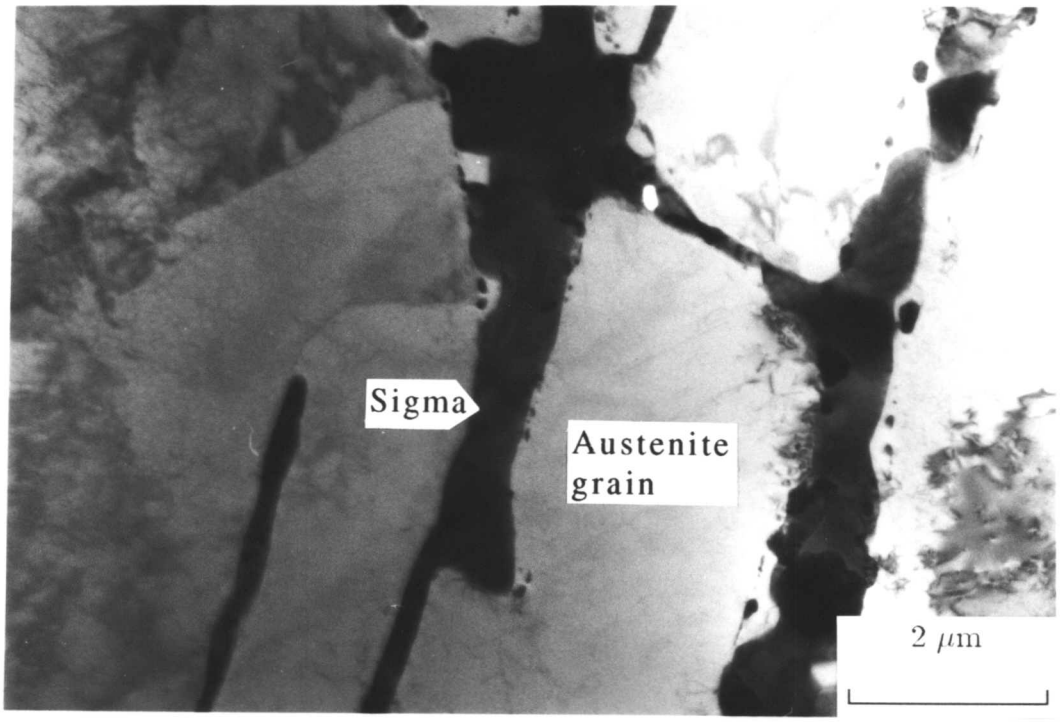

Figure 7.27. Bright field TEM micrograph showing the microstructure of super duplex stainless steel A219 aged at 700 °C for 16 hours. Sigma phase has made a network and there is no sign of ferrite as it has completely decompose to sigma plus austenite. Tables 7.6 and 7.7 show the TEM EDX data of the two phases.

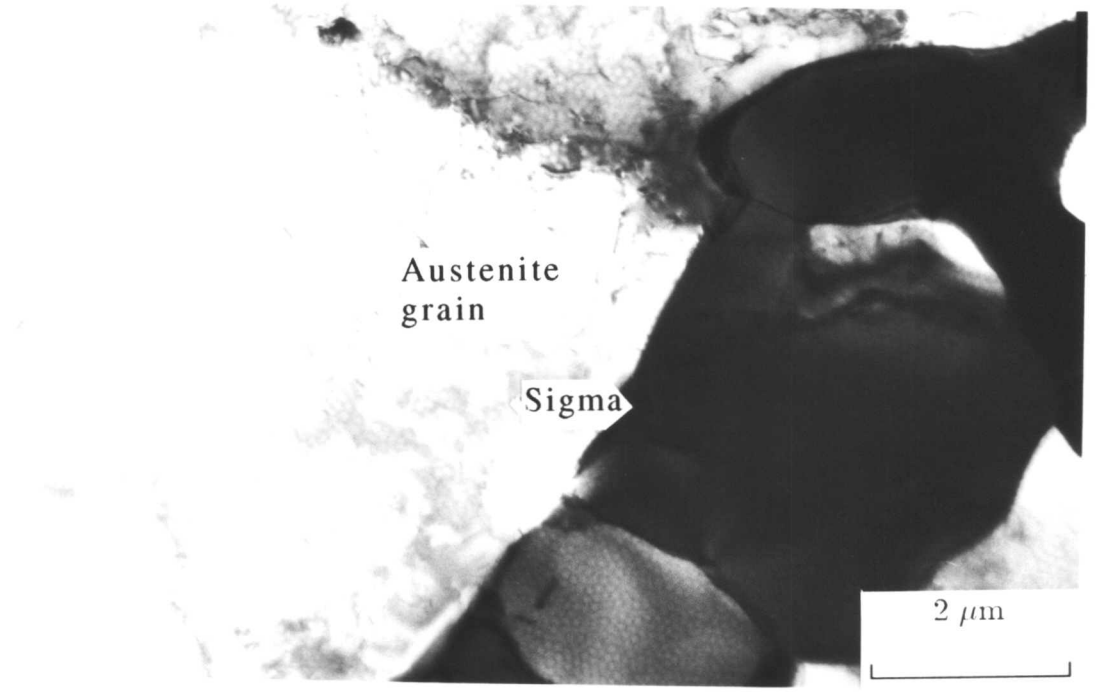

Figure 7.28. Bright field TEM micrograph showing the microstructure of super duplex stainless steel A219 aged at 800 °C for 16 hours. Sigma phase has made a network and there is no sign of ferrite as it has completely decompose to sigma plus austenite. Tables 7.6 and 7.7 show the TEM EDX data of the two phases.

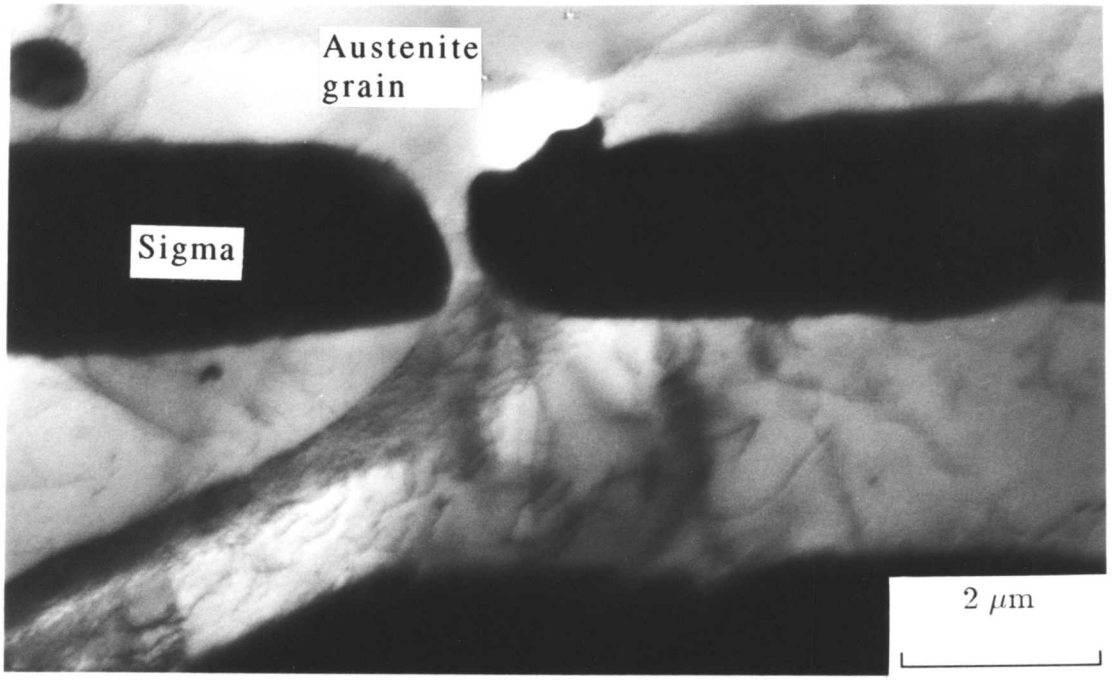

Figure 7.29. Bright field TEM micrograph showing the microstructure of super duplex stainless steel A219 aged at 900 °C for 16 hours. Sigma phase has made a network and there is no sign of ferrite as it has completely decomposed to sigma plus austenite. Tables 7.6 and 7.7 show the TEM EDX data of the two phases.

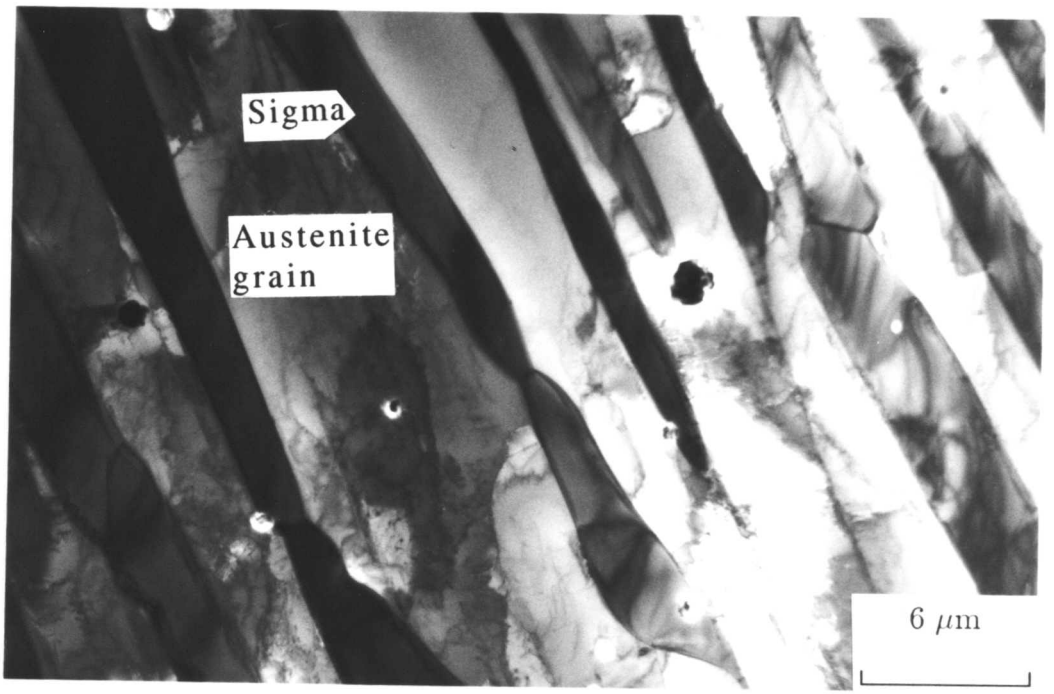

Figure 7.30. Bright field TEM micrograph showing the microstructure of super duplex stainless steel A219 aged at 1000 °C for 16 hours. Sigma phase has made a network and there is no sign of ferrite as it has completely decomposed to sigma plus austenite. Tables 7.6 and 7.7 show the TEM EDX data of the two phases.

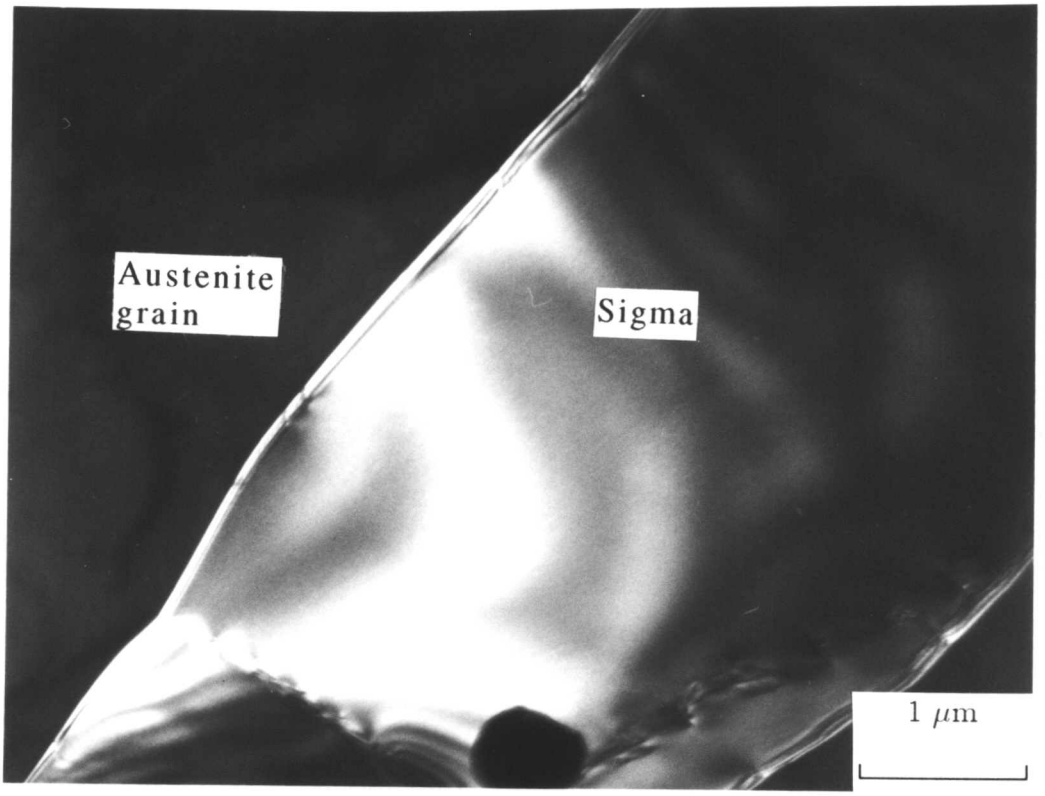

Figure 7.31. Dark field TEM micrograph showing the microstructure of super duplex stainless steel A219 aged at 1000 °C for 16 hours.

Figure 7.32 is a time-temperature-transformation (TTT) diagram for sigma phase formation in super duplex alloy A219 based on the measured volume fraction in the aged specimens. The C-curves for 1 and 5 volume % sigma phase formation is presented in that figure. Note that compared with conventional duplex stainless steels (Figure 7.1) the temperature range where sigma phase precipitates has been widened. Sigma was found to be stable even at the specimens aged at 1050 °C.

7.7 Relation between Volume Fraction of Sigma Phase and Hardness

In the temperature range 700-1050 °C both the hardness of the specimens and volume fraction of sigma phase were found to increase with ageing time. Figure 7.33 shows the variations of hardness and sigma phase volume fraction with temperature for specimens aged for two hours. A very good correlation can be seen between the amount of sigma phase formed and the hardness of the specimens. It was found that a hardness of 320 VHN corresponds to the presence of 0.05 volume fraction of sigma phase. The maximum sigma phase volume fraction of 0.38 was measured in the specimen aged at 900 °C for four

hours. The measured hardness of this specimen was maximum (433 HV).

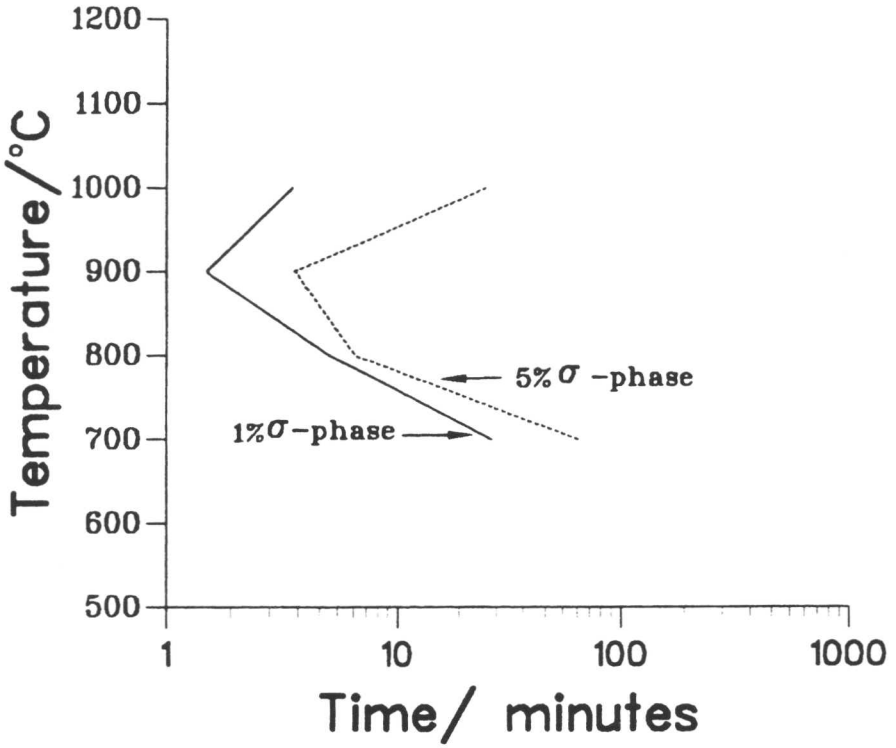

Figure 7.32. C-curves for 1 and 5 vol.% sigma-phase formation in super duplex stainless steel weld metal A219 based on measured volume fraction of sigma in the aged specimens.

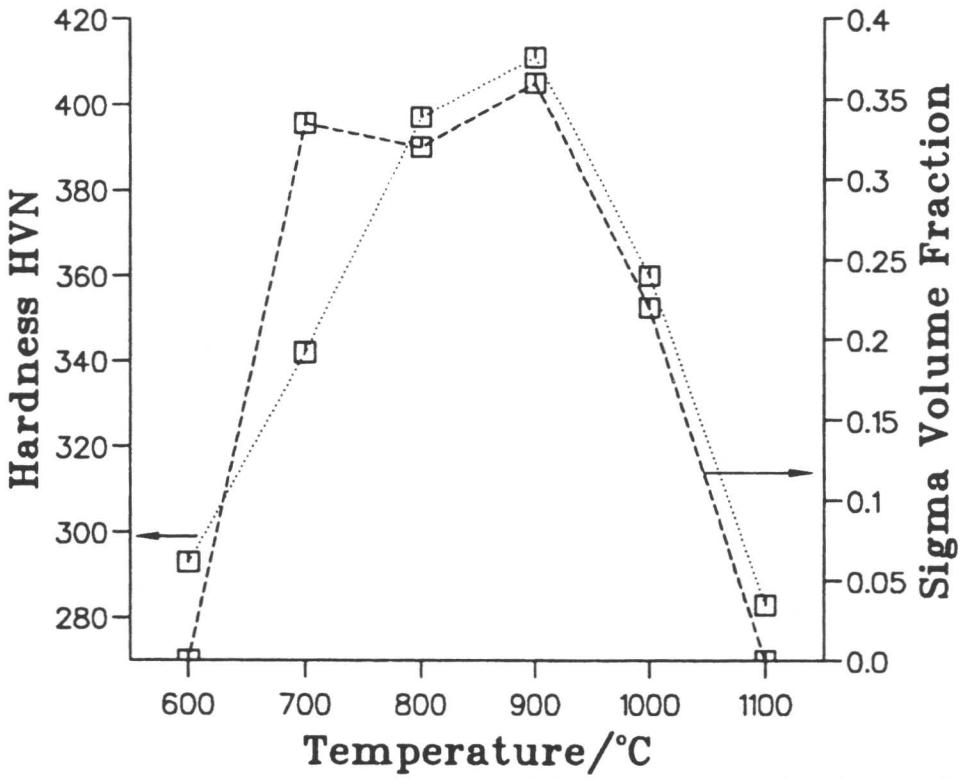

Figure 7.33. Variations of sigma phase volume fraction and hardness with temperature for specimens aged for two hours.

7.8 Partitioning of the Alloying Elements between Austenite and Sigma

The microstructures of specimens aged at 700, 800, 900 and 1000 °C for 16 hours consist mainly of austenite and sigma phase. Tables 7.6 and 7.7 show the TEM EDX data for the sigma phase and austenite respectively. These measurements show that while Cr and Mo partition into sigma phase, Ni partitions into austenite. The data are not all consistent with the thermodynamic calculations; this must be a consequence of the fact that equilibrium has not been achieved for the short time heat-treatments used.

Table 7.6. TEM EDX microanalysis of sigma phase in super duplex weld metal A219 specimens aged at different temperatures for 16 hours (all concentrations in wt.%).

Temperature °C	Fe	Cr	Ni	Mo	Mn	Si
1000	52.0±0.7	34.3±0.5	5.5±0.2	7.1±0.6	0.4±0.1	0.7 ±0.1
900	51.4±0.9	34.0±0.7	5.4±0.1	7.8±0.3	0.7±0.1	0.7 ±0.1
800	53.2±0.9	33.8±0.6	4.9±0.3	6.7±0.4	0.8±0.2	0.7 ±0.1
700	54.0±1.4	34.8±0.7	4.2±0.3	6.0±0.9	0.4±0.1	0.6 ±0.1

Table 7.7. TEM EDX microanalysis of austenite phase in super duplex weld metal A219 specimens aged at different temperatures for 16 hours (all concentrations in wt.%).

Temperature °C	Fe	Cr	Ni	Mo	Mn	Si
1000	61.0±0.3	24.4±0.4	10.5±0.4	1.9±0.2	0.7±0.2	0.5±0.2
900	61.6±0.7	23.9±0.9	10.7±0.6	1.5±0.2	0.9±0.3	0.4±0.1
800	59.2±0.5	24.2±0.4	9.6±0.4	2.8±0.5	0.6±0.1	0.5 ±0.1
700	56.9±0.9	24.7±0.7	10.6±0.4	3.4±0.2	0.9±0.2	0.5±0.1

Figures 7.34 to 7.36 show the partitioning of Cr, Ni and Mo between austenite and sigma phase respectively.

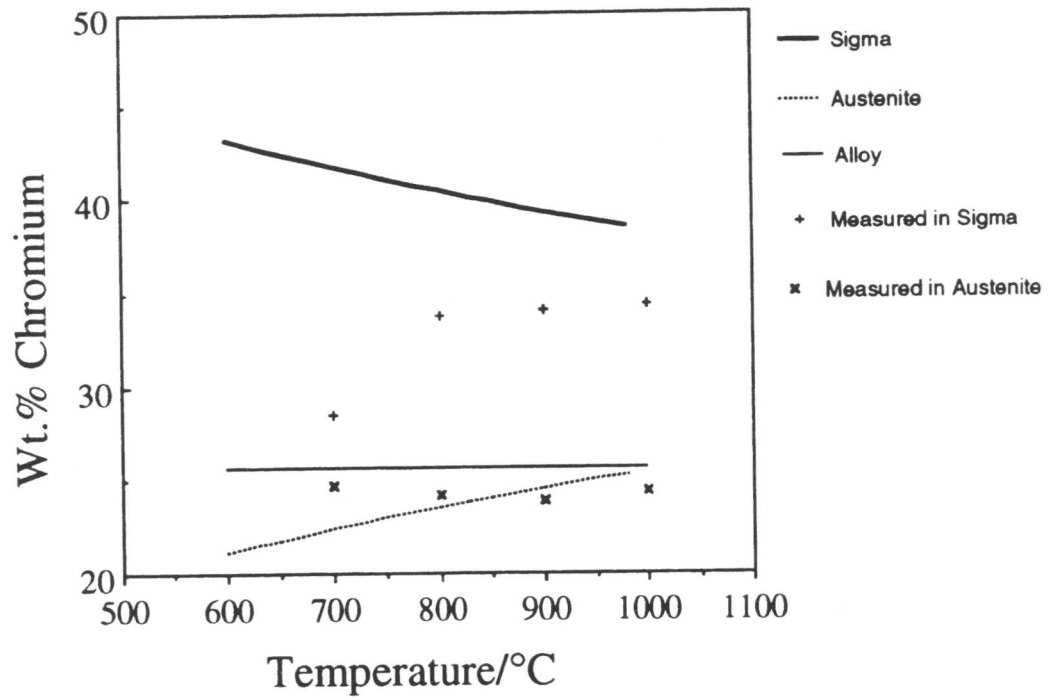

Figure 7.34. The measured partitioning of chromium between austenite and sigma phase in super duplex stainless steel weld metal A219.

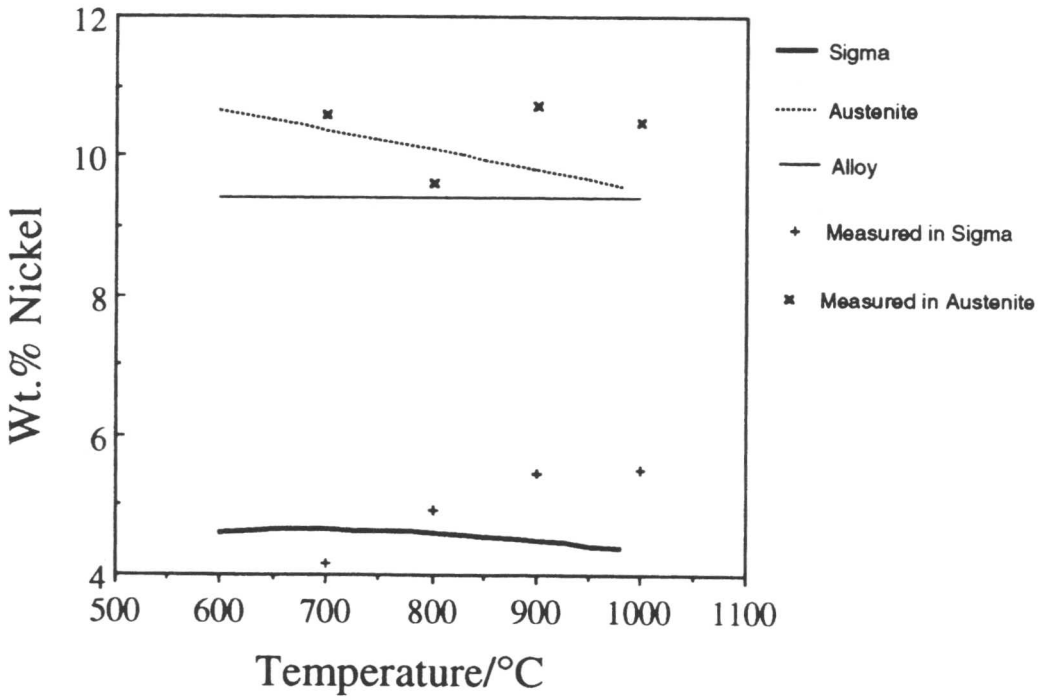

Figure 7.35. The measured partitioning of nickel between austenite and sigma phase in super duplex stainless steel weld metal A219.

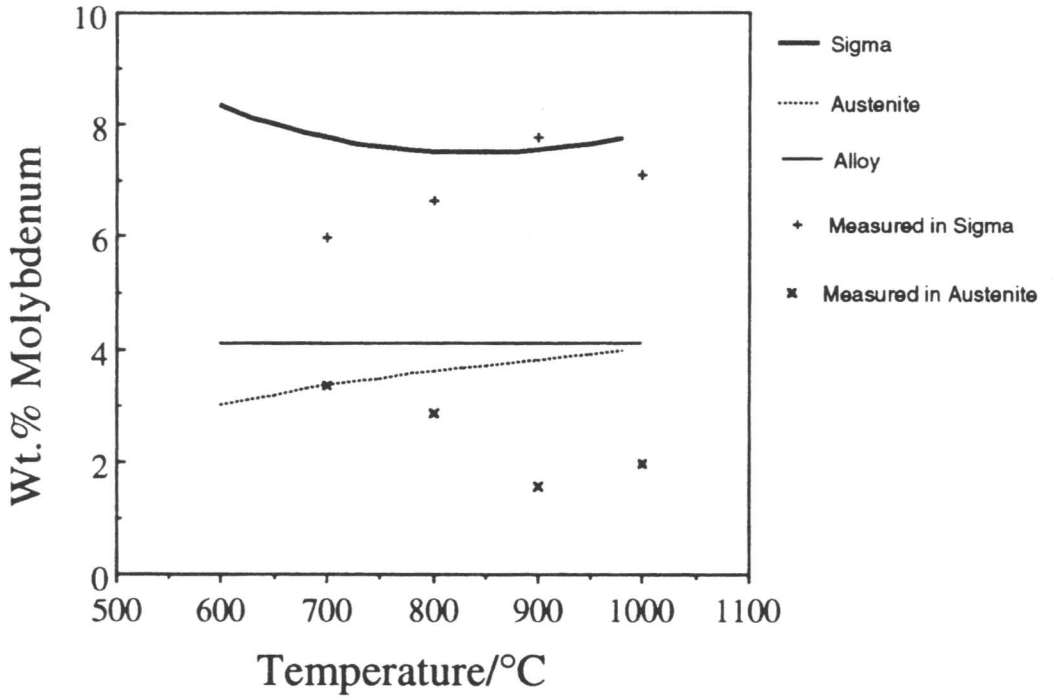

Figure 7.36. The measured partitioning of molybdenum between austenite and sigma phase in super duplex stainless steel weld metal A219.

7.9 Conclusions

1. During ageing over the temperature range 700-1050 °C, sigma phase becomes a more prominent phase than ferrite in super duplex weld metal A219.

2. The measured C-curves for sigma phase formation in alloy A219 show that the temperature range that sigma precipitate has widened for super duplex stainless steel compared with the ordinary grades. This is due to higher amount of Cr and Mo in the super grade (these two elements are very strong sigma formers).

3. Although the thermodynamic calculations show that sigma is not stable at temperatures above 980 °C in super duplex stainless steel alloy A219, it was observed in the specimens aged up to 1050 °C.

4. The hardness of the specimens aged at temperature range 700-1050 °C for enough time was much higher than the received material (in the case of specimen aged at 900 °C for four hours the hardness was found to be 1.5 times of the received material). The optical and TEM observations of the aged specimens showed a massive formation of sigma phase specially in the specimens aged at

700, 800, 900 and 1000 °C for long time. This shows that sigma phase is a hard phase and its presence will increase the hardness of the steel.

5. The TEM EDX data for the sigma phase formed in the aged specimens indicates that sigma phase is rich in Cr and Mo leaving the surrounding area low in Cr and Mo content. As these steels gain their corrosion properties from these two elements precipitation of sigma must have a detrimental consequence on corrosion properties.

Chapter 8

CONCLUSIONS AND FUTURE WORK

The microstructure of duplex stainless steels, particularly the balance between the ferrite and austenite phases can be controlled using heat treatment or alloy modification, in a way which is to a large extent predictable using phase stability calculations. This is particularly true of the trends in microstructure, which rely mostly on the thermodynamics of transformations. For example, there is no doubt that elements like chromium and molybdenum are strong ferrite stabilisers whereas nickel partitions into austenite. The concept of chromium and nickel "equivalents" also seems to work reasonably well in the sense that such parameters can represent the results of multicomponent phase diagram calculations without any major discrepancies.

Some specific results are that both thermodynamic and experimental data show that in most cases, only ferrite and austenite are the stable phases in commercial duplex and super–duplex alloys over the temperature range 1100–1300 °C, over which most of the microstructure evolves during cooling of welds. An exception is alloy A219 which reveals a tendency to form sigma–phase at about 1100 °C due to its exceptionally high chromium and molybdenum concentrations.

The formation of austenite (from ferrite) in all of the alloys is accompanied by a drop in the hardness, but this is not the case if chromium nitride also precipitates on a fine scale, as is the case with A219. Alloy A219 has an exceptionally high nitrogen concentration making it conducive to nitride formation.

Unlike duplex stainless steels, it is found that super–duplex stainless steels cannot solidify into a fully ferritic microstructure. To do so would allow the liquid phase to exist at incredibly low temperatures. Consequently, the super–duplex weld microstructure shows two major categories. The ferrite phase leads solidification, and those regions give a microstructure which is not too different from duplex steels. The trailing austenite front with the liquid leads to a microstructure which looks quite different, with rather blocky austenite. The chemical compositions of the austenite formed by solidification and that formed

by solid state transformation from ferrite will also be different.

The reheated regions of multipass welds consist of two distinct zones, those regions which are ferritised and others which are tempered. The fraction of austenite in the former is always less than in the latter, since the retransformation of newly formed ferrite during cooling is somewhat sluggish. The tempering, on the other hand, causes the fraction of austenite to increase towards equilibrium.

Sigma–phase formation has also been studied. In some cases, microstructures can be produced in which all of the ferrite is replaced by austenite and sigma. This is because the formation of sigma depletes the surroundings of ferrite stabilising elements, causing an enhanced tendency for the remaining microstructure to transform into austenite. The important mechanical property of duplex stainless steels is the strength, which is enhanced by ferrite, when compared with austenitic stainless steels. An examination of the literature indicates that the achievement of toughness does not seem to be a pressing problem for duplex and super–duplex alloys.

Otherwise, the most important property of concern is the corrosion resistance, and requires the establishment of microstructure/corrosion relationships.

What is really needed is detailed kinetic theory capable of predicting the nucleation and growth rate of individual phases, so that the evolution of the microstructure can be studied. At the moment this is rather difficult because the fundamental mechanisms of transformation are not clearly established.

APPENDIX A

```
Copyright S. Sharafi and H. K. D. H. Bhadeshia, University of Cambridge
C DUPLEX STAINLESS STEELS - THERMODYNAMICS AND KINETICS 10 OCTOBER 1990
      IMPLICIT REAL*8(A-H,K-Z), INTEGER(I,J)
      DOUBLE PRECISION D(40,26),CTEMP(40,20),AUST(40,20),NI(40),CR(40),
     &                 A(40,3),CON(3),COEFFT(6,3)
C
C Typical dataset
C
C Identification number T-delta (centigrade) Number of Ctemp-%aust data
C      C  Si Mn P  S  Cr Ni Mo  W Co V
C      Nb Cu Al Sn Ti Pb As Sb Zr B  N
C      O
C  CTEMP VOL% AUST
C CTEMP VOL% AUST
C
       IN=0
       DO 1 I=1,40
          READ(5,*,END=4) D(I,1), D(I,2),IREAD
          READ(5,*)D(I,4),D(I,5),D(I,6),D(I,7),D(I,8),D(I,9),
     &             D(I,10),D(I,11),D(I,12),D(I,13),D(I,14)
          READ(5,*)D(I,15),D(I,16),D(I,17),D(I,18),D(I,19),D(I,20),
     &             D(I,21),D(I,22),D(I,23),D(I,24),D(I,25)
          READ(5,*)D(I,26)
C
                    DO 2 J=1,IREAD
                       READ(5,*)CTEMP(I,J),AUST(I,J)
2                   CONTINUE
C-------------------------------------------------------------------------
C         WRITE(6,33) D(I,1), D(I,2),IREAD
C          WRITE(6,34)D(I,4),D(I,5),D(I,6),D(I,7),D(I,8),D(I,9),
C     &             D(I,10),D(I,11),D(I,12),D(I,13),D(I,14)
C          WRITE(6,34)D(I,15),D(I,16),D(I,17),D(I,18),D(I,19),D(I,20),
C     &             D(I,21),D(I,22),D(I,23),D(I,24),D(I,25)
C          WRITE(6,34)D(I,26)
C33       FORMAT(2D10.2,I9)
C34       FORMAT(12D10.2)
C
C                     DO 22 J=1,IREAD
C                       WRITE(6,34)CTEMP(I,J),AUST(I,J)
C22                   CONTINUE
C
C-------------------------------------------------------------------------

        IN=IN+1
1       CONTINUE
4       CONTINUE
C-------------------------------------------------------------------------
C calculate Ni and Cr equivalents
C  NIEQ = Ni + Co + 0.5Mn + 0.3Cu + 30C + 25N all units wt.%
C                                              note that N read in ppm by wt.
C  CREQ = Cr + 2.0Si + 1.5Mo + 5.0V + 5.5Al + 0.75Nb + 1.5Ti + 0.75W wt.%
C   Ref.27 of Naseem Haddad's Thesis (1989), C, N, Mo coefficients changed
C
       DO 3 I=1,40
       NI(I)=D(I,10) + D(I,13) + 0.5*D(I,6) + 0.3*D(I,16) +
     &       15.0*D(I,4) + 13.0*1.0D-04*D(I,25)
       CR(I)=D(I,9) + 2.0*D(I,5) + 3.0*D(I,11) + 5.0*D(I,14)
```

```
     &       + 5.5*D(I,17) + 0.75*D(I,15) + 1.5* D(I,19) + 0.75*D(I,12)


3      CONTINUE
C end calculation of Ni and Cr equivalents
C-------------------------------------------------------------------------
C
222    CONTINUE
         DO 5 I5=1,IN
                 A(I5,1)=NI(I5)
                A(I5,2)=CR(I5)
                A(I5,3)=D(I5,2)
5        CONTINUE
C
C-------------------------------------------------------------------------
       CALL MREG3(A,IN,CON,COEFFT)
       WRITE(6,103)
103    FORMAT(//10X,'STEEL',' Calculated T-delta ',' Actual   T-delta'/)
       DO 101 I=1,IN
       TDELC=CON(1) + COEFFT(1,1)*A(I,1) + COEFFT(2,1)*A(I,2)
       WRITE(6,102)I,TDELC,A(I,3)
102    FORMAT(10X,I5,2F20.0)
101    CONTINUE

       STOP
       END
C*************************************************************************
C*************************************************************************
C
C      Regression analysis subroutine, four variables
       SUBROUTINE MREG3(A,N,CON,COEFFT)
       IMPLICIT REAL*8 (A-H,O-Z)
       DOUBLE PRECISION A(40,3), XBAR(3), STD(3), SSP(3,3),
      *CORR(3,3),RESULT(13),
      *COEFFT(6,3),RIM(3,3), C(3,4), W(3,3), CON(3)
       INTEGER I, M, N, J, IFAIL,NI
       M = 3
       WRITE (6,99996) M, N, (J,J=1,M), (I,(A(I,J),J=1,M),I=1,N)
       IFAIL = 1
       CALL G02BAF(N, M, A, 40, XBAR, STD, SSP, 3, CORR, 3, IFAIL)
       IF (IFAIL) 20, 40, 20
   20  WRITE (6,99995) IFAIL
       GO TO 60
   40  WRITE (6,99994) (I,XBAR(I),STD(I),I=1,M)
       WRITE (6,99993) (I,I=1,M), (I,(SSP(I,J),J=1,M),I=1,M)
       WRITE (6,99992) (I,I=1,M), (I,(CORR(I,J),J=1,M),I=1,M)
   60  CONTINUE
99996  FORMAT (32H0NUMBER OF VARIABLES (COLUMNS) =, I1/10H NUMBER OF,
      * 22H CASES      (ROWS)     =, I3//17H DATA MATRIX IS:-//1H ,
      * 3I12/(1H , I3, 3D12.4))
99995  FORMAT (22H0ROUTINE FAILS, IFAIL=, I2)
99994  FORMAT (28H0VARIABLE   MEAN     ST. DEV./(1H , I5, 2D11.4))
99993  FORMAT (49H0SUMS OF SQUARES AND CROSS-PRODUCTS OF DEVIATIONS/
      * 1H , 3I12/(1H , I3, 3D12.4))
99992  FORMAT (25H0CORRELATION COEFFICIENTS/1H , 3I12/(1H , I3,
      * 3D12.4))
       NI = M - 1
       IFAIL = 1
       CALL G02CGF(N, M, NI, XBAR, SSP, 3, CORR, 3, RESULT,COEFFT, 6,
      * CON, RIM, 3, C, 3, W, 3, IFAIL)
```

```
      IF (IFAIL) 21, 41, 21
   21 CONTINUE
      WRITE (6,88885) IFAIL
      GO TO 61
   41 CONTINUE
      WRITE (6,88884) (I,(COEFFT(I,J),J=1,3),I=1,NI)
      WRITE (6,88883) (CON(I),I=1,3)
      WRITE (6,88882) (RESULT(I),I=1,13)
   61 CONTINUE
      RETURN
88885 FORMAT (22H0ROUTINE FAILS, IFAIL=, I2/)
88884 FORMAT (43H0VBLE     COEFFT       STD ERR      T-VALUE/2(1H ,
     * I3, 3D13.4/))
88883 FORMAT (6H0CONST, F11.4, 2F13.4/)
88882 FORMAT (32H0ANALYSIS OF REGRESSION TABLE :-//13H       SOURCE,
     * 55H        SUM OF SQUARES  D.F.    MEAN SQUARE     F-VALUE//
     * 18H DUE TO REGRESSION, F14.4, F8.0, 2F14.4/14H ABOUT  REGRES,
     * 4HSION, F14.4, F8.0, F14.4/18H TOTAL            , F14.4,
     * F8.0///29H STANDARD ERROR OF ESTIMATE =, F8.4/11H MULTIPLE C,
     * 18HORRELATION (R)   =, F8.4/29H DETERMINATION (R SQUARED)  =,
     * F8.4/29H CORRECTED R SQUARED        =, F8.4/)
      END
```

APPENDIX B

```
Copyright S. Sharafi and H. K. D. H. Bhadeshia, University of Cambridge
C DUPLEX STAINLESS STEELS - THERMODYNAMICS AND KINETICS 10 OCTOBER 1990
      IMPLICIT REAL*8(A-H,K-Z), INTEGER(I,J)
      DOUBLE PRECISION D(40,26),CTEMP(40,20),AUST(40,20),NI(40),CR(40),
     &                 A(40,3),CON(3),COEFFT(6,3),RESULT(13)
C
C Typical dataset
C
C Identification number T-delta (centigrade) Number of Ctemp-%aust data
C      C  Si Mn P  S  Cr Ni Mo  W Co V
C      Nb Cu Al Sn Ti Pb As Sb Zr B  N
C      O
C  CTEMP VOL% AUST
C CTEMP VOL% AUST
C
       IN=0
       DO 1 I=1,40
          READ(5,*,END=4) D(I,1), D(I,2),IREAD
          READ(5,*)D(I,4),D(I,5),D(I,6),D(I,7),D(I,8),D(I,9),
     &             D(I,10),D(I,11),D(I,12),D(I,13),D(I,14)
          READ(5,*)D(I,15),D(I,16),D(I,17),D(I,18),D(I,19),D(I,20),
     &             D(I,21),D(I,22),D(I,23),D(I,24),D(I,25)
          READ(5,*)D(I,26)
C
                    DO 2 J=1,IREAD
                       READ(5,*)CTEMP(I,J),AUST(I,J)
2                   CONTINUE
C-------------------------------------------------------------------------------

        IN=IN+1
1       CONTINUE
4       CONTINUE
C-------------------------------------------------------------------------------
      AAC=4
      DO 201 IAAC=1,20
      AAN=8
      DO 202 IAAN=1,20
      AAMO=2.4
      DO 203 IMO=1,10
C calculate Ni and Cr equivalents
C  NIEQ = Ni + Co + 0.5Mn + 0.3Cu + 30C + 25N all units wt.%
C                                              note that N read in ppm by wt.
C  CREQ = Cr + 2.0Si + 1.5Mo + 5.0V + 5.5Al + 0.75Nb + 1.5Ti + 0.75W wt.%
C   Ref.27 of Naseem Haddad's Thesis (1989)
C
       DO 3 I=1,40
       NI(I)=D(I,10) + D(I,13) + 0.5*D(I,6) + 0.3*D(I,16) +
     &       AAC*D(I,4) + AAN*1.0D-04*D(I,25)
       CR(I)=D(I,9) + 2.0*D(I,5) + AAMO*D(I,11) + 5.0*D(I,14)
     &       + 5.5*D(I,17) + 0.75*D(I,15) + 1.5* D(I,19) + 0.75*D(I,12)
3      CONTINUE
C end calculation of Ni and Cr equivalents
C-------------------------------------------------------------------------------
C
222    CONTINUE
         DO 5 I5=1,IN
                A(I5,1)=NI(I5)
```

```
                A(I5,2)=CR(I5)
                A(I5,3)=D(I5,2)
5         CONTINUE
C
C-------------------------------------------------------------------------
      CALL MREG3(A,IN,CON,COEFFT,RESULT)
      IF(DABS(RESULT(11)) .LT. 0.891) GOTO 400
      WRITE(6,110)AAC,AAN,AAMO
110   FORMAT(' AAC, AAN, AAMO', 3F8.2)
400   CONTINUE
      AAMO=AAMO+0.5
203   CONTINUE
      AAN=AAN+2.0
202   CONTINUE
      AAC=AAC+2.0
201   CONTINUE
      STOP
      END
C*************************************************************************
C*************************************************************************
C
C     Regression analysis subroutine, four variables
      SUBROUTINE MREG3(A,N,CON,COEFFT,RESULT)
      IMPLICIT REAL*8 (A-H,O-Z)
      DOUBLE PRECISION A(40,3), XBAR(3), STD(3), SSP(3,3),
     *CORR(3,3),RESULT(13),
     *COEFFT(6,3),RIM(3,3), C(3,4), W(3,3), CON(3)
      INTEGER I, M, N, J, IFAIL,NI
      M = 3
      IFAIL = 1
      CALL G02BAF(N, M, A, 40, XBAR, STD, SSP, 3, CORR, 3, IFAIL)
      IF (IFAIL) 20, 40, 20
   20 WRITE (6,99995) IFAIL
      GO TO 60
   40 CONTINUE
   60 CONTINUE
99995 FORMAT (22H0ROUTINE FAILS, IFAIL=, I2)
      NI = M - 1
      IFAIL = 1
      CALL G02CGF(N, M, NI, XBAR, SSP, 3, CORR, 3, RESULT,COEFFT, 6,
     * CON, RIM, 3, C, 3, W, 3, IFAIL)
      IF(DABS(RESULT(11)) .LT. 0.891)GOTO 61
      IF (IFAIL) 21, 41, 21
   21 CONTINUE
      WRITE (6,88885) IFAIL
      GO TO 61
   41 CONTINUE
      WRITE (6,88884) (I,(COEFFT(I,J),J=1,3),I=1,NI)
      WRITE (6,88883) (CON(I),I=1,3)
      WRITE (6,88882) RESULT(11)
   61 CONTINUE
88885 FORMAT (22H0ROUTINE FAILS, IFAIL=, I2/)
88884 FORMAT (43H0VBLE     COEFFT       STD ERR      T-VALUE/2(1H ,
     * I3, 3D13.4))
88883 FORMAT (6H0CONST, F11.4, 2F13.4)
88882 FORMAT ('Multiple regression correlation = ',F8.5)
      RETURN
      END
```

```
Copyright S. Sharafi and H. K. D. H. Bhadeshia, University of Cambridge
C DUPLEX STAINLESS STEELS - THERMODYNAMICS AND KINETICS 10 OCTOBER 1990
      IMPLICIT REAL*8(A-H,K-Z), INTEGER(I,J)
      DOUBLE PRECISION D(40,26),CTEMP(40,20),AUST(40,20),NI(40),CR(40),
     &   A(40,3),CON(3),COEFFT(6,3),CTEMP2(500),VOLAUS(500),ARES(20)
C
C Typical dataset
C
C Identification number T-delta (centigrade) Number of Ctemp-%aust data
C      C  Si Mn P  S  Cr Ni Mo  W Co V
C      Nb Cu Al Sn Ti Pb As Sb Zr B  N
C      O
C  CTEMP VOL% AUST
C CTEMP VOL% AUST
C
       IN=0
       IALL=0
       DO 1 I=1,40
          READ(5,*,END=4) D(I,1), D(I,2),IREAD
          READ(5,*)D(I,4),D(I,5),D(I,6),D(I,7),D(I,8),D(I,9),
     &             D(I,10),D(I,11),D(I,12),D(I,13),D(I,14)
          READ(5,*)D(I,15),D(I,16),D(I,17),D(I,18),D(I,19),D(I,20),
     &             D(I,21),D(I,22),D(I,23),D(I,24),D(I,25)
          READ(5,*)D(I,26)
C
                    DO 2 J=1,IREAD
                       IALL=IALL+1
                       READ(5,*)CTEMP(I,J),AUST(I,J)
                       CTEMP2(IALL)=DLOG(D(I,2)+1.0 - CTEMP(I,J))
                       VOLAUS(IALL)=DLOG(AUST(I,J)+0.1D-1)
2                   CONTINUE
C-------------------------------------------------------------------------
C         WRITE(6,33) D(I,1), D(I,2),IREAD
C          WRITE(6,34)D(I,4),D(I,5),D(I,6),D(I,7),D(I,8),D(I,9),
C     &             D(I,10),D(I,11),D(I,12),D(I,13),D(I,14)
C          WRITE(6,34)D(I,15),D(I,16),D(I,17),D(I,18),D(I,19),D(I,20),
C     &             D(I,21),D(I,22),D(I,23),D(I,24),D(I,25)
C          WRITE(6,34)D(I,26)
C33       FORMAT(2D10.2,I9)
C34       FORMAT(12D10.2)
C
C                    DO 22 J=1,IREAD
C                      WRITE(6,34)CTEMP(I,J),AUST(I,J)
C22                  CONTINUE
C
C-------------------------------------------------------------------------

        IN=IN+1
1       CONTINUE
4       CONTINUE
C-------------------------------------------------------------------------
      AAC=11.0D+00
      AAN=15.0D+00
      AAMO=3.0D+00
C calculate Ni and Cr equivalents
C  NIEQ = Ni + Co + 0.5Mn + 0.3Cu + 30C + 25N all units wt.%
C                                          note that N read in ppm by wt.
```

```
C  CREQ = Cr + 2.0Si + 1.5Mo + 5.0V + 5.5Al + 0.75Nb + 1.5Ti + 0.75W wt.%
C   Ref.27 of Naseem Haddad's Thesis (1989)
C
       DO 3 I=1,40
       NI(I)=D(I,10) + D(I,13) + 0.5*D(I,6) + 0.3*D(I,16) +
     &       AAC*D(I,4) + AAN*1.0D-04*D(I,25)
       CR(I)=D(I,9) + 2.0*D(I,5) + AAMO*D(I,11) + 5.0*D(I,14)
     &       + 5.5*D(I,17) + 0.75*D(I,15) + 1.5* D(I,19) + 0.75*D(I,12)
3      CONTINUE
C end calculation of Ni and Cr equivalents
C-------------------------------------------------------------------------------
C
222    CONTINUE
         DO 5 I5=1,IN
                A(I5,1)=NI(I5)
               A(I5,2)=CR(I5)
               A(I5,3)=D(I5,2)
5        CONTINUE
C
C-------------------------------------------------------------------------------
      CALL MREG3(A,IN,CON,COEFFT)
      WRITE(6,103)
103   FORMAT(//10X,'STEEL',' Calculated T-delta ',' Actual   T-delta'/)
      DO 101 I=1,IN
      TDELC=CON(1) + COEFFT(1,1)*A(I,1) + COEFFT(2,1)*A(I,2)
      WRITE(6,102)I,TDELC,A(I,3)
102   FORMAT(10X,I5,2F20.0)
101   CONTINUE
      CALL MREG2(CTEMP2,VOLAUS,IALL,ARES)
      WRITE(6,104) ARES(6),ARES(7)
104   FORMAT(10X,' COEFFICIENTS ARES6, ARES7',2D12.4)
         DO  1001 I=1,IALL
             VOLA=ARES(6)*CTEMP2(I)+ARES(7)
             VOLA=DEXP(VOLA)-0.1D-1
             VOLB=DEXP(VOLAUS(I))-0.1D-1
             WRITE(6,1000)VOLA,VOLB
1000         FORMAT(2F8.1)
1001         CONTINUE



      STOP
      END
C*******************************************************************************
C*******************************************************************************
      SUBROUTINE MREG2(X,Y,N,RESULT)
      IMPLICIT REAL*8 (A-H,O-Z)
      DOUBLE PRECISION X(500), Y(500), RESULT(20)
      INTEGER I, IFAIL, N
       WRITE(6,99996)(I,X(I),Y(I),I=1,N)
      IFAIL = 1
      CALL G02CAF(N, X, Y, RESULT, IFAIL)
C
C     TEST IFAIL
C
      IF (IFAIL) 20, 40, 20
   20 WRITE (6,99995) IFAIL
      GO TO 60
   40 WRITE (6,99994) (RESULT(I),I=1,5)
      WRITE (6,99993) RESULT(6), RESULT(8), RESULT(10)
```

```
      WRITE (6,99992) RESULT(7), RESULT(9), RESULT(11)
      WRITE (6,99991) (RESULT(I),I=12,20)
   60 CONTINUE
99997 FORMAT (2F10.5)
99996 FORMAT (36H0 CASE     INDEPENDENT     DEPENDENT/10H NUMBER   ,
     * 25H  VARIABLE       VARIABLE//(1H , I4, 2F15.4))
99995 FORMAT (22H0ROUTINE FAILS, IFAIL=, I2/)
99994 FORMAT (46H0MEAN OF INDEPENDENT VARIABLE              = ,
     * F8.4/46H MEAN OF   DEPENDENT VARIABLE               = ,
     * F8.4/46H STANDARD DEVIATION OF INDEPENDENT VARIABLE = ,
     * F8.4/46H STANDARD DEVIATION OF   DEPENDENT VARIABLE = ,
     * F8.4/46H CORRELATION COEFFICIENT                    = , F8.4)
99993 FORMAT (46H0REGRESSION COEFFICIENT                    = ,
     * D12.4/46H STANDARD ERROR OF COEFFICIENT             = ,
     * F8.4/46H T-VALUE FOR COEFFICIENT                    = , F8.4)
99992 FORMAT (46H0REGRESSION CONSTANT                       = ,
     * D12.4/46H STANDARD ERROR OF CONSTANT                = ,
     * F8.4/46H T-VALUE FOR CONSTANT                       = , F8.4)
99991 FORMAT (32H0ANALYSIS OF REGRESSION TABLE :-//13H       SOURCE,
     * 55H        SUM OF SQUARES  D.F.    MEAN SQUARE     F-VALUE//
     * 18H DUE TO REGRESSION, F14.4, F8.0, 2F14.4/14H ABOUT  REGRES,
     * 4HSION, F14.4, F8.0, F14.4/18H TOTAL            , F14.4,
     * F8.0)
      RETURN
      END

C*******************************************************************************
C*******************************************************************************
C
C     Regression analysis subroutine, four variables
      SUBROUTINE MREG3(A,N,CON,COEFFT)
      IMPLICIT REAL*8 (A-H,O-Z)
      DOUBLE PRECISION A(40,3), XBAR(3), STD(3), SSP(3,3),
     *CORR(3,3),RESULT(13),
     *COEFFT(6,3),RIM(3,3), C(3,4), W(3,3), CON(3)
      INTEGER I, M, N, J, IFAIL,NI
      M = 3
      WRITE (6,99996) M, N, (J,J=1,M), (I,(A(I,J),J=1,M),I=1,N)
      IFAIL = 1
      CALL G02BAF(N, M, A, 40, XBAR, STD, SSP, 3, CORR, 3, IFAIL)
      IF (IFAIL) 20, 40, 20
   20 WRITE (6,99995) IFAIL
      GO TO 60
   40 WRITE (6,99994) (I,XBAR(I),STD(I),I=1,M)
      WRITE (6,99993) (I,I=1,M), (I,(SSP(I,J),J=1,M),I=1,M)
      WRITE (6,99992) (I,I=1,M), (I,(CORR(I,J),J=1,M),I=1,M)
   60 CONTINUE
99996 FORMAT (32H0NUMBER OF VARIABLES (COLUMNS) =, I1/10H NUMBER OF,
     * 22H CASES     (ROWS)    =, I3//17H DATA MATRIX IS:-//1H ,
     * 3I12/(1H , I3, 3D12.4))
99995 FORMAT (22H0ROUTINE FAILS, IFAIL=, I2)
99994 FORMAT (28H0VARIABLE   MEAN    ST. DEV./(1H , I5, 2D11.4))
99993 FORMAT (49H0SUMS OF SQUARES AND CROSS-PRODUCTS OF DEVIATIONS/
     * 1H , 3I12/(1H , I3, 3D12.4))
99992 FORMAT (25H0CORRELATION COEFFICIENTS/1H , 3I12/(1H , I3,
     * 3D12.4))
      NI = M - 1
      IFAIL = 1
      CALL G02CGF(N, M, NI, XBAR, SSP, 3, CORR, 3, RESULT,COEFFT, 6,
     * CON, RIM, 3, C, 3, W, 3, IFAIL)
```

```
      IF (IFAIL) 21, 41, 21
   21 CONTINUE
      WRITE (6,88885) IFAIL
      GO TO 61
   41 CONTINUE
      WRITE (6,88884) (I,(COEFFT(I,J),J=1,3),I=1,NI)
      WRITE (6,88883) (CON(I),I=1,3)
      WRITE (6,88882) (RESULT(I),I=1,13)
   61 CONTINUE
88885 FORMAT (22H0ROUTINE FAILS, IFAIL=, I2/)
88884 FORMAT (43H0VBLE     COEFFT       STD ERR      T-VALUE/2(1H ,
     * I3, 3D13.4/))
88883 FORMAT (6H0CONST, F11.4, 2F13.4/)
88882 FORMAT (32H0ANALYSIS OF REGRESSION TABLE :-//13H       SOURCE,
     * 55H        SUM OF SQUARES  D.F.    MEAN SQUARE     F-VALUE//
     * 18H DUE TO REGRESSION, F14.4, F8.0, 2F14.4/14H ABOUT  REGRES,
     * 4HSION, F14.4, F8.0, F14.4/18H TOTAL            , F14.4,
     * F8.0///29H STANDARD ERROR OF ESTIMATE =, F8.4/11H MULTIPLE C,
     * 18HORRELATION (R)   =, F8.4/29H DETERMINATION (R SQUARED)  =,
     * F8.4/29H CORRECTED R SQUARED        =, F8.4/)
      RETURN
      END
```

REFERENCES

Abron, R. H. and Bain, E. C., (1930)
Trans. Amer. Soc. Steel Treating, **8**, p. 837.

Bain, E.C. and Griffiths, W.E., (1927)
Trans. AIME, **75**, p. 166.

Bechtoldt, C. J. and Vacher, H. C., (1957)
J. Res. Nat. Bur. Stand., **58**, p. 7.

Bhadeshia, H.K.D.H.; David, S.A. and Vitek, J.M., (1991)
Materials Science and Technology, **7**, p. 50.

Bowman, A.L.; Arnold, G.P.; Storms, E.K. and Nereson, N.G., (1972)
Acta Cryst. B, **28**, p. 3102.

Briggs, J.Z. and Parker, T.D., (1965)
The Super 12 wt.% Cr Steels, Climax Molybdenum Co., supplement 1983.

Bywater, K.A. and Gladman, T., (1976)
Met. Technology, **3**, 358.

Castro, R. and de Cadenet, J.J., (1968)
Welding Metallurgy of Stainless and Heat-Resisting Steels, Dunod, p. 77.

Chance, J.; Gradwell, K.J.; Coop, W. and Roscoe, C.V., (1982)
Proceeding of Inter. Conference of Duplex Stainless Steels, The USA, Paper 8201-019, p. 371.

Clark, C. A.; Gentil, P. and Guha, P., (1986)
Proceeding of Inter. Conference of Duplex Stainless Steels, The Netherlands, Paper 52, p. 109.

Climax Molybdenum Co., (1977)
Proceedings of Inter. Conference of Stainless Steel, London, p. 57.

Dawson, G.W. and Judson, P., (1982)
Second Intrn. Conf. on Offshore Welded Structure, London, p. 127.

Easterling, K., (1983)
Introduction to the Physical Metallurgy of Welding, London, p. 83.

Eriksson, S., (1934)
Jernkonttorets Annaler, **118**, p. 530.

Evans, D.A. and Jack, K.H., (1957)
Acta Cryst, **10**, p. 769.

Farrar, R. A., (1987)
J. Mat. Sci., **22**, p. 363.

Faucheur, D. and Gilbert, D., (1986)
Proceeding of Inter. Conference of Duplex Stainless Steels, The Netherlands, Paper 38, p. 83.

Folkhard, E., (1988)
Welding Metallurgy of Stainless Steels, Wein -New York, p. 25.

Geisen, W., (1909)
ISI Carnegie Scholarship Memoirs, **1**, p.1.

Gordon, G. M., (1977)
***in** Proc. Firminy Conf. NACE*, Houston, Texas, p. 893.

Guha, P. and Clark, C.A., (1982)
Proceeding of Inter. Conference of Duplex Stainless Steels, The USA, Paper 8201-018, p. 355.

Guillet, L., (1904)
Rev. de Met., **2**, p.155.

Ha, H.C.; Pyun, S.I. and Lim, C., (1991)
Material Science and Engineering, **A131**, p. 231.

Haddad, N.I.A., (1989)
Ph.D. Thesis, University of Cambridge, Dept. of Mat. Sci. and Metallurgy, p. 28.

Hadfield, R.A., (1892)
JISI, **2**, p.49.

Hall, E.O. and Algie, S.H., (1966)
Met. Rev., **11**, p. 61.

Hammar, O. and Svensson, U, (1979)
Proceedings of Inter. Conference of Solidification and Casting of Metals, UK, p. 401.

Hansen, M. and Anderko, K., (1958)
Constitution of Binary Alloys, McGraw-Hill, p. 527.

Herbsleb, G. and Schwaab, P., (1982)
Proceeding of Inter. Conference of Duplex Stainless Steels, USA, Paper 8201-002, p. 15.

Hillert, M.; Jansson, B. and Sundman, B., (1988)
Application of the Compound-Energy Model to Oxide Systems, Zeit. Metallkde.79, p. 81-87.

Hilty, D.C. and Kaveney, T.F., (1977)
Handbook of Stainless Steels, New York, p.3.1.

Hochmann, J.; Desestret, A.; Jolly, P. and Mayound, R., (1974)
Met. Corr. Industrie, 591/592, part I, p. 390.

Hodson, S.M., (1989)
National Physic Laboratory, MTDATA Handbook, Multiphase Theory.

Honeycombe, J. and Gooch, T.G., (1985)
The Weld Inst., UK, Report 286.

Josefsson, B.; Nilsson, J.O. and Wilson, A., (1991)
Internal Report, AB SANDVIK STEEL, Sweden.

Karlsson, L. and Pak, S., (1991)
Inter. Conf. on Stainless Steel, Chiba, Japan, p. 1101.

Karlsson, L.; Pak, S. and Andersson, S.L., (1991)
Inter. Conf. on Stainless Steel, Chiba, Japan, p. 1093.

Kasper, J.S., (1954)
Acta Met., **2**, p. 456.

Kubaschewski, O., (1982)
Iron-Binary Phase Diagrams, Springer-Verlag Berlin, p. 31.

Laing, B.S.; Jones, R.L.; Randall, M.D. and Teale, R.A., (1986)
Proceeding of Inter. Conference of Duplex Stainless Steels, The Netherlands, Paper 29, p. 30.

Leach, J.C.C.; Rodgers, A. and Sheehan, G., (1978)
Secondary Steelmaking, The Metals Society (London), p.73.

Leach, J.C.C., (1982)
Steel Times, **210(10)**, p.577.

Leslie, W.C., (1981)
The Physical Metallurgy of Steels, Mc Graw-Hill, Washington.

Machara, Y., (1983)
Metal Science, **17**, p. 541.

Maehara, Y.; Ohmori, Y.; Murayama, J.; Fujino, N. and Kunitake, T., (1983)
Metal Sci., **17**, p. 541.

Marshall,P., (1984)
Austenitic Stainless Steels, Elsevier Applied Science Publishers, London.

Mundt, R. and Hoffmeister, H., (1983)
Arch. Eisenhuttenwes, **54(6)**, p. 253.

Nagano, H.; Kudo, T.; Inaba, Y. and Harada, M., (1981)
Metaux Corrosion Industrie, **No. 667**, p. 23.1.

Netzsch Company, (1989)
Instrument Manual, Germany, p. 1-6.

Nilsson J.O. and Liu, P., (1988)
AB Sandvik Steel, Internal Report, No 5603.

Nilsson J.O. and Liu, P., (1991)
Inter. Conf. on Stainless Steel, Chiba, Japan, p. 1109.

Noble, D.N. and Gooch, T.G., (1986)
The Weld. Inst., UK, Report 321.

Olsson, J. and Nordin, S., (1986)
Proceeding of Inter. Conference of Duplex Stainless Steels, The Netherlands, Paper 48, p. 219.

Perteneder, E.; Tosch, J.; Reiterer, P. and Rabensteiner, G., (1986)
Proceeding of Inter. Conference of Duplex Stainless Steels, The Netherlands, Paper 21, p. 48.

Pickering, F.B., (1984)
Conf. Proc. Stainless Steel '84, Paper 2, p. 2.

Redmond, J.D. and Miska, K.H., (1982)
Chemical Engineering, October, p.79.

Rideout, S.; Manly, W.D.; Kamen, E.L.; Lement, B.S. and Beck, P.A., (1951)
Trans. AIME, **2**, p. 872.

Rivlin, V.G. and Raynor, G.V., (1980)
Inter. Metals Reviews, **1**, p. 21.

Roscoe, C.V. and Gradwell, K.J., (1986)
Proceeding of Inter. Conference of Duplex Stainless Steels, The Netherlands, Paper 34, p. 126.

Roscoe, C.V.; Gradwell, K.J. and Lorimer, G.W., (1984)
Proceeding of Inter. Conference of Stainless Steels, Sweden, p. 563.

Rouault, A.; Herpin, P. and Fruchart, R., (1970)
Ann. Chim, **5**, p. 461.

Sakai, J.; Matsushima, I.; Kamemura, Y.; Tanimura, M. and Osuka, T., (1982)
Proceeding of Inter. Conference of Duplex Stainless Steels, The USA, Paper (8201-010), p. 211.

Schaeffler, A.L., (1949)
Metal Progress, **56**, p. 680.

Schuller, H. J., (1965)
Arch. Eisenhuttenwes, **34**, p. 61.

Schweitzer, P.A., (1983)
Corrosion and Corrosion Protection Handbook, Second Edition, p. 69-84.

Sedriks, A.J., (1979)
Corrosion of Stainless Steels, Wiley, p.50-67.

Sedriks, A. J., (1983)
Inter. Metal Reviews, **28**, p. 295.

Seferian, D., (1959)
Metallurgie de la Soudure, Dunod, Paris.

Skuin, K. and Kreyssing, T., (1978)
Neue Hutte, **23(1)**, p. 22.

Smith, R. and Nutting, J., (1957)
British Journal of Applied Physics, **7**, p. 214-217.

Solomon, H.D. and Devine, T.M., (1979)
Mi Con 78, ASTM STP, p.430.

Southwick, P. D., (1978)
Ph.D. Thesis, University of Cambridge, Dept. of Mat. Sci. and Metallurgy.

Southwick, P.D., and Honeycombe, R.W.K., (1980)
Met. Sci., **14**, p. 253.

Strangwood, M. and Druce, S.G., (1990)
Material Science and Technology, **6**, 237.

Strutt, A.J.; Lorimer, G.W.; Roscoe, C.V. and Gradwell, K.J., (1986)
Proceeding of Inter. Conference of Duplex Stainless Steels, The Hague, The Netherlands, Paper 3, p. 310.

Sully, A.H. and Brandes, E.A., (1967)
Chromium, 2nd Edition, p. 77.

Sump, C. H. and Bodine, G. C., (1982)
Proceeding of Inter. Conference of Duplex Stainless Steels, The USA, Paper 8201-004, p. 71.

Suutala, N., (1983)
Third Scandinavian Symposium in Material Science, Finland, p. 53.

Suutala, N.; Takalo, T. and Mosio, T., (1979)
Met. Trans., **10A**, p. 513.

Thorvaldsson, T.; Erickson, H.; Kutka, J. and Salwen, A., (1985)
Proceeding of Inter. Conference of Stainless Steels, The Institute of Metals, p. 101.

Truman, J.E., Coleman, M.J. and Pirt, K.R., (1977)
Br. Corros. J., **12**, p. 236.

Truman, J.E., (1979)
Stainless Steel Industry, **7(39)**, p.3.

Truman, J.E., (1980)
The Metallurgist and Materials Technologist, **2**, p.75.

Wilde, B. E., (1977)
U.S. Patent, No. 4002510, Issued January 11th 1977.